Title
Three-Dimensional Coded Aperture and Compton Gamma-Ray Imaging for Near-field Applications

Author
Frame, Emily Anne

Publication Date
2022

Peer reviewed|Thesis/dissertation

Three-Dimensional Coded Aperture and Compton Gamma-Ray Imaging for Near-field Applications

by

Emily Anne Frame

A dissertation submitted in partial satisfaction of the

requirements for the degree of

Doctor of Philosophy

in

Nuclear Engineering

in the

Graduate Division

of the

University of California, Berkeley

Committee in charge:

Professor Kai Vetter, Chair
Professor Lee Bernstein
Professor Michael Nacht
Professor Jasmina Vujic

Fall 2022

Three-Dimensional Coded Aperture and Compton Gamma-Ray Imaging for Near-field Applications

Abstract

Three-Dimensional Coded Aperture and Compton Gamma-Ray Imaging for Near-field Applications

by

Emily Anne Frame

Doctor of Philosophy in Nuclear Engineering

University of California, Berkeley

Professor Kai Vetter, Chair

There is an ever-growing need for instrumentation that provides both high-resolution and sensitive three-dimensional (3-D) gamma-ray imaging capabilities across a wide range of photon energies under near-field conditions. Such technology is particularly critical to the fields of emergency response and contamination remediation, nuclear security and safeguards, and nuclear medicine. To meet this technological demand, this dissertation presents a proof-of-principle gamma-ray imaging prototype that functions as both a coded aperture and Compton imager, with the former modality suited to energies below a few hundred keV and the latter suited to energies above a few hundred keV. This prototype integrates a novel coded aperture design with a Compton camera that consists of two high-purity germanium (HPGe) double-sided strip detectors (DSSDs). The two imaging modalities are operated serially in the near field via a single detection system. The design and pattern optimization of the coded aperture as well as the methodologies developed for coded aperture and Compton image reconstruction are discussed. Furthermore, this work includes 3-D gamma-ray images of sources of various shapes and energies ranging from about 100 keV to 1 MeV in the near field to demonstrate the broad imaging capabilities of the system.

This dissertation investigates the collective use of coded aperture and Compton imaging in the fields of nuclear safeguards and nuclear medicine. In nuclear safeguards, uranium holdup is one of the more insidious problem of materials accounting and control. Both coded aperture and Compton imaging can be applied to solve this problem, offering the possibility of visualizing and quantifying uranium holdup via the 186-keV gamma-ray emission of ^{235}U and 1001-keV gamma-ray emission of ^{238}U, respectively. Three-dimensional coded aperture and Compton images of highly-enriched uranium (HEU) pellets are included in this work.

Another important application of the proposed technology is facilitating the development of a powerful cancer treatment known as targeted alpha-particle therapy (TAT). Arguably the most promising TAT radionuclide that has been proposed is ^{225}Ac. The development of

^{225}Ac-based radiopharmaceuticals has been hampered due to the lack of effective means to study the daughter redistribution of these agents in small animals at the preclinical stage. The ability to directly image the daughters, namely ^{221}Fr and ^{213}Bi, via their gamma-ray emissions would be a boon for preclinical studies. That said, conventional medical imaging technologies, including single photon emission computed tomography (SPECT) based on pinhole or parallel-hole collimation, cannot be employed due to sensitivity limitations. As an alternative, this dissertation investigates the use of coded aperture and Compton imaging as complementary modalities to image ^{221}Fr via its 218-keV gamma-ray emission and ^{213}Bi via its 440-keV gamma-ray emission, respectively. This work includes images of ^{221}Fr and ^{213}Bi in tumor-bearing mice injected with ^{225}Ac-based radiopharmaceuticals. These results are the first demonstration of visualizing and quantifying the ^{225}Ac daughters in small animals via gamma-ray imaging and serve as a stepping stone for future radiopharmaceutical studies.

To all who have inspired me.

Contents

List of Figures

List of Tables

List of Acronyms

ARM Angular Resolution Metric

CLI Cerenkov Luminescence Imaging

CT Computed Tomography

CZT Cadmium Zinc Telluride

DSSD Double-Sided Strip Detectors

FBP Filtered Back-Projection

FCFV Fully-Coded Field-of-View

FDA Food and Drug Administration

FWHM Full-Width at Half-Maximum

GGH Generalized Geometry Holdup

HEU Highly Enriched Uranium

HPGe High-Purity Germanium

IAEA International Atomic Energy Agency

LBNL Lawrence Berkeley National Laboratory

LET Linear Energy Transfer

MIP Maximum Intensity Projection

ML-EM Maximum-Likelihood Expectation-Maximization

MRI Magnetic Resonance Imaging

MURA Modified Uniformly Redundant Arrays

NMAC Nuclear Materials Accounting and Control

NNSA National Nuclear Security Agency

ORNL Oak Ridge National Laboratory

PCFV Partially-Coded Field-of-View

PET Positron Emission Tomography

ROI Region-of-Interest

SIS Struck Innovative Systems

SNM Special Nuclear Material

SNR Signal-to-Noise Ratio

SPECT Single Photon Emission Computed Tomography

TAT Targeted Alpha-Particle Therapy

TRT Targeted Radionuclide Therapy

TV Total Variation

UCSF University of California San Francisco

UPS Uninterruptible Power Supply

URA Uniformly Redundant Arrays

WGU Weapons Grade Uranium

Acknowledgments

The following acknowledgements have been the most daunting to write. They represent to me the closing credits of a major chapter in my life. A chapter full of academic and personal growth, good and bad adventures, and several remarkable people without whom this dissertation would not be possible. To these people, I want to express my gratitude. The sincerest way I know how is by sharing my inner thoughts.

For almost decade, I've documented all aspects of my life in journals - Moleskin only. A recommendation given by my Dad for easing my anxiety. Included below are several entries that highlight those who have shaped my time in grad school.

To my advisor, Kai. Your enthusiasm and encouragement kept me going.

> *06 March 2017. Berkeley, CA. I'm positive Kai thinks I'm an idiot. I had the dumbest response to one of his questions in class today. God, how embarrassing.*
>
> *27 January 2018. Hiroshima, Japan. From Miyajima, we rushed to the symposium and arrived at the poster session just in time. I was happy when Kai stopped by my poster. We had an enjoyable chat. The oral presentations followed. I nodded off during the presentations themselves, but livened up when Kai provided commentary at the end. He did a phenomenal job educating the speakers and audience on the not-so-harmful levels of radiation.*
>
> *07 July 2022. Berkeley, CA. In the morning, I met with Kai, Lucian, and Don. We discussed my progress on the small-animal paper. Kai showed great excitement when I presented the quantification estimates. His excitement motivates me tremendously. In fact, I had the most productive day.*
>
> *10 October 2022. Berkeley, CA. Following my presentation at group meeting, Kai and I grabbed a coffee together. We discussed the matter of the author list, and while he doesn't fully agree with my stance, he supports my decision. At some point in the conversation, he told me that he was proud of all that I have accomplished. I needed to hear that, especially now at a time when I've been doubting myself.*

To my mentors, Don and Lucian. I couldn't have asked for a more complementary team of researchers. Don, the mathematician and theorist. Lucian, the experimentalist. Thank you for hanging in there with me - through all of the late nights and weekends.

> *19 February 2019. Berkeley, CA. Had my first meeting with Don up at LBL. He went over the basics of image reconstruction. I find him to be both incredibly knowledgeable and humble - a refreshing combination in academia. He'll make for a good mentor.*

18 December 2019. Berkeley, CA. A late night in lab, frantically prepping the detectors for tomorrow's measurement. Pump-down, cool-down, ramp-up. Everything was going wrong. I called Lucian in a panic and projected my frustrations on him. He was patient. The problems are now fixed. I feel terrible, knowing that I must have disrupted his family time. I called back to apologize.

03 March 2022. Berkeley, CA. Lucian invited me to give a talk at his startup, Ziteo, this afternoon. The talk was followed by a tour of the lab and office space. I was impressed by the legitimacy of it all. Until today, I merely saw Lucian as my mentor, not the boss of his own company. Thinking about the tireless hours that he's spent with me - guiding me through both lab and life. And now realizing that he has been simultaneously building his own company. He finds the time.

05 May 2022. Berkeley, CA. Don met me at Etcheverry this afternoon. We spent over six hours - nonstop - working in that wretched basement. There's a problem with the Compton image reconstruction. We got nowhere.

To the National Nuclear Security Consortium. Thank you for funding this work under award numbers DE-NA0003180 and DE-NA0003996 and providing me with unique research opportunities.

18 July 2017. Las Vegas, NV. A long drive to the Nevada Test Site - the desert spanned miles. The DAF is in complete isolation, surrounded by wire fencing. As we stepped out of the car, the heat immediately hit me. Over an hour wait at the security checkpoint. Once cleared, we toured the inside. An over-designed facility, originally built for the production and testing of nuclear weapons. Funny enough, by the time construction was complete, nuclear weapons testing was banned in the US. The DAF is now a site for conducting subcritical and critical experiments. We watched Godiva go critical. To be honest, I was more interested in the interlocking doors. Made of thick steel. Opening slowly in the most dramatic manner. The doors came in pairs. When the first door closed, the second opened.

To my friends. You all have filled my life with fun and laughter, alleviating the stresses of grad school. I wish I could highlight each and every one of you.

12 December 2017. Isla Del Sol, Bolivia. A four-hour bus ride to Copacabana. We were cramped in the back, where I passed out. Upon arrival, we had trout for lunch, a specialty of the area. From lunch, we took a private boat to Isla del Sol - a small island surrounded by Lake Titicaca. The lake itself is expansive and situated at over 4000 meters. Truly breathtaking. As soon as the boat docked, we dropped our bags at the hostel and trekked along the edge of the island to see the Inca ruins. For dinner, trout - again. Following, we found a random spot on the island, where we deliriously attempted to count all of the stars in the sky.

We got lost on the way back to the hostel, but eventually made it. Maria and I found our room to be infested with bugs. We convinced - maybe forced - Justin and Mauricio to share their room with us. Justin finagled his own twin bed, while Maria, Mauricio, and I shared the other twin. It was cramped to say the least. We awoke to sounds of the owner knocking on the door - he finally brought us the toilet paper. In the morning, we took turns in the shower. Freezing cold water and a shower head that, if adjusted slightly, would electrocute you. An experience to laugh back on.

03 March 2019. Berkeley, CA. I arrived home at 8 in the morning. Exhausted from the night. After less than two hours of sleep, I was awakened by a message from Chedly and Sachi. They spontaneously decided to rent a car and drive aimlessly up the coast. They convinced me - I hopped in the car. We drove along the 101 up to Salt Point. I stuck my head out of the window to take in the sun and salty air. I was rejuvenated, no longer exhausted. We had dinner at a quaint diner on the coast and climbed the rocks where we watched the sunset over the ocean. At dark, we drove home while listening to Sachi's sad song playlist. By the time we arrived to Berkeley, I was asleep in the backseat.

To my old housemates on MLK. The decor was always tacky.

05 May 2020. Berkeley, CA. Walked down to San Pablo with the roomies. We went grocery shopping at the Latin and Middle Eastern markets. On the way home, we found a blue velvet loveseat - only a few stains - on the street. We lugged it back to the house. The remainder of the afternoon was spent redecorating the living room to match the aesthetic of the couch. The day ended with a game of Codenames.

To my current housemates at the co-op on Hillegass & Parker (HIP). I see HIP as a microcosm of society in that 57 of us from all different cultural and socioeconomic backgrounds have come together under one roof. Together, somehow, we've formed a community. A community built on cooperation and dysfunction and filled with harmony and chaos. The lessons I've learned and memories I've made here will stay with me forever.

23 October 2021. Berkeley, CA. The Bay is experiencing a proper thunderstorm tonight. I stayed home this evening, keeping warm by the burning fireplace with several blankets wrapped around me. Sounds of crackling logs and raindrops tapping the window panes put me at peace. The windows were slightly cracked, letting in a fresh breeze. The cool air brushed against my face - a perfect contrast to the heat from the fire. I eventually migrated to the dining room where an assortment of odd festivities and intellectual conversations were taking place. As midnight approached, the number of housemates in the room grew exponentially; they were trickling in from their respective evenings. Many were drenched having just braved

the rain. At this point, the rain was hitting harder. I can't articulate why this particular moment was so special. A moment that I wish could have been frozen in time. Somehow 57 strangers from all walks of life have turned a mere house into a community.

Finally, to Mom and Dad. You both have instilled such independence in me, giving me the space to both make dumb mistakes and learn from them. I know I'm handful - always pushing the envelope as Mom would say. Nevertheless, you both are there for me for me when it matters most. The one constant through all of life's changes.

30 July 2014. Prague, Czech Republic. I picked up Mom, Dad, and Susan at the airport last night. Their flight was delayed. After getting settled at the hotel, they still had energy to explore the city. We went for a brief walk around Vaclavske Namesti, and from there, I took them to Popo for their first Czech beer. They seemed to appreciate the authentic hole-in-the-wall feel of the place. Afterwards, we went to my favorite kebab stand for a late-night snack. Interacting with them felt so familiar - even after six months of me being gone. I'm happy they're here.

21 April 2021. Wilmington, North Carolina. It's been a stressful couple of weeks between tensions at the co-op and an insurmountable pile of work. I needed to get out. I spontaneously booked tickets to Wilmington, hoping to recharge and clear my head. Dad picked me up from the airport and drove straight to the house. The last time we were together must have been the end of 2016. As I walked through the front door, everything felt oddly familiar despite this being my first visit to the new house. It was as if I were back home in Tennessee. The smell, the furniture - it was all the same.

Chapter 1

Introduction and Motivation

1.1 Gamma-Ray Imaging

Gamma-ray imaging is a powerful tool that can be used for the detection, localization, and characterization of radioactive sources. Such capabilities are critical to numerous applications, including astrophysics [1], emergency response and contamination remediation [2], nuclear security and safeguards [3], and nuclear medicine [4]. Of particular interest to this work is the role of gamma-ray imaging in resolving morphological features associated with the emission of gamma rays over a broad range of energies from 100 keV to 1 MeV in the near field. Here the near field is considered to be in the order of the extension of the imaging instrument and where beam divergence and solid angle effects need to be factored into the image reconstruction.

Gamma-ray imaging can be realized with different approaches, including gamma-ray optics based on diffractive or reflective lenses [5, 6, 7], spatially or temporally-modulating collimators [8, 9, 10, 11, 12, 13], and scattering instruments [14, 15, 16, 17]. For energies greater than 100 keV, lens-based systems are not practical due to the requirement of a large focal length. More appropriate is the use of either a collimator- or scattering-based imager. Both methods preferentially select gamma rays based on their incoming direction. The constraints on directionality are imposed so that photons incident on a detector can be easily traced back to their source of origin.

Collimator-based imaging alone encompasses a variety of techniques, including pinhole, parallel-hole, and coded aperture imaging. All of the above rely on elements of highly-attenuating material to physically select which gamma rays are observed by the detector. Scattering-based instruments, most relevantly Compton cameras, are distinguished by the absence of a collimator. Instead of restricting photons before detection, Compton cameras impose constraints after detection. These constraints are based on an interaction criterion and kinematics.

The simplest and most conventional of collimator-based imagers are those based on either pinhole or parallel-hole collimation. Such systems are known to achieve high spatial reso-

lution, but often suffer from poor imaging sensitivity as consequence of a collimator-driven trade-off between resolution and sensitivity. As an alternative, coded apertures were first introduced by Ables [8] and Dicke [9] to decouple the dependence of resolution on sensitivity; and thus provide the maximum possible sensitivity among collimator-based systems. The main idea behind the coded aperture design is to increase photon acceptance by opening many small pinholes arranged in an optimal fashion, as opposed to widening a single opening. However, as with any collimator, coded apertures experience a degradation of response at high photon energies, because unwanted photon penetration through the mask becomes more probable. For this reason, coded apertures are better suited to low photon energies, typically below a few hundred keV.

For energies above a few hundred keV, Compton-scattering-based imagers are appealing as these instruments rely on the dominant interaction process at these energies, namely Compton scattering, and they do not require a collimator that would otherwise decrease the instrument sensitivity. Recent advances in 3-D position-sensitive semiconductor detectors based on cadmium zinc telluride (CZT) and high-purity germanium (HPGe) have enabled the fabrication of compact Compton cameras that can be operated in a wide range of environments. These instruments, however, suffer in performance at energies below a few hundred keV. Photons in this energy range have a higher photoelectric absorption cross section, thereby inducing fewer Compton-scattering events. Furthermore, even if a low-energy photon induces a scattering event, the subsequently scattered photon often has a short range, which degrades the image resolution.

To enable effective operation across a wide range of photon energies, this work proposes coded aperture and Compton imaging as complementary modalities with the former suited to energies below a few hundred keV and the latter suited to energies above a few hundred keV. The proposed imager integrates a novel coded aperture design with a Compton camera, consisting of two HPGe double-sided strip detectors (DSSDs). This system does not combine coded aperture and Compton data to produce a single image as seen in past works [18, 19, 20], but rather employs the same detector to operate serially in two different modes. Several imagers with this capability have already been proposed [21, 22]. The key distinction is that the presented technology enables 3-D imaging in the near field.

Near-field operation enables both high sensitivity and lateral spatial resolution; and even depth resolution from a single viewing angle. While Compton cameras have been heavily investigated for near-field applications [14, 23], coded aperture imagers historically have been designed to work under far-field conditions, most notably for X-ray and gamma-ray astronomy [24] and some terrestrial imaging [25, 26]. In the past two decades, there has been some work in adapting the coded aperture concept to the near field [27, 28, 29]; and these works have shown that this adaptation comes with several challenges. Under near-field conditions, coded apertures are subject to more severe collimation and magnification effects, which can result in image degradation. Given these effects, little success has been achieved in 3-D coded aperture imaging in the near field. A decade-old study [29] presents a promising 3-D coded aperture image, but since then, there have been few, if any, demonstrations of such capabilities. The results presented here reinforce the idea that coded apertures have 3-D

imaging capabilities. Furthermore, this dissertation demonstrates how the serial operation of 3-D coded aperture and Compton imagers can serve novel applications in the near field.

1.2 Applications

1.2.1 Nuclear Safeguards

The threat of unauthorized acts involving nuclear and other radiological materials has grown significantly since the end of the Cold War. Events such as the attacks on September 11, 2001 in the United States have reinforced the idea that terrorist organizations are capable of conducting large-scale violent operations to pursue their aims and have the potential to engage in nuclear terrorism. In addition to civilian fatalities, a main objective of terrorism is to inflict maximum psychological and financial damages.

The potential for using radiological materials to achieve these ends can be illustrated by one of the most harmful radiological accidents to date, the "Goiania Accident". In the mid-1980s, a ^{137}Cs orphan source from an abandoned radiotherapy machine in Goiania, Brazil was stolen, dismantled, and sold for parts. As a result, over $100,000$ people had to be surveyed, and of these, over 300 were found to be contaminated [30]. The cost of the response and remediation was huge, on the order of tens of millions (in USD). Even today, the psychological impact still lingers - a stigma associated with being from the region [31].

In response to the threat of radiological materials, intentionally or unintentionally, getting into the wrong hands, the International Atomic Energy Agency (IAEA) and National Nuclear Security Agency (NNSA) have led global and national efforts to establish reliable systems of nuclear materials accounting and control (NMAC). According to the IAEA, one of the main objectives of a NMAC system is:

> *to maintain and report accurate, timely, complete and reliable information on the locations, quantities and characteristics of nuclear material present at the facility* [32]

for the purpose of detecting any actions that could lead to the unauthorized removal or misuse of nuclear materials. Among all possible criminal acts, those involving special nuclear material (SNM), including ^{235}U and ^{239}Pu, evoke the most concern. This concern is due to the fact that only a small difficult-to-detect mass of SNM is required to create a catastrophic event.

One of the key elements of a NMAC system at a facility level is instrumentation that can localize and quantify nuclear material. Nondestructive instruments based on passive gamma-ray detection are oftentimes employed for such purposes as most nuclear materials have gamma-ray signatures. Currently, the majority of detection systems employed at nuclear facilities are solely capable of gamma-ray spectroscopy. These conventional methods depend on assumptions about the material shape and activity distribution to enable

quantification. Such assumptions introduce errors, which can lead to material loss. Three-dimensional gamma-ray imaging can be applied to solve this problem. The ability to visualize nuclear materials would eliminate the need for so many assumptions, thereby providing more accurate quantification estimates.

1.2.2 Nuclear Medicine

Nuclear medicine is one of the more integral and dynamic branches of medicine with continual innovations in technology and diagnostic and therapeutic agents. This medical speciality employs biomolecules tagged with radioisotopes to diagnose and treat diseases as well as study physiological functions. These agents, known as radiotracers in diagnostics and radiopharmaceuticals in therapy, seek out specific molecular targets or hallmarks of disease in the body.

In diagnostics, radiotracers typically emit photons, either directly or indirectly, so that the tracer can be non-invasively visualized throughout the body using an external imaging device. Currently, there are two imaging modalities employed in nuclear medicine, those based on either single photon emission computed tomography (SPECT) or positron emission tomography (PET). These non-invasive systems provide longitudinal (i.e. relating to the observation of data on the same subject at multiple time points) and quantitative images that can be used to diagnose a wide range of diseases and/or monitor disease-specific treatments.

Switching out a diagnostic radioisotope for one that emits a different type of radiation, such as beta or alpha particles, converts the radiotracer into a radiopharmaceutical for radioimmunotherapy or targeted radionuclide therapy (TRT). Although much of nuclear medicine focuses on diagnostics, there has been growing interest in TRT. The first successful application of TRT took place in 1946 with the use of ^{131}I for the treatment of hyperthyroidism [33]. Since then, an increasing number of radionuclides and biomolecule combinations have been explored to treat a broad spectrum of diseases from non-Hodgkin's lymphoma to prostate carcinoma.

Great attention has been given to alpha-particle-based radiopharmaceuticals since the U.S. Food and Drug Administration (FDA) approved ^{223}Ra-dichloride for castration-resistant prostate cancer in 2013 [34]. A vital step in FDA approval is the preclinical evaluation of the drug under investigation in small animal models of human disease. Due to clinical familiarity, PET and SPECT scanners have been popular tools in preclinical studies. Over the past two decades, great strides have been made in improving the resolution of these two modalities to be useful for small animals. However, conventional PET and SPECT systems are applicable to a limited category of radionuclides, and the latter modality suffers from poor imaging sensitivity. All of the above have challenged their use in the investigation of novel alpha-particle therapies, particularly those based on ^{225}Ac. Overcoming the limitations of conventional PET and SPECT technologies is of particular interest to this work, which investigates alternative imaging modalities based on coded aperture and Compton techniques.

1.3 Dissertation Structure

This dissertation focuses on 3-D coded aperture and Compton gamma-ray imaging for near-field applications. The role of these two modalities in nuclear safeguards and the preclinical evaluation of targeted alpha-particle therapy (TAT) is of great interest here. Chapter 2 provides an overview of TAT. Chapter 3 introduces fundamental principles in gamma-ray imaging, specifically those pertaining to coded aperture and Compton imaging. Chapter 4 introduces a proof-of-principle gamma-ray imaging prototype, hereinafter referred to as the Dual-Modality Imager, which functions as both a coded aperture and Compton imager. All methods critical in the development and implementation of the Dual-Modality Imager are discussed in this chapter. Chapter 5 demonstrates the broad imaging capabilities of the Dual-Modality Imager by presenting 3-D images of gamma-ray sources of various shapes and energies in the near field. These results include images of HEU pellets and tumor-bearing mice injected with ^{225}Ac agents. The former images are of relevance to nuclear safeguards, and the latter are of growing interest to TAT. Finally, Chapter 6 summarizes this work and discusses opportunities for further study.

1.4 Relevant Papers

This dissertation includes content from the following papers, of which I am the first author:

- **E. Frame**, R. Barnowski, D. Gunter, L. Mihailescu, and K. Vetter, "A dual-modality volumetric gamma-ray imager for near-field applications," *IEEE Transactions on Nuclear Science*, 2022. [35]
- **E. Frame**, K. Bobba, D. Gunter, L. Mihailescu, A. Bidkar, R. Flavell, and K. Vetter, "Coded aperture and Compton imaging for the development of targeted alpha-particle therapy," *under submission*, 2022. [36]

Chapter 2

Targeted Alpha-Particle Therapy

Chapter 2 provides a high-level view of targeted alpha-particle therapy (TAT), a type of targeted radionuclide therapy (TRT) based on alpha-particle emissions. To begin, Section 2.1 provides a general overview of TRT with a focus on radionuclide selection. Section 2.2 discusses the advantages of using alpha particles for therapy and evaluates three promising alpha-particle emitters for TAT: ^{211}At, ^{225}Ac, and ^{213}Bi in terms of their decay characteristics, production pathways, and clinical implementation. Finally, Section 2.3 discusses conventional methods for studying radiopharmaceuticals in a preclinical setting and presents limitations in applying such methods to the evaluation of alpha-particle emitters. This discussion sets the stage for the remainder of this work, which seeks to develop and implement an alternative preclinical tool for evaluating TAT.

2.1 Targeted Radionuclide Therapy

The objective of cancer therapy is to destroy malignant cells while minimizing damage to healthy tissue. The most conventional non-surgical treatments are chemotherapy and external beam radiation therapy due to their high cytotoxicity. Unfortunately, the non-specificity of these treatments can result in toxic side effects.

Over the last few decades, there has been a greater understanding of the molecular differences between diseased and normal cells. This knowledge has led to the development of targeted radionuclide therapy (TRT), also known as just radionuclide therapy. Unlike conventional therapies, TRT employs a combination treatment that consists of radionuclides bonded tightly to tumor-specific carrier molecules. The carrier molecules facilitate the delivery of the radionuclides to the targeted tissue. By combining the specificity of molecular targeting with the cytotoxicity of ionizing radiation, TRT offers great promise of selective cell killing.

The potential success of TRT depends critically on the choice of both the radionuclide and carrier molecule or delivery agent. While a complete evaluation of suitable delivery agents is beyond the scope of this work, the following are key considerations. The carrier

molecule should have rapid tumor uptake with minimal binding in non-target tissue. Furthermore, the metabolic components and excretion routes should be considered. An ideal radiopharmaceutical has rapid clearance without redistribution to healthy tissue. Once the pharmaceutical reaches the tumor site, a radionuclide is required that maximizes the radiation dose in the tumor while sparing the surrounding radiosensitive tissue. The following section details important considerations in selecting radionuclides for TRT.

2.1.1 Radionuclide Selection

Several factors govern the suitability of a radionuclide for TRT. While the selection process is often driven by practical considerations such as ease of production and cost, the success of the treatment requires careful consideration of the physical attributes of the radionuclide. Specifically, its decay characteristics should be well-suited to the size and presentation of the cancer.

Table 2.1 summarizes key attributes of clinically-relevant radionuclides. The first consideration is the physical half-life as this characteristic directly relates to the rate at which the radiation dose is delivered. The optimal dose rate generally requires the physical half-life to match the biological turnover of the radiopharmaceutical *in vivo*. A shorter half-life or faster decay rate is particularly suited to rapidly dividing tumors, while a longer half-life or slower decay rate can prove more effective for indolent malignancies. That said, a longer physical half-life may also be associated with a suboptimal dose rate.

Table 2.1: Physical characteristics of therapeutic radionuclides.

Isotope	Type [particles/decay]	Half-life	Max Particle Energy [MeV]	Mean Range in Tissue [mm]	γ-ray Emissions [keV]
^{67}Cu	β (100%)	61.8 hr	0.577	0.27	91.3 (7.01%) 93.3 (16.1%) 184 (48.7%)
^{177}Lu	β (100%)	6.73 day	0.498	0.28	113 (6.43%) 208 (11.1 %)
^{131}I	β (100%)	8.02 day	0.807	0.40	284 (6.15 %) 364 (81.7%) 637 (7.18 %)
^{186}Re	β (92.5%)	3.72 day	1.07	0.92	137 (9.42%)
^{188}Re	β (100%)	17.0 hr	2.12	2.43	155 (15.1%)

Isotope	Type [particles/decay]	Half-life	Max Particle Energy [MeV]	Mean Range in Tissue [mm]	γ-ray Emissions [keV]
^{153}Sm	β (100%)	46.3 hr	0.808	0.53	103 (30.0%) 69.7 (4.86%)
^{90}Y	β (100%)	64.0 hr	2.28	2.76	–
^{225}Ac	α (100%)	10.0 day	5.83	0.04-0.1	99.1 (1.02%)
^{211}At	α (41.8%)	7.21 hr	5.87	0.04-0.1	687 (0.261%)
^{212}Bi	α (35.9%)	60.6 min	6.09	0.04-0.1	727 (6.59%)
^{213}Bi	α (2.09%)	45.6 min	5.87	0.04-0.1	440 (26.1%)
^{224}Ra	α (100%)	3.66 day	5.69	0.04-0.1	241 (4.11%)
^{226}Th	α (100%)	30.6 min	6.34	0.04-0.1	111 (3.29%)
^{227}Th	α (100%)	18.7 day	6.04	0.04-0.1	50.1 (8.04%) 236 (12.4%) 256 (7.04%)
^{230}U	α (100%)	20.8 day	5.89	0.04-0.1	–
^{67}Ga	Auger (5.0%)	3.26 day	0.18	0.001-0.02	93.3 (39.2%) 184 (21.2%) 300 (16.8%)
^{123}I	Auger (13.7%)	13.3 hr	0.16	0.001-0.02	159 (83.0%)
^{125}I	Auger (23.0%)	59.4 day	0.35	0.001-0.02	35.5 (6.68%)

Other key considerations include the type and range of particle emissions as illustrated in Figure 2.1. Three types of emissions are relevant to TRT: Auger electrons, beta particles, and alpha particles. Of the three particulates, Auger electrons have the shortest range ($<$ 500 nm), traveling distances of less than a cell diameter. This means the radionuclide must be incorporated into the cell nucleus, if not into the DNA, to achieve cell kill. Despite this apparent limitation, studies have shown that Auger-electron emitters, most notably ^{67}Ga, ^{123}I, and ^{125}I, can play a significant role in the treatment of micrometastases due to

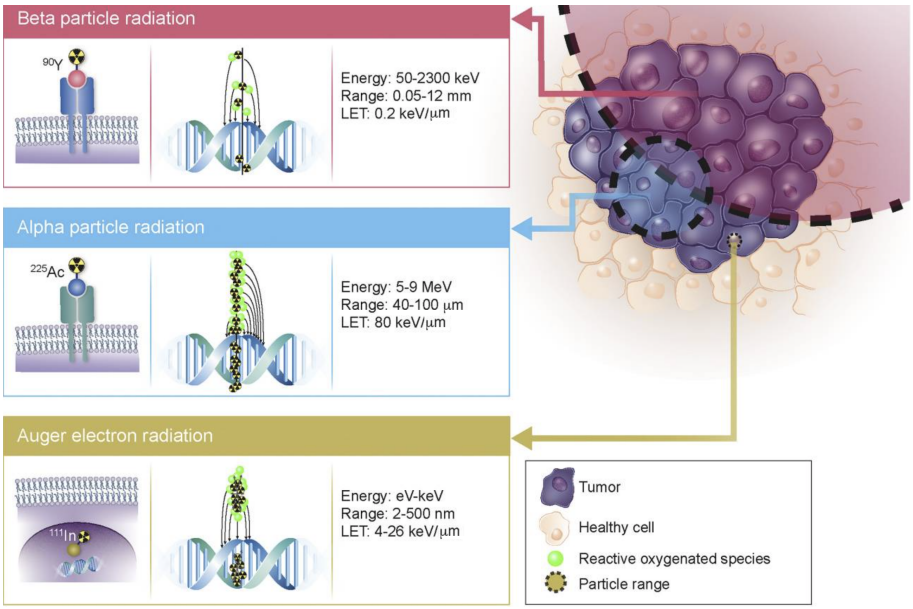

Figure 2.1: Comparison of particle energies, ranges, LETs, and DNA damage potencies [37].

their highly-localized and cytotoxic dose deposition [38, 39].

Both beta and alpha particles travel distances that exceed a cell diameter, making them better suited to pharmaceuticals that localize on the cell surface. An important implication of a longer range is the ability of a particle to induce damage to multiple neighboring cells. This so-called *crossfire effect* negates the need to target every cell within the tumor, but can also result in the damage of healthy tissue. This is particularly true if the particle range exceeds the extent of the targeted lesion.

Availability and familiarity with radiolabeling chemistry has generally supported the use of beta-particle emitters for TRT. Among those clinically-approved include ^{131}I, ^{90}Y, and ^{177}Lu. The relatively long ranges of beta particles makes them well-suited to medium to large-sized tumors. Their effectiveness, however, is challenged by a relatively low linear energy transfer (LET); around 0.2 keV/μm. This necessitates the administration of a high radionuclide concentration to achieve cell kill.

Historically, alpha-particle emitters have been disregarded for therapeutic use, owing largely to half-life constraints and complex decay schemes. Nevertheless, there has always been a growing interest in the use of alpha particles as they offer two distinct advantages over conventional beta-particle therapies. First, alpha particles enable more selective cell killing due to their shorter ranges, on the order of a few cell diameters (< 0.1 mm). This emission range is particularly suited to the treatment of leukemia, small lesions, and most metastatic diseases. Second, alpha-particle emitters are densely ionizing with an LET that is roughly 500 times greater than that of beta-particle emitters. Consequently, a lower activity of alpha-particle radiation can be administered to the patient.

2.2 Alpha-Particle Emitters

An alpha particle is a helium nucleus (^{4}He) with a mass that is roughly 8000 times larger than that of a beta particle. The heavy nature of alpha particles suppresses deflection, resulting in an almost linear track along which the maximum energy deposition occurs near the end. Unlike beta particles, alpha particles are nearly monoenergetic with an initial kinetic energy that typically falls between 5 and 9 MeV. This yields a corresponding emission range of 40 to 100 μm in tissue. Given their short range, alpha particles induce a crossfire effect that can be easily contained within the targeted site, thereby minimizing toxic side effects.

Alpha particles are also advantageous in that they deposit energy within a small volume of tissue with a mean energy deposition of 80 keV/μm. With such high LET, alpha particles are effective at cell killing. In other words, the primary target of high-LET radiation is the cell DNA in which a single particle track is likely to produce an irreparable double-strand break. In contrast, low-LET emissions, such as beta particles, exhibit less cytotoxicity as they are more likely to produce reparable single-strand breaks.

The list of viable alpha-particle emitters for TAT is admittedly short for reasons including impractical half-lives, complex decay pathways, unresolved chemistry, limited availability and/or production constraints. By eliminating these obstructions, alpha-particle radiation will undoubtably serve as a powerful tool for cancer therapy. Table 2.2 summarizes radionuclides that are actively being studied for TAT. The following sections provide a thorough review of the more promising candidates, namely ^{211}At, ^{225}Ac, and ^{213}Bi.

Table 2.2: Candidates for TAT.

Parent	Daughters	Half-life	α/decay	Max α Energy [MeV]	Other Decay	γ-ray Emissions [keV]
^{225}**Ac**†		10.0 day	100%	5.83	–	99.1 (1.02%)
	^{221}Fr	4.90 min	100%	6.34	–	218 (11.6%)
	^{217}At	32.3 ms	99.9%	7.07	β (0.0120%)	–
	^{213}**Bi**†	45.6 min	2.09%	5.87	β (97.9%)	440 (26.1%)
	^{213}Po	4.20 μs	100%	8.38	–	
	^{209}Tl	2.20 min	–	–	β (100%)	117 (84.3%) 465 (96.9%) 1567 (99.8%)
	^{209}Pb	3.25 hr	–	–	β (100%)	–
	^{209}Bi	stable	–	–	–	–
^{211}**At**†		7.21 hr	41.8%	5.87	EC (58.2%)	–
	^{211}Po	0.516 s	100%	7.45	–	
	^{207}Bi	31.6 y	–	–	EC (100%)	570 (97.7%)
	^{207}Po	stable	–	–	–	–

Parent	Daughters	Half-life	α/decay	Max α Energy [MeV]	Other Decay	γ-ray Emissions [keV]
^{224}**Ra**†		3.66 day	100%	5.69	–	241 (4.11%)
	^{220}Rn	55.6 s	100%	6.29	–	–
	^{216}Po	0.145 s	100%	6.78	–	–
	^{212}Pb	10.6 hr	–	–	β (100%)	239 (43.3%)
						300 (3.28%)
	^{212}**Bi**†	60.6 min	35.9%	6.09	β (64.1%)	727 (6.58%)
	^{212}Po	0.299 μs	100%	8.78	–	–
	^{208}Tl	3.05 min	–	–	β (100%)	510 (22.5%)
						583 (84.5%)
						2615 (99.0%)
	^{208}Pb	stable	–	–	–	–
^{227}**Th**†		18.7 day	100%	6.04	–	50.1 (8.04%)
						236 (12.4%)
						256 (7.04%)
	^{223}**Ra**†	11.4 day	100%	5.87	–	154 (5.62%)
						269 (13.7%)
						324 (3.94%)
	^{219}Rn	3.96 s	100%	6.82	–	271 (10.8%)
						402 (6.37%)
	^{215}Po	1.78 ms	100%	7.39	–	–
	^{211}Pb	36.1 min	–	–	β (100%)	405 (3.79%)
						832 (3.53%)
	^{211}Bi	2.14 min	99.7%	6.62	β (0.276%)	351 (12.9%)
	^{207}Tl	4.77 min	–	–	β (100%)	–
	^{207}Pb	stable	–	–	–	–
^{230}**U**†		20.8 day	100%	5.89	–	–
	^{226}**Th**†	30.6 min	100%	6.34	–	111 (3.29%)
	^{222}Ra	38.0 s	100%	6.56	–	324 (2.78%)
	^{218}Rn	35.0 ms	100%	7.13	–	–
	^{214}Po	164 μs	100%	7.69	–	–
	^{210}Pb	22.3 yr	–	–	β (100%)	–

† Alpha emitters of interest.

2.2.1 Decay Characteristics

Astatine-211

Figure 2.2 illustrates the decay scheme of ^{211}At. Astatine-211 has a half-life of 7.21 hours, which is attractive for a number of reasons. These include providing sufficient time for both isotope separation and radiolabeling and being well-suited to the pharmacokinetics of a variety of delivery agents such as peptides and monoclonal antibodies. Astatine-211 decays via a branched pathway to stable ^{207}Pb. Each pathway yields a single alpha-particle emission. The most probable decay route starts with electron capture to ^{211}Po. Polonium-211 decays rapidly via alpha-particle emission to ground state, followed by the emission of 77- to 92-keV X rays. Several studies have demonstrated these emissions to be useful for *in-vivo* imaging of ^{211}At [40, 41], the possibility of which would enable the treatment to be monitored. The alternative decay route of ^{211}At begins with direct alpha-particle emission to ^{207}Bi. Bismuth-207 decays via electron capture to ground state, followed by the emission of a 570-keV gamma ray. Attempts have been made to image ^{211}At via this gamma-ray emission [42, 43]. However, the 570-keV emission line was shown to be statistically disadvantageous due to the long 31.6-year half-life of ^{207}Bi.

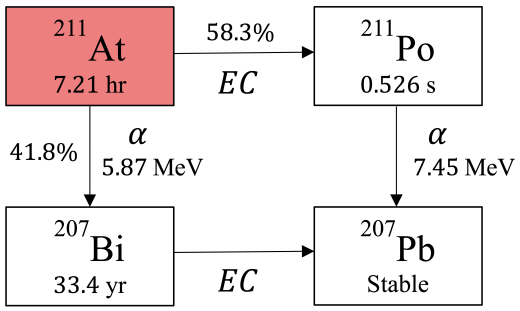

Figure 2.2: Decay scheme of ^{211}At.

Actinium-225/Bismuth-213

Figure 2.3 illustrates the decay scheme of ^{225}Ac (and ^{213}Bi). Actinium-225 is a relatively long-lived radiometal with a half-life of 10 days and decays via a branched pathway to near stable ^{209}Bi. Each pathway consists of six short-lived daughters and yields four alpha particles. The predominant decay route of ^{225}Ac shows alpha-particle contributions from the daughters ^{221}Fr (4.90 min half-life), ^{213}Bi (45.6 min half-life), and ^{213}Po (4.2 μs half-life). Furthermore, ^{221}Fr and ^{213}Bi emit highly-abundant gamma rays following their decay. The former daughter emits a 218-keV photon with a branching ratio of 11.6% and the latter emits a 440-keV photon with a branching ratio of 26.1%.

Given the rapid cascade of alpha-particle emissions from its decay progeny, ^{225}Ac has strong appeal as a so-called in-vivo generator, known more recently as a nanogenerator. The

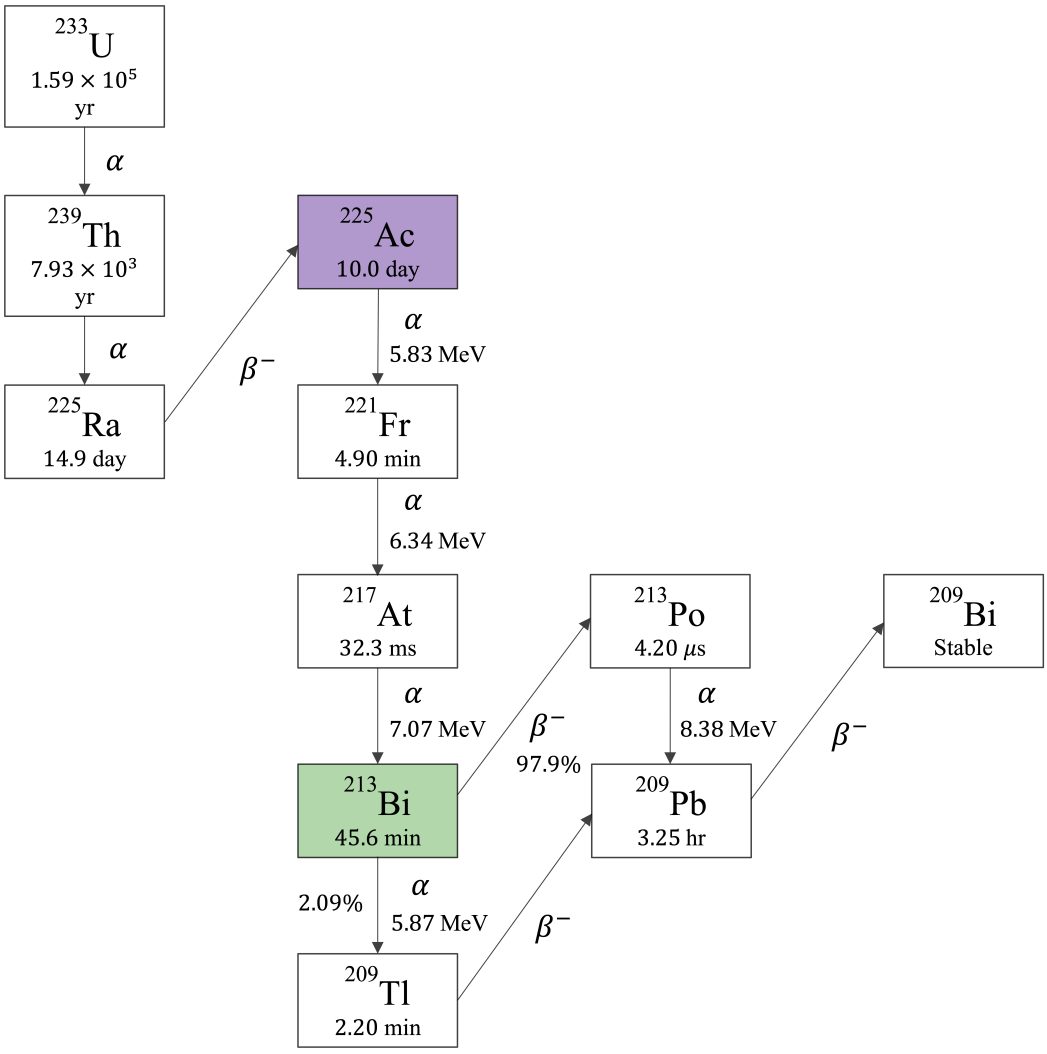

Figure 2.3: Decay scheme of ^{225}Ac and ^{213}Bi.

long half-lives of nanogenerators can permit an efficient delivery to the tumor site at which alpha particles from the daughters can be produced *in vivo*. If retention of the daughters is realized, the tumor cells can be eradicated with greater efficacy.

Embedded within the ^{225}Ac decay scheme exists a more widely-studied radionuclide for TAT - the great granddaughter ^{213}Bi. Bismuth-213 has a significantly shorter half-life of only 45.6 minutes, which would necessitate an onsite ^{225}Ac/^{213}Bi generator system to enable clinical use. Bismuth-213 decays via a branched pathway to ^{209}Bi. Each pathway yields a single alpha-particle emission. The predominant branch begins with beta-particle emission to ^{213}Po. Polonium-213 decays rapidly to ground state by alpha-particle emission. The alternative decay route of ^{213}Bi starts with direct alpha-particle emission to ^{209}Tl. Thallium-

209 decays via beta-particle emission to ground state with the accompaniment of gamma rays at 117 keV and 465 keV. These photon emissions are not statistically advantageous for imaging due to the 2.09% branching ratio of the decay pathway. Comparatively, the 440-keV gamma ray emitted directly by ^{213}Bi is more prevalent; and thus more advantageous for imaging.

2.2.2 Production

Astatine-211

The research and development of ^{211}At-based radiopharmaceuticals has been severely impeded by its limited availability. The production of ^{211}At can be realized via the decay of spallation-produced ^{211}Rn. However, this approach is too complex and time-consuming to meet the demands of routine clinical production. Currently, the predominant nuclear reaction to produce ^{211}At is direct activation of natural bismuth, generally in metallic form, with alpha particles. The activation of bismuth: $^{209}\mathrm{Bi}(\alpha, 2n)^{211}\mathrm{At}$ is possible at energies ranging from 21 to 40 MeV with a maximum cross-section at 31 MeV. In this energy range, however, ^{210}At can be produced as well. Astatine-210 is not compatible with pharmaceutical applications for the following reason. With an 8.1-hour half-life, ^{210}At decays to ^{210}Po. Polonium-210 is a long-lived and highly-toxic radioisotope, particularly to the bone marrow. To limit the production of ^{210}At, the alpha-particle beam energy must be restricted to 28-29 MeV. Unfortunately, there are only a few cyclotrons in the United States that are capable of accelerating alpha particles to energies beyond 28 MeV; thereby limiting the availability of ^{211}At [44, 45].

Actinium-225/Bismuth-213

The main production route of $^{225}\mathrm{Ac}/^{213}$Bi is based on radiochemical separation from ^{229}Th sources, which originate from the decay of fissile ^{233}U. The majority of ^{233}U was produced between 1954 and 1970 via neutron irradiation of ^{232}Th for the purpose of fueling nuclear weapons and reactors. Between 1995 and 2005, ^{229}Th was extracted from the ^{233}U stockpiles and stored at Oak Ridge National Laboratory (ORNL, Oak Ridge, TN) [46]. To-date, ORNL is the only facility in the United States producing significant amounts of ^{225}Ac with a maximum annual production of 33 GBq. While this amount is sufficient to conduct preclinical studies and some clinical testing, the current supply of ^{225}Ac is insufficient for medical use in hospitals worldwide. Consequently, a variety of accelerator-based production pathways have been investigated, including the irradiation of ^{232}Th targets with highly-energetic protons and the irradiation of ^{226}Ra targets with neutrons, protons, deuterons or photons. As of now, the most aggressively pursued of these routes include $^{226}\mathrm{Ra}(\gamma, n)^{225}\mathrm{Ra}$ and $^{226}\mathrm{Ra}(n, 2n)^{225}\mathrm{Ra}$, both of which produce ^{225}Ra to serve as a "cow" for ^{225}Ac [47].

2.2.3 Clinical Studies

Astatine-211

Two clinical phase I trials have been conducted using ^{211}At-labeled antibodies: the first as a treatment for recurrent malignant brain tumors [48] and the second as an ovarian cancer treatment [49]. In the brain cancer study, 71 to 347 MBq of ^{211}At-ch81C6 was administered locally into a resection cavity of eighteen patients at Duke University (Durham, North Carolina). No patient enrolled in the study showed dose-limiting toxicity. Furthermore, the median survival time was 54 weeks. This clinical trial demonstrated that TAT with ^{211}At-ch81C6 can be safe and result in the prolonged survival of patients with recurrent brain tumors. In the second clinical trial, nine women with recurrent ovarian carcinoma were treated via an intraperitoneal injection of ^{211}At-MX35 F(ab′)$_2$ at the University of Gothenburg, Sweden. The results indicate a well-tolerated treatment with no toxic side effects.

Actinium-225/Bismuth-213

A number of clinical trials have been initiated and executed using ^{213}Bi- and ^{225}Ac-labeled radioconjugates for the treatment of leukemia, Non-Hodgkins lymphoma, malignant melanoma, bladder cancer, glioma, neuroendocrine tumors, and prostate cancer. These trials are summarized in Table 2.3.

The pioneering first-in-human study that paved the way for TAT evaluated the use of an anti-CD33 antibody (HuM195) radiolabeled with ^{213}Bi [50]. Eighteen patients with relapsed myeloid leukemia were treated with 10 to 37 MBq/kg of ^{213}Bi-HuM195. While myelosuppression was seen in all evaluable patients, the treatment produced no extramedullary toxicity. The drug rapidly localized to expected areas of leukemia involvement, including the bone marrow, liver, and spleen, without significant uptake in other organs. Furthermore, 14 of 15 evaluable patients had reductions in circulating blasts, and 14 of 18 patients had reductions in bone marrow blasts.

The development and implementation of ^{225}Ac-PSMA-617 marks a major advancement in TAT. The clinical efficacy of PSMA-617 radiolabeled with the beta-emitter ^{177}Lu inspired the idea of combining the ligand with the highly-cytotoxic alpha-particle emitter ^{225}Ac. The ligand PSMA-617 has several attractive pharmacokinetic properties, including fast tumor uptake, extended tumor retention, and rapid clearance of unbound ligand. The first clinical study of ^{225}Ac-PSMA-617 was conducted at the University Hospital Heidelberg in Germany [51]. Two patients with late-stage metastatic castration-resistant prostate cancer were treated bimonthly with 100 kBq/kg of ^{225}At-PSMA-617 as a form of salvage therapy. The therapeutic efficacy was evaluated using ^{68}Ga-PSMA-11 PET/CT imaging. Figure 2.4 shows the PET/CT scans of the first patient, both before and after treatment. These images reveal remarkable therapeutic success. Following treatment, both patients experienced complete remission and showed no signs of hematologic toxicity.

Table 2.3: Clinical trials with ^{225}At-and ^{213}Bi-labeled radioconjugates. Adapted from [52].

Cancer	Radioconjugate	Patients	Ref [Year]
Leukemia	^{213}Bi-HuM195-mAb	18	[50] (2002)
	^{213}Bi-HuM195-mAb	31	[53] (2010)
	^{225}Ac-HuM195-mAb	36	[54] (2017)
Lymphoma	^{213}Bi-anti-CD20-mAb	12	[55] (2004)
Melanoma	^{213}Bi-9.2.27-mAb	16	[56] (2005)
	^{213}Bi-9.2.27-mAb	22	[57] (2007)
	^{213}Bi-9.2.27-mAb	38	[58] (2011)
Bladder	^{213}Bi-anti-EGFR-mAb	9	[59] (2017)
	^{213}Bi-anti-EGFR-mAb	12	[60] (2018)
Glioma	^{213}Bi-Substance P	20	[61] (2006)
	^{213}Bi-Substance P	5	[62] (2010)
	^{213}Bi-Substance P	17	[63] (2010)
	^{213}Bi-Substance P	9	[64] (2018)
	^{213}Bi-Substance P	20	[65] (2019)
	^{225}Ac-Substance P	21	[66] (2020)
Neuroendocrine Tumors	^{213}Bi-DOTATOC	8	[67] (2014)
	^{225}Ac-DOTATOC	34	[68] (2015)
Prostate	^{225}Ac-PSMA-617	2	[51] (2016)
	^{225}Ac-PSMA-617	14	[69] (2017)
	^{225}Ac-PSMA-617	40	[70] (2018)

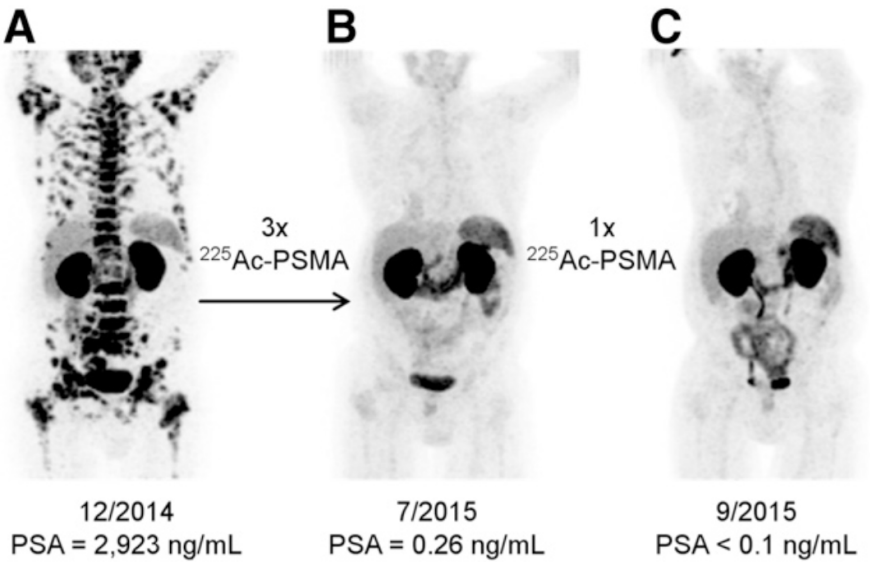

Figure 2.4: ^{68}Ga-PSMA-11 PET/CT scans of patient with metastatic prostate cancer undergoing TAT with ^{225}Ac-PSMA-617. (A) tumor spread before treatment, (B) two months after the third cycle of ^{225}Ac-PSMA-617, and (C) two months after one additional cycle [51].

2.2.4 Daughter Redistribution

Up until recently, TAT focused greatly on radionuclides with a single alpha-particle emission, including ^{211}At and ^{213}Bi. Clinical trials have demonstrated the feasibility and safety of these therapies. However, the short half-lives of ^{211}At and ^{213}Bi limit their therapeutic efficacy. For example, the treatment of solid tumors require longer penetration times; and thus longer-lived radionuclides. Furthermore, longer half-lives are needed in the treatment of tumors in less accessible sites, where the targeting agent is taken up slowly.

More recent studies have shown remarkable success with ^{225}Ac, a longer-lived nuclide with multiple alpha-particle emissions [51, 69, 70]. However, ^{225}Ac does not have a well-understood coordination chemistry, which limits the number of suitable delivery agents. Furthermore, the delivery agent will be challenged by the nuclear recoil effect associated with alpha-particle emission. This effect, in addition to the different chemical properties of the ^{225}Ac daughters, can result in their release from the radiopharmaceutical preparation. According to the conservation of momentum, the recoil energy imparted to an alpha-particle emitting daughter is

$$E_D = \frac{m_\alpha}{m_D} E_\alpha \tag{2.1}$$

where m_α is the rest mass of the alpha particle, m_D is the mass of the daughter nuclide, and

E_α is the kinetic energy of the alpha particle. In most cases, the recoil energy E_D of the daughter is at least 100 keV, which is more than 1000 times larger than the binding energy of any chemical compound.

If the alpha-particle emitting daughters are generated and retained inside the cancerous cells after internationalization, they can contribute to the cytotoxic effect. Otherwise, free daughters produced either on the surface of the target cell or during the circulation of the radiopharmaceutical can diffuse or be transported to various organs, thereby resulting in unwanted toxicity. In the case of ^{225}Ac, the redistribution of its longer-lived daughters, namely ^{221}Fr and ^{213}Bi, evokes the most concern. A greater understanding of their redistribution is needed before ^{225}Ac-based radiopharmaceuticals can be approved for clinical use.

2.3 Preclinical Studies of Alpha-Particle Emitters

The preclinical evaluation of novel radiopharmaceuticals is a vital step in drug development. Preclinical studies often employ small animal models of human disease to evaluate potential therapies. The success of treatment depends critically on the pharmacokinetics of the drug under investigation. Pharmacokinetics can be defined as the movement of a pharmaceutical throughout the body. This term encompasses the absorption, distribution, metabolism, and excretion of the drug [71]. To gain insight on the pharmacokinetics, a biodistribution analysis is oftentimes performed. This analysis involves tracking the pharmaceutical in specific regions of an animal.

A typical pharmacokinetic study starts with the administration of the drug under investigation in multiple mice. These mice are subsequently sacrificed at different time points post-injection for a biodistribution analysis. Following each sacrifice, organs are dissected, weighed, and counted to assess the drug accumulation at the given time interval [72, 73, 74]. A scintillation counter is oftentimes employed to quantify drug accumulation if the radiopharmaceutical has a strong gamma-ray signature. This entire approach is time-consuming, laborious, and arguably unethical as a large number of animals are required. Furthermore, postmortem analysis prohibits the ability to monitor the biodistribution in individual animals, and organ counting is susceptible to selection bias because unforeseen drug accumulation in unharvested organs is missed.

Overcoming the limitations of invasive pharmacokinetic studies is the primary motivation of small-animal molecular imaging [75]. The non-invasive nature of imaging offers the exciting possibility of evaluating the time-dependent behavior of radiopharmaceuticals *in vivo*. This enables the collection of a complete set of biodistribution data from a single animal, thereby reducing biological variability and improving data quality. Furthermore, molecular imaging is a more ethical practice that requires fewer animals.

2.3.1 Small-Animal Molecular Imaging

The term molecular imaging can be defined as the non-invasive visualization of biological processes at the molecular and cellular level in living organisms. Generally speaking, molecular imaging requires specialized instrumentation used in combination with an imaging probe or agent that is designed to accumulate in a specific organ or attach to certain cells. Such techniques can be used for early detection, characterization, and monitoring of disease as well as drug development with the latter being of interest to this work.

A number of molecular imaging modalities exist, including optical, targeted ultrasound, and nuclear medicine imaging. The former two modalities are beyond the scope of this work as they rely on non-radioactive probes such as light and sound. Conversely, nuclear medicine imaging employs radioactive agents that consist of molecules labeled with radioisotopes that typically emit photons, either directly or indirectly. These so-called radiotracers can be delivered by way of injection and distribute throughout the body according to the natural uptake of the carrier molecule.

Due to their high penetrative power, photons emitted by the tracer can easily leave the body to then be observed by an external imaging instrument. The generated image reflects the local concentration of the radiotracer within the body. Because this concentration depends on cell and organ function, nuclear medicine imaging is considered a *functional* modality and should not be conflated with *structural* or *anatomical* modalities, such as standard computed tomography (CT) and magnetic resonance imaging (MRI).

Nuclear medicine imaging is playing a growing role in preclinical studies. The imaging modalities that have received the greatest attention are positron emission tomography (PET) and single-photon emission computed tomography (SPECT). Both of these modalities were originally developed for human use and are now well-established clinical tools in nuclear medicine. Clinical familiarity has been the main rationale for extending PET and SPECT to preclinical applications.

The preclinical adaptation of PET and SPECT comes with two main design challenges. First, the spatial resolution must be improved significantly to distinguish individual organs on a smaller scale. This is typically achieved by scaling down PET and SPECT imagers. The miniaturization of these systems can also provide a more practical and cost-effective means to conduct small-animal research. Second, these miniaturized systems must exhibit improved sensitivity as small animals require lower doses of radiation than humans. Addressing these two challenges has been on-going area of research.

2.3.2 Small-Animal PET

PET is a functional imaging modality that employs an agent radiolabeled with positron emitters. Table 2.4 lists popular PET radionuclides. PET primarily employs isotopes of light elements, such as carbon, nitrogen, oxygen, and fluorine. Because these elements are the main constituents of organic molecules, PET radionuclides can be incorporated into

Table 2.4: Common positron-emitting radionuclides for PET.

Isotope	Half-life	Production Source
^{76}Br	16.2 hr	cyclotron, reactor
^{11}C	20.4 min	cyclotron
^{64}Cu	12.7 hr	cyclotron, reactor
^{18}F	110 min	cyclotron
^{68}Ga	67.6 min	^{68}Ge/^{68}Ga generator
^{124}I	4.18 day	cyclotron, reactor
^{13}N	9.97 min	cyclotron
^{15}O	2.04 min	cyclotron

biomolecules without disturbing their biological activity[1]. The downside is that many of these positron emitters have short half-lives, imposing strict time requirements on the delivery, administration, and *in vivo* evaluation of the radiopharmaceutical.

Figure 2.5 illustrates the physical process of positron emission. Once emitted from the nucleus, the positron travels distances up to several millimeters before undergoing an annihilation reaction with an electron in the tissue. The annihilation of the positron and electron results in the simultaneous emission of two gamma rays. From the conservation of energy, each annihilation photon carries an energy of 511 keV - independent of the radionuclide. This energy is equivalent to the rest mass of the positron or electron. From the conservation of momentum, the two annihilation photons propagate outward from the site of annihilation in opposite directions.

PET imaging exploits both the simultaneous and collinear nature of the double photon emission. A conventional PET imager employs a single or multiple closed rings of gamma-ray detectors (typically scintillators) with the subject to be imaged in the center. With this setup, only photons registered by two opposing detectors within a specified time window (around 2 to 20 ns) are declared coincidence events. For each event, the site of annihilation should be located along the line joining the two detectors, the so-called line-of-response. The

[1]Fluorine is a bioisoteric substitute for hydrogen.

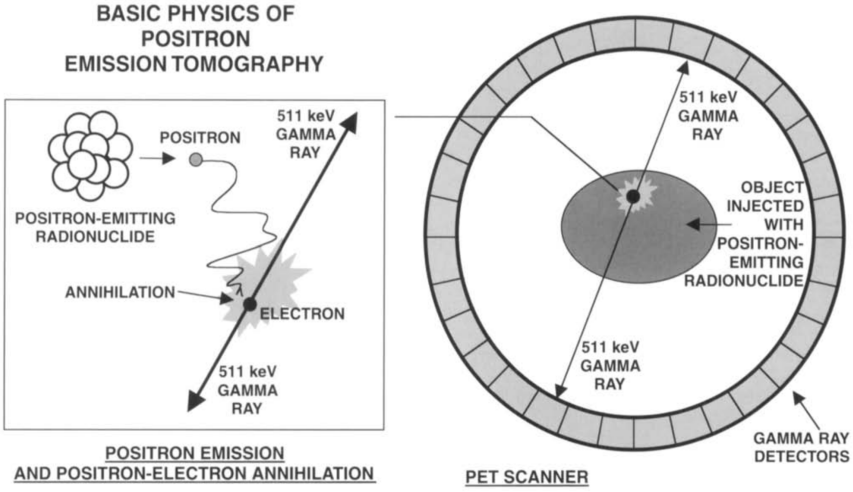

Figure 2.5: The left illustrates the physical processes of positron emission. The right shows a schematic of a PET imaging system, featuring a closed ring of gamma-ray detectors [76].

total number of coincidence events observed by the detector pair is roughly proportional to the total concentration of the radionuclide along the line-of-response. Based on this relation, the radionuclide concentration can be reconstructed from the coincidence events. Early in the history of PET, image reconstruction was performed using simple filtered back-projection. Modern PET now employs iterative reconstruction techniques that can correct for attenuation [77].

PET imagers can achieve sensitivities and resolutions that are well-suited to small-animal applications. Because PET does not rely on a physical collimator, sensitivities as high as 10^{-1} have been reported [78]. The image resolution is fundamentally limited by physical factors, namely positron range and photon non-collinearity, rather than by design. Despite these physical limitations, sub-millimeter resolutions have been demonstrated with small-animal PET systems [79, 80].

2.3.3 Small-Animal SPECT

Similarly to PET, SPECT is a functional imaging modality based in nuclear medicine. The distinction lies in the choice of imaging probe as well as instrumentation. SPECT depends on tracers labeled with radioisotopes that directly emit single gamma rays via radioactive decay. Because these photons have unique energies, SPECT has the advantage of simultaneously imaging multiple probes labeled with different radioisotopes. Table 2.5 summarizes the most commonly-used SPECT radionuclides.

SPECT is often performed using a so-called gamma camera, which typically consists of a scintillation crystal optically coupled to an array of photomultiplier tubes. The camera

Table 2.5: Common gamma-ray-emitting radionuclides for SPECT.

Isotope	Half-life	γ-Ray Energy [keV]	Branching Ratio [%]	Production Source
^{67}Ga	3.26 day	93.3	39.2	cyclotron
^{123}I	13.3 hr	159	83.0	cyclotron
^{131}I	8.02 day	364	81.8	cyclotron, reactor
^{111}In	2.80 day	171 245	90.0 94.0	cyclotron
^{99m}Tc	6.01 hr	141	89.0	^{99}Mo/^{99m}Tc generator
^{209}Tl	2.20 min	117	84.3	cyclotron

is mounted on a gantry to enable rotation around the subject to be imaged so that multiple projections can be collected at different viewing angles. A tomographic reconstruction algorithm can then applied to convert the projections into a 3-D gamma-ray image [81, 82].

Due to the isotropic nature of gamma-ray emissions, SPECT systems often employ a collimator to restrict the direction of photons emitted from the body. The most popular collimator for clinical use is the parallel-hole collimator due to its large field-of-view, while the pinhole (or multi-pinhole) design is gaining popularity in small-animal studies due to its high spatial resolution. Past works have demonstrated sub-millimeter resolutions with pinhole systems [83, 84]. Section 3.4.1 discusses the pinhole and parallel-hole designs in more detail.

2.3.4 Limitations of PET and SPECT in Alpha-Particle Emitter Studies

The application of the molecular imaging paradigm to evaluating alpha-particle-based radiopharmaceuticals in small animals would be a boon to the rapid and efficient development of TAT. While conventional small-animal molecular imaging techniques, such as PET and SPECT, have been employed to great effect in the past, there are several considerations that confound the application of these existing modalities to the preclinical evaluation of TAT.

Because alpha-particle emitters are inherently neutron-rich, positron decay is not likely to result in their subsequent decay chain. Indeed, the decay series of ^{211}At, ^{225}Ac, and ^{213}Bi do not include positron emission. Thus, PET scanners cannot be used to image these radionuclides without significantly modifying the radiopharmaceutical to accommodate a positron

emitter. Consquently, several PET isotopes have been investigated as chemical surrogates for TAT radionuclides. In the case of ^{225}Ac, one of the more promising positron-emitting analogs that has been proposed is ^{134}Ce. Advantages of ^{134}Ce include similar chemical properties and a half-life of 75.9 hours, which enables the radiopharmaceutical to be tracked over several days [85]. PET imaging of ^{134}Ce and other positron-emitting surrogates can be employed to assess the efficacy of alpha-particle-based agents in small animals. However, this method cannot provide information about the daughter redistribution, which has been the Achilles heel in developing ^{225}Ac-based therapies.

In principle, SPECT systems can directly image alpha-particle emitters if photon emissions accompany their decay. The decay scheme of ^{211}At yields 77- to 92-keV X rays from the daughter ^{211}Po. For all practical purposes, these X-ray emissions can be used to directly assess the biodistribution of ^{211}At due to the short half-life of ^{211}Po (0.516 seconds). Furthermore, the decay scheme of ^{225}Ac includes gamma-ray emissions from the daughters ^{221}Fr and ^{213}Bi at 218 keV and 440 keV, respectively. The ability to image these lines would be of great use in evaluating the daughter redistribution of ^{225}Ac-based radiopharmaceuticals.

In practice, SPECT imagers have a limited photon energy range at which they are effectively operational. At energies above about 300 keV, they experience a degradation of response as unwanted photon penetration through the collimator becomes more probable. Furthermore, even at energies below 300 keV, conventional SPECT suffers from poor imaging sensitivity, on the order of 10^{-4} for a small-animal system, due to a collimator-driven tradeoff between sensitivity and resolution [86]. This tradeoff is not ideal for preclinical studies, which involve imaging low doses of radiation on a small scale. In the case of TAT, studies would require particularly low amounts of activity to be administered (less than 20 kBq) due to the high efficacy of alpha particles.

Chapter 3

Principles of Gamma-Ray Imaging

Chapter 3 introduces fundamental principles in gamma-ray imaging, namely those most relevant to coded aperture and Compton imaging. These two modalities are the focus of this work, and collectively, they are capable of imaging a broad range of gamma-ray sources, which can serve applications in fields such as nuclear safeguards and medicine. Sections 3.1 and 3.2 discuss gamma-ray sources and interaction mechanisms, respectively. This discussion provides a foundation for Section 3.3, which gives a high-level view of gamma-ray detection in the context of germanium semiconductor detectors with a double-sided strip configuration. An introduction to gamma-ray imaging naturally follows in Section 3.4. This section discusses the simplest and most conventional of imaging methods, namely pinhole and parallel-hole imaging, as a launchpad to more advanced techniques. Furthermore, a distinction between far- and near-field imaging is made here with the latter being of interest to this work. Finally, Sections 3.5 and 3.6 introduce the concepts of coded aperture and Compton imaging, respectively, and provide analytical analyses of their imaging performances.

3.1 Gamma-ray Sources

3.1.1 Origin

The radiations of primary concern to this work are gamma rays, and thus a discussion about the mechanisms by which they are created is essential. Following a variety of nuclear reactions, including many radioactive decay processes, a product nucleus is formed in an excited state. Within a short period of time (on the order of picoseconds or less), the excited nucleus transitions to lower-lying nuclear levels via gamma-ray emission. The gamma ray itself is a photon or "packet" of electromagnetic energy.

The energy of the gamma ray is equal to the difference in energy between the two nuclear states involved in the transition. These nuclear states have well-defined energies, and thus gamma-ray energies are specific and unique to the radioisotopes that emit them. Because of this, gamma rays are analogous to fingerprints in that they can be used for isotopic

identification. Their energies range roughly from 0.1 to 10 MeV, depending on the nuclear reaction from which they originate. Gamma rays based on alpha-particle or beta-particle decay generally have energies below a few MeV, whereas those based on capture reactions can have energies as high as 10 MeV [87, 88].

There is often confusion surrounding the difference between gamma rays and other forms of electromagnetic radiation, namely X rays. Apart from the fact that X rays typically have lower energies (usually less than 100 keV), the key distinction between gamma rays and X rays lies in their origin. X rays are produced either from the transition of electrons in excited atomic shells or from the acceleration of charged particles. The former are known as characteristic X rays and have energies that are unique to the atoms (or elements) that emit them; not the isotopes themselves. The latter are known as bremsstrahlung and have a continuous energy spectrum.

3.1.2 Gamma-Ray Background

All gamma-ray detectors record some degree of background radiation, which if not accounted for, can ultimately degrade the quality of the gamma-ray image. Familiarity with the various sources of gamma-ray background is critical in discriminating the detector signal associated with the source of interest. Compared to neutrons, gamma-ray background is more varied and often more difficult to characterize. Specifically, gamma-ray background is a combination of primordial, cosmogenic, and man-made sources, with the former being the largest contributor.

3.1.2.1 Primordial Background

Primordial background primarily comes from the decay of ^{238}U, ^{232}Th, and ^{40}K. In the case of ^{238}U and ^{232}Th, no significant gamma rays arise from their direct decay, but prominent emissions do result from the subsequent decay of their progeny as shown in Tables 3.1-3.2. Moreover, the direct decay of ^{40}K, with a half-life of 1.28×10^9 years, results in the emission of a 1.46-MeV gamma ray with a branching ratio of 11%.

3.1.2.2 Man-made Background

In addition to natural sources of radiation, there can be components of gamma-ray background due to human activity. Man-made radioisotopes are primarily a result of nuclear weapons testing and nuclear reactor accidents. These isotopes include ^{134}Cs, with a half-life of 2.06 years, and ^{137}Cs, with a half-life of 30.1 years. Both cesium isotopes have strong gamma-ray signatures as outlined in Table 3.3. In fact, the relative gamma-ray abundance of ^{134}Cs and ^{137}Cs in the atmosphere can be used to distinguish a nuclear reactor accident from nuclear weapons testing. While releases from nuclear reactors include both cesium isotopes, weapons testing produces virtually no ^{134}Cs. For this reason, and due to its shorter half-life, ^{134}Cs is a good marker for more recent reactor accidents.

Table 3.1: Prominent gamma-ray energies in the ^{238}U decay series. Daughters ranked by decay order. Photon energies ranked from highest to lowest branching ratio for each isotope.

Isotope	Half-life	Energy [keV]	Branching Ratio [%]
^{238}U	4.47×10^{9} yr	–	–
^{234}Th	24.1 day	63.3	4.85
		92.4	2.81
		92.8	2.77
^{234m}Pa	1.17 min	1001	0.837
		766	0.294
^{234}U	2.46×10^{5} yr	–	–
^{230}Th	7.54×10^{4} yr	–	–
^{226}Ra	1.60×10^{3} yr	186	3.60
^{222}Rn	3.82 day	–	–
^{218}Po	3.10 min	–	–
^{214}Pb	26.8 min	352	37.6
		295	19.3
		242	7.43
^{214}Bi	19.9 min	609	46.1
		1764	15.4
		1120	15.1
^{214}Po	164 μs	–	–
^{210}Pb	22.3 yr	46.5	4.25
^{210}Bi	5.01 day	–	–
^{210}Po	138 day	–	–
^{206}Pb	stable	–	–

Table 3.2: Prominent gamma-ray energies in the ^{232}Th decay series. Daughters ranked by decay order. Photon energies ranked from highest to lowest branching ratio for each isotope.

Isotope	Half-life	Energy [keV]	Branching Ratio [%]
^{232}Th	1.41×10^{10} yr	–	–
^{228}Ra	5.75 yr	–	–
^{228}Ac	6.15 hr	911	25.8
		969	15.8
		338	11.3
^{228}Th	1.91 yr	84.4	1.22
^{224}Ra	3.66 day	241	4.10
^{220}Rn	55.6 s	–	–
^{216}Po	0.145 s	–	–
^{212}Pb	10.6 hr	239	43.3
		300	3.28
^{212}Bi	60.6 min	727	6.58
^{212}Po	299 ns	–	–
^{208}Tl	3.05 min	2615	99.0
		583	84.6
		511	22.6
		861	12.4
^{208}Pb	stable	–	–

Table 3.3: Prominent gamma-ray signatures of ^{134}Cs and ^{137}Cs. Photon energies ranked from highest to lowest branching ratio for each isotope.

Isotope	Half-life	Energy [keV]	Branching Ratio [%]
^{134}Cs	2.06 yr	605	97.6
		796	85.5
		569	15.4
		802	8.69
		563	8.35
		1365	3.01
^{137}Cs	30.1 yr	662	85.1

3.2 Gamma-ray Interactions

Gamma-ray detection, and ultimately gamma-ray imaging, fundamentally depends on the manner in which gamma rays interact within the detector medium. Thus, knowledge of their interaction mechanisms is critical in understanding the design and operation of gamma-ray imagers. Unlike charged particles, gamma rays are neutral and do not continuously lose energy as they traverse through matter. Instead, they travel some distance, along a straight path, before interacting with an atom. In just a single interaction, the gamma ray can either be fully absorbed by the absorbing medium and disappear or scatter at an angle.

There are three interaction processes that play a significant role in gamma-ray detection: photoelectric absorption, Compton scattering, and pair production. All three mechanisms lead to the partial or complete transfer of gamma-ray energy to electron energy. Moreover, these processes are probabilisitic, depending strongly on the gamma-ray energy and both the electron density and atomic number of the absorbing medium. Figure 3.1 shows the energy dependence of the various interaction processes in germanium, a popular detection medium. Photoelectric absorption predominates for low-energy gamma rays (less than 150 keV in Ge), pair production predominates for high-energy gamma rays (greater than 8 MeV in Ge), and Compton scattering is most probable at energies between these two extremes. The following section discusses each interaction mechanism in more detail.

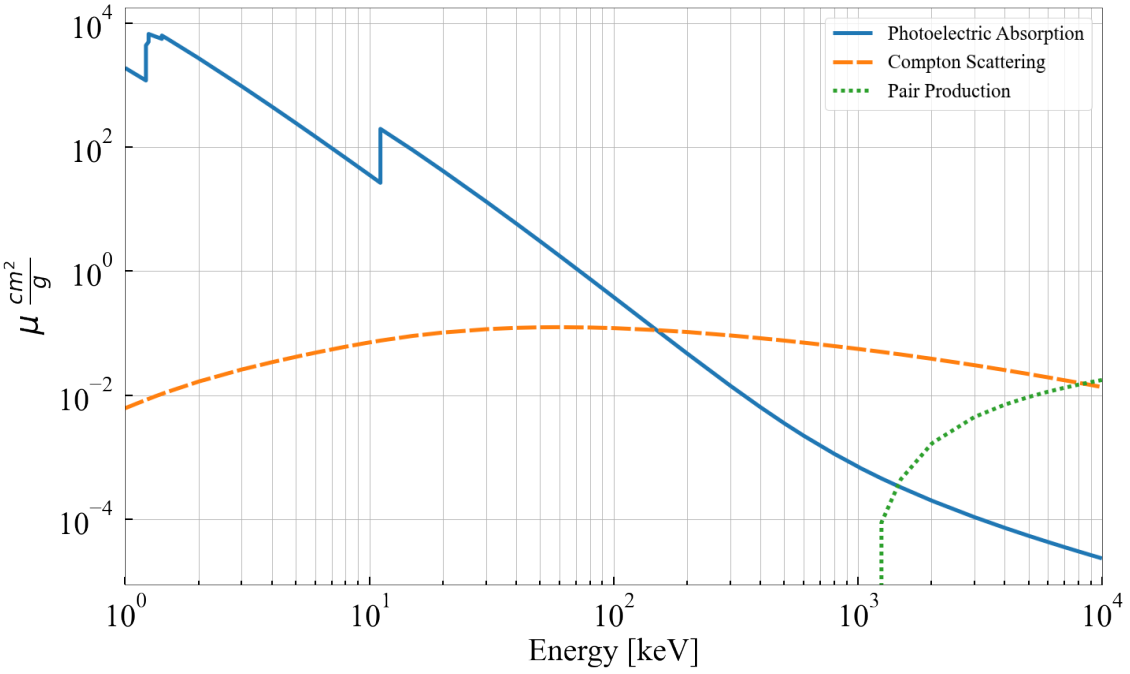

Figure 3.1: Mass attenuation coefficients (in units of cm^2/g) in germanium for photoelectric absorption, Compton scattering, and pair production. These interaction processes are detailed in Section 3.2.1. A definition of the mass attenuation coefficient is provided in Section 3.2.2.

3.2.1 Interaction Mechanisms

3.2.1.1 Photoelectric Absorption

Starting with the photoelectric effect, a gamma-ray, with energy that exceeds the binding energy of an inner shell electron in the atom, disappears by transferring all of its energy to the inner shell electron. This so-called photoelectron is subsequently ejected from the atom and carries off a kinetic energy that is equivalent to the photon energy E_γ minus its binding energy E_b. The photoelectron behaves similarly to a beta particle in its passage through matter, transferring its energy via ionization, excitation, bremsstrahlung production, and/or Cherenkov radiation.

As previously shown in Figure 3.1, photoelectric absorption is favored among low-energy gamma rays. Moreover, because this process involves the interaction between a photon and electron, the magnitude of the photoelectric effect is enhanced greatly for materials with a high electron density; this parameter is proportional to the atomic number Z. Thus, as a

rough approximation:

$$\mu_{pe} \propto \frac{Z^n}{E_\gamma^3} \tag{3.1}$$

where μ_{pe} is the probability of photoelectric absorption (per unit path length). The exponent n can vary from 3 for low-energy gamma rays to 5 for those with high energy.

Photoelectric absorption is the only interaction whereby all of the photon energy is transferred to the electron. In the context of detection, the photon (incident or scattered) must eventually undergo photoelectric absorption in the detector medium for the detector to recover information about the incident photon energy. Knowledge of the incident photon energy is required for both coded aperture and Compton imaging.

3.2.1.2 Compton Scattering

In a Compton scattering interaction, the gamma ray elastically collides with a loosely bound outer shell electron (assumed initially at rest). In the collision, both momentum and energy are conserved, and the incident photon transfers a portion of its energy to the outer shell electron; this electron is subsequently known as the recoil electron. As a result, the incident photon is deflected from its initial path. The relation between the incident photon energy E_γ, the scattered photon energy E'_γ, and the scattering angle θ is given by:

$$E'_\gamma = \frac{E_\gamma}{1 + \frac{E_\gamma}{m_e c^2}(1 - \cos\theta)} \tag{3.2}$$

where $m_e c^2$ is the rest mass of the electron and equivalent to 0.511 MeV. The kinetic energy of the recoil electron E_{e^-} is therefore:

$$E_{e^-} = E_\gamma - E'_\gamma \quad . \tag{3.3}$$

All scattering angles θ are possible, so in theory, the energy transferred to the electron can range anywhere from zero to a large fraction of the photon energy. If θ is extremely small with $\cos\theta \approx 1$, the scattered photon proceeds in the forward direction with nearly the same energy as the incident gamma-ray; and thus, the energy transferred to the electron is approximately zero. On the other extreme, for $\theta = \pi$ with $\cos\theta \approx -1$, the photon backscatters in the direction of origin. This extreme results in the maximum energy being transferred to electron:

$$E'_\gamma\Big|_{\theta=\pi} = \frac{E_\gamma}{1 + \frac{2E_\gamma}{m_e c^2}} \tag{3.4}$$

$$E_{e^-}\Big|_{\theta=\pi} = E_\gamma - \frac{E_\gamma}{1+\frac{2E_\gamma}{m_e c^2}} \quad . \tag{3.5}$$

Similar to photoelectric absorption, the probability μ_{cs} of Compton scattering (per unit path length) is enhanced greatly for high-Z materials. Specifically, μ_{cs} increases linearly with Z. The energy dependence of the Compton effect is given by the Klein-Nishina formula [89]. This formula is too complex to discuss here, but simply put, μ_{cs} decreases monotonically with increasing photon energy. A rough approximation of μ_{cs} can be stated as follows:

$$\mu_{cs} \propto \frac{Z}{E_\gamma} \quad . \tag{3.6}$$

It's important to highlight a key difference between the photoelectric and Compton processes. The photoelectric effect is an absorption process in which the photon is fully absorbed and disappears. In a Compton scattering interaction, the incident photon is replaced by a scattered photon of lower energy. In the context of detection, an incident photon of sufficiently high energy often undergoes multiple Compton scatterings in the detector medium. Moreover, if the scattered photon does not escape the detector, the photon will eventually have low enough energy to be fully absorbed in the detector medium via the photoelectric effect. In the context of this work, for Compton imaging to be possible, the incident photon must induce both Compton scattering and photoelectric absorption in the detector.

3.2.1.3 Pair Production

If a gamma-ray, with an energy that exceeds 1.02 MeV, passes near the nucleus of an atom, the photon can annihilate in the strong electric field. The result is the formation of an electron-positron pair. Because the sum total of the electron and positron rest masses amounts to 1.02 MeV, this is the minimum energy required to produce the pair. Any excess photon energy above the 1.02-MeV threshold goes into the kinetic energy shared by the electron and positron. The electron-positron pair tends to travel in the forward direction with the positron ultimately slowing down and annihilating into two 511-keV annihilation photons.

While neither coded aperture nor Compton imaging depend on pair production, such an interaction can act as a loss mechanism in Compton imaging. For energies at a few MeV, pair production begins to compete with Compton scattering, thereby reducing the number of events that can be used for Compton imaging. However, this work is interested in photon energies that fall below the 1.02-MeV threshold; and thus, losses due to pair production are negligible.

3.2.2 Attenuation

The attenuation of gamma rays through a medium is an important concept in gamma-ray imaging, particularly for methods based on mechanical collimation. The principle of attenuation not only drives the choice of detector medium, but also influences the collimator design. Thus, a brief discussion of this principle follows.

As a monoenergetic beam of gamma rays passes through matter, photons are removed from the beam by either absorption or scattering with the beam intensity decreasing in an exponential manner. The probability per unit path length μ that a photon is removed from the beam is given by:

$$\mu_{tot} = \mu_{pe} + \mu_{cs} + \mu_{pp} \tag{3.7}$$

where μ_{tot} is called the linear attenuation coefficient in units of cm^{-1}. Because μ_{tot} varies with absorber density ρ, it is often more convenient to use the mass attenuation coefficient defined as $[\mu_{tot}/\rho]$ in units of $[\text{cm}^2/\text{g}]$.

If a narrow beam of monoenergetic photons with an intensity I_0 passes through an absorber of thickness t, the intensity I of the emergent beam is given by:

$$I = I_0 \; e^{-\left(\frac{\mu_{tot}}{\rho}\right)(\rho)(t)} \quad . \tag{3.8}$$

The above can be rearranged as the transmission fraction $[I/I_0]$, defined as the probability of a photon at a given energy being fully transmitted (i.e. without interacting) through the absorber. Conversely, the attenuation fraction $[1 - I/I_0]$ represents the probability of a photon being lost in the medium due to either absorption or scattering.

Figures 3.2 and 3.3 illustrate the exponential decay of the transmission probability with respect to absorber thickness at different photon energies in germanium and tungsten, respectively[1]. Note the transmission probability increases with increasing photon energy; and thus, the attenuation probability decreases with increasing energy. This can be attributed to the negative correlation between the attenuation coefficient μ_{tot} and photon energy E_γ as previously demonstrated in Equations 3.1 and 3.6.

As gamma-ray detection requires the incident photon to interact in the detector medium, a medium with a sufficient thickness should be chosen to attenuate photons in the energy range of interest. Furthermore, in collimator-based imaging, the thickness (and atomic density) of the collimator material are important design considerations as the collimator serves to fully absorb photons in a given direction.

[1]Germanium is a popular detection medium, and tungsten is a popular collimator material.

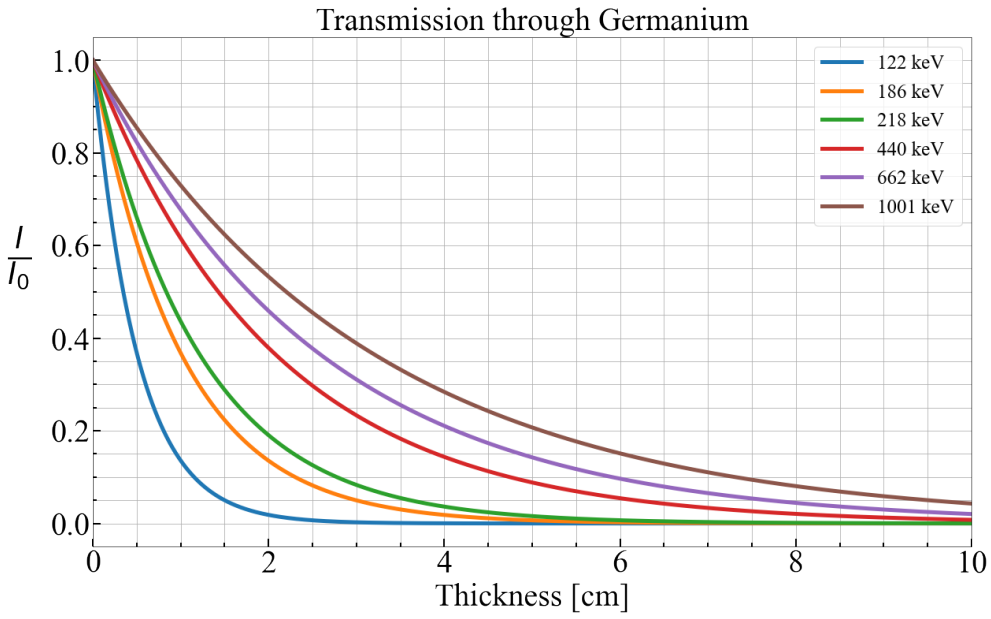

Figure 3.2: Transmission probability through germanium (a popular detection medium) at different photon energies.

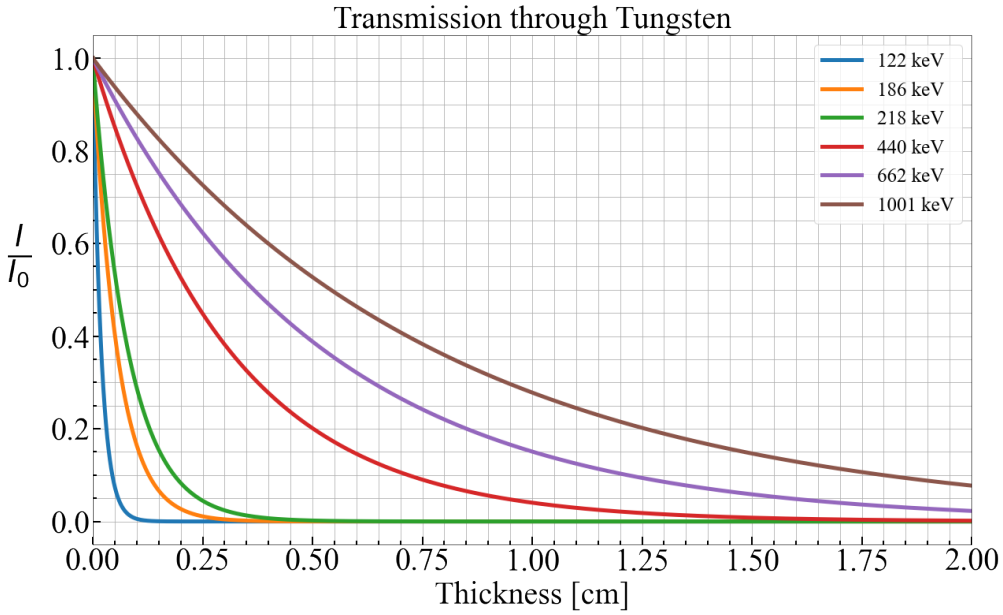

Figure 3.3: Transmission probability through tungsten (a popular collimator material) at different photon energies.

3.3 Gamma-ray Detection

Gamma-ray imaging at the most fundamental level depends on the detection of gamma rays. Detection can be simply defined as the mere indication of the photon presence via its interaction in a detector medium. In the context of this work, detection encompasses the extraction of several parameters including the energy and position of interaction. While the process of recovering this information varies with detector, all gamma-ray detectors must carry out two distinct functions. First, the instrument must act as a conversion medium in which gamma rays have a high probability of interacting to yield fast electrons; and second, the detector must facilitate the ionization, migration, and collection of these secondary particles.

Because gamma rays are uncharged, the photons themselves are "invisible" to the detector. The presence of a photon can only be revealed indirectly via the movement of a free electron created by photoelectric absorption, Compton scattering or pair production. This charged particle goes on to induce multiple ionization events along its track, subsequently producing additional charge carriers. In an applied electric field, the collective migration of these so-called information carriers generates an electric pulse that contains information about the original gamma-ray interaction.

The accuracy and precision of the information carried by the pulse is fundamentally limited by the statistics of the charge carriers. The only way to reduce statistical fluctuations is to increase the number of information carriers per pulse. The use of semiconductor materials can facilitate the production of a large number of carriers, and consequently, semiconductor detectors have superior energy resolution. In fact, germanium semiconductors are considered the gold standard in gamma-ray spectroscopy with a nominal energy resolution of 0.2% at 662 keV. The energy resolution plays an important role in gamma-ray imaging, particularly in Compton imaging as discussed in Section 3.6. For this reason, germanium detectors are the focus of this work. The basic concepts behind these detectors are introduced in the following section.

3.3.1 Germanium Semiconductor Detectors

3.3.1.1 Ionization

Germanium semiconductors, like all crystalline materials, consist of allowed energy bands in which electrons exist. Electrons occupy either the valence band where they are bound to specific lattice sites or the conduction band where they are free to migrate throughout the crystal. The two bands are separated by a bandgap, the size of which determines how easily the valence electrons can migrate to the conduction band.

If a valence electron gains sufficient energy to overcome the bandgap, the bound electron will be liberated to the conduction band. Subsequently, a "hole" will be created in its place. The hole itself is a vacancy in the valence band and has properties that resemble a "positive

electron". The combination of the liberated electron and hole is referred to as an electron-hole pair. This pair is the fundamental information carrier in semiconductor detectors.

When a gamma-ray interacts in a semiconductor, the photon liberates a valence electron. The now fast electron passes through the semiconductor and continuously loses its energy by producing additional electron-hole pairs. The number of pairs produced is governed by the average energy required to produce an information carrier. In solids, this energy threshold is closely related to the width of the bandgap.

Because semiconductors by definition have small bandgaps (0.7-eV in Ge), they require relatively little energy to create a single electron-hole pair. For example, compared to about 30 eV in gases and 100 eV in scintillators, germanium only requires 2.96 eV (on average) to produce an information carrier. Thus, for a given incident gamma ray, a large number of information carriers, proportional to the deposited photon energy, can be produced.

The small bandgap of germanium also facilitates the thermal generation of charge carriers at room temperature. To avoid thermally-induced leakage current, germanium detectors must be cooled down to liquid nitrogen temperatures.

3.3.1.2 Charge Migration and Collection

For semiconductors to operate as detectors, they must facilitate the movement of charge carriers. In the case of planar germanium detectors, this is achieved by fabricating p^+ and n^+ blocking electrodes on opposite sides of an ultra-pure germanium crystal. The p^+ and n^+ electrodes create a p-n junction across which conduction electrons near the interface diffuse from the n^+ side to the p^+ side where they combine with holes. In the diffusion process, the electron leaves behind a positive ion on the n^+ side and forms a negative ion on the p^+ side. The net effect is a build-up of negative space charge on the p^+ side and positive space charge on the n^+ side.

The accumulation of positive and negative space charge, on opposing sides of the junction, creates an electric field that prevents further charge diffusion. Because the majority carriers (free electrons for the n^+ side and holes for the p^+ side) have been depleted around the interface, this zone is known as the depletion region and has attractive properties for gamma-ray detection. The electric field that exists forces any electron created in the region to migrate to the n^+ electrode, and similarly any hole to drift to the p^+ electrode. The motion of the electrons and holes induces a current that persists until the charge carriers are fully collected at their respective contacts.

To increase the likelihood of a photon creating an electron-hole pair in the depletion zone, this region can be extended by applying a reverse-bias. Furthermore, greater depletion depths can be achieved by reducing the impurity concentration in the bulk crystal. Using advanced purification techniques, germanium crystals with impurity concentrations as low as 10^{10} atoms/cm^3 can be achieved, hence the name high-purity germanium (HPGe) detectors.

3.3.1.3 Signal Formation

The movement of charge carriers in a semiconductor detector induces charge on nearby electrodes, giving rise to a signal. The signal begins to form immediately at the start of charge carrier motion. Once the charge carriers have been fully collected at the electrodes, the charge induction process ends with the time-dependent signal being fully formed.

The shape of the signal is determined by the relationship between the induced current on a given electrode and the instantaneous position of the charge carrier within the detector. Shockley [90] and Ramo [91] developed a sophisticated and convenient method for calculating the induced charge on any electrode using the concept of weighting field. Not to be mistaken for the electric field, which defines charge drift, the weighting field determines how charge couples to an electrode.

The Shockley-Ramo theorem states that the instantaneous current i induced on a given electrode is equivalent to:

$$i = q\vec{v} \cdot \vec{E}_0 \tag{3.9}$$

where q is the charge of the carrier, $\vec{v}$ is its instantaneous velocity, and $\vec{E}_0$ is the weighting field. While the charge carrier velocity $\vec{v}$ depends on the charge mobility and electric field strength, the weighting field $\vec{E}_0$ depends on the electrode geometry and the positioning of electrodes with respect to one another. The above principle can also be stated as:

$$Q = q\Delta\psi_0 \tag{3.10}$$

where Q is the charge induced on a given electrode and ψ_0 is the weighting potential. The weighting potential, as a function of position, describes how strongly a charge at a specific location couples to a given electrode. Mathematically, the weighting potential can be solved by the Laplace transform under the following assumptions: the electrode of interest is at unit potential (1V), all other electrodes are grounded (0V), and space charge in the detector volume is negligible. If the time-dependency of the carrier position is factored into the equation, then the time profile of the induced charge, or the induced current, can be solved to determine the shape of the output signal [88, 92].

The current induced on a given electrode is often integrated on a charge-sensitive preamplifier, which generates a voltage pulse. The shape of this pulse carries important information about the gamma-ray interaction. For germanium semiconductors, the characteristic signal features a sharp rising edge, determined by the charge collection process in the detector, with an amplitude proportional to the deposited photon energy.

3.3.2 Double-Sided Strip Detectors

Gamma-ray imaging often requires knowledge of both the energies and positions of all photon interactions induced by the same incident gamma-ray. To recover this information, an

advanced detector design is needed. The approach used in this work is to subdivide the detector electrodes into independent segmented strips and position them in an orthogonal orientation on opposite sides of a bulk semiconductor crystal. Such a detector is known as a double-sided strip detector (DSSD), a schematic of which is shown in Figure 3.4.

The potential difference between the p^+ and n^+ electrodes on opposite faces produces an electric field perpendicular to the strip planes. This field causes the electrons and holes created within the volume to drift along the field lines in opposite directions. The strips to which the electrons drift collectively constitute the detector anode and those to which the holes drift constitute the cathode.

If the strip widths are small compared to the detector thickness, the weighting potentials show a rapid rise in close proximity to the electrodes. In other words, charge motion near the electrode surface contributes most strongly to the induced signal. This is known as the *small-pixel effect*. Given this effect, the motion of holes contributes primarily to the signal induced on the cathode, and the motion of electrons contributes primarily to that induced on the anode. This means that the collection of electrons and that of holes are detected separately, and each produces an output signal with an amplitude that corresponds to the deposited photon energy.

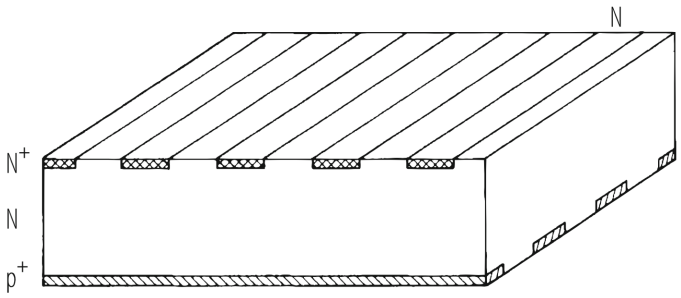

Figure 3.4: Simple schematic of a DSSD [93].

3.3.2.1 Determination of (x, y) Interaction Position

Figure 3.5 illustrates the process of determining the (x, y) position of a gamma-ray interaction in a double-sided strip detector. This example arbitrarily assigns the x-direction along the length of the anode (or electron-collecting) strips and the y-direction along the length of the cathode (or hole-collecting) strips. The (x, y) interaction position is obtained by matching the x and y trigger electrodes based on their trigger time and pulse amplitudes.

In practice, the process of strip matching can be simplified into two steps. First, trigger electrodes are correlated by time coincidence. For strips that trigger within a given time window, their signals are assumed to be from the same interaction or series of interactions

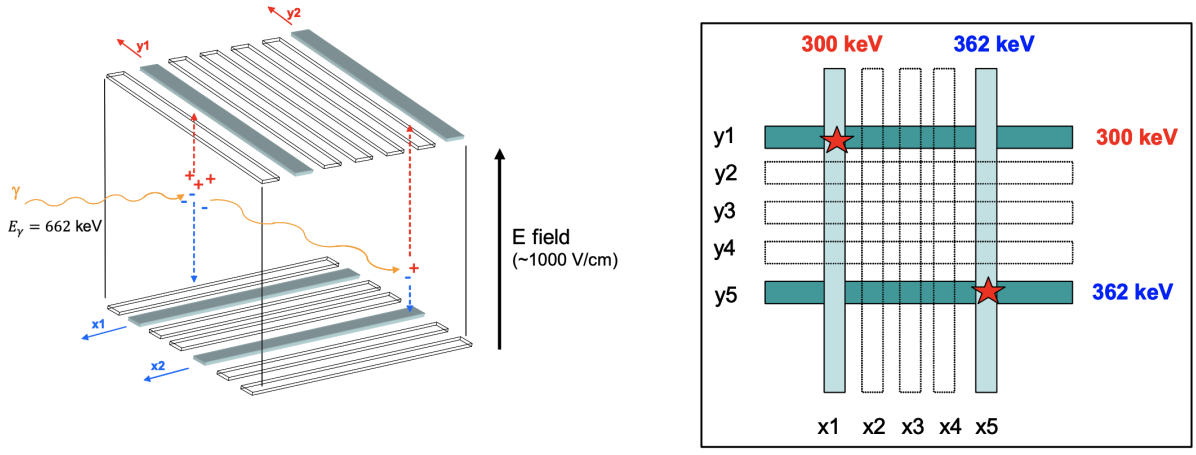

Figure 3.5: DSSD in which an incident gamma ray with an energy of 662 keV undergoes a series of two interactions. This results in the triggering of four strips. Left, the electric field causes electrons and holes to be collected on x (anode) and y (cathode) strips, respectively. Right, (x, y) position determination by matching the trigger strips based on energy deposition [94].

induced by a given incident gamma ray. The coincidence window should be selected based on the maximum charge collection time in the detector.

Second, for a given group of time-correlated strips, the x and y strips are matched by pulse amplitude or energy deposition. The intersection of the electrode pair determines the (x, y) interaction position with an accuracy determined by the strip pitch (i.e the distance between the centers of two adjacent strips). Furthermore, the number of strip pairs in the same coincidence window corresponds to the the total number of interactions induced by the incident gamma ray.

Going back to the example in Figure 3.5, an incident gamma ray with an energy of 662 keV induces a series of two interactions within the detector volume. The net effect is the triggering of four strips. In the first interaction, the incident photon interacts via Compton scattering with a partial energy deposition of 300 keV. In the second interaction, the scattered photon deposits an additional 362 keV via photoelectric absorption. The two interactions collectively constitute a so-called doubles event with two associated energy depositions and positions of interaction.

3.3.2.2 (x, y) Position Interpolation

The strip matching method discussed in the previous section limits the (x, y) positional accuracy to the strip pitch. In theory, segmented detectors can achieve a finer position resolution via interpolation techniques. One such method is to analyze the transient signals

induced on the two neighboring electrodes bordering the collecting electrode.

The amplitude of the transient signal falls exponentially with charge carrier distance from the electrode border. By relating the pulse amplitude difference between the two neighboring strips, the interaction position can be interpolated between their borders. The amplitude difference R_s can be quantified as follows:

$$R_s = \frac{(A_{s-1} - A_{s+1})}{(A_{s-1} + A_{s+1})} \tag{3.11}$$

where A_{s-1} and A_{s+1} are the amplitudes of the transient signals induced on the neighboring electrodes. Finally, the interpolated (x, y) position can be obtained by:

$$x = x_s + k_x \cdot R_s \tag{3.12}$$

$$y = y_s + k_y \cdot R_s \tag{3.13}$$

where x_s and y_s are the coordinates of the collecting electrode, and k_x and k_y are proportionality factors determined experimentally [95].

3.3.2.3 Depth (z) of Interaction Determination

The depth (z) of a gamma-ray interaction, along the thickness of the detector, can be determined by the difference in the arrival time of the electrons at the anode and holes at the cathode. Their collection times vary due to differences in drift distance. For example, if an incident gamma ray interacts near the cathode, the holes travel a relatively short distance before collection. Conversely, the electrons must travel the full extent of the detector volume, resulting in a longer collection time. Figure 3.6 illustrates the distinct time profiles of the cathode and anode output signals at different depths of interaction.

The arrival time of the charge carriers is reflected in the leading edge of the signal, and can be represented by the T_{50} rise time; defined as the time at which the signal reaches 50% of its final amplitude. Under the assumption that electrons and holes have constant drift velocities in the detector volume, a linear relationship between their arrival time difference ΔT_{50} and depth z of interaction can be approximated by:

$$z = z_0 + k_z \cdot \Delta T_{50} \tag{3.14}$$

where z_0 is a constant depth near the center of the detector and k_z is a proportionality factor. The proportionality factor used in this work was determined experimentally by a depth scanning measurement [96].

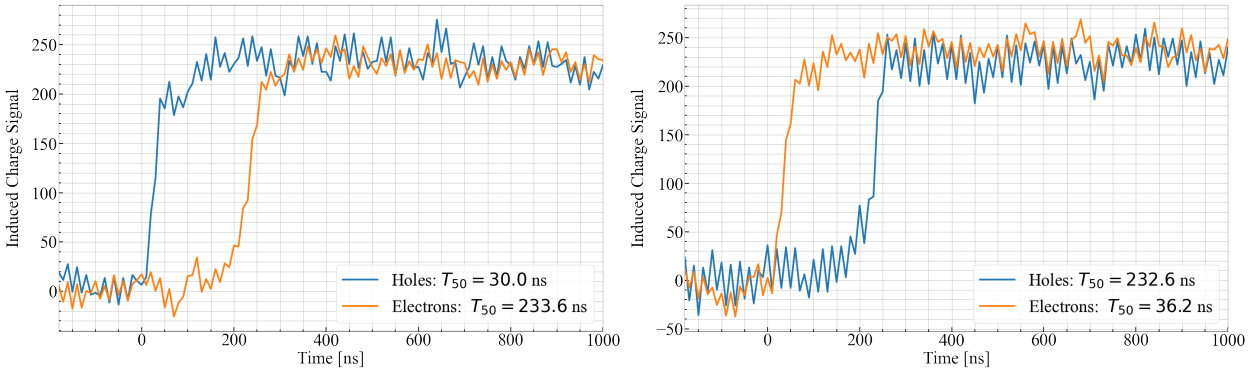

(a) Near Cathode (b) Near Anode

Figure 3.6: The induced electron and hole signals (digitized) for a gamma-ray interaction that took place near the (a) cathode and (b) anode in one of the HPGe DSSDs of the Dual-Modality Imager. The timing difference ΔT_{50} is used to determine the depth z of interaction. Note the pulse tails represent the decay of the fully-collected charge down to baseline.

3.4 Gamma-ray Imaging Basics

Gamma-ray imaging is the process of mapping the intensity of gamma-ray radiation over space. The image space can be defined in either two dimensions by an angular (θ, ϕ) coordinate system or three dimensions by a Cartesian (x, y, z) coordinate system. Furthermore, the image space is discretized into either pixels or voxels that are assigned an arbitrary color. The pixel or voxel color is selected based on the gamma-ray intensity in that region. The colored pixels collectively form the gamma-ray image, which appears as a heat map of the photon spatial distribution.

Gamma-ray imaging can be realized with different approaches, which for all practical purposes can be divided into one of two categories: collimator- or kinematics-based imaging. Both methods preferentially select gamma rays based on their incoming direction. The constraints on directionality are imposed so that photons incident on a detector can be easily traced back to their source of origin. Collimator-based imaging alone encompasses a variety of techniques, including pinhole, parallel-hole, and coded aperture imaging. All of the above rely on elements of highly-attenuating material to physically select which gamma rays are observed by the detector. Kinematics-based instruments, most relevantly Compton cameras, are distinguished by the absence of a collimator. Instead of restricting photons before detection, kinematics-based imagers impose constraints after detection.

3.4.1 Conventional Imaging Methods

3.4.1.1 Pinhole Imaging

The simplest gamma-ray imaging method is based on pinhole collimation. The pinhole imager consists of a position-sensitive detector in front of which a collimator is situated. The collimator itself consists of a highly-attenuating sheet through which a single aperture or hole has been drilled.

Consider a point source in the field-of-view of a pinhole imager. The point source can be assumed isotropic such that gamma rays are emitted with equal intensity in all directions (4π). Because photons travel in straight lines, only gamma rays emitted in one direction can pass through the aperture to be registered by the detector. All remaining photons, incident on the collimator, are absorbed by the material. Figure 3.7 illustrates this concept. The result is a one-to-one correspondence between the source location and the position of photon interaction in the detector.

Now consider a distributed source, or collection of point sources, in a two dimensional space. Each point along the source should correspond to a distinct detector pixel. This means that the counts recorded by the detector should materialize into an inverted and rescaled projection of the source. Figure 3.8 illustrates this concept. Note this projection does not represent the source distribution in the image space. An additional step, known as image reconstruction, is required to map the projection back to the image space. Methods of image reconstruction are outlined in Section 3.4.3.

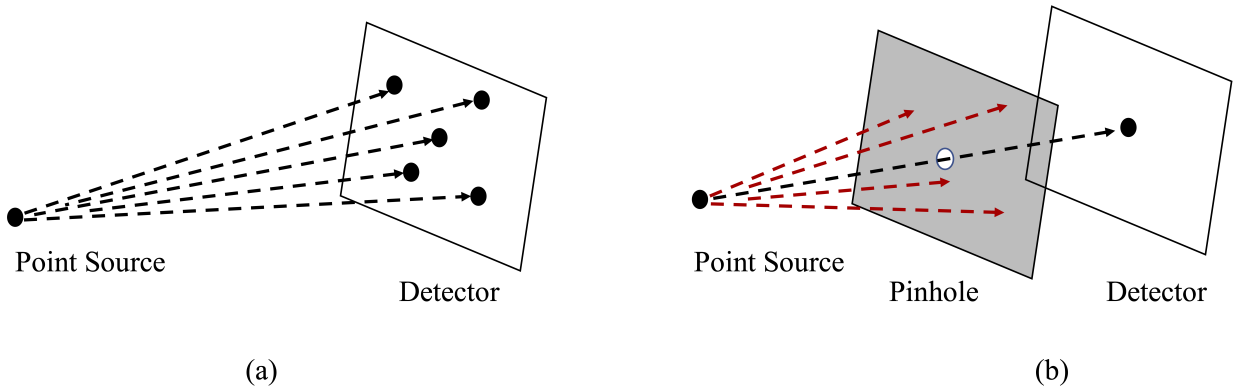

Figure 3.7: A point source in the field-of-view of a detector (a) without and (a) with a pinhole collimator present. Black and red dashed arrows represent gamma rays observed and not observed by the detector, respectively. Note that in (a) the positions of interaction in the detector are not unique to the source location, whereas in (b) a one-to-one correspondence between the source and detector is established.

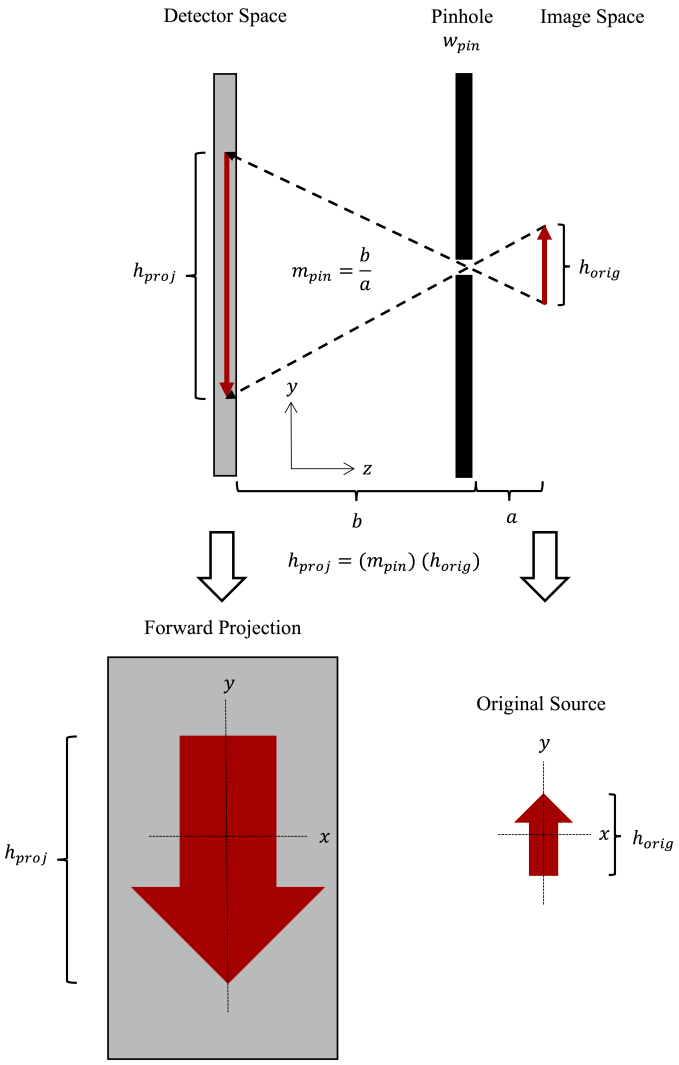

Figure 3.8: An (x, y) distributed source in the field-of-view of a pinhole imager, featuring a position-sensitive detector and a pinhole collimator with an aperture width of w_{pin}. Black dashed arrows represent gamma rays admitted through the collimator. The forward projection appears inverted and magnified (due to $a < b$) on the detector plane.

The rescaling of the projected source depends on (1) the normal distance a between the source and collimator planes and (2) the normal distance b between the collimator and detector planes. Using simple geometry (and neglecting inversion), the size ratio of the projected source h_{proj} to the original h_{orig} can be determined by:

$$m_{pin} = \frac{h_{proj}}{h_{orig}} = \frac{b}{a} \tag{3.15}$$

where m_{pin} is the magnification factor of the pinhole. The source appears magnified for $a < b$ and minified for $a > b$. Moreover, the source appears true-to-size for $a = b$.

The magnification factor m_{pin} strongly impacts both the field-of-view and image resolution. The field-of-view FoV can be defined as the extent of the image space seen by the imager:

$$FoV = \frac{l_d}{m_{pin}} \tag{3.16}$$

where l_d is the length of the detector. Note there is a negative correlation between the field-of-view and magnification factor; the FoV shrinks in closer proximity to the imager.

Figure 3.9 illustrates the influence of the collimator and detector designs on image resolution. The collimator design dictates the geometric resolution $\delta r_{geo,\ pin}$, while the detector design governs the intrinsic resolution $\delta r_{int,\ pin}$. By summing $\delta r_{geo,\ pin}$ and $\delta r_{int,\ pin}$ in quadrature, the resolution δr_{pin} of the pinhole imager can be determined by:

$$\delta r_{pin} \approx \sqrt{\delta r^2_{geo,\ pin} + \delta r^2_{int,\ pin}} \quad . \tag{3.17}$$

Using simple geometry, the geometric resolution $\delta r_{geo,\ pin}$ in full-width at half-maximum (FWHM) can be defined as:

$$\delta r_{geo,\ pin} \approx w_{pin} + \left(\frac{a}{b}\right)(w_{pin}) = w_{pin} + \frac{w_{pin}}{m_{pin}} \tag{3.18}$$

where w_{pin} is the pinhole diameter. Equation 3.18 assumes the nominal w_{pin} and effective pinhole diameters are equivalent, i.e. no unwanted photon penetration through the collimator. The intrinsic resolution $\delta r_{int,\ pin}$ can be defined as:

$$\delta r_{int,\ pin} \approx (2a)\tan\left(\frac{\delta\theta}{2}\right) \approx (a)\,(\delta\theta) \tag{3.19}$$

in FWHM. Here $\delta\theta$ is the angular resolution of the pinhole imager defined as:

$$\tan\left(\frac{\delta\theta}{2}\right) = \frac{w_d}{2b} \rightarrow \delta\theta \approx \frac{w_d}{b} \tag{3.20}$$

where w_d is the lateral position resolution of the detector in FWHM, and for all practical purposes, can be approximated as the width of a detector pixel. Incorporating Equation 3.20 into Equation 3.19, the intrinsic resolution $\delta r_{int,\ pin}$ becomes:

$$\delta r_{int,\ pin} \approx \left(\frac{a}{b}\right)(w_d) = \frac{w_d}{m_{pin}} \quad . \tag{3.21}$$

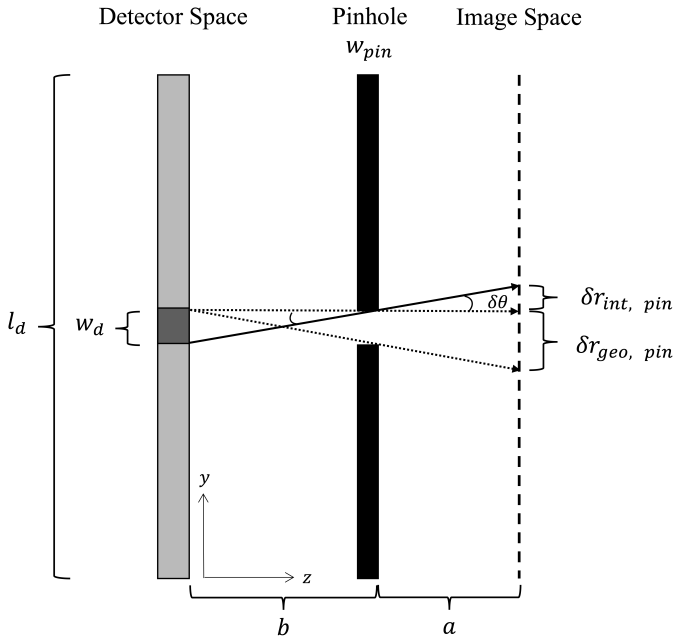

Figure 3.9: Determination of the geometric $\delta r_{geo,\ pin}$ and intrinsic $\delta r_{int,\ pin}$ resolutions of a pinhole imager, featuring a position-sensitive detector with a pixel width of w_d and a pinhole collimator with an aperture width of w_{pin}.

Finally, incorporating Equations 3.18 and 3.21 into Equation 3.17, the resolution δr_{pin} of the pinhole imager becomes:

$$\delta r_{pin} \approx \sqrt{\left[w_{pin} + \frac{w_{pin}}{m_{pin}}\right]^2 + \left(\frac{w_d}{m_{pin}}\right)^2} \tag{3.22}$$

in FWHM. Note image resolution improves significantly with increasing magnification m_{pin}. Furthermore, resolution gains can be realized by reducing the widths of the pinhole w_{pin} and detector pixels w_d.

The pinhole, however, cannot be made infinitesimally small as w_{pin} limits the geometric sensitivity. This parameter can be defined as the fraction of photons emitted by the source that pass through the aperture. For an aperture of circular geometry, the geometric sensitivity $\epsilon_{geo,\ pin}$ can be approximated by:

$$\epsilon_{geo,\ pin} \approx \frac{w_{pin}^2}{16a^2} \cos^3\theta \tag{3.23}$$

where θ is the angle between the incident photon direction and the normal to the aperture. Equation 3.23 assumes the nominal w_d and effective pinhole diameters are equivalent. In

reality, this assumption fails at high photon energies (above a few hundred keV) as unwanted photon penetration through the collimator material becomes more probable.

From Equations 3.22 and 3.23, there is a collimator-driven tradeoff between resolution and sensitivity. By decreasing the pinhole width w_{pin}, the geometric resolution $\delta r_{geo,\ pin}$ improves but the geometric sensitivity $\epsilon_{geo,\ pin}$ diminishes. Eliminating this tradeoff is the primary motivation behind the coded aperture design discussed later in Section 3.5.

The best approach for improving the pinhole sensitivity is decreasing the source-to-aperture distance a. A reduction in a is also advantageous from a resolution standpoint due to a subsequently larger magnification factor. Of course, in turn, the field-of-view suffers. For this reason, pinhole imagers are most effective at imaging small sources in close proximity to the aperture.

3.4.1.2 Parallel-Hole Imaging

A limitation of pinhole imagers is the restricted field-of-view. For situations that necessitate a larger image space, a parallel-hole collimator is the better choice. The collimator consists of an array of small tubes, typically of hexagonal or circular shape, fabricated from a heavy absorber. The tubes are situated directly on top of a position-sensitive detector, forming the imager.

Figure 3.10 illustrates the concept of parallel-hole imaging. Only photons traveling in a line perpendicular to the collimator can be registered by the detector. Similarly to a pinhole imager, the result is a one-to-one correspondence between the source and detector. However, in this case, the projection is an upright, true-to-size image of the source.

Because the projection is not magnified (or minified), the field-of-view FoV of the parallel-hole imager can be defined as the length l_d of detector: $FoV = l_d$. The absence of magnification provides a FoV advantage over pinhole imagers, but also degrades the geometric resolution $\delta r_{geo,\ par}$. Figure 3.11 illustrates the influence of the parallel-hole design on the image resolution. Using simple geometry, the geometric resolution $\delta r_{geo,\ par}$ in FWHM can be defined as:

$$\delta r_{geo,\ par} \approx w_{par} + \left(\frac{a}{l_{par}}\right)(w_{par}) \tag{3.24}$$

where w_{par} is the width of tube opening and l_{par} is the tube length. Equation 3.24 assumes the nominal l_{par} and effective tube lengths are equivalent and states that resolution gains can be realized by fabricating longer and more narrow tubes. The intrinsic $\delta r_{int,\ par}$ resolution of the detector can be defined as:

$$\delta r_{int,\ par} \approx (a)\,(\delta\theta) \approx \left(\frac{a}{l_{par}}\right)(w_d) \tag{3.25}$$

in FWHM. Equations 3.24 and 3.25 are equivalent to Equations 3.18 and 3.21 for a pinhole

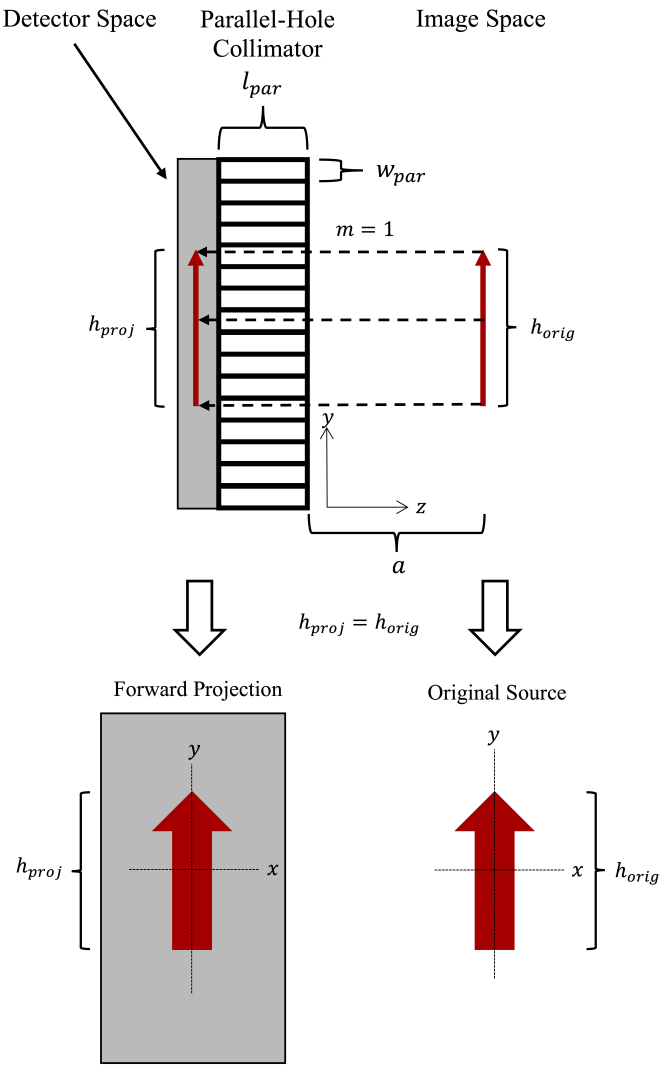

Figure 3.10: An (x, y) distributed source in the field-of-view of a parallel-hole imager, featuring a position-sensitive detector and a collimator with a tube length l_{par} and opening width w_{par}. Black dashed arrows represent gamma rays admitted through the tubes. The forward projection appears as a direct image of the source.

collimator, except here $\delta r_{geo,\ par}$ and $\delta r_{int,\ par}$ depend on a fixed tube length l_{par} as opposed to the collimator-to-detector distance b. From a practical standpoint, there is less flexibility with parallel-hole imagers in terms of improving resolution, because fabricating longer tubes poses more difficulties than simply adjusting the distance b.

Similarly to pinhole systems, parallel-hole imagers suffer from a collimator-driven tradeoff between resolution and sensitivity. The geometric sensitivity of a parallel-hole collimator can

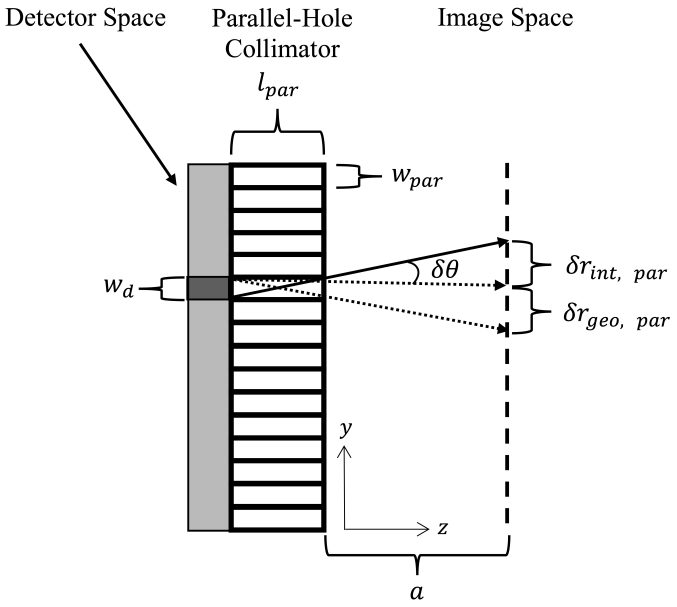

Figure 3.11: Determination of the geometric $\delta r_{geo,\ par}$ and intrinsic $\delta r_{int,\ par}$ resolutions of a parallel-hole imager, featuring a position-sensitive detector with a pixel width w_d and a parallel-hole collimator with a tube length l_{par} and opening width w_{par}.

be defined as:

$$\epsilon_{geo,\ par} \approx K^2 \left(\frac{w_{par}}{l_{par}}\right)^2 \left[\frac{w_{par}^2}{(w_{par}+t)^2}\right] \tag{3.26}$$

where t is the septal thickness and K is a constant that depends on the tube shape. Equation 3.26 assumes the nominal l_{par} and effective tube lengths are equivalent. In reality, the effective tube length is slightly less than l_{par} due to septal penetration, i.e. the ability of gamma rays to cross over from one tube to another to be registered by the detector. Septal penetration degrades the image quality. Such effects can be reduced by increasing the septal thickness t. However, thicker walls obstruct a larger area of the detector surface, thereby worsening the sensitivity. The better option is to construct thinner walls from a material with a sufficiently large attenuation coefficient μ.

It is interesting to note that the geometric sensitivity of a parallel-hole collimator does not depend on the source-to-collimator distance a. In other words, the geometric sensitivity remains constant in the field-of-view. Figure 3.12 illustrates this concept via the inverse relationship between the sensitivity of a single tube and exposed detector area. While the sensitivity of a single tube decreases proportionally with $[1/a^2]$, the exposed detector area, or number of tubes passing photons, increases with a^2. Thus, the impact of a on sensitivity

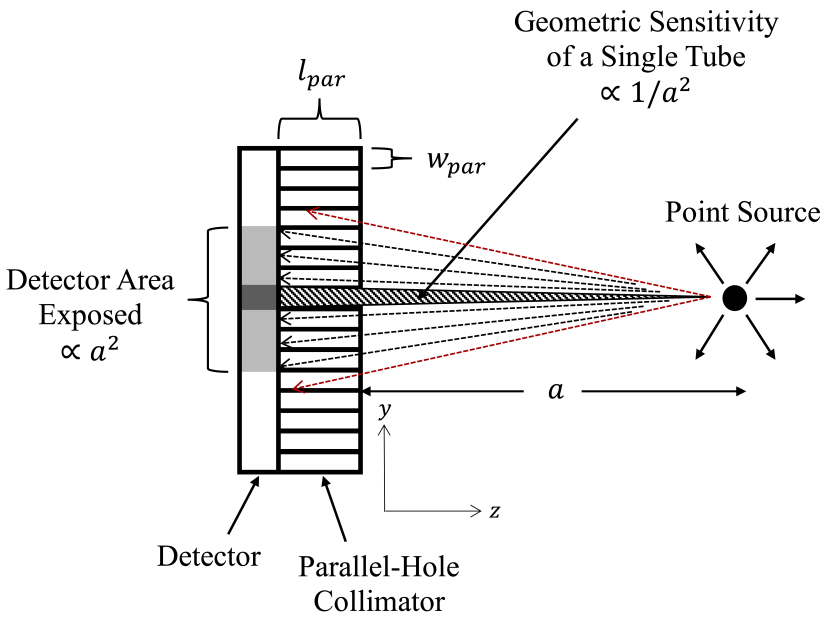

Figure 3.12: Determination of the geometric sensitivity of a parallel-hole imager, featuring a position-sensitive detector, a collimator with a tube length l_{par} and opening width w_{par}, and a source at a distance a from the collimator. Black and red dashed arrows represent gamma rays admitted and not admitted through the tubes, respectively. The geometric sensitivity of a single hole decreases as $[1/a^2]$, while the area of the detector exposed increases as a^2. Adapted from [97].

cancels out [97].

3.4.2 Far-Field and Near-Field Imaging

Gamma-ray imaging can be categorized as either far- or near-field imaging. The distinction lies in the source-to-detector geometry. Consider a point source in the field-of-view of a detector. In the far field, the source-to-detector distance is sufficiently large such that the incident gamma-ray flux exhibits no divergence with respect to the size of the detector. In other words, the photons reach the detector along essentially parallel paths. Given this phenomenon, the detector can be considered a point with no solid angle effects. This means the far-field response depends only on the source direction, not the distance. As the point source is brought closer to the detector into the near-field regime, beam divergence and solid angle effects become significant such that both the source direction and distance impact the response.

The line that distinguishes the far field from the near field can be defined as the distance at which the divergence θ_{div} of the incident photon beam is less than the angular resolution

$\delta\theta$ of the imager:

$$\theta_{div} < \delta\theta \quad . \tag{3.27}$$

For an on-axis point source, the beam divergence θ_{div} can be defined as

$$\theta_{div} = 2\tan^{-1}\left(\frac{l_d}{2z}\right) \tag{3.28}$$

where l_d is the length of the detector and z is the source-to-detector distance. From the above definitions, the far-field approximation can be stated as follows:

$$z > \frac{l_d}{2\tan\left(\frac{\delta\theta}{2}\right)} \quad . \tag{3.29}$$

Additional interpretations of the far- and near-field regimes as they pertain to coded aperture and Compton imaging can be found in Sections 3.5 and 3.6, respectively.

3.4.3 Image Reconstruction

The process of generating a set of detector data from a gamma-ray distribution is called *solving the forward problem* or forward projection. The projection, or collection of counts recorded by the detector, is not an accurate depiction of the source distribution, because the projection exists in the detector space as opposed to the image space in which the true source exists. The objective of image reconstruction is to map the projection in the detector space back to the image space, thereby reconstructing the source distribution. This is known as *solving the inverse problem.*

3.4.3.1 Formulation of the Inverse Problem

The forward problem seeks to map the source distribution Λ in the image space to the detector space. The detector measurement D can be defined as:

$$D = A \cdot \Lambda \quad . \tag{3.30}$$

Here D can be represented as an $I \times 1$ matrix in real space: $D \in \mathbb{R}^I$, where a single element is i and a single measurement in that element is d_i. The source distribution Λ can be expressed as a $J \times 1$ matrix in real space: $\Lambda \in \mathbb{R}^J$, where a single element is j and the gamma-ray intensity in that element is λ_j. The so-called system response A maps the source distribution in the image space to the detector space: $\mathbb{R}^j \rightarrow \mathbb{R}^i$.

Because the source distribution Λ is an unknown, the inverse problem in principal provides the desired solution. At first glance, the inversion of the forward problem seems to be

a reasonable method:

$$\hat{\Lambda} = A^{-1} \cdot D \tag{3.31}$$

where $\hat{\Lambda}$ is the estimated or reconstructed source distribution. Unfortunately, in practice, the system response cannot be inverted because A is ill-posed and/or too large. Furthermore, inversion can enhance noise and result in negative values, which physically are impossible. The following presents alternative methods, by no means all, for solving the inverse problem given these constraints.

3.4.3.2 Back-projection and Filtered Back-projection

Back-projection is often the first step in image reconstruction. Mathematically, back-projection can be defined as the transpose of the forward problem:

$$B = A^T \cdot D \approx \hat{\Lambda} \quad . \tag{3.32}$$

The back-projection operator A^T smears the projection data back to the image space along the direction in which the data was measured. The back-projected image B is blurred due to the finite detector resolution, collimator resolution, and attenuation factors. If multiple views are considered, the change in perspective results in additional blurring, which often appears as a $[1/r]$ point spread function.

To reduce the blurring effect, a spatial frequency filter can be applied to the detector data before the back-projection step. This process is known as filtered back-projection (FBP) and is one of the simplest methods of image reconstruction [98]. A geometric filter suppresses components of low frequency and amplifies those of high frequency, thereby sharpening the image. However, this filter alone can enhance noise at higher frequencies. The addition of a high-frequency filter (e.g. Shepp-Logan) is required for noise suppression. Moreover, FBP can produce negative artifacts, resulting in a non-physical representation of the source distribution.

3.4.3.3 Iterative Reconstruction Based on Maximum-Likelihood Expectation-Maximization

Analytical reconstruction algorithms such as filtered back-projection are based on a single reconstruction. Iterative algorithms, on the other hand, use multiple iterations in which the current reconstruction converges to a better one; and consequently, the computational demands are higher. If computational power is a non-issue, iterative methods are appealing as they allow for accurate modeling of the physical system. Furthermore, such methods can account for Poisson noise. A number of iterative reconstruction algorithms have been proposed [99, 100], and in gamma-ray imaging, the most popular by far are those based

on Maximum-Likelihood Expectation-Maximization (ML-EM). The reason is that ML-EM inherently accounts for the stochastic nature of the detector data.

The following is a derivation of the ML-EM algorithm. The detector observations D can be discretized into pixels, where d_i represents the counts observed in detector pixel $i = 1, 2, ..., I$. The unknown source distribution Λ can be discretized into image voxels, where λ_j represents the unknown source emissions in image voxel $j = 1, 2, ..., J$.

Poisson statistics governs the measured detector data D as follows:

$$P\left(D = d_i|\mu_i\right) = \exp\left[-\mu_i\right]\frac{\left(\mu_i\right)^{d_i}}{d_i!} \tag{3.33}$$

where μ_i is the expectation of d_i and can be defined as:

$$\mu_i = \sum_{j'}^{J}\left(a_{ij'}\right)\left(\lambda_{j'}\right) \tag{3.34}$$

where λ_j is to be estimated from the detector observations D. The system response a_{ij} is the probability that an emission from image voxel j is registered by detector pixel i.

Because the Poisson variables d_i are independent, the likelihood of Λ can be expressed as:

$$L\left(\Lambda\right) = \prod_{i}^{I}\exp\left[-\mu_i\right]\frac{\left(\mu_i\right)^{d_i}}{d_i!} \quad . \tag{3.35}$$

Furthermore, the log-likelihood L^* is:

$$L^* = \log\left(L\left(\Lambda\right)\right) = \sum_{i}^{I}\left[\left(d_i\right)\log\left(\mu_i\right) - \mu_i - \log\left(d_i!\right)\right] \quad . \tag{3.36}$$

Inserting Equation 3.34 gives:

$$L^* = \log\left(L\left(\Lambda\right)\right) = \sum_{i}^{I}\left[d_i\log\left(\sum_{j'}^{J}\left(a_{ij'}\right)\left(\lambda_{j'}\right)\right) - \sum_{j'}^{J}\left(a_{ij'}\right)\left(\lambda_{j'}\right) - \log\left(d_i!\right)\right] \quad . \tag{3.37}$$

Differentiating L^* with respect to λ_j yields:

$$\frac{\partial L^*}{\partial \lambda_j} = \sum_i^I \left[\frac{(d_i)\,(a_{ij})}{\sum_{j'}^J (a_{ij'})\,(\lambda_{j'})} - a_{ij} \right] \quad . \tag{3.38}$$

The objective now is to find an iterative (convergent) algorithm that assures maximum likelihood of λ_j and provides a positivity constraint on all components of λ_j. To start, the algorithm can take the form [101]:

$$\lambda_j^{k+1} = \lambda_j^k + \Delta_j^k \frac{\partial L^*}{\partial \lambda_j}\left(\lambda_j^k\right) \quad . \tag{3.39}$$

On each iteration k, each component λ_j moves in a direction that increases L^* by a factor Δ_j^k. Inserting the derivative from Equation 3.38 yields:

$$\lambda_j^{k+1} = \lambda_j^k + \Delta_j^k \sum_i^I \left[\frac{(d_i)\,(a_{ij})}{\sum_{j'}^J (a_{ij'})\left(\lambda_{j'}^k\right)} - a_{ij} \right] \rightarrow \tag{3.40}$$

$$\lambda_j^{k+1} = \lambda_j^k + \Delta_j^k \sum_i^I \frac{(d_i)\,(a_{ij})}{\sum_{j'}^J (a_{ij'})\left(\lambda_{j'}^k\right)} - \Delta_j^k \sum_i^I a_{ij} \quad . \tag{3.41}$$

The negative term in the above expression can cause negative artifacts: $\lambda_j < 0$. To prevent this, Δ_j^k must be chosen such that the negative term cancels out:

$$\lambda_j^{k+1} = \lambda_j^k + \Delta_j^k \sum_i^I \frac{(d_i)\,(a_{ij})}{\sum_{j'}^J (a_{ij'})\left(\lambda_{j'}^k\right)} - \Delta_j^k \sum_i^I a_{ij} \tag{3.42}$$

$$\lambda_j^{k+1} = \Delta_j^k \sum_i^I \frac{(d_i)\,(a_{ij})}{\sum_{j'}^J (a_{ij'})\left(\lambda_{j'}^k\right)} \tag{3.43}$$

$$0 = \lambda_j^k - \Delta_j^k \sum_i^I a_{ij} \quad . \tag{3.44}$$

Thus, Δ_j^k is chosen to be:

$$\Delta_j^k = \frac{\lambda_j^k}{\sum_i^I a_{ij}} \quad . \tag{3.45}$$

This leads to the well-known ML-EM algorithm as presented by Shepp and Vardi [102]:

$$\hat{\lambda}_j^{k+1} = \frac{\hat{\lambda}_j^k}{\sum_i^I a_{ij}} \sum_i^I \frac{(d_i)\,(a_{ij})}{\sum_{j'}^J (a_{ij'}) \left(\hat{\lambda}_{j'}^k\right)} \tag{3.46}$$

where $\hat{\lambda}_j^k$ is the reconstructed source intensity in image voxel j as calculated after k iterations. This multiplicative update algorithm starts with an initial guess λ_j^0 satisfying $\lambda_j^0 > 0$ and can be broken down into two steps: (1) expectation and (2) maximization. The expectation step:

$$\sum_{j'}^J (a_{ij'}) \left(\hat{\lambda}_{j'}^k\right) \tag{3.47}$$

determines the expected projection from the current estimate of the source distribution. The maximization step:

$$\hat{\lambda}_j^k \sum_i^I \frac{(d_i)\,(a_{ij})}{\sum_{j'}^J (a_{ij'}) \left(\hat{\lambda}_{j'}^k\right)} \tag{3.48}$$

determines the relative difference between the expected and measured projections and applies a correction to the estimate of the source distribution at each iteration k.

The advantage of ML-EM over filtered back-projection is that positivity is preserved; that is, if the initial estimate $\hat{\Lambda}^{k=0}$ is positive, and all elements in A and D are positive, then all subsequent iterations k remain non-negative. Moreover, as the number of iterations increases, image contrast improves. However, if k is too large, noise amplification can result. In practice, the optimal value of k is determined experimentally such that a good balance exists between the image contrast and noise.

3.5 Coded Aperture Imaging

Coded apertures were first introduced by Ables [8] and Dicke [9] as a means to decouple the dependence of resolution on sensitivity. This dependency is a major shortcoming of the conventional pinhole and parallel-hole designs. The main idea behind the coded aperture is to increase photon acceptance by opening many small pinholes as opposed to widening a single one. The pinholes are optimally arranged to form the coded aperture or mask. The mask in front of a position-sensitive detector collectively constitutes the coded aperture imager.

Figure 3.13 illustrates the concept of coded aperture imaging. Consider a point source in the field-of-view of a coded aperture device. Photons incident on the mask are either absorbed by 'opaque' elements or admitted through 'transparent' elements to be registered by the detector. With multiple transparent or open elements, multiple projections of the point source are cast on the detector. In fact, the overall projection appears as the mask pattern (or fraction of one). The pattern is shifted on the detector plane by an amount commensurate with the angular displacement of the source.

Furthermore, given an extended source or a collection of point sources, projections via different openings can overlap and the detector image resembles several overlapping mask patterns. This process is known as multiplexing. The objective of multiplexing is to increase the signal level with respect to the underlying noise, thereby improving the image quality.

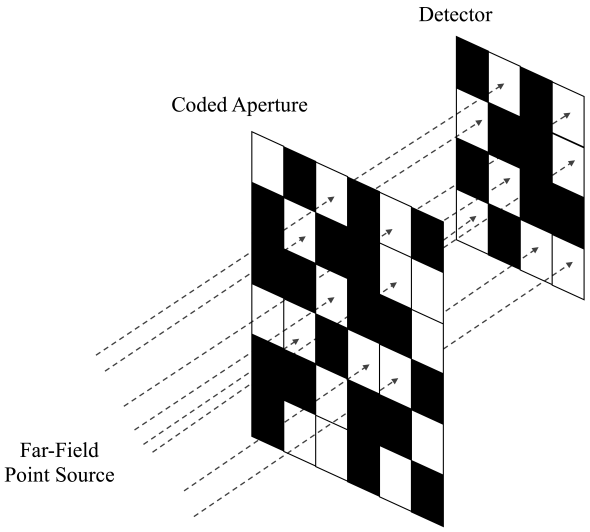

Figure 3.13: Schematic of a coded aperture imager, featuring a position-sensitive detector, mask, and point source in the far field. Opaque (closed) elements are represented in black and transparent (open) elements in white.

3.5.1 Cross-Correlation

The following describes a conventional method for reconstructing two-dimensional sources in coded aperture imaging. Assuming a two-dimensional detector plane with uniform binning and sensitivity, the detector measurement D can be determined by convolution:

$$D = A * \Lambda \tag{3.49}$$

where $*$ is the convolution operator, A is the mask pattern, often represented as a binary array of ones and zeros, and Λ is the two-dimensional source distribution.

The source distribution can be estimated using the well-known cross-correlation method:

$$\hat{\Lambda} = A^T * D = A^T * (A * \Lambda) = \left(A^T * A\right) * \Lambda \tag{3.50}$$

assuming background noise is negligible [103, 104]. The above expression is analogous to back-projection. If the autocorrelation function $\left[A^T * A\right]$ is a delta function:

$$\hat{\Lambda} = \Lambda \tag{3.51}$$

and the image is perfectly reconstructed. However, the autocorrelation is never a delta function. In practice, the mask pattern A is optimized to have an autocorrelation that consists of a single peak and flat sidelobes at a level related to the mask open fraction (i.e. ratio of the open to total mask area). To push the sidelobes closer to zero, a decoding matrix G can be applied in the following manner:

$$\hat{\Lambda} = G * D = G * (A * \Lambda) = (G * A) * \Lambda \quad . \tag{3.52}$$

The decoding matrix G is selected such that $[G * A]$ is as close as possible to a delta function. Normally G is a binary array similar to A and selected based on the aperture design [28, 103, 105].

3.5.2 Mask-Detector Arrangements

In coded aperture imaging, the field-of-view can be divided into two distinct regions: (1) fully-coded field-of-view (FCFV) in which all detected photons are modulated by the mask, and (2) partially-coded field-of-view (PCFV) in which only a fraction of the detected photons is coded. Ideally, the image space should be restricted to the FCFV as partial coding can lead to a sub-optimal image reconstruction.

The sizes of the FCFV and PCFV depend on the mask-detector arrangement. There are three practical arrangements as illustrated in Figure 3.14. The following is a discussion of the three cases and assumes a point source located in the far field. A similar argument can be applied to the near field if magnifications effects are considered.

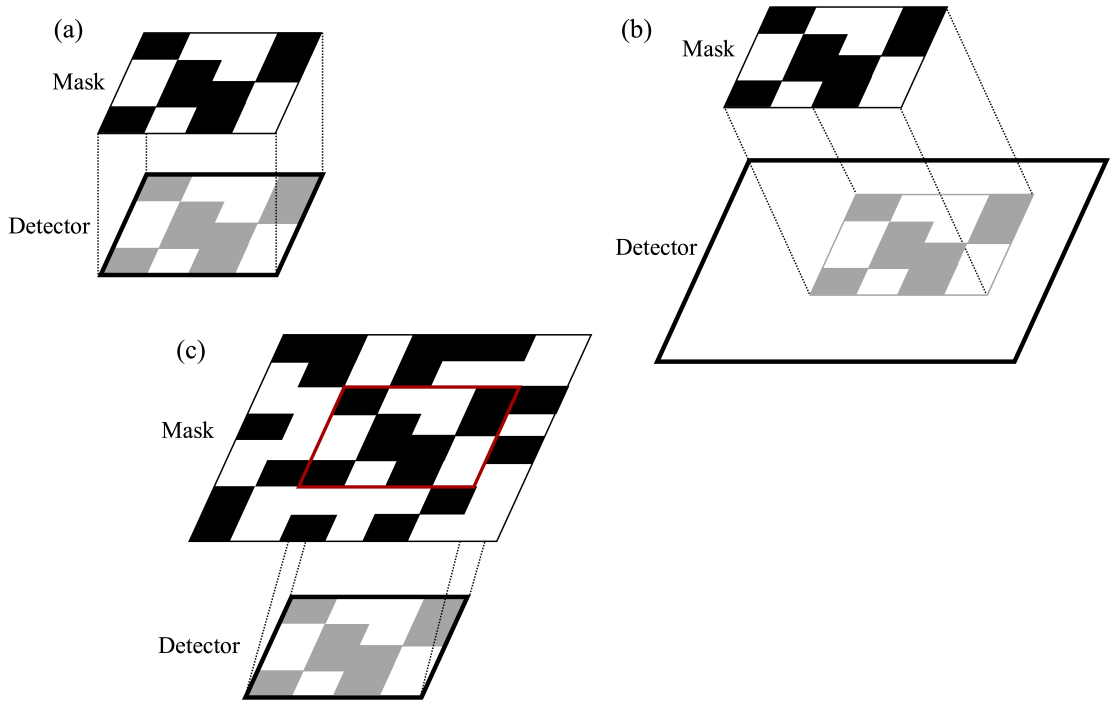

Figure 3.14: Three mask-detector arrangements: (a) the detector and mask have the same size, (b) the detector is larger than the mask, and (c) the mask is larger than the detector. In arrangement (c), the detector can only capture a fraction of the mask pattern (indicated by the red box). A far-field point source is assumed in all cases.

The simplest geometric arrangement is the (a) box camera with a detector and mask of equal dimensions. This configuration suffers from a field-of-view that is entirely partially-coded, except for the on-axis direction. A possible solution is to (b) increase the dimensions of the detector. Oftentimes, however, fabrication constraints and cost limit the detector size. A more practical arrangement (c) employs a larger mask with a more reasonably-sized detector. Figure 3.15 illustrates how both arrangement (b) and (c) widen the FCFV. Note arrangement (c) only permits a fraction of the mask pattern to be projected across the full detector in the FCFV. For such cases, the mask pattern needs to be optimized such that all sections of the mask seen by the detector are unique to prevent ambiguities in the image reconstruction [24].

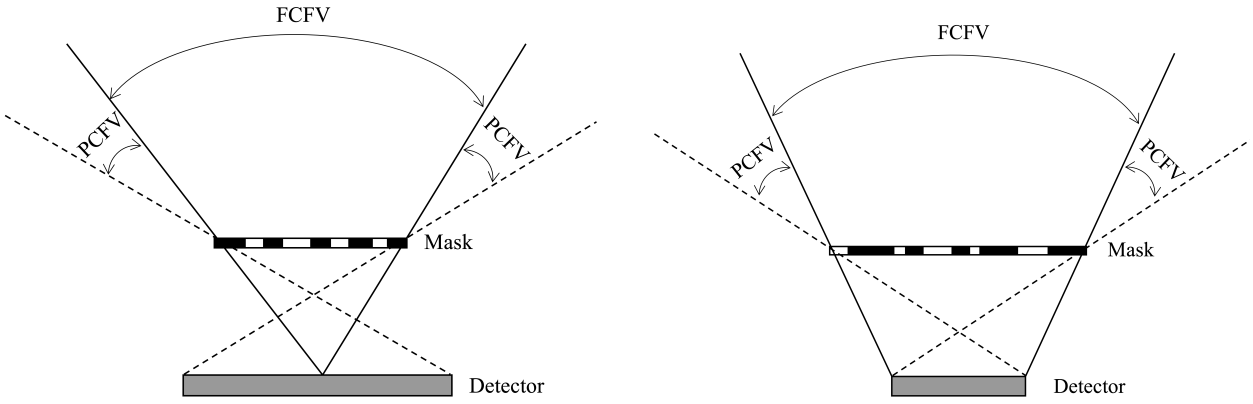

(a) Larger Detector (b) Smaller Detector

Figure 3.15: Illustration of the FCFV and PCFV for geometric arrangements where the detector is (a) larger and (b) smaller than the mask. In arrangement (a), shielding is assumed to cover the solid angle of the detector not occupied by the mask.

3.5.3 Field-of-View, Resolution, and Geometric Sensitivity

The source-mask and mask-detector arrangements play an important role in determining both the field-of-view FoV and resolution δr_{ca} of a coded aperture. These two parameters are strictly related to one another and governed by the magnification coefficient m:

$$m = \frac{h_{proj}}{h_{orig}} = 1 + \frac{b}{a} \tag{3.53}$$

as illustrated in Figure 3.16. Here m is defined as the ratio of the projection of an individual mask element to the mask element itself, and as with previous usage, a is the normal distance between the source and mask planes, and b is the normal distance between the mask and detector planes. Note m is not equivalent to the magnification m_{pin} of a pinhole. As previously defined by Equation 3.53, the magnification coefficient m_{pin} represents the ratio of the *source* projection to the original. The relationship between m and m_{pin} can be stated as follows: $m = m_{pin} + 1$.

According to Equation 3.53, as the distance between the source and mask increases, the magnification factor m approaches one: $m \to 1$. The distance at which there are no discernible magnification effects, such that the mask projection appears true-to-size, can be considered the far field. In the near field, where magnification effects exist, there is a tradeoff between field-of-view and resolution as demonstrated below.

Assuming the size l_d of the detector is less than or equal to the size l_m of the mask, the

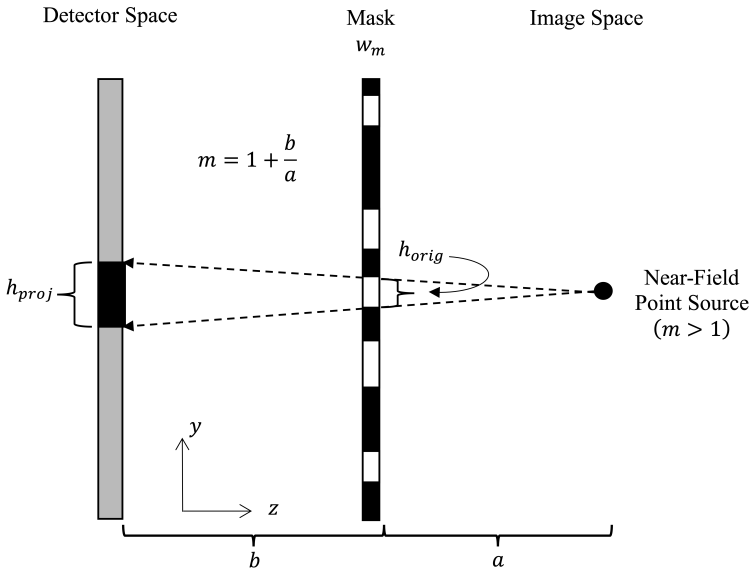

Figure 3.16: Determination of the coded aperture magnification factor m.

extent of the field-of-view FoV can be defined as:

$$FoV = \frac{(m)\,(l_m) - l_d}{m - 1} \tag{3.54}$$

as illustrated in Figure 3.17. Here FoV is considered to be the FCFV in which all detected photons are modulated by the mask. According to the above relation, the FoV widens by increasing the size l_m of the mask and/or decreasing the size l_d of the detector. If these dimensions are fixed, the best strategy for widening the FoV is to reduce the magnification factor m.

The resolution δr_{ca} of a coded aperture imager depends on the magnification factor m as well as both the detector and mask designs. A general definition of δr_{ca} can be stated as follows:

$$\delta r_{ca} \approx \sqrt{\delta r^2_{geo,\ ca} + \delta r^2_{int,\ ca}} \tag{3.55}$$

where $\delta r_{geo,\ ca}$ is dictated by the aperture design and $\delta r_{int,\ ca}$ is governed by the detector design. The geometric resolution $\delta r_{geo,\ ca}$ of the coded aperture in FWHM can be defined similarly to that of a pinhole:

$$\delta r_{geo,\ ca} \approx w_m + \left(\frac{a}{b}\right)(w_m) = \frac{(m)\,(w_m)}{m - 1} \tag{3.56}$$

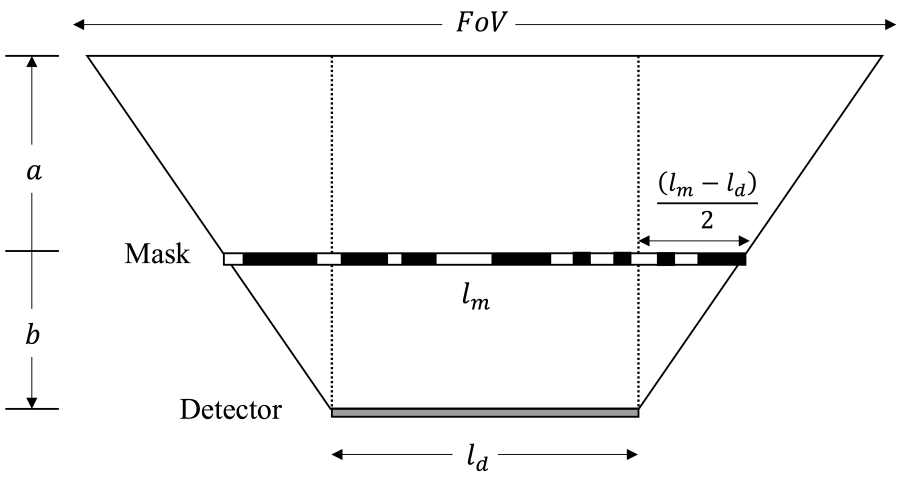

Figure 3.17: Determination of the coded aperture field-of-view for the case: $l_d < l_m$.

where w_m is the width of an individual mask element of square geometry. Because m and m_{pin} are not the same, the interpretation of $\delta r_{geo,\ ca}$ with respect to magnification varies slightly from $\delta r_{geo,\ pin}$ of a pinhole in Equation 3.18. The intrinsic resolution $\delta r_{int,\ ca}$ can be defined as:

$$\delta r_{int,\ ca} \approx \left(\frac{a}{b}\right)(w_d) = \frac{w_d}{m-1} \tag{3.57}$$

in FWHM. The above is equivalent to $\delta r_{int,\ pin}$ in Equation 3.21, except here an adjustment has been made to account for the new definition of the magnification factor m.

Incorporating Equations 3.56 and 3.57 into Equation 3.55, the resolution δr_{ca} of the coded aperture imager becomes:

$$\delta r_{ca} \approx \left(\frac{1}{m-1}\right)\sqrt{[(m)\,(w_m)]^2 + w_d^2} \tag{3.58}$$

where δr_{ca} represents the lateral (x, y) resolution in FWHM. Because the magnification factor m must always be greater than or equal to one: $m \geq 1$, the above relation states that resolution improves as m increases. This can be realized by increasing the mask-to-detector distance b and/or decreasing the source-to-mask distance a, but these adjustments come at the expense of field-of-view FoV. In situations that necessitate a wide FoV, a better strategy for improving resolution is to reduce the sizes w_d and w_m of the detector and mask pixels, respectively. That said, a smaller w_m more strictly limits the mask thickness if collimation effects are to be avoided [106].

Unlike in the cases of pinhole and parallel-hole collimators, reducing the size w_m of the mask openings does not negatively impact the geometric sensitivity $\epsilon_{geo,\ ca}$ of a coded

aperture[2]. If $\epsilon_{geo,\ ca}$ is defined as the fraction of photons emitted by the source that pass through the aperture, then:

$$\epsilon_{geo,\ ca} \approx \frac{(A_d)\,(\rho)}{4\pi a^2}\cos^3\theta \tag{3.59}$$

where ρ is the open fraction of the mask, θ is the angle between the incident photon direction and the normal to the detector, and A_d is the surface area of the detector visible to the source. While increasing the open fraction can improve sensitivity, a larger ρ does not necessarily improve the image signal-to-noise ratio as demonstrated in the following section.

3.5.4 Signal-to-Noise Ratio

The performance of any gamma-ray imager depends on its ability to faithfully reconstruct a source in terms of its intensity and spatial distribution. For detection tasks, the quality of an image can be evaluated by the signal-to-noise ratio (SNR). The SNR determines the minimum source strength that can be detected above background noise.

The main motivation behind the coded aperture design is to improve the SNR beyond that of a conventional pinhole camera, while maintaining the resolution of a single pinhole. Adding infinitely more open elements does not necessarily enhance the SNR of a coded aperture. Potential improvements depend on several factors including the source distribution, mask pattern, and reconstruction strategy.

Fenimore [107] derived the most widely-recognized expression of the SNR based on Poisson statistics. Accorsi et al. [106] slightly modified this derivation to account for mask penetration:

$$SNR_j \approx \frac{\sqrt{(n)\,(I_t)}\sqrt{(\rho)\,(1-\rho)}\,(1-\mu_T)\,(\psi_j)}{\sqrt{(1-\mu_T)\,[\rho+(1-2\rho)\,(\psi_j)]+\mu_T}} \tag{3.60}$$

where SNR_j is defined on an image pixel-by-pixel basis. Here n is the total number of mask elements, ρ is the open fraction, μ_T is the transmission probability of the opaque elements, I_t is the total source intensity, and ψ_j is the ratio of the source intensity in image pixel j to I_t. The sum of all ψ_j can be normalized to one. The textbook treatment of the SNR [107] includes a detector noise term $\mathscr{E}$ due to electronic noise, leakage current, etc. Equation 3.60 drops $\mathscr{E}$ as most modern detection systems have negligible noise. It should also be noted here that the above was derived for a uniformly redundant array (URA) and assumes uniform sensitivity across a two-dimensional image plane. Because of these assumptions, Equation 3.60 does not necessarily apply to all imaging scenarios. That said, this definition provides a good foundation for understanding the general performance of a coded aperture.

[2]This assumes the open fraction ρ remains constant.

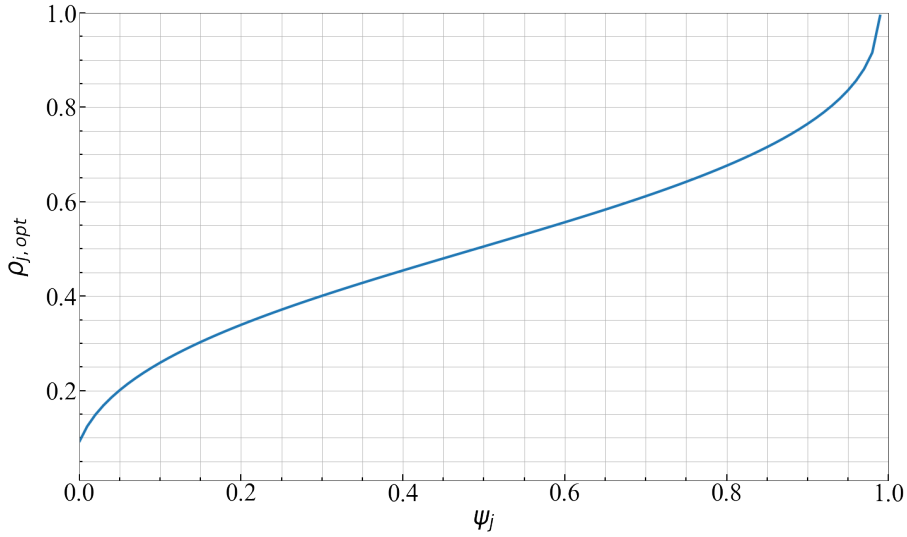

Figure 3.18: Optimal open fraction ρ as a function of the relative intensity ψ with a transmission probability $\mu_T = 0.01$. Adapted from Accorsi [106].

Setting to zero the derivative of SNR_j with respect to ρ yields the optimal open fraction $\rho_{j,\,opt}$:

$$\rho_{j,\,opt} \approx \frac{\mu_T + (\psi_j)(1-2\mu_T) - \sqrt{[\mu_T + (\psi_j)(1-2\mu_T)]^2 - (1-\mu_T)(2\psi_j - 1)[(\psi_j)(1-\mu_T) + \mu_T]}}{(1-\mu_T)(2\psi_j - 1)} \,. \tag{3.61}$$

Figure 3.18 illustrates the relationship between $\rho_{j,\,opt}$ and ψ_j. For large ψ_j, the optimal open fraction is greater than 0.5. In fact, given a point source with $\psi_j \approx 1$, the ideal mask pattern is an anti-pinhole with a single opaque element. For small ψ_j, the optimal open fraction is less than 0.5.

The SNR of a pinhole can be crudely approximated from Equation 3.60 by the following adjustment:

$$\rho_{pin} = \frac{1}{n} \tag{3.62}$$

which represents a single open element. A simple comparison between the SNR_{ca} of a coded aperture and the SNR_{pin} of a pinhole can now be made:

$$\frac{SNR_{ca}}{SNR_{pin}} \approx \frac{\sqrt{\rho_{ca}(1-\rho_{ca})}\sqrt{\rho_{pin} + (1-2\rho_{pin})(\psi_j)}}{\sqrt{\rho_{pin}(1-\rho_{pin})}\sqrt{\rho_{ca} + (1-2\rho_{ca})(\psi_j)}} \tag{3.63}$$

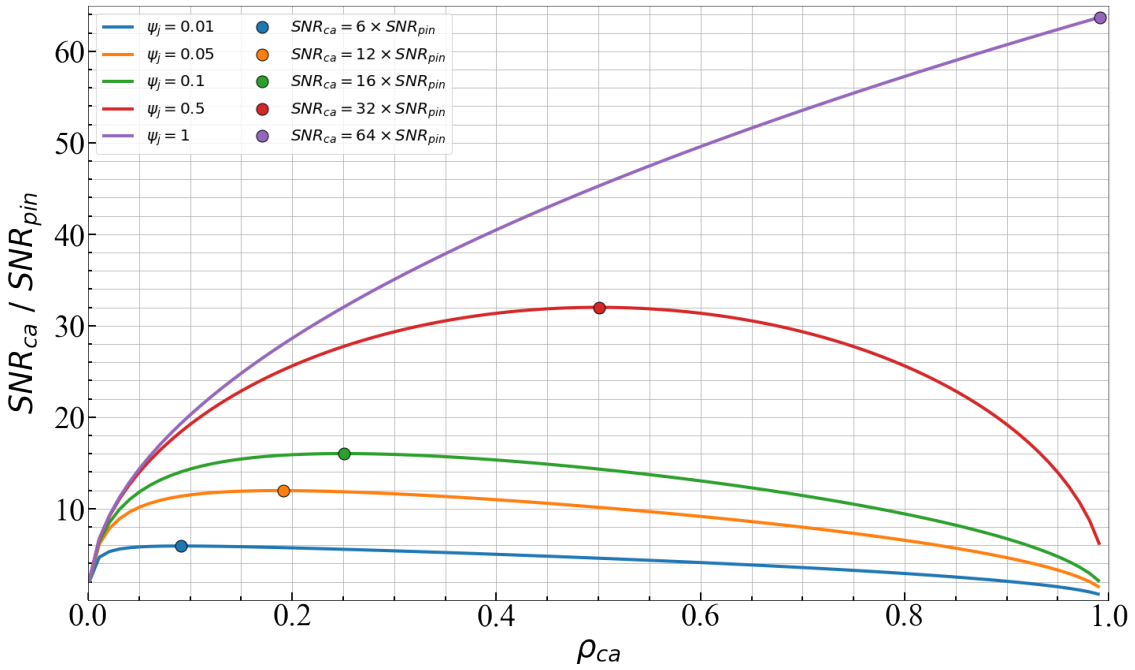

Figure 3.19: SNR_{ca}/SNR_{pin} as a function of the coded aperture open fraction ρ_{CA} for various ψ_j. The coded aperture and pinhole masks are assumed to have equivalent dimensions: $n_{ca} = n_{pin} = 64 \times 64$. The circular markers indicate the maximum gains in SNR_{ca} with respect to ρ_{CA} for a given ψ_j.

assuming mask penetration is negligible: $\mu_{T,\ ca} = \mu_{T,\ pin} = 0$ and the coded aperture and pinhole collimator have equivalent dimensions: $n_{ca} = n_{pin}$. The ratio $[SNR_{ca}/SNR_{pin}]$ represents the performance advantage of a coded aperture over a pinhole, where

$$\frac{SNR_{ca}}{SNR_{pin}} > 1 \tag{3.64}$$

indicates superior performance by the coded aperture.

Figure 3.19 illustrates the performance advantage of a coded aperture as a function of its open fraction ρ_{ca} for various ψ_j. As ψ_j increases, the gains in coded aperture performance become more significant. Fenimore [107] concluded that the largest gains are achieved with a 50% open fraction: $\rho_{ca} = 0.5$. This conclusion assumed a detector with high background noise. In most imaging scenarios, however, detector noise is negligible. Furthermore, the fraction of the total source intensity in each image pixel j is oftentimes much less than one: $\psi_j << 1$. Under these conditions, to observe a smaller ψ_j, a coded aperture with an open fraction of less than 50% is favored.

3.6 Compton Imaging

Collimator-based imaging is not effective at energies above a few hundred keV, because unwanted photon penetration through the collimator becomes more probable. Furthermore, Compton scattering is the dominant interaction mechanism in this energy range (up to several MeV). Scattering is detrimental to the image reconstruction given one of two scenarios. First, the scattered photon can escape the detector, resulting in partial energy deposition. If an energy discrimination window has been established, photon escape acts as a mechanism of sensitivity loss. Second, the scattered photon can induce a series of interactions that eventually leads to photoelectric absorption in the detector. In this case, energy discrimination can not be used to reject the event. If the imager has no capability of tracking the photon interaction history, the event is oftentimes mispositioned between the interaction positions, which ultimately degrades the image resolution.

Compton imaging circumvents the above limitations by providing a collimator-less approach that takes advantage of Compton scattering kinematics. This approach generally requires the incident gamma ray to interact by two mechanisms: (1) Compton scattering followed by (2) photoelectric absorption. Depending on the incident energy, the photon can undergo a series of scattering interactions before final absorption. This series of interactions is called a Compton event. To increase the likelihood of such events, multiple layers of position-sensitive detectors can be employed. With this setup, one detector can act as a scatterer in which the incident gamma ray undergoes Compton scattering, and a separate detector can act as an absorber in which the scattered photon is fully absorbed via the photoelectric effect.

By measuring the energy depositions and positions of the first two interactions in a given event, a so-called Compton cone can be back-projected into the image space using Compton kinematics. The surface of this cone contains all possible positions from which the incident photon could have originated. The overlap of several back-projected cones provides an estimate of the source distribution.

Figure 3.20 provides a schematic of a back-projected Compton cone. The cone has a vertex at the first interaction site. The symmetry axis is defined by the first r_1 and second r_2 interaction positions. The distance r_{12} between r_1 and r_2 is called the lever arm: $r_{12} = r_2 - r_1$. Based on the Compton scattering formula in Equation 3.2, the opening angle θ of the cone can be defined as:

$$\cos\theta = 1 + m_e c^2 \left(\frac{1}{E_\gamma} - \frac{1}{E'_\gamma} \right) \quad . \tag{3.65}$$

In practice, the incident gamma-ray E_γ is known. The energy E'_γ of the scattered gamma-ray cannot be directly measured, because spectroscopic detectors are only sensitive to the energy transferred to electrons. Instead, E'_γ is determined by

$$E'_\gamma = E_\gamma - E_1 \tag{3.66}$$

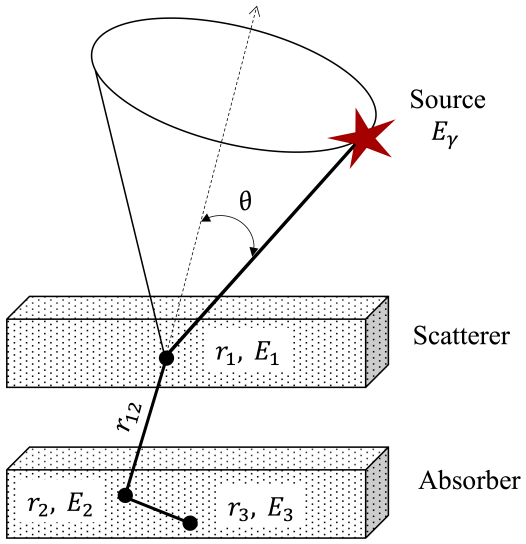

Figure 3.20: Schematic of a back-projected Compton cone produced from a triples event (i.e. two scatterings followed by absorption) in a Compton imager. The imager features two position-sensitive detectors. The symmetry axis of the Compton cone is defined by the first r_1 and second r_2 interaction positions. The opening angle θ is defined by the energy deposition E_1 at the first interaction site and the incident photon energy E_γ.

where E_1 is the energy imparted to the Compton-scattered electron (i.e. energy deposited within the detector) at the first interaction site.

It should be noted here that the process of back-projecting Compton cones varies slightly between the far and near field. Figure 3.21 illustrates the distinction between the two regimes. In the far-field, the distance between the source and detector far exceeds the detector dimensions such that the detector can be considered a point. In other words, if you move the vertex of the cone within the detector volume, the estimate of the incident photon direction remains unchanged. Thus, the image space can be characterized as a two-dimensional celestial sphere where the cone arcs are projected as rings. As the rings overlap, the source direction in flux units (photons cm^{-2} s^{-1} keV^{-1}) can be determined. In the near-field regime, the variations in the cone vertices are no longer negligible. The cones are back-projected in a three-dimensional space where the cone surfaces overlap. This provides an estimate of both the source direction and distance in density units (photons cm^{-3} s^{-1} keV^{-1}).

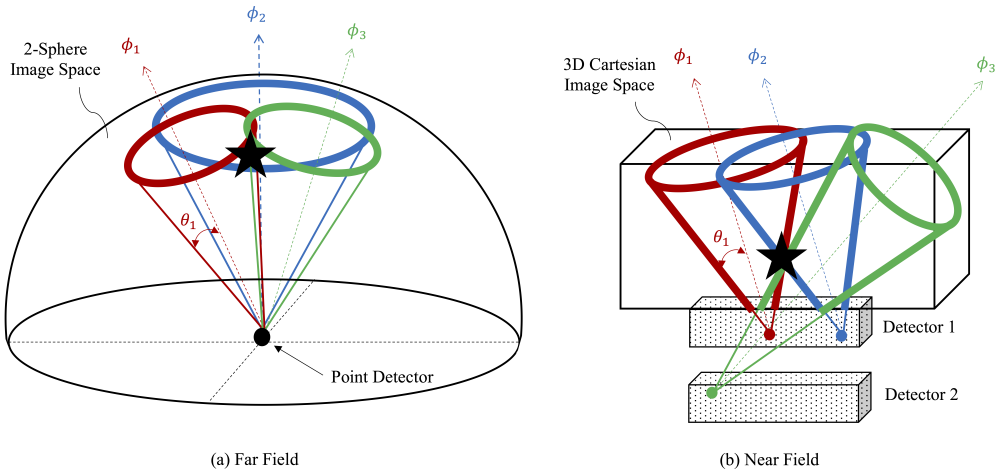

Figure 3.21: Compton back-projection depends on whether a source is the near or far field. Illustrated are three back-projected Compton cones, with different scattering axes ϕ, in the (a) far versus (b) near field. In the far field, cones are back-projected on a celestial sphere. In the near field, cones are back-projected in a 3-D Cartesian space. The bolded outlines represent the cone regions that intersect the image space, and the black star represents the source location.

3.6.1 Gamma-ray Tracking

Gamma-ray tracking is an integral processing step in Compton imaging. This step determines the exact or most likely interaction sequence for a given event. Generally speaking, interactions cannot be sequenced by time of occurrence due to the finite time resolution of the detector.

In some cases, relativistic kinematics can be used to determine the exact sequencing. According to the kinematics relation in Equation 3.65, the following condition must be satisfied for energy and momentum to be conserved:

$$-1 \leq \cos\theta \leq 1 \quad .$$

For events in which the incident photon energy E_γ is less than 256 keV, the above constraint is satisfied only if the preceding interaction has a smaller energy deposition than that of the subsequent interaction.

For events in which E_γ is greater than 256 keV, the sequencing is less straightforward. In such cases, kinematics can only provide constraint if the event satisfies the following two criteria: (1) two interactions only and (2) one of the two interactions has an energy deposition that exceeds the maximum limit for Compton scattering. Equation 3.5 defines the maximum limit as $E_{max} = E_{e^-}\ (\theta = \pi)$, and Figure 3.22 shows E_{max} as a function of the

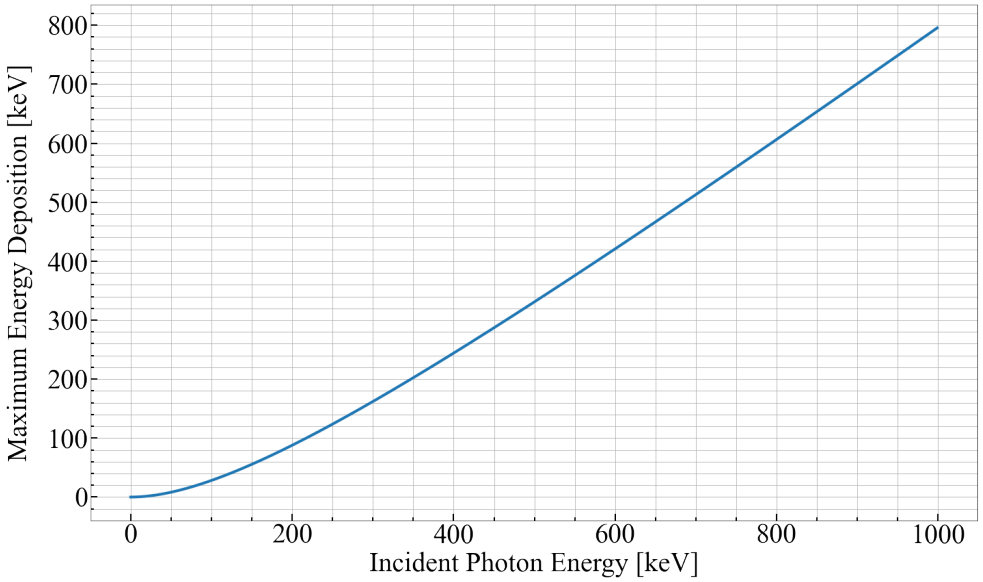

Figure 3.22: The maximum energy that can be deposited in a Compton scattering interaction for a given incident photon energy.

incident photon energy E_γ. To better explain, consider a two-interaction event in which the interactions are labeled A and B. The interaction sequence might either be AB or BA. If the energy deposition of interaction A exceeds E_{max}, then B must necessarily be the first interaction via Compton scattering and A must necessarily be the second interaction via photoelectric absorption. For all other scenarios in which this limit is not exceeded or there are three or more interactions, the sequencing is ambiguous and statistical arguments must be made. The statistical arguments employed in this work are discussed in Section 4.2.1.

3.6.2 Angular Resolution

Although the back-projection of a Compton event should ideally produce a sharp cone, in reality the Compton cone is not well-defined due to Doppler broadening and uncertainties in the measured energy depositions and positions of interaction. These uncertainties propagate to the incertitude in the cone opening angle, thereby resulting in a blurring effect. This effect gives the cone a small thickness, which effectively represents the angular resolution of the Compton imager.

The following is a derivation of the Compton angular resolution using error propagation as laid out by Mihailescu et al. [108]. The opening angle θ of the Compton cone can be expressed as:

$$\cos\theta = 1 + \frac{1}{K_0} - \frac{1}{K_d} \quad . \tag{3.67}$$

From Equation 3.65:

$$K_0 = \frac{E_\gamma}{m_e c^2} \tag{3.68}$$

$$K_d = \frac{(E_\gamma - E_1)}{m_e c^2} \tag{3.69}$$

where E_1 is the energy deposited at the first interaction site. The uncertainty $\delta\theta$ in the opening angle can be broken down into two main error components:

$$\delta\theta = \sqrt{\delta^2\theta_E + \delta^2\theta_r} \tag{3.70}$$

where $\delta\theta_E$ considers the uncertainty in the energy depositions and $\delta\theta_r$ accounts for the uncertainty in the interaction positions. The first error component $\delta\theta_E$ can be defined as:

$$\delta^2 \cos\theta_E = \frac{1}{K_0^4}\delta^2 K_0 + \frac{1}{K_d^4}\delta^2 K_d \quad . \tag{3.71}$$

Note that δK_0 and δK_d are not the same. While both δK_0 and δK_d account for the finite energy resolution of the detector, δK_d also accounts for the uncertainty in E_1 due to Doppler broadening [109, 110].

The second error component $\delta\theta_r$ can be expressed as:

$$\delta^2 \cos\theta_r = (\sin\theta\delta\theta_r)^2 \tag{3.72}$$

where $\delta\theta_r$ accounts for the finite position resolution of the detector. The uncertainty $\delta\phi$ in the scattering direction can be transferred to $\delta\theta_r$ as follows:

$$\delta^2\theta_r = \delta^2\phi \approx \sin^2\delta\phi = \frac{2\delta^2 r}{r_{12}^2} \tag{3.73}$$

as illustrated in Figure 3.23. Here r_{12} is lever arm or distance between the first and second interaction sites. The above definition employs a small-angle approximation: $\delta\phi \approx \sin\delta\phi$ and assumes identical position resolutions in all three physical coordinates: $\delta x = \delta y = \delta z = \delta r$.

Plugging Equation 3.73 into Equation 3.72 gives:

$$\delta^2 \cos\theta_r = 2\left(1 - \cos^2\theta\right)\frac{2\delta^2 r}{r_{12}^2} \quad . \tag{3.74}$$

Finally, by incorporating the two error components in Equations 3.71 and 3.74 into Equation

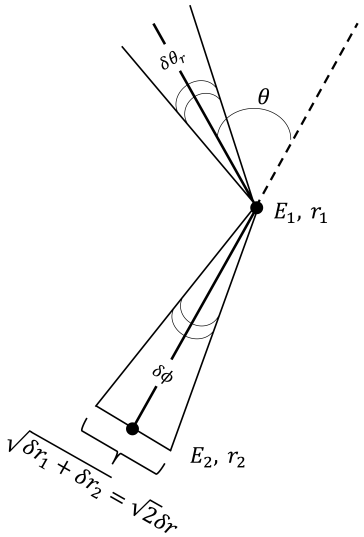

Figure 3.23: Depiction of the first two interaction positions, r_1 and r_2, and the associated uncertainty $\delta\phi$ in the scattering direction. $\delta\phi$ contributes to the overall angular uncertainty of the Compton cone. Adapted from [108].

3.70, the overall angular uncertainty in cosine becomes:

$$\delta \cos\theta = \sqrt{\frac{1}{K_0^4}\delta^2 K_0 + \frac{1}{K_d^4}\delta^2 K_d + 2\left(1 - cos^2\theta\right)\frac{\delta^2 r}{r_{12}^2}} \tag{3.75}$$

where the angular resolution $\delta\theta$ is determined by the inverse cosine of the above expression. While $\delta\theta$ can be improved by employing detectors with superior energy and position resolutions, the angular resolution is fundamentally limited by Doppler broadening, the severity of which can be partially controlled by the choice of detector material [111].

Chapter 4

Methods of Dual-Modality Imaging

Chapter 4 describes various methods critical in the development and implementation of the Dual-Modality Imager, a cart-based platform that provides both coded aperture and Compton imaging capabilities. This platform was not designed for a specific application, but rather envisioned for more general-purpose imaging scenarios. This work employs the Dual-Modality Imager to merely demonstrate the feasibility of applying coded aperture and Compton imaging to near-field applications; thereby informing the next generation of more specialized imagers.

The remainder of Chapter 4 is structured as follows. Section 4.1 describes the hardware components of the Dual-Modality Imager and includes a detailed discussion of the coded aperture design and pattern optimization. Section 4.2 summarizes strategies for event reconstruction, an integral processing step in both coded aperture and Compton imaging. Sections 4.3 and 4.4 outline methods of coded aperture and Compton image reconstruction, respectively. Finally, Section 4.5 demonstrates the performance of the Dual-Modality Imager at both the detection and imaging level.

4.1 The Dual-Modality Imager

4.1.1 System Overview

The Dual-Modality Imager is a cart-based gamma-ray imaging prototype that functions as both a coded aperture and Compton imager. The cart houses two 3-D position-sensitive HPGe DSSDs manufactured by Lawrence Berkeley National Laboratory (LBNL). The two detectors are housed in the same cryostat and separated by a distance of 10 mm to maximize the solid angle between them. Each detector consists of a planar HPGe crystal with an active volume of $74 \times 74 \times 15$ mm^3 surrounded by 2-mm wide guard rings to reduce leakage current. The opposite faces of each detector have 37×37 orthogonal strip electrodes with a strip pitch of 2 mm. This electrode configuration gives an intrinsic granularity of 1369 pixels of 2-mm width.

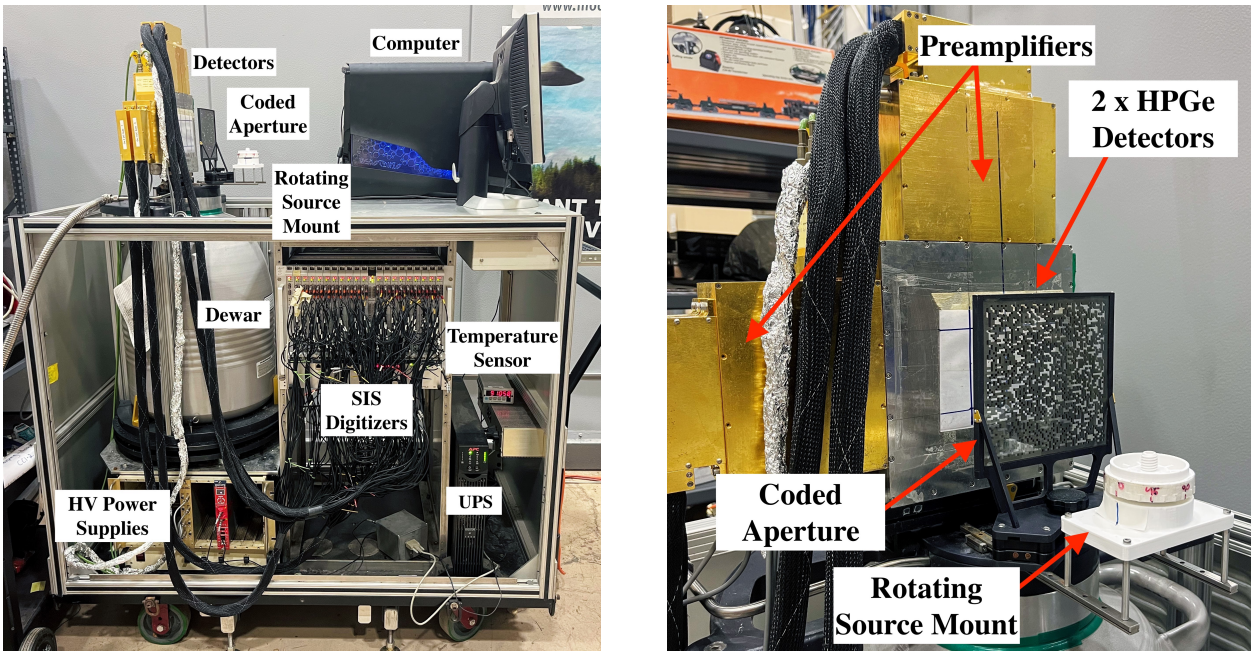

(a) (b)

Figure 4.1: (a) The Dual-Modality Imager in its entirety. (b) A close-up of the detector-mask arrangement.

The strips are wire-bonded to a custom readout board, which is connected to a flex circuit that feeds the signals through the exterior of the cryostat. From there the signals are distributed on four motherboards, two for each detector, with each housing 37 compact charge-sensitive preamplifiers. This amounts to 148 channels in total. The preamplifier signals from each channel are sent to a readout module that digitizes and filters the raw waveforms to extract information about the pulse shape and amplitude. The readout module itself consists of 19 individual 8-channel digitization units with FPGAs that are commercially available from Struck Innovative Systems (SIS) with a model number SIS3302. The digitizers are housed in a VME crate consisting of a SIS3150 VME-to-USB2.0 interface to transfer data to a host computer.

Figure 4.1a shows the fully-assembled cart, which includes a variety of other equipment critical to the operation of the system:

- 30L liquid nitrogen dewar to cool the detectors,
- temperature sensor,
- NIM bin that contains both a preamplifier power supply and a dual-channel high-voltage power supply to bias the detectors (operated at 800 V),

- uninterruptible power supply (UPS) in the event of a power outage, and
- desktop computer to communicate with the system (via a Graphical User Interface) and acquire and analyze the data.

The last critical component of the cart is the coded aperture, the design of which is discussed in Section 4.1.2. The mask is fastened to a stand situated at an adjustable distance in front of the front detector with the centers of the mask and detector planes aligned. Figure 4.1b shows a close-up of the mask-detector arrangement. The coded aperture combined with the front detector constitutes the coded aperture imager, while the front and back detectors collectively form the Compton camera.

The current geometric arrangement illustrated in Figure 4.2 does not allow the simultaneous use of both modalities without a cost to imaging performance. This is particularly true in the near field. Because the Compton modality is characterized by a finite angular resolution, decreasing the distance between the imager and source will significantly improve the image spatial resolution. However, with the coded aperture in place, the minimum standoff distance is limited to the distance between the mask and front detector. Furthermore, the mask allows fewer photons to reach the detector, thereby reducing the Compton imaging sensitivity. For these reasons, the two modalities are operated separately with the mask removed in the Compton mode.

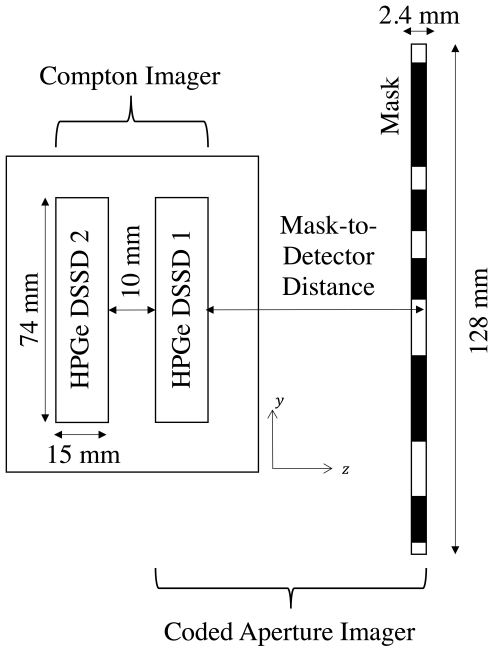

Figure 4.2: A schematic of the Dual-Modality Imager, illustrating the coded aperture and Compton geometries.

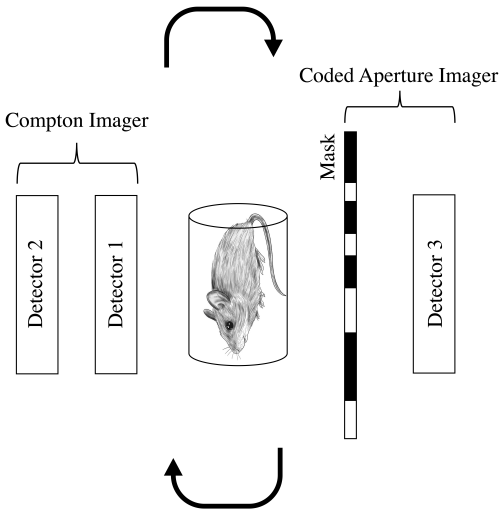

Figure 4.3: A schematic of a coded aperture and Compton imager that enables simultaneous use of both modalities without a cost to imaging performance. Black arrows represent the possible rotation of the imager around the source. This system could be of use to small-animal imaging applications.

In designing a more specialized imager for time-sensitive applications that require simultaneous use, a third detector can be introduced on the opposite side of the mask. In this configuration, the Compton camera would be formed by the original two detectors and the coded aperture imager would formed by the mask and newly-added third detector as illustrated in Figure 4.3. This allows the source to be positioned in between the two modalities in a configuration that is well-suited to both.

4.1.2 Coded Aperture Design

The Dual-Modality Imager was originally conceived as a single-modality Compton imager, consisting of just two detectors [112]. Thus, the design of the coded aperture was heavily influenced by (a) the pre-existing system as well as (b) the conditions under which the new system was to be operated. Regarding (b), the coded aperture was envisioned for general-purpose imaging scenarios across a range of magnifications in the near- to far-field. This work, however, solely focuses on the near-field application of the coded aperture. Keeping both (a) and (b) in mind, the following discussion presents major design considerations in developing the coded aperture.

Table 4.1 summarizes the design features of the coded aperture. The mask is of square geometry consisting of 64×64 square elements with a 50% open fraction. The open fraction was selected based on the study by Fenimore [107][1]. Each individual element has a 2×2 mm^2

[1]In hindsight a smaller open fraction should have been chosen based on the discussion in Section 3.5.4.

Table 4.1: Design specifications of the coded aperture employed by the Dual-Modality Imager.

Material	tungsten
Thickness	2.4 mm
Array type	random
Array size	64×64 elements
Element face shape	square
Element face size	2×2 mm^2
Element side profile	trapezoidal
Open fraction	50%

face to match the detector pixels and limit collimation effects. The mask area in its entirety is roughly four times the area of the detector. By employing a mask with larger dimensions than the detector, the field-of-view widens, which in turn enables more extended sources to be imaged.

Another important design consideration is the material and thickness of the opaque elements. The objective is the complete attenuation of photons in the energy range of interest, as the transmission of unwanted photons leads to image degradation. This objective is achieved by employing a material of high atomic number and sufficient thickness. The mask is fabricated out of 2.4-mm-thick tungsten, which ensures roughly 90% attenuation at 250 keV.

While increasing the thickness would improve the absorption efficiency at higher energies, a thicker mask is not always ideal due to weight constraints and collimation effects. The latter effect arises from photons that enter through an open element at an oblique angle of incidence to then be stopped by a neighboring closed element. The impact on the detector measurement is twofold: (1) lower sensitivity with fewer photons being registered by the detector, and (2) lower coding contrast given that there is a modulation in the intensity of the mask projection. The severity of (2) is heightened in the near field where photons from a single point source hit the imager at varying angles of incidence, and the ultimate impact of (2) is a sub-optimal image reconstruction in terms of both image contrast and resolution.

To mitigate collimation effects, the mask has diverging elements as opposed to parallel-facing ones. Specifically, the elements have trapezoidal profiles that diverge in the image space and converge in the detector space at a distance of 210 mm (Figure 4.4d). When flipped, the coded aperture naturally transforms into a converging mask with elements that now converge in the image space and diverge in the detector space (Figure 4.4b). The optimal mode of operation depends on the application as illustrated in Figure 4.4. The diverging mask is useful for imaging sources located at the extremities of the field-of-view, while the

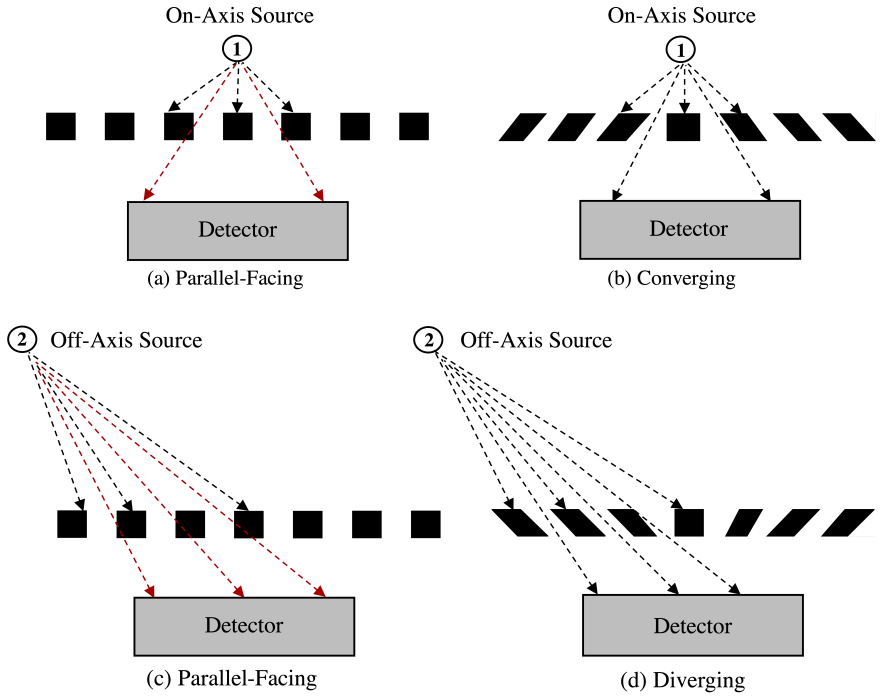

Figure 4.4: Illustration of (1) an on-axis point source being imaged by (a) a parallel-facing versus (b) converging coded aperture and (2) an off-axis point source being imaged by (c) a parallel-facing versus (d) diverging coded aperture in the near field. Red arrows represent photons that enter through an open element and travel partially through a neighboring closed element. This results in a modulation in the intensity of the mask projection, thereby degrading the coding contrast. In imaging scenarios (1) and (2), the sensitivity and coding contrast improve by employing the (b) converging and (d) diverging coded apertures, respectively.

converging mask is ideal for imaging sources located at the center of the field-of-view.

To demonstrate this, the following evaluates the sensitivity profiles of the mask in the diverging and converging modes as well as that of a similarly-designed mask with parallel-facing elements. The sensitivities were determined analytically by:

$$s_{j,\ ca} = \sum_{i}^{I} a_{ij} \tag{4.1}$$

where $s_{j,\ ca}$ is the sensitivity of the coded aperture imager at image voxel j, and a_{ij} is the system response at detector pixel i and image voxel j. The system response a_{ij} was generated at 122 keV using a ray-tracing method outlined in Section 4.3.3. Here $s_{j,\ ca}$ represents the absolute sensitivity defined as the fraction of total emitted photons that are registered by

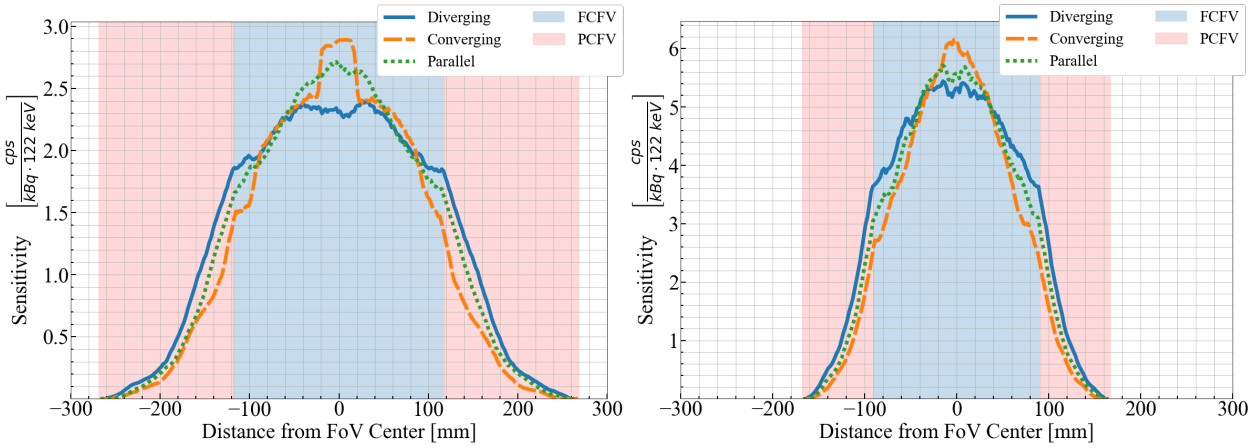

(a) $m = 1.5$ ($a + b = 270$ mm) (b) $m = 2$ ($a + b = 180$ mm)

Figure 4.5: Sensitivity profiles across the horizontal axis of an image plane at a fixed mask-to-detector distance of $b = 90$ mm. The profiles were analytically generated at a magnification of (a) $m = 1.5$ and (b) $m = 2$ for a mask with diverging, converging, and parallel-facing elements. The blue region represents the extent of the FCFV, and the red region represents the PCFV. Note the amplitude of the sensitivity profile at $m = 1.5$ is less than that at $m = 2$. This should be expected as the normal distance a between the image and mask planes is greater at $m = 1.5$.

the detector.

The sensitivity $s_{j,\,ca}$ was computed across the horizontal axis of an image plane at two magnifications: $m = 1.5$ and $m = 2$ at a fixed mask-to-detector distance of 90 mm. This distance is consistent with that which we employ for coded aperture imaging later on. Figure 4.5 shows the sensitivity profiles of the diverging, converging, and parallel-facing masks at the different magnifications in both the partially-coded field-of-view (PCFV) and fully-coded field-of-view (FCFV). In the PCFV, unmodulated photons were assumed to be absorbed by an external shield; and thus, these photons do not contribute to the detector measurement.

In comparing the three masks in the field-of-view, a larger sensitivity would indicate less collimation effects. With this in mind, the converging mask most effectively mitigates collimation effects near the center of the FCFV, while the diverging mask is most effective at the edges of the FCFV and all throughout the PCFV. Furthermore, the parallel-facing mask exhibits middle-of-the-road performance across the extent of the field-of-view. This is true at both magnifications. Of particular interest to this work is imaging centrally-located sources in the near field; thus, only the converging mask is used.

4.1.3 Coded Aperture Pattern Optimization

The mask pattern strongly impacts the attainable quality of the image. In designing the optimum pattern, the objective is the maximization (or minimization) of a specific quality metric Q. While Q can be a function of many performance characteristics, oftentimes this metric is a representation of the SNR. The maximization of the SNR is partially realized by having an optimal balance between the number of transparent and opaque mask elements. Equally important is the arrangement of the mask elements. In other words, all sections of the mask that can be projected onto the detector must be unique to avoid ambiguities in the image reconstruction. Mathematically, a section is deemed unique if the sidelobes of its periodic correlation are flat.

The most commonly-used aperture patterns are uniformly redundant arrays (URAs) and modified uniformly redundant arrays (MURAs) due to their perfectly flat sidelobes [24, 105, 113, 114]. However, the correlation properties of these patterns are only ideal at a fixed magnification m. Oftentimes, URAs and MURAs are designed for the far field where the source projects a true-to-size pattern: $m = 1$.

In the near field, the pattern appears magnified. The degree of magnification depends on the source distance as shown by Equation 3.53. For a source distributed along multiple depth planes, the detector sees mask projections with varying degrees of magnification. For URAs and MURAs, the different magnifications can lead to ambiguities in the image reconstruction. Furthermore, URAs and MURAs only exist for a limited number of open fractions and array sizes, with the latter restricting the choice of detector [115, 116]. To avoid these restrictions, this work uses a combinatorial search technique, known as the *Great Deluge Algorithm*, to generate a random array that is optimized across a range of magnifications [117].

4.1.3.1 Derivation of Quality Function

To generate a random array, the following two-step optimization strategy was applied: (1) derive a quality function Q that reflects the SNR and (2) perform a minimization of Q. The following outlines these two steps.

Starting with step (1), let the mask be represented by a square matrix of ones (transparent elements) and zeros (opaque elements). This matrix is subdivided into equally-sized submatrices that are separated consecutively by one bin as illustrated in Figure 4.6. Each submatrix effectively represents a section of the mask projected onto the detector at a given image voxel. The shift of the submatrix is determined by the lateral position of the image voxel. Furthermore, the size of the submatrix is determined by the distance of the image voxel as this distance impacts the magnification of the mask projection.

Assuming the detector and mask have equivalent bin sizes, the total number of bins in each submatrix n_s can be determined as follows: $n_s = n_d/m^2$, where n_d is the total number of detector bins and m, as with previous usage, is the magnification factor. Here the size of the detector n_d is roughly 1/4 the size of the mask n_m. Thus, the size of each submatrix

should be:

$$n_s = \frac{n_m}{4m^2} \quad . \tag{4.2}$$

A correlation matrix F is then produced at a certain magnification. Each row in F represents the periodic correlation of a given submatrix across the mask array. Each element f_{uv} is computed by: $f_{uv} = \langle U, V \rangle / n_s$ where $\langle U, V \rangle$ is the inner product of the U^{th} and V^{th} submatrices, and u and v are both indices that vectorize the shifts in x and y. F should be a square matrix of size $N \times N$ where N represents the total number of submatrices in the mask array.

Furthermore, F can be expanded to accommodate the correlation across multiple magnifications. The correlation was performed across $m = 1$ and $m = 2$ in order to prevent the possibility of a submatrix at $m = 2$ resembling a portion of a submatrix at $m = 1$. In this case, F now consists of four correlation matrices:

$$F = \begin{bmatrix} F_{11} = \begin{bmatrix} \langle U_{m=1}, V_{m=1} \rangle & \cdots \\ \vdots & \ddots \end{bmatrix} & F_{12} = \begin{bmatrix} \langle U_{m=1}, V_{m=2} \rangle & \cdots \\ \vdots & \ddots \end{bmatrix} \\ F_{21} = \begin{bmatrix} \langle U_{m=2}, V_{m=1} \rangle & \cdots \\ \vdots & \ddots \end{bmatrix} & F_{22} = \begin{bmatrix} \langle U_{m=2}, V_{m=2} \rangle & \cdots \\ \vdots & \ddots \end{bmatrix} \end{bmatrix} \tag{4.3}$$

where F_{11} represents the correlation matrix at $m = 1$ only, and F_{22} represents the correlation matrix at $m = 2$ only. Note F_{11} is inherently four times smaller than F_{22}. Thus, F_{11} is oversampled by repeating each element an appropriate number of times to match the size of F_{22}. The correlation matrices F_{12} and F_{21} are equivalent and represent the correlation between $m = 1$ and $m = 2$. For this correlation to be feasible, the submatrices at $m = 2$ are oversampled to match the size of the submatrices at $m = 1$.

For the mask to have uniform sensitivity across the extent of the field-of-view, the diagonal elements of F (or F_{11} and F_{22}) should be equal to the mask open fraction ρ. Furthermore, for the mask to be perfectly unique, the off-diagonal elements should be equal to ρ^2. Thus, the ideal correlation matrix would take the form:

$$F_{ideal} = \begin{bmatrix} \boldsymbol{\rho} & \rho^2 & \rho^2 & \rho^2 & \rho^2 \\ \rho^2 & \boldsymbol{\rho} & \rho^2 & \rho^2 & \rho^2 \\ \rho^2 & \rho^2 & \boldsymbol{\rho} & \rho^2 & \rho^2 \\ \rho^2 & \rho^2 & \rho^2 & \boldsymbol{\rho} & \rho^2 \\ \rho^2 & \rho^2 & \rho^2 & \rho^2 & \boldsymbol{\rho} \end{bmatrix} \quad . \tag{4.4}$$

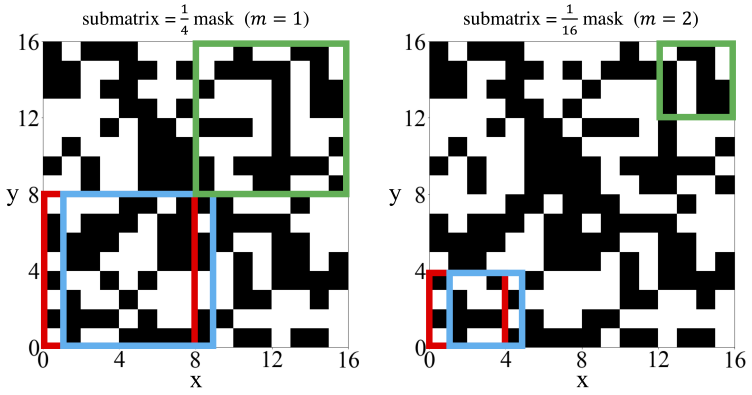

Figure 4.6: Illustration of subdividing a 16×16 aperture array into submatrices with sizes that correspond to a magnification of (a) $m = 1$ and (b) $m = 2$ for a detector whose area is $\frac{1}{4}$ that of the mask. The black and white squares represent zeros and ones, respectively. The red and blue boxes outline the first two submatrices at the zero and first shifts, respectively. The green box outlines the last submatrix in the array. This mask array is *not* employed by the Dual-Modality Imager; it is being used as a simple illustration.

Based on F_{ideal}, the quality function Q can be defined as:

$$Q = \frac{1}{N} \sum_{u,\, v\ (u=v)}^{N} (f_{uv} - \rho)^4 + \frac{1}{N^2 - N} \sum_{u,\, v\ (u \neq v)}^{N} \left(f_{uv} - \rho^2\right)^4 \tag{4.5}$$

where the first sum represents the deviation of the diagonal elements from ρ and the second sum represents the deviation of the off-diagonal elements from ρ^2.

4.1.3.2 Minimization of Quality Function

Because the quality function in Equation 4.5 represents a deviation from ideal conditions, step (2) is to minimize Q. Minimization of Q is equivalent to maximizing the SNR. To perform the minimization, the Great Deluge Algorithm proposed by Dueck [118] was employed. This combinatorial search strategy starts with a random array of a specified open fraction; here an open fraction of 50% was selected. For each iteration, an element in the array is chosen at random and tentatively toggled from one to zero (or vice versa). The quality metric Q is then computed. As this is a minimization problem, the modification is only accepted if the resulting Q is below a given "water-level". By gradually lowering this threshold, the problem converges. Here the algorithm converged to around the same Q value after about 1000 iterations (irrespective of the seed).

4.1.4 Performance Comparison of Coded Aperture Patterns

This section provides an analytical performance comparison of the random array employed by the Dual-Modality Imager and a standard MURA. Figure 4.7a displays the 64×64 random array, and Figure 4.7b displays a similarly-sized 2×2 mosaicked MURA whose basic pattern measures 31×31 elements. The MURA was generated using the method provided by Gottesman and Fenimore [113].

The performance of the two arrays was evaluated in terms of their correlation properties. Using the method outlined in the previous section, the following correlation matrices were generated: F_{11}, F_{22}, F_{33}, F_{44}, where the subscripts indicate the correlation at $m = 1,\ 2,\ 3$ and 4, respectively. Note each of these correlation matrices were generated at a single magnification only, as opposed to across multiple magnifications as shown by Equation 4.3. A randomly-selected row was extracted from each correlation matrix. Remember the row represents the periodic correlation of a certain submatrix across the entire array, and the submatrix is determined by the location of a certain image voxel. Figure 4.8 shows the periodic correlations at the four different magnifications for the random array and MURA. The correlations are represented as a two-dimensional map in the x and y dimensions.

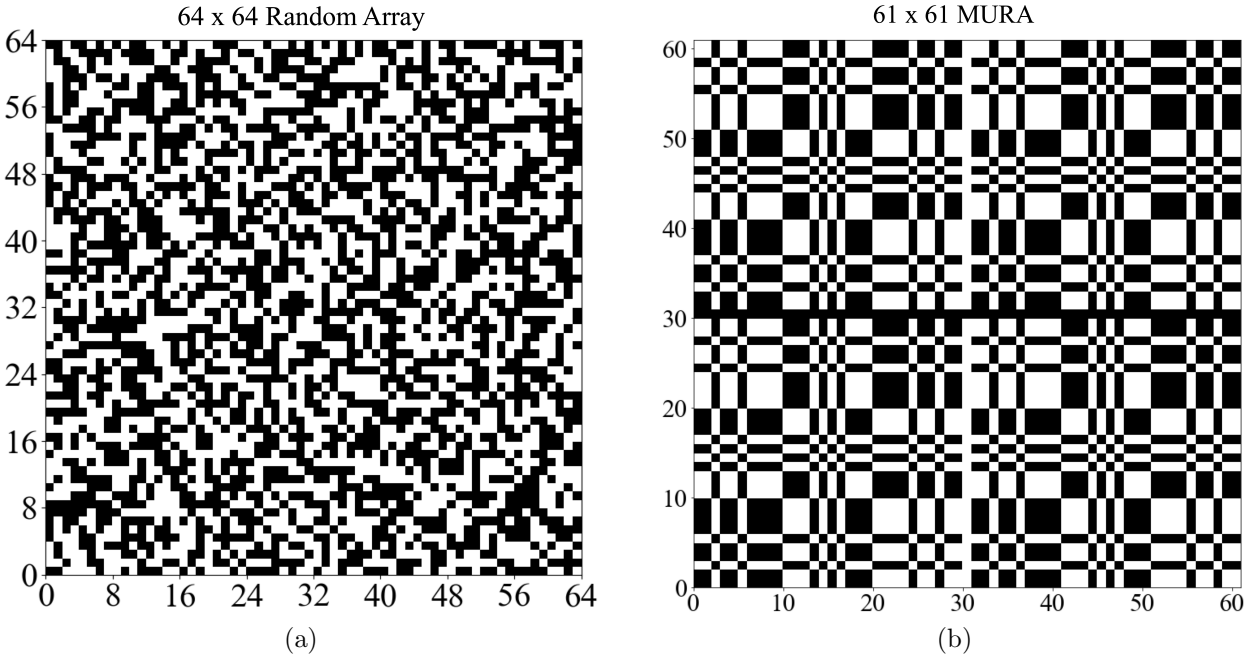

Figure 4.7: (a) 64×64 random array (in the converging configuration) employed by the Dual-Modality Imager. (b) 2×2 mosaicked MURA with a 31×31 basic pattern. Both (a) and (b) have a 50% open fraction. The black and white squares represent opaque and transparent elements, respectively.

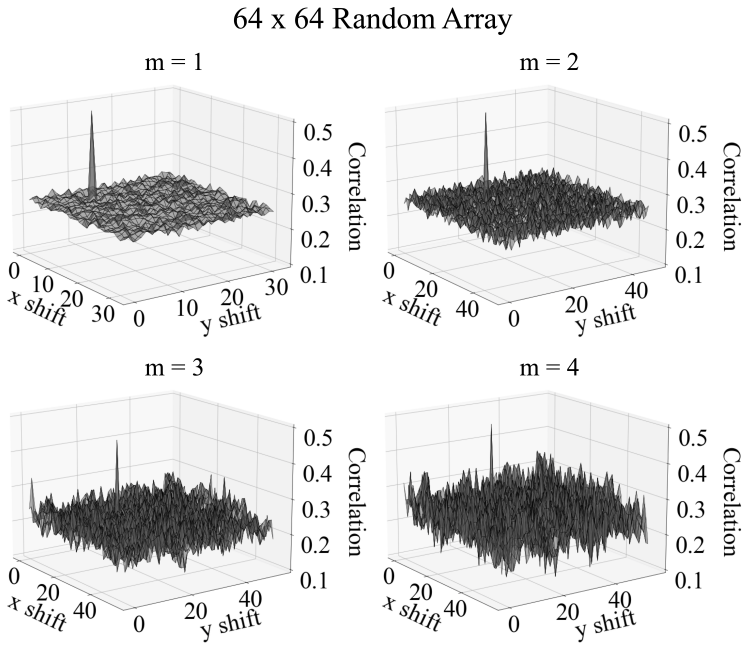

(a)

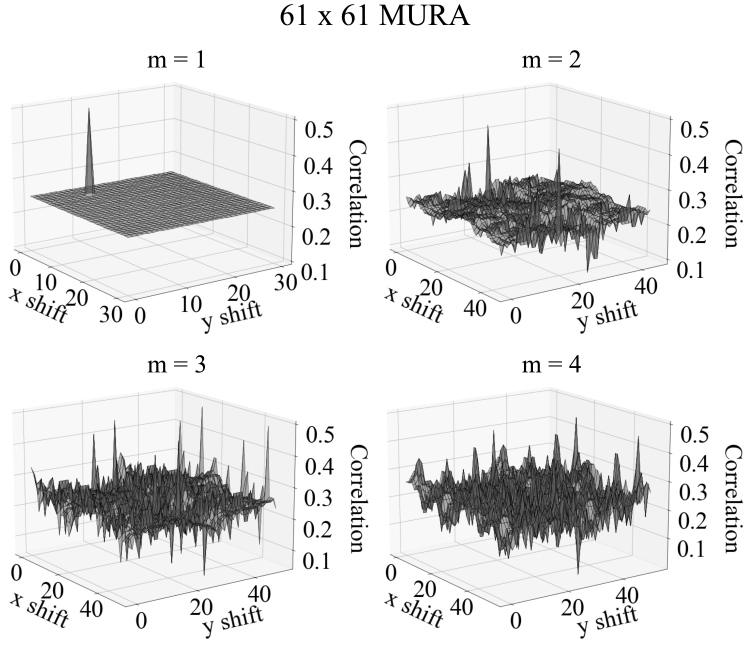

(b)

Figure 4.8: (a) Periodic correlation of a randomly-selected submatrix across the (a) random array and (b) MURA shown in Figure 4.7. The correlation was performed for submatrices of various sizes that correspond to different magnifications: $m = 1,\ 2,\ 3$ and 4.

Table 4.2: The mean μ_P, standard deviation σ_P, and kurtosis Kurt[P] of the sidelobes of the random array and MURA at different magnifications m as illustrated in Figure 4.8.

	Random Array			MURA		
m	μ_P	σ_P	Kurt[P]	μ_P	σ_P	Kurt[P]
1	0.251	0.00752	3.01	0.250	0.000520	1.00
2	0.252	0.0155	2.96	0.236	0.0202	15.9
3	0.250	0.0297	2.94	0.250	0.0329	10.5
4	0.243	0.0381	2.86	0.265	0.0499	4.69

A perfect correlation should yield a single peak with an amplitude of ρ and flat sidelobes at a level of ρ^2 based on the discussion in the previous section. Additional spikes in the sidelobes indicate potential ambiguities in the image reconstruction. The standard deviation and kurtosis of the sidelobes can be used as measures of their flatness. The standard deviation describes the variability of a distribution around the mean, while the kurtosis describes the outliers of the distribution. In other words, a low kurtosis indicates several modest deviations from the mean, and a high kurtosis indicates a few extreme outliers. Mathematically, the kurtosis of the sidelobes Kurt[P] can be defined as:

$$\text{Kurt}[P] = \frac{\sum_{v\ (u\neq v)}^{N} (p_v - \mu_P)^4}{(N-1)\,\sigma_P^4} \tag{4.6}$$

where P is a row in the correlation matrix, excluding the diagonal element (i.e. at $u = v$). A single element in P is p_v and represents the sidelobe level at a certain x and y shift. μ_P and σ_P are the mean and standard deviation of P, respectively.

Table 4.2 provides the standard deviation and kurtosis values of the sidelobes of the random array and MURA displayed in Figure 4.8. To have a better understanding of kurtosis values, a standard Gaussian distribution has a kurtosis of 3. Thus, a kurtosis much greater than 3 indicates spikes lying far outside the standard deviation of the mean. In the context of mask performance, we can confidently say that both a high standard deviation and kurtosis lead to ambiguities in the image reconstruction. However, we do not know definitively which of these two metrics is more detrimental to the reconstruction.

Keeping this in mind, at $m = 1$, the MURA has sidelobes with both a smaller standard deviation and kurtosis. This indicates that the MURA has superior imaging performance in the absence of magnification. In the near field, however, magnification effects always exist. Even the slightest deviation from $m = 1$ creates variance in the MURA sidelobes for reasons discussed in [119]. At $m > 2$, the random array shows superior performance with sidelobes

that have both a smaller standard deviation and kurtosis.

For both the random array and MURA, the standard deviation of the sidelobes increases with greater magnification. This should be expected as these arrays were not designed to operate at such high magnifications. Specifically, the MURA was optimized at $m = 1$, and the random array was optimized across $m = 1$ and $m = 2$. Thus, in this work, the random array is usually employed for $m < 2$ to avoid ambiguities in the image reconstruction.

4.2 Event Reconstruction

Event reconstruction is the process of reconstructing the interaction history of gamma rays in a single or multiple detectors. The objective is to determine the series of all interactions induced by the same incident photon, as well as the energy deposition and position associated with each interaction. This set of interactions is referred to as a gamma-ray event.

With DSSDs, event reconstruction starts by extracting information from the trigger strips. Important parameters include the trigger time and pulse amplitude, both of which are calculated by the FPGAs on the SIS3302 modules. The FPGAs apply a fast and slow trapezoidal filter to the digitized signals [120]. The fast filter generates a trigger, while the slow filter shapes the signal to determine the ADC amplitude. This information, along with the associated raw waveform, is transferred to the desktop computer for additional processing, including an energy calibration and computation of the T_{50} rise time.

Following feature extraction, the trigger strips are grouped into events using the matching technique discussed in Section 3.3.2.1. Here the strips are correlated by a coincidence window of 250 ns, reflecting the maximum charge drift time in the detectors. For each time-correlated group, anode and cathode strips from the same detector are matched by an energy window determined by the energy resolution of the detectors. Any group that contains unmatchable strips is ignored; otherwise, the collection of strip pairs is accepted as an event.

The number of strip pairs in an event corresponds to the number of interactions. Thus, events are classified as single-interaction, double-interaction, triple-interaction, etc. Single-interaction events occur within a single detector only, while those of multiple interactions can take place within one or both detectors.

For each event, the energy deposition and position of each interaction must be determined. The energy deposition of an interaction is simply the energy shared by the strip pair. The sum total of the energy depositions within an event is presumed to be the incident photon energy. The intersection of the strip pair provides the (x, y) interaction position. The depth z of interaction is determined by the ΔT_{50} timing as previously discussed in Section 3.3.2.3.

4.2.1 Gamma-Ray Tracking Algorithm

Gamma-ray tracking is an additional processing step in event reconstruction. The objective is to sort interactions within the same event by occurrence. Here this step is performed offline after all of the data has been collected. In coded aperture imaging, gamma-ray tracking can

be skipped if only single-interaction events are considered. In Compton imaging, this step is unavoidable as the back-projection of a Compton cone depends on a properly-sequenced, multiple-interaction event. For this reason, great effort has been made in developing a reliable tracking algorithm.

As previously discussed in Section 3.6.1, interactions cannot be sequenced by time of occurrence due to the finite time resolution of the detectors. In some cases, relativistic kinematics can prohibit certain sequences; however, frequently the kinematics is ambiguous and statistical arguments must be made. By considering the underlying physics of gamma-ray interactions in matter, the relative probability of each sequence can be determined.

For simplicity, the tracking algorithm employed in this work considers double-interaction events only and assumes that the first interaction must necessarily occur via Compton scattering and the second via photoelectric absorption. That said, the algorithm can easily be extended to account for events of higher multiplicity. Based on the energy depositions E_1 and E_2 at the first and second interactions sites, respectively, the probability P_{tot} of a given sequence is defined as the product of three terms:

$$P_{tot} = P_{kn} \cdot P_{pe} \cdot P_{attn} \tag{4.7}$$

where, as defined below, each term represents the likelihood of a different interaction process within the detector.

The first term P_{kn} considers the differential cross section of the first interaction as given by the Klein-Nishina formula. The differential cross section $[\partial\sigma_{cs}/\partial\Omega]$ measures the probability that a photon of incident energy E_γ scatters at an angle θ and is given by:

$$\frac{\partial^2\sigma_{cs}}{\partial^2\Omega} = \frac{1}{2}r_e^2\left(\frac{E'_\gamma}{E_\gamma}\right)^2\left[\left(\frac{E_\gamma}{E'_\gamma}\right) + \left(\frac{E'_\gamma}{E_\gamma}\right) - (1-\underline{\mu}^2)\right] \tag{4.8}$$

as derived by Berestetskii et al. [121], where the constant r_e is the classical electron radius and $\underline{\mu} = cos\theta$. Here the incident photon energy E_γ is assumed to be the sum of the two deposited energies: $E_\gamma = E_1 + E_2$ and the scattered photon energy E'_γ to be equivalent to the energy deposited at the second interaction site: $E'_\gamma = E_2$. Furthermore, the scattering angle θ is related to E'_γ by the kinematic relation in Equation 3.2.

Note the differential cross section provided above is in units of cm^2/steradian. To make P_{kn} a dimensionless quantity, Equation 4.8 is divided by the Compton scattering cross section σ_{cs}:

$$P_{kn} = \frac{1}{\sigma_{cs}|_{E_\gamma}}\left[\frac{\partial^2\sigma_{cs}}{\partial^2\Omega}\right] \quad . \tag{4.9}$$

Here σ_{cs} (in units of cm^2) is evaluated at E_γ and can be defined as:

$$\sigma_{cs}|_{E_\gamma} = 2\pi \int_{-1}^{1} d\underline{\mu} \left[\frac{\partial^2 \sigma_{cs}}{\partial^2 \Omega}\right] \tag{4.10}$$

$$= 2\pi \int_{\frac{E_\gamma}{1+2E_\gamma/m_e c^2}}^{E_\gamma} dE'_\gamma \left|\frac{d\underline{\mu}}{dE'_\gamma}\right| \left[\frac{\partial^2 \sigma_{cs}}{\partial^2 \Omega}\right] = 2\pi \int_{\frac{E_\gamma}{1+2E_\gamma/m_e c^2}}^{E_\gamma} dE'_\gamma \left[\frac{m_e c^2}{\left(E'_\gamma\right)^2}\right] \left[\frac{\partial^2 \sigma_{cs}}{\partial^2 \Omega}\right] \tag{4.11}$$

where $m_e c^2$, as with previous usage, is the rest mass of an electron. The above integral can be performed by either integrating over all angles θ or changing the variable of integration to the scattered photon energy E'_γ. The latter integration turns out to be easier and yields:

$$\sigma_{cs}|_{E_\gamma} = \frac{2\pi r_e^2}{\alpha} \left[\frac{\alpha\left(\alpha+2\right)}{2\left(1+\alpha\right)^2} + \frac{8}{\alpha} + \frac{\left(\alpha^2-4\alpha-8\right)}{\alpha^2} \ln\left(1+\alpha\right)\right] \tag{4.12}$$

where

$$\alpha = \frac{2E_\gamma}{m_e c^2} \quad . \tag{4.13}$$

The second term P_{pe} considers the photoelectric absorption cross section σ_{pe} of the second interaction:

$$P_{pe} = \frac{\sigma_{pe}|_{E'_\gamma}}{\sigma_{tot}|_{E'_\gamma}} = \frac{\mu_{pe}|_{E'_\gamma}}{\mu_{tot}|_{E'_\gamma}} \tag{4.14}$$

where σ_{pe} (in units of cm^2) is normalized by the total photon interaction cross section σ_{tot} (in units of cm^2). The cross sections σ_{pe} and σ_{tot} can be substituted for the photoelectric absorption μ_{pe} and total μ_{tot} linear attenuation coefficients (in units of cm^{-1}), respectively. Both μ_{pe} and μ_{tot} are evaluated at the scattered photon energy E'_γ (or E_2) in germanium and are extracted from the NIST database [122].

The third term P_{attn} considers the exponential attenuation probability between the first and second interaction sites:

$$P_{attn} = e^{-\left(\mu_{tot}|_{E'_\gamma}\right)(t_{12})} \tag{4.15}$$

where t_{12} is the distance traveled by the scattered photon *in the detector medium*. Note t_{12} is not necessarily the same as the lever arm r_{12}. Because this work employs two detectors with a 10-mm separation distance, the scattered photon may travel partially through air before reaching the second interaction site. The distance traveled through air is neglected in the calculation of t_{12}.

Finally, the likelihood P_{tot} of an interaction sequence can be computed as the product of P_{kn}, P_{pe}, and P_{attn} as shown by Equation 4.7. For a double-interaction event, P_{tot} is calculated for each of the two possible sequences. Only the most probable sequence is used in the image reconstruction.

4.3 Coded Aperture Image Reconstruction

4.3.1 Event Selection

Coded aperture imaging requires an incident photon transmitted through the mask to interact at least once within the detector. For applications in which the source is well-defined, stricter requirements can be imposed to reduce background noise. In this work, the incident photon energy is known, which leads to the following event selection criteria:

1. only single-interaction events are considered,
2. the energy deposition must fall within a specified region-of-interest (ROI) near the known incident energy, and
3. the depth of interaction must be less than 6 mm from the detector surface facing the image space.

The purpose of the first criterion is twofold. First, single-interaction events do not require gamma-ray tracking; and thus the possibility of a sequencing error is avoided. Second, the coded aperture modality is used for low-energy photons, the majority of which interact once via photoelectric absorption. While some low-energy photons can undergo multiple interactions, such events can be ignored without a significant loss to imaging sensitivity. The second criterion is enforced to mitigate event misclassification, and ultimately image noise. By requiring full energy deposition within the detector, events prompted by wanted and unwanted photons can be discriminated[2]. Finally, the third criterion reduces image blurring by accounting for the finite detector volume in which photons can interact at multiple depths. Selecting events within a limited range in depth prevents photons with oblique angles of incidence from introducing spatial errors beyond the lateral position resolution of the detector; the next section discusses this in more detail. It should be noted here that all three criteria lead to event loss. The impact on imaging sensitivity is evaluated in Section 4.5.1.2.

[2]Event misclassification is still possible. For example, if escape from the detector is imminent, an unwanted photon with an incident energy above the ROI can undergo one scattering interaction with an energy deposition that falls within the ROI. Background subtraction should be performed to suppress these so-called down-scattered events, but is not applied in this work.

4.3.2 Event Binning

In coded aperture imaging, events are binned by interaction position such that the detector data materializes into a distinct pattern. Up until now, there has been an implicit assumption that photons are registered on a two-dimensional detector plane at a certain mask-to-detector distance b. Under this assumption, the binning process is relatively straightforward. Events are divided into (x, y) bins with a size determined by the lateral position resolution of the detector; this work uses 2 mm^2 bins.

In practice, the detector has a finite volume in which photons interact at multiple distances. Ignoring the depth of interaction in the binning process can lead to image blurring. This is demonstrated later on in Section 4.5.2. The degree of blurring is directly correlated to the photon angle of incidence with an increased effect as sources move further off-axis. Furthermore, the type of blurring depends on the source-to-detector distance. In the far-field where photons reach the detector in parallel, off-axis sources appear radially blurred. In the near-field where photons hit the detector at varying angles of incidence, on-axis sources look symmetrically blurred, while those off-axis appear asymmetrically blurred.

To mitigate this blurring effect, events should be binned by depth of interaction as well. The bin thickness should not be made infinitely small as this leads to a computationally expensive image reconstruction and does not necessarily enhance the image quality. This work applies the following strategy to determine the optimal bin thickness.

First, the maximum angle θ_{max} at which a photon can be incident on the detector is calculated. This angle is determined by the boundaries of the field-of-view as illustrated in Figure 4.9a. Assuming a detector and mask with fixed dimensions, θ_{max} varies inversely with the mask-to-detector distance b:

$$\theta_{max} = \tan\left(\frac{l_m - l_d}{2b}\right) \tag{4.16}$$

where, as with previous usage, l_m and l_d are the dimensions of the mask and detector, respectively.

As the incident photon travels at θ_{max} through the bulk of the detector, the lateral shift in its position becomes more prominent. The minimum depth at which this shift exceeds the lateral resolution w_d of the detector determines the optimal bin thickness t_{bin}:

$$t_{bin} = \frac{w_d}{\tan\left(\theta_{max}\right)} \tag{4.17}$$

as illustrated in Figure 4.9b.

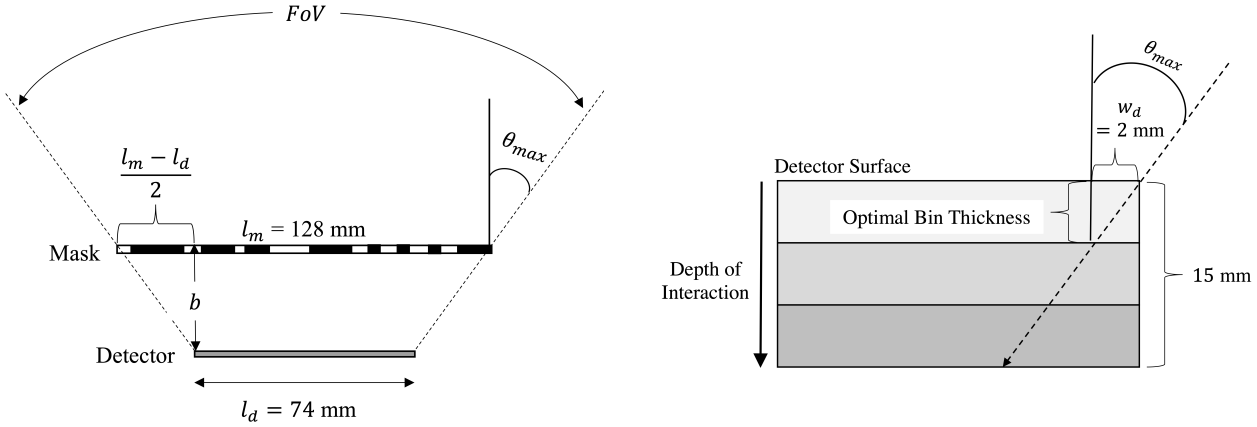

Figure 4.9: (a) Determination of the maximum angle of photon incidence θ_{max} and (b) determination of the optimal bin thickness given θ_{max}.

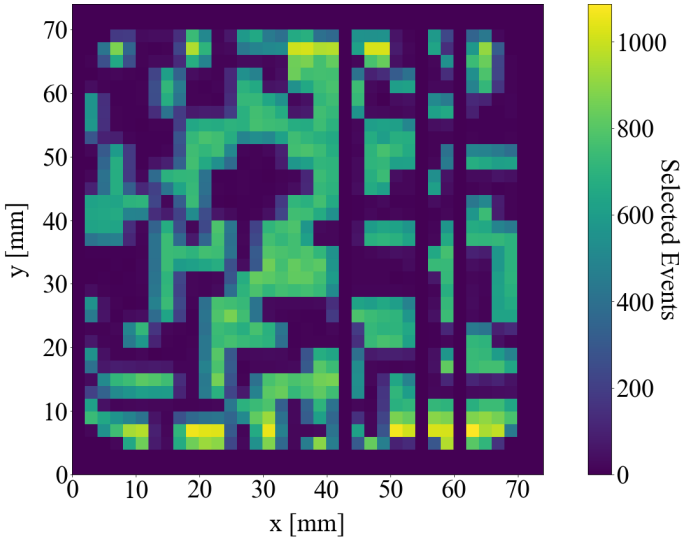

Figure 4.10: Detector measurement of a ^{57}Co disc source of 2-mm diameter in the coded aperture mode. The source was centrally positioned at a distance of 90 mm from the mask with the mask positioned at a distance of 90 mm from the detector (magnification factor $m = 2$). Only single-interaction events with an energy around 122 keV and a depth-of-interaction of less than 5 mm from the detector surface were selected. These events were grouped into $2 \times 2 \times 5-\text{mm}^3$ bins. Note bins around the edges of the detector and bin columns near the center of the detector do not contain any events. These regions represent dead detector strips.

In the case of the Dual-Modality Imager, the optimal bin thickness ranges from 3 mm to 6 mm for mask-to-detector distances: $50 \leq b \leq 90$ mm, respectively. Because the detector has a 15-mm-thick volume, multiple layers of detector data in depth should be considered if event loss is to be avoided. In such cases, the system response A should be expanded to account for each detector layer. However, to avoid a computationally-expensive image reconstruction, this work computes A at the center of the surface layer only and only selects events within this layer. This can be performed without a large loss to sensitivity as the majority of low-energy photons interact near the detector surface. Figure 4.10 provides an illustration of the binned detector data at the surface layer.

4.3.3 Ray Tracing to Generate System Response

The system response A is the basic mathematical model for a linear image process. In the context of gamma-ray imaging, A maps the gamma-ray distribution Λ in the image space to the detector space:

$$A \cdot \Lambda = D \rightarrow$$

$$\overset{\text{Image Voxels } j \longrightarrow}{\underset{\text{Detector Pixels } i \downarrow}{}} \begin{pmatrix} a_{ij} & \cdots \\ \vdots & \ddots \end{pmatrix} \cdot \begin{pmatrix} \lambda_j \\ \vdots \end{pmatrix} = \begin{pmatrix} d_i \\ \vdots \end{pmatrix}$$

where Λ is a $J \times 1$ matrix in which a single image voxel is j and the mean number of photon emissions in that voxel is λ_j, and D is an $I \times 1$ matrix in which a single detector pixel is i and the total number of events in that pixel is d_i. The system response A is a 2-D matrix in which the columns correspond to image voxels in a 3-D space, and the rows correspond to detector pixels in a 2-D space[3]. Each element a_{ij} in A represents the probability that a photon emitted at image voxel j is registered by detector pixel i.

For a coded aperture device, the probability a_{ij} can be defined as:

$$a_{ij} = \underbrace{\epsilon_d}_{Efficiency\ Term} \underbrace{\left[\frac{w_d^2 cos\theta}{4\pi \left| \overrightarrow{U^i} - \overrightarrow{V^j} \right|^2 + 2w_d^2 cos\theta} \right]}_{Solid\ Angle\ Term} \underbrace{e^{-\mu L}}_{Attenuation\ Term} . \tag{4.18}$$

[3]If multiple layers of detector data in depth were to be considered, the columns would correspond to detector voxels in a 3-D space.

The above probability can be broken down into three main terms. The first term ϵ_d represents the efficiency of the detector pixel as determined experimentally. The second term accounts for the detector solid angle. The solid angle calculation depends on the width w_d of the detector pixel, the angle θ between the incident photon direction and the normal to the detector, and the distance $\left|\overrightarrow{U^i} - \overrightarrow{V^j}\right|$ between the center V^j of image voxel j and the center U^i of detector pixel i. Note the quantity $[2w_d^2 cos\theta]$ in the denominator accounts for sources that are exceptionally close to the detector, where the $\left[1/\left|\overrightarrow{U^i} - \overrightarrow{V^j}\right|^2\right]$ approximation does not hold. Computationally speaking, the solid angle calculation is straightforward and quick. Finally, the third term accounts for photon attenuation through the mask and depends on the linear attenuation coefficient μ_{tot} of the mask material and the length L traveled by the photon in the mask material. The attenuation coefficent μ_{tot} varies with photon energy and is extracted from the NIST database [122]. The calculation of the attenuation length L is complex and computationally-expensive, because a ray-tracing analysis is required.

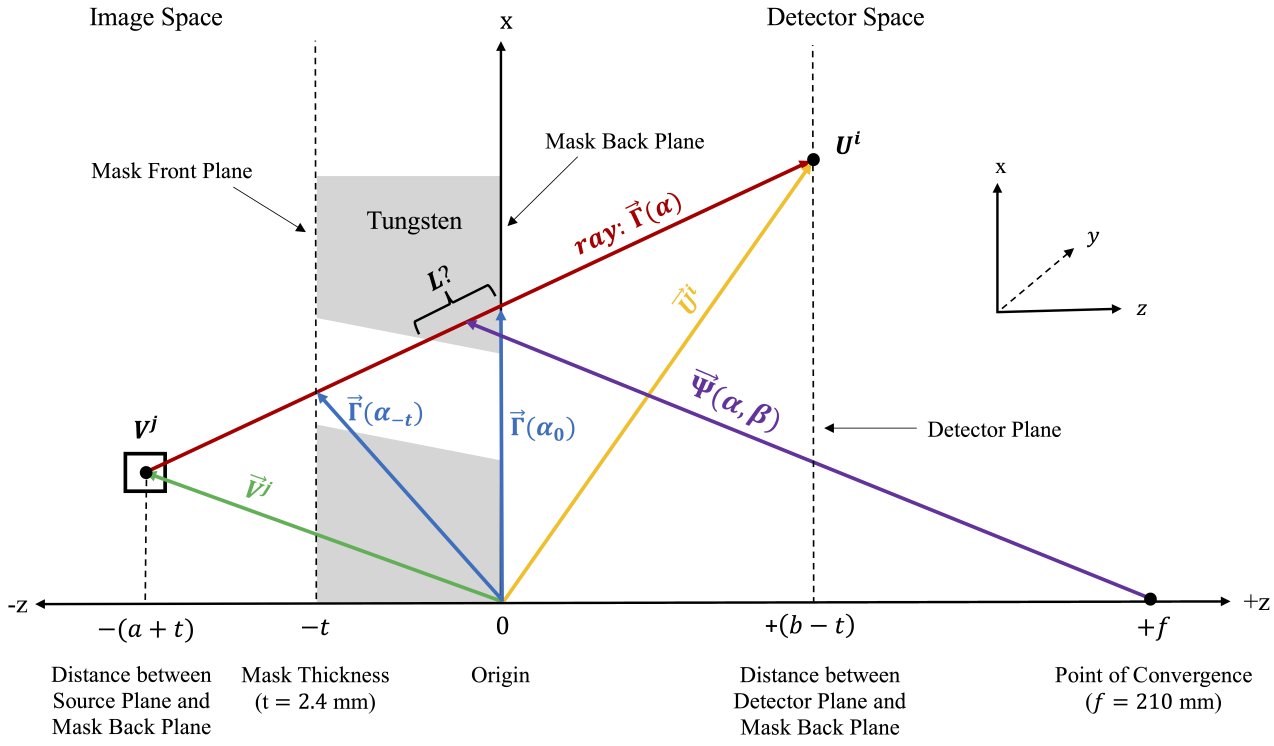

Figure 4.11: Ray tracing through a tungsten mask with elements that converge at a point $F = (0, 0, f)$ in the detector space (diverging configuration). The point V^j in the image space is located at a z-distance of a from the mask front plane or $(a + t)$ from the mask back plane. The point U^i in the detector space is located at a z-distance of b from the mask front plane or $(b - t)$ from the mask back plane.

The objective of ray tracing is to determine the attenuation length L traveled through the mask material by a photon emitted in a given direction. Figure 4.11 illustrates the geometry of the ray-tracing analysis applied to the mask in the diverging configuration. Here the origin in the x- and y-directions is defined at the center of the mask and the origin in z- direction at the back plane of the mask (nearest the detector). For each voxel j in the image space, four rays are drawn from its center to four equidistant points on a given detector pixel i. Each of the four rays has an associated attenuation length L. This work uses the average of the four attenuation lengths in the calculation of a_{ij} to improve the accuracy of the system response.

For a given ray connecting a point V^j on image voxel j and a point U^i on detector pixel i, the unit vector of this ray is defined by:

$$\hat{r} = \frac{\overrightarrow{U^i} - \overrightarrow{V^j}}{\left|\overrightarrow{U^i} - \overrightarrow{V^j}\right|} \tag{4.19}$$

where $\overrightarrow{V^j}$ and $\overrightarrow{U^i}$ are vectors from the origin to the points V_j and U_i, respectively, and take the form:

$$\overrightarrow{V^j} = V_x^j\hat{i} + V_y^j\hat{j} - (a+t)\hat{k} \tag{4.20}$$

$$\overrightarrow{U^i} = U_x^i\hat{i} + U_y^i\hat{j} + (b-t)\hat{k} \tag{4.21}$$

$$\overrightarrow{U^i} - \overrightarrow{V^j} = \left(U_x^i - V_x^j\right)\hat{i} + \left(U_y^i - U_y^j\right)\hat{j} + (a+b)\,\hat{k} \tag{4.22}$$

where $\hat{i}$, $\hat{j}$, and $\hat{k}$ are unit vectors in the $x-$, $y-$, and z-directions, respectively. The ray itself is defined by:

$$\overrightarrow{\Gamma}(\alpha) = \overrightarrow{V^j} + (\alpha)\,(\hat{r}) \tag{4.23}$$

where the ray $\overrightarrow{\Gamma}(\alpha)$ is a function of α. Here α is an affine parameter ranging from $(-\infty, \infty)$. The intersection of the ray through the mask is a line segment between α_{-t} and α_0. The vector $\overrightarrow{\Gamma}(\alpha_{-t})$ describes where the ray intersections at $z = -t$, and the vector $\overrightarrow{\Gamma}(\alpha_0)$ describes where the ray intersections at $z = 0$. Here t denotes the thickness of the mask; in this work, $t = 2.4$ mm.

The parameter α_{-T} is determined by the following dot product:

$$\overrightarrow{\Gamma}(\alpha_{-t}) \cdot \hat{k} = -T \rightarrow \tag{4.24}$$

$$\left[\overrightarrow{V^j} + (\alpha_{-t})\,(\hat{r})\right] \cdot \hat{k} = -T \rightarrow \tag{4.25}$$

$$-(a+t)+\frac{\alpha_{-t}}{\left|\overrightarrow{U^i}-\overrightarrow{V^j}\right|}(a+b)=-T\rightarrow \tag{4.26}$$

$$\alpha_{-t}=\frac{a\left|\overrightarrow{U^i}-\overrightarrow{V^j}\right|}{a+b} \quad . \tag{4.27}$$

Similarly, the parameter α_0 is determined by:

$$\overrightarrow{\Gamma}(\alpha_0)\cdot\hat{k}=0\rightarrow \tag{4.28}$$

$$\left[\overrightarrow{V^j}+(\alpha_0)(\hat{r})\right]\cdot\hat{k}=0\rightarrow \tag{4.29}$$

$$-(a+t)+\frac{\alpha_0}{\left|\overrightarrow{U^i}-\overrightarrow{V^j}\right|}(a+b)=0\rightarrow \tag{4.30}$$

$$\alpha_0=\frac{(a+t)\left|\overrightarrow{U^i}-\overrightarrow{V^j}\right|}{a+b} \quad . \tag{4.31}$$

For a given point on the ray $\overrightarrow{\Gamma}(\alpha)$ where $\alpha_{-t}\leq\alpha\leq\alpha_0$, we want to determine whether the point lies in tungsten or a hole. To do this, we must first define the walls of the mask elements. The wall structure is determined via the projection of a pre-determined two-dimensional mask function $M(x,y)$ from the point of convergence F to a particular mask plane, where $M(x,y)$ is defined as:

$$M(x,y)=\begin{cases}0 & \text{if a point } (x,y) \text{ is in a hole}\\ 1 & \text{if a point } (x,y) \text{ is in tungsten}\end{cases} \quad . \tag{4.32}$$

For convenience, we project the mask function $M(x,y)$ on the back plane of the mask (facing the detector). The (x,y) point at which we evaluate $M(x,y)$ is located on the line $\overrightarrow{\Psi}(\alpha,\beta)$, which connects the focal point F with a point on the ray $\overrightarrow{\Gamma}(\alpha)$:

$$\overrightarrow{\Psi}(\alpha,\beta)=\overrightarrow{F}+\beta\left(\overrightarrow{\Gamma}(\alpha)-\overrightarrow{F}\right) \tag{4.33}$$

where $\overrightarrow{F}$ is a vector from the origin to the point of convergence F:

$$\overrightarrow{F}=0\hat{i}+0\hat{j}+f\hat{k} \quad . \tag{4.34}$$

In this example, the point F lies in the detector space at a distance $z=f$, where $f=210$ mm in this work. This indicates that the mask is in the diverging configuration. In the converging configuration, the point F is moved to the image space at a distance $z=-(f+t)$.

The line $\overrightarrow{\Psi}(\alpha,\beta)$ is a function of both α and β, where β is an affine parameter that ranges from $0 \leq \beta \leq 1$. If $\beta = 0$, then the point Ψ is located at the point of convergence F. Furthermore, if $\beta = 1$, then Ψ is located on the ray $\overrightarrow{\Gamma}(\alpha)$. For simplicity, $\overrightarrow{\Psi}(\alpha,\beta)$ is always evaluated at β_0:

$$\overrightarrow{\Psi}(\alpha,\beta_0) = \overrightarrow{F} + \beta_0\left(\overrightarrow{\Gamma}(\alpha) - \overrightarrow{F}\right) \tag{4.35}$$

where β_0 defines the point at which the line $\overrightarrow{\Psi}(\alpha,\beta)$ intersects the mask back plane at $z = 0$. If this intersection takes place in tungsten, then the point on the ray $\overrightarrow{\Gamma}(\alpha)$ lies in tungsten. Similarly, if the intersection occurs in a hole, then the point on the ray lies in a hole. We compute the parameter β_0 by the following dot product:

$$\left[\overrightarrow{\Psi}(\alpha,\beta_0)\right]\cdot\hat{k} = 0 \rightarrow \tag{4.36}$$

$$\left[\overrightarrow{F} + \beta_0\left(\overrightarrow{\Gamma}(\alpha) - \overrightarrow{F}\right)\right]\cdot\hat{k} = 0 \quad . \tag{4.37}$$

Note the parameter β_0 is a function of α when we assert the above condition.

Once we compute $\overrightarrow{\Psi}(\alpha,\beta_0)$, we evaluate the mask function $M(x,y)$ at this point: $M\left(\overrightarrow{\Psi}(\alpha,\beta_0)\right)$ to determine whether the point on the ray $\overrightarrow{\Gamma}(\alpha)$ lies in tungsten or in a hole. We solve for $\overrightarrow{\Psi}(\alpha,\beta_0)$ ranging from $\alpha_{-t} < \alpha < \alpha_0$ with a step-size $\Delta\alpha$ of 0.2 mm and compute $M(x,y)$ at each point Ψ. The sum of all $M\left(\overrightarrow{\Psi}(\alpha,\beta_0)\right)$ from $\alpha_{-t} \leq \alpha \leq \alpha_0$ gives the length L traveled in tungsten by the ray $\overrightarrow{\Gamma}(\alpha)$:

$$L = \sum_{\alpha-t}^{\alpha_0} M\left(\overrightarrow{\Psi}(\alpha,\beta_0)\right)\Delta\alpha \quad . \tag{4.38}$$

Note $M(x,y)$ is dimensionless, whereas $\Delta\alpha$ has dimensions of length.

The calculation of the attenuation length L is the most computationally-expensive step in building the system response. Because this work requires a multitude of system responses, each for a specific imaging scenario, we need a fast algorithm. To reduce the computational time, this work removes the calculation of L from the algorithm. Instead, the attenuation lengths are extracted from a look-up table[4].

The look-up table contains values of L for all possible locations and directions that the ray $\overrightarrow{\Gamma}(\alpha)$ could be incident on the mask back plane. The table takes the form of a two-dimensional matrix in which each row corresponds to the incident (x,y) location of $\overrightarrow{\Gamma}(\alpha)$ and each column corresponds to the incident (θ,ϕ) direction of $\overrightarrow{\Gamma}(\alpha)$. Each element in the matrix is an attenuation length L and is computed using the method outlined above. In

[4]This work uses two separate look-up tables, one for the diverging mask and one for the converging mask.

building the system response, only the incident (x, y) location and (θ, ϕ) direction of the ray $\overrightarrow{\Gamma}(\alpha)$ on the mask back plane is computed. The attenuation length L at these two parameters is then extracted from the look-up table.

4.3.4 ML-EM with Penalty Functions for Binned Data

The cross-correlation method presented in Section 3.5.1 is the most conventional method of coded aperture image reconstruction. This analytical approach has the advantage of being computationally efficient and yields a perfect image reconstruction if the mask array has ideal correlation properties and background noise is negligible. In reality, several factors cause a deviation from ideal conditions. These include collimation effects and varying degrees of magnification associated with the finite thickness of the source. Furthermore, cross-correlation is only applicable to 2-D source distributions, whereas the imaging problem in this work involves 3-D distributions. In addition to putting strict limitations on the imaging problem, this method ignores the Poisson nature of the detection process, which can result in noise amplification.

An alternative method employed by this work is iterative image reconstruction based on Maximum-Likelihood Expectation-Maximization (ML-EM) [123, 124]. ML-EM is a more forgiving approach because the algorithm is built on a probabilistic model of photon emissions. The unknown source distribution Λ, which can be represented in 3-D, is determined from the detector data D and system response A as follows:

$$\hat{\lambda}_j^{k+1} = \frac{\hat{\lambda}_j^k}{s_{j,\ ca}} \sum_i^I \frac{(d_i)\,(a_{ij})}{\sum_{j'}^J (a_{ij'}) \left(\hat{\lambda}_{j'}^k\right)} \tag{4.39}$$

where $\hat{\lambda}_j^k$ is the estimated source strength in voxel j as calculated after k iterations and d_i is the sum of events in detector pixel i. The system response a_{ij} is the probability that a photon emitted from image voxel j is registered by detector pixel i and is determined by the ray tracing method outlined in Section 4.3.3. The sensitivity $s_{j,\ ca}$ of the coded aperture is defined by $s_{j,\ ca} = \sum_i^I a_{ij}$ so that $s_{j,\ ca}$ is the probability that an emission from voxel j is detected in any of the detector pixels.

Equation 4.39 represents the textbook treatment of ML-EM [102] as derived in Section 3.4.3.3. This version of ML-EM is based on the maximization of the log-likelihood L^* as defined by Equation 3.36 and oftentimes provides an ill-posed problem. To have a well-posed problem, we introduce penalty functions $\tau(\lambda_j)$ to adjust the reconstruction based on *prior* knowledge of the source distribution. Rather than maximize the log-likelihood L^*, we want to maximize $(L^* + \tau)$, where positive τ is a desirable property of the source and negative τ

is a penalty. Thus, the penalized ML-EM must satisfy:

$$\frac{\partial}{\partial \lambda_j}\left(L^* + \tau\right) = 0 \quad . \tag{4.40}$$

Recalling the derivation of ML-EM in Section 3.4.3.3, we begin with the L^* term:

$$\frac{\partial L^*}{\partial \lambda_j} = \sum_i^I \left[\frac{\left(d_i\right)\left(a_{ij}\right)}{\sum_{j'}^J a_{ij'}\lambda_{j'}} - a_{ij} \right] \quad . \tag{4.41}$$

We define the sensitivity $s_{j,\ ca}$ of an image voxel j by:

$$s_{j,\ ca} = \sum_j^J a_{ij} \geq 0 \tag{4.42}$$

so that:

$$\frac{\partial L^*}{\partial \lambda_j} = \sum_i^I \left[\frac{\left(d_i\right)\left(a_{ij}\right)}{\sum_{j'}^J a_{ij'}\lambda_{j'}} \right] - s_{j,\ ca} \quad . \tag{4.43}$$

Let's now consider the penalty function term τ. We define:

$$\tau_j = \frac{\partial \tau}{\partial \lambda_j} \tag{4.44}$$

and decompose τ_j into two terms:

$$\tau_j^+ = \frac{1}{2}\left[|\tau_j| + \tau_j\right] \geq 0 \tag{4.45}$$

$$\tau_j^- = \frac{1}{2}\left[|\tau_j| - \tau_j\right] \geq 0 \tag{4.46}$$

so that:

$$\tau_j = \tau_j^+ - \tau_j^- \quad . \tag{4.47}$$

Now we combine L^* and τ:

$$\frac{\partial}{\partial \lambda_j}\left(L^* + \tau\right) = \sum_i^I \left[\frac{\left(d_i\right)\left(a_{ij}\right)}{\sum_{j'}^J a_{ij'}\lambda_{j'}}\right] + \tau_j^+ - s_{j,\ ca} - \tau_j^- \quad . \tag{4.48}$$

Similarly to Equation 3.39, the iterative algorithm takes the form:

$$\lambda_j^{k+1} = \lambda_j^k + \Delta_j^k \frac{\partial}{\partial \lambda_j}\left(L^* + \tau\right) \quad . \tag{4.49}$$

To maintain positivity, we choose Δ_j^k to be:

$$\Delta_j^k = \frac{\lambda_j^k}{s_{j,\ ca} + \tau_j^{-(k)}} \quad . \tag{4.50}$$

Finally, the combination of Equations 4.49 and 4.50 yields the penalized-formulation of the ML-EM algorithm:

$$\hat{\lambda}_j^{k+1} = \frac{\hat{\lambda}_j^k}{s_{j,\ ca} + \tau_j^{-(k)}} \left[\sum_i^I \frac{\left(d_i\right)\left(a_{ij}\right)}{\sum_{j'}^J \left(a_{ij'}\right)\left(\hat{\lambda}_{j'}^k\right)} + \tau_j^{+(k)}\right] \quad . \tag{4.51}$$

Note the penalty function τ has yet to be defined; thus far, we have only stated τ to be a function of λ_j. The following discussion defines two penalty functions that have incorporated into the ML-EM algorithm employed by this work: (1) Tikhonov regularization (TIK) and (2) total variation (TV).

A common problem in ML-EM is noise amplification in image voxels with small sensitivities. If there is no penalty, ML-EM gives:

$$\hat{\lambda}_j^{k+1} = \frac{\hat{\lambda}_j^k}{s_{j,\ ca}} \sum_i^I \frac{\left(d_i\right)\left(a_{ij}\right)}{\sum_{j'}^J \left(a_{ij'}\right)\left(\hat{\lambda}_{j'}^k\right)} \tag{4.52}$$

which can blow-up the intensity $\hat{\lambda}_j^{k+1}$ for small $s_{j,\ ca}$. To prevent this, the following penalty

function τ_{TIK} can be applied:

$$\tau_{TIK} = -\epsilon^2 \sum_{j'}^{J} \left(\frac{s^2_{max,ca}}{s_{j',ca}} \right) \left(\hat{\lambda}_{j'} \right) \tag{4.53}$$

so that:

$$\tau^{+}_{j,TIK} = 0 \tag{4.54}$$

$$\tau^{-}_{j,TIK} = \frac{(\epsilon^2)\left(s^2_{max,ca}\right)}{s_{j,\ ca}} \quad . \tag{4.55}$$

By incorporating τ_{TIK} into Equation 4.51, the ML-EM algorithm takes the form:

$$\hat{\lambda}^{k+1}_{j} = \frac{\left(\hat{\lambda}^{k}_{j}\right)(s_{j,\ ca})}{s^2_{j,\ ca} + (\epsilon^2)\left(s^2_{max,ca}\right)} \left[\sum_{i}^{I} \frac{(d_i)\,(a_{ij})}{\sum_{j'}^{J} (a_{ij'}) \left(\hat{\lambda}^{k}_{j'}\right)} \right] \tag{4.56}$$

where ϵ adjust the impact of the regularization. This first penalty function suppresses undue noise amplification in voxels with small sensitivities and leads to the well-known Tikhonov regularization. In the notation presented here, the Tikhonov regularization is proportional to $\epsilon : 0 < \epsilon \ll 1$ and suppresses noise amplification in voxels with sensitivities $s_{j,\ ca} < (\epsilon)\,(s_{max,ca})$. Values in the range $0.01 \leq \epsilon \leq 0.1$ were tested and employed throughout this work.

The second penalty function τ_{TV} is the well-known total variation penalty, which is designed to suppress voxel-scale variations between neighboring voxels and should only be applied in imaging scenarios where the activity distribution has known uniformity. This penalty function can be defined as summation of the differences $\left|\hat{\lambda}_m - \hat{\lambda}_n\right|$ for all pairs of neighboring image voxels:

$$\tau_{TV} = -\frac{\eta}{2} \sum_{m,n} \frac{(N_{mn})\,(s_{ca,max})}{C_m} \left|\hat{\lambda}_m - \hat{\lambda}_n\right| \tag{4.57}$$

where:

$$N_{m,n} \equiv \begin{cases} 1 & \text{if } m \text{ and } n \text{ are neighboring voxels} \\ 0 & \text{if } m \text{ and } n \text{ are not neighboring voxels} \end{cases} \tag{4.58}$$

$$C_m \equiv \sum_{n} N_{mn} = \text{number of neighbors of voxel } m \tag{4.59}$$

where the C_m term normalizes the effects of many neighbors. For this analysis, each image voxel m was assumed to be surrounded by $C_m = 26$ neighboring voxels. The parameter $\eta : 0 < \eta \ll 1$ adjusts the impact of total variation on the reconstruction and nudges the solution towards uniformity. Values in the range $0.01 \leq \eta \leq 0.03$ were tested and employed throughout this work. Note the factor $1/2$ in the above summation prevents double counting.

Now we want to take the derivative of τ_{TV}:

$$\tau_{j,TV} \equiv \frac{\partial \tau}{\partial \lambda_j} = -\frac{\eta}{2} \sum_{m,n} \frac{(N_{mn})\,(s_{ca,max})}{C_m} \frac{\partial}{\partial \lambda_j} \left| \hat{\lambda}_m - \hat{\lambda}_n \right| \tag{4.60}$$

and we observe that:

$$\frac{\partial \lambda_m}{\partial \lambda_n} = \delta_{mn} \tag{4.61}$$

$$\left| \hat{\lambda}_m - \hat{\lambda}_n \right| = \sqrt{\left(\hat{\lambda}_m - \hat{\lambda}_n \right)^2} \tag{4.62}$$

so that:

$$\frac{\partial}{\partial \lambda_j} \left| \hat{\lambda}_m - \hat{\lambda}_n \right| = \frac{\left(\hat{\lambda}_m - \hat{\lambda}_n \right)}{\sqrt{\left(\hat{\lambda}_m - \hat{\lambda}_n \right)^2}} (\delta_{mj} - \delta_{nj}) \tag{4.63}$$

$$= \text{sign}\left(\hat{\lambda}_m - \hat{\lambda}_n \right) (\delta_{jm} - \delta_{jn}) \quad . \tag{4.64}$$

Note the above definition is symmetric in m and n. The penalty function $\tau_{j,TV}$ now takes the form:

$$\tau_{j,TV} \equiv \frac{\partial \tau}{\partial \lambda_j} = -\frac{\eta}{2} \sum_{m,n} \frac{(N_{mn})\,(s_{ca,max})}{C_m} \text{sign}\left(\hat{\lambda}_m - \hat{\lambda}_n \right) (\delta_{jm} - \delta_{jn}) \quad . \tag{4.65}$$

In the above summation, either image voxel m or n must equal image voxel j due to the delta functions. The summation evaluated over n for $m = j$ is equivalent to the summation over m for $n = j$. Thus, the two summations over m and n can be combined into a single summation:

$$\tau_{j,TV} = -\frac{(\eta^2)\,(s_{ca,max})}{C_j} \sum_n (N_{jn}) \,\text{sign}\left(\hat{\lambda}_j - \hat{\lambda}_n \right) \tag{4.66}$$

$$= \frac{(\eta^2)\,(s_{ca,max})}{C_j} \sum_n (N_{jn}) \,\text{sign}\left(\hat{\lambda}_n - \hat{\lambda}_j \right) \quad . \tag{4.67}$$

For simplicity, let's rewrite the above as:

$$\tau_{j,TV} = \left(\eta^2\right)\left(s_{ca,max}\right)\left(\Xi_j\right) \tag{4.68}$$

$$\Xi_j \equiv \frac{1}{C_j}\sum_n \left(N_{jn}\right)\text{sign}\left(\hat{\lambda}_n - \hat{\lambda}_j\right) \tag{4.69}$$

where $-1 \leq \Xi_j \leq 1$. If Ξ_j is positive, then one should increase $\hat{\lambda}_j$ to decrease TV; likewise, if Ξ_j is negative, one should decrease $\hat{\lambda}_j$ to decrease TV:

$$\begin{aligned}\Xi_j > 0 &\rightarrow \text{increase } \hat{\lambda}_j \\ \Xi_j < 0 &\rightarrow \text{decrease } \hat{\lambda}_j \quad .\end{aligned}$$

When implementing iterative ML-EM, the vector Ξ_j must be evaluated for each iteration:

$$\Xi_j^k = \frac{1}{C_j}\sum_n \left(N_{jn}\right)\text{sign}\left(\hat{\lambda}_n^k - \hat{\lambda}_j^k\right) \quad . \tag{4.70}$$

The functions $\Xi_j^{\pm}$ can be written as:

$$\begin{aligned}\Xi_j^{(k)+} &= \frac{1}{2}\left[\left|\Xi_j^k\right| + \Xi_j^k\right] \\ \Xi_j^{(k)-} &= \frac{1}{2}\left[\left|\Xi_j^k\right| - \Xi_j^k\right]\end{aligned}$$

and separate out the positive and negative parts of Ξ_j.

Finally, by incorporating $\Xi_j^{\pm}$ into Equation 4.56, the ML-EM algorithm takes the form:

$$\hat{\lambda}_j^{k+1} = \frac{\left(\hat{\lambda}_j^k\right)\left(s_{j,\ ca}\right)}{s_{j,\ ca}^2 + \left(\epsilon^2\right)\left(s_{max,ca}^2\right) + \left(\eta^2\right)\left(s_{max,ca}\right)\left(s_{j,\ ca}\right)\left(\Xi_j^{-(k)}\right)} \times \left[\sum_i^I \frac{\left(d_i\right)\left(a_{ij}\right)}{\sum_{j'}^J \left(a_{ij'}\right)\left(\hat{\lambda}_{j'}^k\right)} + \left(\eta^2\right)\left(s_{max,ca}\right)\left(\Xi_j^{+(k)}\right)\right] \quad . \tag{4.71}$$

All coded aperture image reconstructions presented in this work are generated using the above formulation [101].

4.3.5 Image Reconstruction with Multiple Perspectives

As a coded-aperture device, the detector can theoretically provide information for 3-D image reconstruction in the near field from just a single viewing angle. The magnification associated with the relative distance of the mask and source provides information about the source distance. However, the depth resolution can improve significantly by acquiring data from different viewing angles. This can also be said for the Compton camera.

Given the limited mobility of the Dual-Modality Imager, the imager cannot be rotated around the source to acquire multiple perspectives. As an alternative, the source is rotated around a well-defined axis and data is acquired for a fixed amount of time at each viewing angle θ. The impact on the reconstruction algorithm is straightforward. New data channels are added to the detector matrix D for each perspective as follows:

$$D = \begin{bmatrix} D(\theta_0) \\ D(\theta_1) \\ \\ \vdots \\ \\ D(\theta_n) \end{bmatrix} . \tag{4.72}$$

Furthermore, the system matrix A must be expanded to account for the detector data from the additional perspectives. To do this, we first define a new source image space $J(\theta)$ for each angle θ by a simple rotation operation:

$$J(\theta) = J(\theta_0) \cdot \begin{bmatrix} \cos\theta & 0 & \sin\theta \\ 0 & 1 & 0 \\ -\sin\theta & 0 & \cos\theta \end{bmatrix} \tag{4.73}$$

where $J(\theta)$ is a matrix of (x, y, z) voxel positions and essentially represents a rearrangement of the initial image space $J(\theta_0)$ at angle $\theta = 0°$. Note the above operation performs a counter-clockwise rotation of $J(\theta_0)$ around a fixed y-axis. Next, for each $J(\theta)$, we compute a corresponding system response $A(\theta)$ using the ray-tracing method outlined in Section 4.3.3. We can now expand the system matrix A as follows:

$$A = \begin{bmatrix} A(\theta_0) \\ A(\theta_1) \\ \\ \vdots \\ \\ A(\theta_n) \end{bmatrix} . \tag{4.74}$$

Note that while both the detector data D and system response A must be expanded to accommodate multiple perspectives, the dimensions of the gamma-ray distribution Λ remain unchanged. The imaging problem now takes the form:

$$\begin{bmatrix} A(\theta_0) \\ A(\theta_1) \\ \\ \vdots \\ \\ A(\theta_n) \end{bmatrix} \cdot [\Lambda] = \begin{bmatrix} D(\theta_0) \\ D(\theta_1) \\ \\ \vdots \\ \\ D(\theta_n) \end{bmatrix} . \tag{4.75}$$

The above method can be applied to the Compton modality as well.

4.4 Compton Image Reconstruction

4.4.1 Event Selection

Compton imaging can be realized by a multitude of interaction scenarios, including triple interactions, double Compton scatterings with the scattered photon escaping, etc. However, this work only accepts a small fraction of these as Compton events. Assuming the incident photon energy is known, Compton events are selected based on the following criteria:

1. only double-interaction events are considered,
2. the sum of the energy depositions must fall within a specified ROI near the known incident energy,
3. only interactions with an opening angle θ in the range $-0.4 < cos\theta < 1$ are accepted,
4. the distance between the two interactions (i.e. the lever arm) must be greater than 14 mm, and
5. back-projection criterion (discussed later in Section 4.4.2.4).

The first two criteria are intended to restrict the analysis to Compton-photoelectric events only. The second two criteria arise from the imaging properties of the events. Perfect Compton kinematics dictate that the incident photon must originate from a 3-D cone in space. However, uncertainties in the energy depositions and positions of interaction blur this cone. In practice, the uncertainties in energy render the blurring in back-scattered photons ($-1 < cos\theta < -0.4$) virtually worthless for image reconstruction. Likewise, events with short lever arms (< 14 mm) produce large uncertainty in the cone axis; which, in turn, blurs the back-projected cone. Criteria 3 and 4 are imposed to eliminate such low-resolution events from the analysis; and thus, there is a trade-off between image resolution and sensitivity. This tradeoff is demonstrated in Section 4.5.3.

4.4.2 Analytical Model for Compton Cone Back-projection

The back-projection of Compton cones provides an initial estimate of the source distribution and serves as input for list-mode ML-EM. The objective of Compton back-projection is to determine the weights of image voxels intersected by Compton cones. Each weight w_{ij} effectively represents the probability that a photon emitted at image voxel j resulted in Compton event i. To estimate these weights, Gunter et al. [125] derives an analytical model that predicts the expected rate of Compton events from the rate of emissions from a single image voxel. The derivation of the model can be broken down into three main steps which determine:

1. photon emission rate from a single image voxel,
2. photon density distribution in the detector given step (1), and
3. rate of Compton events given step (2).

The rate in step 3 divided by the rate of photon emissions defines the Compton system response w_{ij} that is used in ML-EM. The following provides a high-level discussion of each step. The meanings of mathematical symbols presented in this section are mostly consistent with the usage in Gunter et al. [125] and may differ from previous usage in this work.

4.4.2.1 Photon Emission Rate from an Image Voxel

The distribution of photon emissions can be described as:

$$A\left(\vec{x},\ E\right) = \frac{[\text{emissions}]}{[\text{sec}]\,[\text{keV}]\,[\text{m}^3]}$$

where $A\left(\vec{x},\ E\right)$ is the activity density at $\vec{x}$ from the emission line at energy E. In general, $A\left(\vec{x},\ E\right)$ is a continuous function of $\vec{x}$ and E, but in imaging applications, $A\left(\vec{x},\ E\right)$ is often discretized into a large number of voxels with each voxel containing a constant amount of activity:

$$A\left(\vec{x},\ E\right) = A\left(E\right) \cdot \Omega\left(\vec{x} - \vec{C}\right) \tag{4.76}$$

where $A\left(E\right)$ is the activity within the voxel, $\Omega\left(\vec{x}\right)$ is the voxel spatial distribution, and capital $\vec{C}$ is the voxel center. Conveniently, the voxel distribution can be defined by a Gaussian function:

$$\Omega\left(\vec{x}\right) = \left(\frac{6}{\pi}\right)^{\frac{3}{2}} \exp\left[\frac{-6\left|\vec{x}\right|^2}{L^2}\right] \tag{4.77}$$

where L is the voxel width. A Gaussian, as opposed to a cubic, voxel function is selected because the function is rotationally symmetric and simplifies calculations later on.

4.4.2.2 Photon Density Distribution in the Detector

The photon phase-space density Φ can be defined as:

$$\Phi\left(\vec{x},\ \vec{p}\right) = \frac{[\#\text{ photons}]}{\left[\text{keV}^3\right]\left[\text{m}^3\right]}$$

where $\vec{x}$ describes the position of the photon emission and $\vec{p}$ represents the photon momentum. Because Compton scattering is crucial in this analysis, Φ is decomposed based on the number of scattering interactions:

$$\Phi^n\left(\vec{x},\ \vec{p}\right) = \text{photon density following } n \text{ scatters}$$

$$\Phi\left(\vec{x},\ \vec{p}\right) = \sum_{n=0}^{\infty} \Phi^n\left(\vec{x},\ \vec{p}\right) \tag{4.78}$$

where Φ^0 corresponds to the photon density *entering the detector* and Φ^n corresponds to the photon density following the n^{th} scatter *within* the detector. The utility of this decomposition is threefold: (1) Φ^0 is easily computed for a Gaussian voxel source, (2) Φ^{n+1} is easily computed from Φ^n in terms of known differential cross-sections, and (3) the rate of interactions in a given region is easily computed from Φ within that region.

In general, the photon density Φ^0 incident on a detector can originate from either near- or far-field sources. Far-field sources are essentially independent of the detector position, i.e. there are no parallax effects if the detector system moves. These sources are not of concern in this analysis. Near-field sources arise from isotropic emissions as described by $A\left(\vec{x},\ E\right)$ in Equation 4.76, and the subsequent photon density Φ^0 can be approximated as:

$$\Phi^0\left(\vec{x},\ \vec{p}\right) = \int\int\int d^3\vec{z} \int dE \quad A\left(\vec{z},\ E\right)\ \frac{\text{Att}\left(\vec{x},\ \vec{z},\ E\right)}{4\pi c\ \left|\vec{x}-\vec{z}\right|^2}\ \delta^3\left(\vec{p} - E\frac{\left(\vec{x}-\vec{z}\right)}{\left|\vec{x}-\vec{z}\right|}\right) \tag{4.79}$$

where the variable of integration $\vec{z}$ represents the position of photon emission, $\vec{x}$ describes the position of the flux being measured, lowercase c is the speed of light, and the attenuation function Att is a dimensionless term defined by a line integral of the attenuation coefficient μ:

$$\text{Att}\left(\vec{x},\ \vec{z},\ E\right) \equiv \exp\left[-\left|\vec{x}-\vec{z}\right| \int_0^1 d\kappa \quad \mu\left(\kappa\ \vec{x} + (1-\kappa)\ \vec{z},\ E\right)\right] \tag{4.80}$$

where the variable of integration κ is an affine parameter of the line segment. The photon phase-space density Φ^{n+1} that arises from the scattering of photons in the photon density Φ^n can be defined as:

$$\Phi^{n+1}\left(\vec{x},\ \vec{p}\right) = \int\int\int d^3\vec{z} \int\int\int d^3\vec{k} \quad \Phi^n\left(\vec{z},\ \vec{k}\right) \times \\ \frac{\mathrm{Att}\left(\vec{x},\ \vec{z},\ |\vec{p}|\right)\ \mu\left(\vec{z},\ \left|\vec{k}\right|\right)}{\left|\vec{x}-\vec{z}\right|^2} \frac{f_{cs}\left(\left|\vec{k}\right|\right)\ P_{kn}\left(\left|\vec{k}\right|,\ |\vec{p}|\right)}{|\vec{p}|^2} \times \\ \delta\left[|\vec{p}| - \frac{m_e\left|\vec{k}\right|}{m_e + \left|\vec{k}\right| - \frac{\vec{k}\cdot\vec{p}}{|\vec{p}|}}\right]\ \delta^2\left(\frac{\vec{p}}{|\vec{p}|},\ \frac{(\vec{x}-\vec{z})}{|\vec{x}-\vec{z}|}\right) \tag{4.81}$$

where m_e is the electron mass, P_{kn} is the Klein-Nishina weighting function previously defined by Equation 4.9, and f_{cs} is fraction of Compton interactions defined by:

$$f_{cs} \equiv \frac{\sigma_{cs}\left(E\right)}{\sigma_{tot}\left(E\right)}$$

where σ_{cs} and σ_{tot} are the Compton scattering and total interaction cross sections, respectively.

4.4.2.3 Compton Event Rate in the Detector

This work considers a Compton event to be the simultaneous detection of two interactions, labeled here as D_1 and D_2. The first interaction D_1 is the initial Compton scattering of the incident photon having momentum k_1 at location x_1 in the detector. The measured position of D_1 is $r_1\left(\pm\lambda_1\right)$, and the measured energy deposition is $E_1\left(\pm\epsilon_1\right)$. The scattered photon subsequently propagates with momentum k_2 to location x_2 and interacts via photoelectric absorption. The measured position of this second interaction D_2 is $r_2\left(\pm\lambda_2\right)$, and the measured energy deposition is $E_2\left(\pm\epsilon_2\right)$.

To determine the rate of such events, we start by computing the rate of photoelectric absorptions D_2 that result from all single-scattered photons:

$$\mathrm{Rate}\left(D_2\right) = \mathrm{Eff}\left(\vec{r_2},\ E_2\right) \int\int\int d^3\vec{x}_2 \int\int\int d^3\vec{k}_2 \quad \Phi^1\left(\vec{x}_2,\ \vec{k}_2\right) \times \\ \mu\left(\vec{x}_2,\ \left|\vec{k}_2\right|\right)\ f_{pe}\left(\left|\vec{k}_2\right|\right)\ c\ D_x\left(\vec{x}_2|\vec{r}_2,\ \lambda_2\right)\ D_E\left(\left|\vec{k}_2\right|\left|E_2,\ \epsilon_2\right.\right) \tag{4.82}$$

where the variables of integration $\vec{x}$ and $\vec{k}$ represent the *actual* interaction position and momentum deposited in the detector, respectively. The variables r and E represent the *reported*

position and energy deposition of interaction D, respectively. The term f_{pe} represents the fraction of photoelectric absorptions defined by:

$$f_{pe} \equiv \frac{\sigma_{pe}\left(E\right)}{\sigma_{tot}\left(E\right)}$$

where σ_{pe} is the photoelectric absorption cross section. The single-scattered photon density Φ^1 arises from Φ^0 and is determined by Equation 4.81:

$$\begin{aligned}\Phi^1\left(\vec{x}_2,\ \vec{k}_2\right) = \int\int\int d^3\vec{x}_1 \int\int\int d^3\vec{k}_1 \quad & \Phi^0\left(\vec{x}_1,\ \vec{k}_1\right) \times \\ & \frac{\mathrm{Att}\left(\vec{x}_2,\ \vec{x}_1,\ \left|\vec{k}_2\right|\right)\ \mu\left(\vec{x}_1,\ \left|\vec{k}_1\right|\right)}{\left|\vec{x}_2-\vec{x}_1\right|^2}\ \frac{f_{cs}\left(\left|\vec{k}_1\right|\right)\ P_{kn}\left(\left|\vec{k}_1\right|,\ \left|\vec{k}_2\right|\right)}{\left|\vec{k}_2\right|^2} \times \\ & \delta\left[\left|\vec{k}_2\right| - \frac{m_e\left|\vec{k}_1\right|}{m_e + \left|\vec{k}_1\right| - \frac{\vec{k}_1\cdot\vec{k}_2}{\left|\vec{k}_2\right|}}\right]\ \delta^2\left(\frac{\vec{k}_2}{\left|\vec{k}_2\right|},\ \frac{\left(\vec{x}_2-\vec{x}_1\right)}{\left|\vec{x}_2-\vec{x}_1\right|}\right) \quad .\end{aligned} \tag{4.83}$$

Here the first delta function describes the kinematics of Compton scattering. The second delta function enforces equivalency between the direction of the scattered photon momentum and the direction from the first to second interaction.

Note the rate formula in Equation 4.82 imposes a generalization for the description of the Compton imager. This formula considers detectors that report the interaction position as (r_i, λ_i) and deposition energy as (E_i, ϵ_i), where λ_i is the spatial resolution of interaction r_i and ϵ_i is the energy resolution at energy E_i. The spatial region is described by function D_x and the energy interval by function D_E, where:

$$\begin{aligned} D_x\left(\vec{x}|\vec{r},\ \lambda\right) &= \exp\left[-\frac{\left|\vec{x}-\vec{r}\right|^2}{2\lambda^2}\right] \\ D_E\left(k|E,\ \epsilon\right) &= \exp\left[-\frac{\left(k-E\right)^2}{2\epsilon^2}\right] \quad . \end{aligned}$$

In reality, the detection system does not report all interactions. We can account for this by employing an efficiency function $\mathrm{Eff}\left(\vec{r},\ E\right)$ that satisfies $0 < \mathrm{Eff}\left(\vec{r},\ E\right) < 1$.

Equation 4.82 considers scattered photons from all regions in the detector. We are interested in restricting this rate to only those interactions that are consistent with the detection of the first interaction D_1. Such restrictions are accomplished by integrating the appropriate detector functions (i.e. Eff, D_x, D_E) for the D_1 interaction; thereby limiting the ranges of x_1 and k_1. Consequently, the rate of coincident events (D_1, D_2) is given by:

$$\begin{aligned}\text{Rate}\left(D_1,\ D_2\right) = \text{Eff}\left(\vec{r_1},\ E_1\right)\ \text{Eff}\left(\vec{r_2},\ E_2\right) \int\int\int d^3\vec{x}_1 \int\int\int d^3\vec{k}_1 \quad \Phi^0\left(\vec{x}_1,\ \vec{k}_1\right)\ c \times \\ \int\int\int d^3\vec{x}_2 \int\int\int d^3\vec{k}_2 \quad \mu\left(\vec{x}_1,\ \left|\vec{k}_1\right|\right)\ f_{cs}\left(\left|\vec{k}_1\right|\right)\ \mu\left(\vec{x}_2,\ \left|\vec{k}_2\right|\right)\ f_{pe}\left(\left|\vec{k}_2\right|\right) \times \\ \frac{\text{Att}\left(\vec{x}_2,\ \vec{x}_1,\ \left|\vec{k}_2\right|\right)}{\left|\vec{x}_2 - \vec{x}_1\right|^2}\ \frac{P_{kn}\left(\left|\vec{k}_1\right|,\ \left|\vec{k}_2\right|\right)}{\left|\vec{k}_2\right|^2} \times \\ \delta\left[\left|\vec{k}_2\right| - \frac{m_e\left|\vec{k}_1\right|}{m_e + \left|\vec{k}_1\right| - \frac{\vec{k}_1\cdot\vec{k}_2}{\left|\vec{k}_2\right|}}\right]\ \delta^2\left(\frac{\vec{k}_2}{\left|\vec{k}_2\right|},\ \frac{\left(\vec{x}_2 - \vec{x}_1\right)}{\left|\vec{x}_2 - \vec{x}_1\right|}\right) \times \\ D_x\left(\vec{x}_2|\vec{r}_2,\ \lambda_2\right)\ D_E\left(\left|\vec{k}_2\right||E_2,\ \epsilon_2\right)\ D_x\left(\vec{x}_1|\vec{r}_1,\ \lambda_1\right)\ D_E\left(\left|\vec{k}_1\right| - \left|\vec{k}_2\right||E_1,\ \epsilon_1\right) \quad .\end{aligned} \tag{4.84}$$

This 12-dimensional integral is the fundamental definition of the Compton event rate, but to be useful, several simplifications are made. The delta functions inherently remove three dimensions of integration. Furthermore, several terms can be assumed constant and removed from the integrals. These include the interaction fractions f_{cs} and f_{pe}, the attenuation coefficient μ, the attenuation function Att, the Klein-Nishina weighting function P_{kn}, and the efficiency functions Eff:

$$\begin{aligned} f_{cs1} &\equiv f_{cs}\left(E_1 + E_2\right) \\ f_{pe2} &\equiv f_{pe}\left(E_2\right) \\ \mu_1 &\equiv \mu\left(\vec{r}_1,\ E_1 + E_2\right) \\ \mu_2 &\equiv \mu\left(\vec{r}_2,\ E_2\right) \\ \text{Att}_{ext} &\equiv \text{Att}\left(\vec{c},\ \vec{r}_1,\ E_1 + E_2\right) \\ \text{Att}_{int} &\equiv \text{Att}\left(\vec{r}_1,\ \vec{r}_2,\ E_2\right) \\ P_{kn}^{12} &= P_{kn}\left(E_1 + E_2, E_2\right) \\ \text{Eff}_1 &\equiv \text{Eff}\left(\vec{r}_1,\ E_1\right) \\ \text{Eff}_2 &\equiv \text{Eff}\left(\vec{r}_2,\ E_2\right) \end{aligned}$$

where Att_{ext} and Att_{int} represent the attenuation functions for the incident and scattered photons, respectively. The remaining simplifications applied to Equation 4.84 are outlined in Gunter et al. [125] and lead to the following rate equation:

$$\text{Rate}\,(D_1,\ D_2) = \underbrace{\left[L^3 A_{E_\gamma}\right]}_{1}\underbrace{\left[\text{Eff}_1\ \text{Eff}_2\ \text{Att}_{int}\ \text{Att}_{ext}\right]}_{2}\underbrace{\left[\frac{2\pi\ \lambda_1^2\ \lambda_2^2}{r_s^2\ r_{12}^2}\right]}_{3}\underbrace{\left[\mu_1\ \lambda_1\ \mu_2\ \lambda_2\ f_{cs1}\ f_{pe2}\ P_{kn}^{12}\right]}_{4}$$
$$\underbrace{\exp\left[-\frac{\left(E_\gamma - E_1 - E_2\right)^2}{2\left(\epsilon_1^2 + \epsilon_2^2\right)}\right]}_{5}\underbrace{\text{CC}\left(\vec{\alpha}\cdot\vec{\beta},\ \underline{\mu};\ \Sigma_i\right)}_{6} \quad . \tag{4.85}$$

Here the first term $\left[L^3 A_{E_\gamma}\right]$ represents the emissions per second within an image voxel, where A_{E_γ} is the activity from the emission line at energy E_γ. The second term consists of dimensionless coefficients that reduce the fraction of emissions. The third term is also dimensionless and characterizes the solid angles associated with the detector volumes and depends on the spatial resolutions λ_1 and λ_2 of the interactions and the distances r_s and r_{12}, where r_s is the distance between the center of the image voxel and first position of interaction and r_{12} is the lever arm or distance between the two positions of interaction. The fourth term is a dimensionless interaction term that primarily depends on the energy depositions E_1 and E_2 and characterizes the probabilities of the two interactions within the detector and the probability of Compton scatter. Note only the first term $\left[L^3 A_{E_\gamma}\right]$ provides dimensions in the above rate equation, which has units in counts per second.

The last two terms are the most crucial to this analysis. The fifth term suppresses the rate for energies $(E_1 + E_2)$ far from the spectral line at E_γ. The sixth term, referred to as the Compton cone function CC, suppresses the rate for image voxels that are not located on the Compton cone. The CC function can be defined as:

$$\text{CC}\left(\vec{\alpha}\cdot\vec{\beta},\ \underline{\mu};\ \Sigma_i\right) \equiv \frac{1}{\left(2\pi\ \Sigma_1^2\right)\left(2\pi\ \Sigma_2^2\right)}\int\limits_{S^2} d^2\vec{\Omega}_1 \int\limits_{S^2} d^2\vec{\Omega}_2 \quad \Theta\left(\vec{\Omega}_1\cdot\vec{\beta}\right)\ \Theta\left(\vec{\Omega}_2\cdot\vec{\alpha}\right)$$
$$\exp\left[-\frac{1}{2\Sigma_1^2}\left[1-\left(\vec{\Omega}_1\cdot\vec{\beta}\right)^2\right] - \frac{1}{2\Sigma_2^2}\left[1-\left(\vec{\Omega}_2\cdot\vec{\alpha}\right)^2\right]\right]\ \exp\left[-\frac{\left[\left(\vec{\Omega}_1\cdot\vec{\Omega}_2\right)-\underline{\mu}\right]^2}{2\Sigma_3^2}\right] \tag{4.86}$$

where the variables of integration Ω_1 and Ω_2 correspond to the directions of the incident and scattered photons, respectively, and the operator Θ represents a heavyside step function. The vector β denotes the direction from the center C of the image voxel to the detector:

$$\beta \equiv \frac{\vec{r}_1 - \vec{C}}{r_s}$$

and the vector α points from the first position r_1 to the second position r_2 of interaction:

$$\alpha \equiv \frac{\vec{r_2} - \vec{r_1}}{r_{12}}$$

denoting the direction of the scattered photon. The CC function determines the imaging properties of the Compton camera and has the most significance in this analysis. The details of this calculation are complicated and beyond the scope of this work. In practice, the following analytical approximation can be employed:

$$\begin{aligned} \mathrm{CC}\left(\nu,\ \underline{\mu};\ \Sigma_i\right) \approx & \frac{\Sigma_3}{\sqrt{\Sigma_3^2 + \left(1-\nu^2\right)\Sigma_1^2 + \left(1-\underline{\mu}^2\right)\Sigma_2^2}} \times \\ & \exp\left[-\frac{\left(\sqrt{1-\nu^2} - \chi\right)^2 \Delta^2}{2\left[\Sigma_3^2 + \left(1-\nu^2\right)\Sigma_1^2 + \left(1-\underline{\mu}^2\right)\Sigma_2^2\right]}\right] \end{aligned} \tag{4.87}$$

where:

$$\nu = \vec{\alpha} \cdot \vec{\beta}$$

$$\underline{\mu} = \max\left(-1,\ 1 - \frac{\left(m_e\right)\left(E_1\right)}{\left(E_1 + E_2\right)E_2}\right)$$

$$\sigma \equiv \mathrm{sign}\left(\underline{\mu}\sqrt{1-\nu^2} - \nu\sqrt{1-\underline{\mu}^2}\right)$$

$$\gamma \equiv \max\left(\epsilon,\ \left(\underline{\mu}\right)\left(\nu\right) + \sqrt{1-\underline{\mu}^2}\ \sqrt{1-\nu^2}\right) \quad [\epsilon \approx 0.0001]$$

$$\Delta \equiv \sigma\sqrt{1-\gamma^2}$$

$$\chi \equiv \frac{\left(\nu\right)\left(\Delta\right)}{\gamma}$$

$$\Sigma_1 = \frac{L}{\sqrt{12}r_s}$$

$$\Sigma_2 = \frac{\sqrt{\lambda_1^2 + \lambda_2^2}}{r_{12}}$$

$$\Sigma_3 = \frac{\epsilon_1 \epsilon_2 \left(\epsilon_1^2 + \epsilon_2^2\right)^{\frac{3}{2}} m_e}{\left[\epsilon_1^2 E_2 + \epsilon_2^2 \left(E_\gamma - E_1\right)\right]^2}$$

where Σ_1 describes the uncertainty due to the finite size of the image voxel, Σ_2 the uncertainty in the measured positions of interaction, and Σ_3 the uncertainty in the energy depositions. In combination, these three terms describe the angular resolution of the Compton imager. The uncertainty Σ_3 should vary depending on the energy deposition, but in this work, this uncertainty is defined by a constant. This simplification provides reasonable results. Possible improvements may be realized by accounting for the energy dependency of Σ_3. Note the underlined coefficient $\underline{\mu}$ represents the cosine of the cone opening angle, not the attenuation coefficient μ.

Finally, we compute the back-projected weight w_{ij} by normalizing Equation 4.85 by the activity term $\left[L^3 A_{E_\gamma}\right]$:

$$w_{ij} \equiv \frac{\text{Rate}\left(D_1,\ D_2\right)}{L^3 A_{E_\gamma}} \tag{4.88}$$

so that w_{ij} is a dimensionless probability that serves as the system response of the Compton imager.

4.4.2.4 Compton Back-projection Criterion

Oftentimes we desire an image space that closely surrounds the source of interest to enable a computationally-efficient and tractable reconstruction. In Compton imaging, imposing such tight restrictions can result in edge effects. These effects are related to Compton cones, mostly those that have been sequenced incorrectly, that just barely graze the edges of the image space. These edges, which tend to have lower sensitivities than the center image voxels, can blow up during the iterative reconstruction process due to the sensitivity normalization in the ML-EM algorithm. This noise amplification can be suppressed via Tikhonov regularization as described in Section 4.3.4. However, to completely eliminate the noisy corners requires heavy regularization, which in turn degrades the rest of the image. For this reason, this work selectively removes undesirable cones prior to the iterative reconstruction step.

Only Compton cones whose total probability density functions exceed a given threshold T are considered:

$$t_i = \sum_j^J w_{ij}$$

$$\begin{aligned} t_i \geq T \rightarrow &\quad \text{keep Compton event } i \\ t_i < T \rightarrow &\quad \text{eliminate Compton event } i \end{aligned} \tag{4.89}$$

where t_i is the summation of back-projected weights over all image voxels j for a given Compton event i. This summation reflects the number of image voxels intersected by the cone. Thus, if a cone grazes the outskirts of the image space, the associated t_i should be small. That said, t_i is not indicative of which image voxels are intersected. For example, if a cone with a small opening angle intersects the center of the image space, the associated t_i might not exceed T. These desirable events are thrown-away using the above criterion, but nonetheless represent a small fraction of those eliminated from the reconstruction.

The threshold T is selected on a case-by-case basis as the optimal T varies depending on the size of the image space and attributes related to the source of interest. Because of this variability, this work does not account for event loss due to the back-projection criterion in calculating the imaging sensitivity of the Compton camera (as reported in Section 4.5.1.2). For each imaging problem, a histogram of all t_i for Compton events $i = 1, 2, ..., I$ is generated as illustrated in Figure 4.12. The start of the histogram generally features a sharp edge. This edge represents back-projected cones with a significantly small t_i. The threshold T is selected at the point where the histogram edge transitions into a valley.

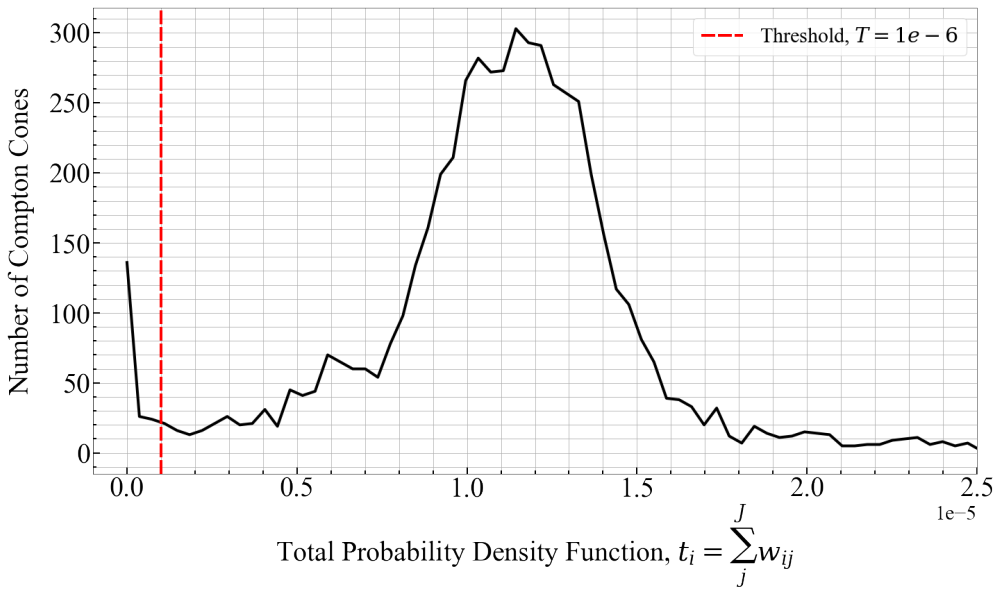

Figure 4.12: Histogram of the summed weights $t_i = \sum_j^J w_{ij}$ for all Compton events $i = 1, 2, ..., I$. The Compton data were acquired from an ^{225}Ac point-like source at the 440-keV emission line of the daughter ^{213}Bi. The red dashed line is located at the threshold T.

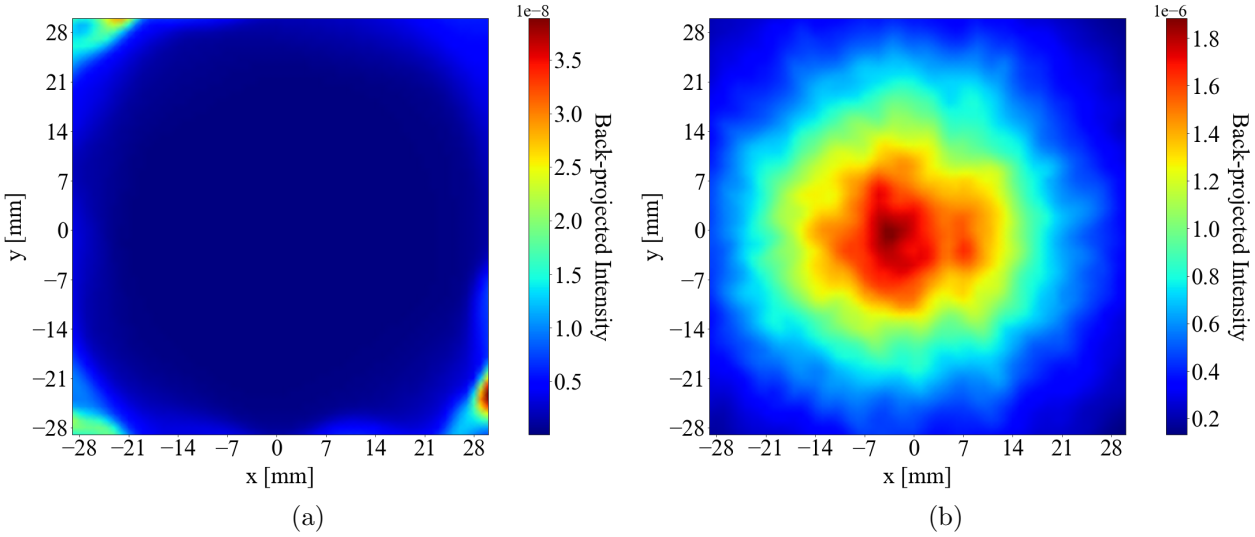

Figure 4.13: 2-D Compton back-projections of an ^{225}Ac point-like source produced from (a) events that fall below the threshold: $t_i < T$ and (b) events that exceed the threshold: $t_i \geq T$. Both images were produced from the data displayed in Figure 4.12.

Using the same Compton data as displayed in Figure 4.12, back-projected images were produced from (a) events that fall below the threshold: $t_i < T$ and (b) events that exceed the threshold: $t_i \geq T$. Figure 4.13 displays 2-D slices of the back-projections. Note the intensity scales of these images are not equivalent to the values of t_i displayed in Figure 4.12. The back-projected intensity t_j represents the summation of back-projected weights over all events $i = 1, 2, ...I$ in a given image voxel j:

$$t_j = \sum_{i}^{I} w_{ij} \quad .$$

Back-projection (a) illustrates the impact of undesirable cones directed towards the edges of the reconstruction space. There is a significant concentration of intensity at the corners. Back-projection (b) illustrates the impact of eliminating undesirable cones that graze the edges of the image space. Now the source intensity is concentrated at the center.

It's important to note that the back-projection criterion in Equation 4.89 inherently introduces bias into the image reconstruction. For example, if the threshold T is set too high, then the intensity can appear overly concentrated in the center region. More work needs to be done in developing a standardized and unbiased approach to eliminating edge effects. This should include improvements to the gamma-ray tracking algorithm so that more Compton cones are sequenced correctly and directed inside of the image space.

4.4.3 ML-EM with Penalty Functions for List-mode Data

Unlike coded aperture imaging, where the detector data can easily be binned by position of interaction, Compton imaging produces cones that are defined by multiple parameters, including the measured energy depositions and positions of two interactions and the uncertainties associated with each energy and position. The large Compton parameter space, relative to the number of collected data elements, makes binning the data extremely challenging. For this reason, Compton events are fed as list-mode data into the image reconstruction [126]. Similar to Equation 4.71 derived in Section 4.3.4, the following list-mode formulation of the ML-EM algorithm is applied in this work:

$$\hat{\lambda}_j^{k+1} = \frac{\left(\hat{\lambda}_j^k\right)\left(s_{j,\ ci}\right)}{s_{j,\ ci}^2 + \left(\epsilon^2\right)\left(s_{max,ci}^2\right) + \left(\eta^2\right)\left(s_{max,ci}\right)\left(s_{j,\ ci}\right)\left(\Xi_j^{-(k)}\right)} \times \left[\sum_i^I \frac{w_{ij}}{\sum_{j'}^J \left(w_{ij'}\right)\left(\hat{\lambda}_{j'}^k\right)} + \left(\eta^2\right)\left(s_{max,ci}\right)\left(\Xi_j^{+(k)}\right)\right] \quad . \tag{4.90}$$

Here w_{ij} serves as the system response and represents the expected probability of a Compton event i from an emission originating in image voxel j. The matrix elements w_{ij} are calculated from the analytical model derived in Section 4.4.2.

It is important to note that Equation 4.90 is equivalent to Equation 4.71 with the condition that each observation consists of a single event ($d_i = 1$) and "unobserved" events ($d_i = 0$) are ignored. The advantage of this formulation is that w_{ij} need not be evaluated for unobserved combinations of interactions. The problem is that the sensitivity term $s_{j,\ ci}$ for the Compton imager requires a sum of w_{ij} over all possible events i, including those with $d_i = 0$. And unfortunately, the role of $s_{j,\ ci}$ is crucial in list-mode ML-EM because $s_{j,\ ci}$ accounts for unobserved events and provides overall normalization. Conceptually, $s_{j,\ ci}$ is just the probability that an arbitrary emission from image voxel j is observed somewhere in the detector system. Based on this observation, the sensitivity can be evaluated without the explicit calculation of all possible w_{ij}.

Assume a point source located at a position (x, y, z) where the origin lies at the center of the front face of a detector. We can then approximate the Compton sensitivity $s_{j,\ ci}$ by the following integral over the detector surface:

$$s_{j,\ ci}\left(x, y, z\right) \approx \frac{1}{4\pi} \int d\alpha \int d\beta \ \frac{z}{\left[\left(x-\alpha\right)^2 + \left(y-\beta\right)^2 + z^2\right]^{\frac{3}{2}}} \quad . \tag{4.91}$$

The above accounts for sources that are exceptionally close to the detector, where the $1/R^2$

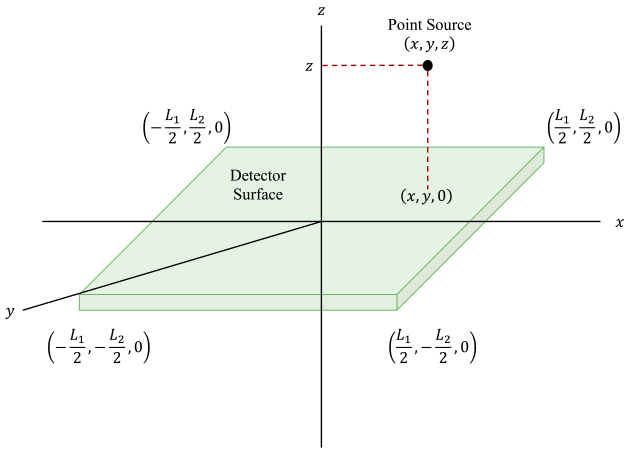

Figure 4.14: An illustration of a planar detector surface over which an integration is performed to determine the Compton sensitivity $s_{j,\ ci}$.

approximation does not hold. In reality, the Compton sensitivity also varies with the incident photon energy. Equation 4.91 neglects this dependency, but serves as a good approximation. The true sensitivity should simply scale by a constant factor related to the incident energy.

Figure 4.14 provides an illustration of the detector surface over which we integrate. We define the surface from $-\frac{L_1}{2} < x < \frac{L_1}{2}$ and $-\frac{L_2}{2} < y < \frac{L_2}{2}$, where L_1 and L_2 are the dimensions of a planar detector. In this work, $L_1 = L_2 = 37$ mm. The sensitivity $s_{j,\ ci}$ now becomes:

$$s_{j,\ ci}\left(x, y, z\right) \approx \frac{z}{4\pi} \int_{-\frac{L_1}{2}}^{\frac{L_1}{2}} d\alpha \int_{-\frac{L_2}{2}}^{\frac{L_2}{2}} d\beta \, \frac{1}{\left[\left(x-\alpha\right)^2 + \left(y-\beta\right)^2 + z^2\right]^{\frac{3}{2}}} \quad . \tag{4.92}$$

This integral can be evaluated in closed analytical form and expressed as a sum over four terms:

$$s_{j,\ ci}\left(x, y, z\right) \approx \frac{1}{4\pi} \sum_{m=1}^{2} \sum_{n=1}^{2} \arcsin\left[\left(U_m\right)\left(V_n\right)\right] \left(-1\right)^{m+n} \tag{4.93}$$

where

$$U_m = \frac{u_m}{\sqrt{u_m^2 + z^2}}, \quad -1 < U_m < 1$$

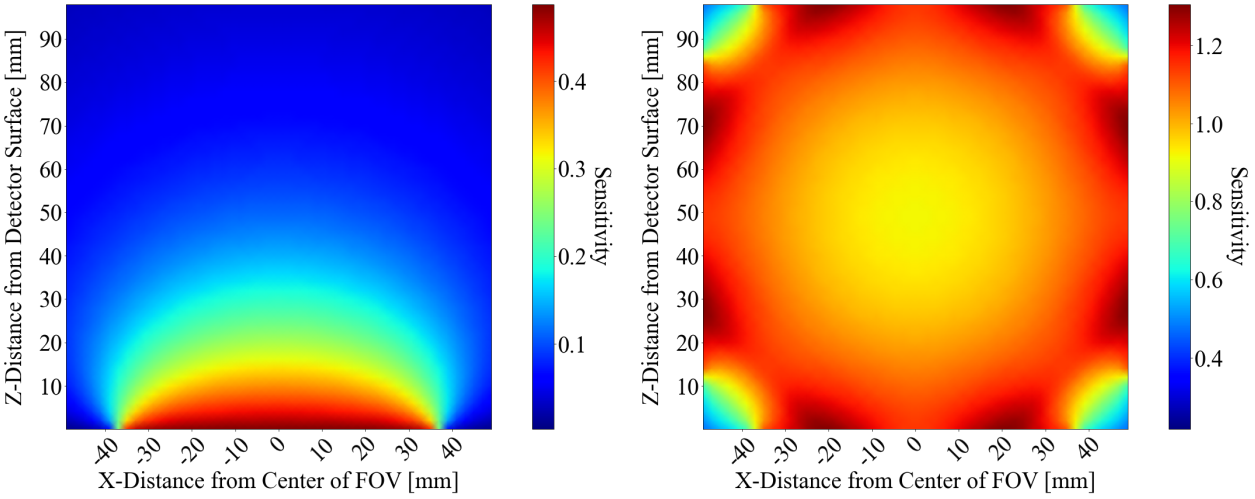

(a) Single Viewing Angle

(b) Eight Viewing Angles

Figure 4.15: Compton sensitivity maps generated for (a) a single viewing angle and (b) eight (45°) viewing angles using Equation 4.93. Each map is displayed in 2-D along the x- and z-directions. In (a), the x-axis at $z = 0$ corresponds the detector surface and the z-axis corresponds to the distance away from the surface.

$$V_n = \frac{v_n}{\sqrt{v_n^2 + z^2}}, \quad -1 < V_n < 1$$

where

$$u_1 = x + \frac{L_1}{2} \quad v_1 = y + \frac{L_2}{2}$$

$$u_2 = x - \frac{L_1}{2} \quad v_2 = y - \frac{L_2}{2} \quad .$$

Using the above solution, the sensitivities $s_{j,\,ci}$ for both one and eight (45°) viewing angles were computed. The latter is simply the sum of sensitivities over all angles. Figure 4.15 displays the sensitivity maps in 2-D along the x- and z-directions. For map (a) of a single viewing angle, the x-axis at $z = 0$ corresponds to the detector surface and the z-axis corresponds to the distance away from the surface. Note the sensitivity precipitously drops as the z-distance increases. Map (b) is employed in scenarios where the source is rotated in 45° increments. The low sensitivities in the corners of (b) arise from non-physical image voxels that lie outside of the original image space when the image space is oriented at 45°, 135°, 225° or 315°. Performing the image reconstruction in these corners can cause artifacts.

4.5 Imaging Performance

4.5.1 Detector Performance

Imaging performance is strongly controlled at the detector level by parameters such as spectroscopic response and position resolution, with the former encompassing both energy resolution and imaging sensitivity. This section only evaluates the spectroscopic response of the Dual-Modality Imager as the position resolution has already been heavily investigated by Chivers [96]. From this previous work, the DSSDs demonstrated a depth resolution as good as 0.5 mm in FWHM. For all practical purposes, the lateral position resolution of DSSDs can be approximated in FWHM as the strip pitch; this work approximates the lateral position resolution to be 2 mm in FWHM. In reality, the distribution of events within a strip has a standard deviation of pitch/$\sqrt{12}$. In theory, DSSDs can achieve a finer position resolution by using interpolation methods [108]. Such methods were previously explored by Lazar [95], but are not employed in this work.

4.5.1.1 Energy Resolution

In the context of this work, the importance of energy resolution is twofold. First, both coded aperture and Compton imaging require knowledge of the incident gamma-ray energy. This requirement is realized by selecting only those events that fall within a specified region-of-interest (ROI) around the known incident energy. The size of the ROI is dictated by the energy resolution of the detectors. With improved energy resolution, the ROI can be reduced, and events prompted by wanted and unwanted photons can be better discriminated; thereby mitigating image noise. Second, in Compton imaging, the uncertainty in the first energy deposition, of which the finite energy resolution of the detectors is a partial contributor[5], propagates to the uncertainty in the opening angle of the Compton cone and blurs the image. To mitigate this blurring effect, as well as enable better event discrimination, this work employs detectors based on HPGe - the gold-standard in terms of energy resolution.

In the case of the Dual-Modality Imager, the determination of energy resolution is not straightforward due to its multi-channel design. The imager has 148 individual channels in total with each channel having a distinct energy resolution. The overall energy resolution of the system includes contributions from each individual channel as well as factors related to the event reconstruction process. The following analyzes the energy resolution at different gamma-ray energies for several classes of detector data: unreconstructed data, single-interaction events, and double-interaction events. Here unreconstructed data represents the detector data before the event reconstruction process and is used to determine the energy resolution of the individual channels.

Figure 4.16 shows an unreconstructed energy spectrum produced after a 5-minute multi-source (^{241}Am, ^{133}Ba, ^{57}Co, ^{137}Cs, and ^{60}Co) measurement. This spectrum incorporates the unreconstructed data from all 148 channels and represents the maximum intrinsic sensitivity

[5]Doppler broadening also contributes to the uncertainty in the energy deposition.

of the system. By considering the unreconstructed data from a single channel only, the energy resolution of that channel can be defined as the FWHM of a Gaussian-fitted photopeak:

$$FWHM|_{E_\gamma} = 2.36\ \sigma|_{E_\gamma} \tag{4.94}$$

where σ is the standard deviation of the photopeak evaluated at a specific gamma-ray energy E_γ. Figure 4.17 shows an example of fitting a 1-D Gaussian to a photopeak at 662 keV from the unreconstructed data of an individual channel. This fitting process was performed for each channel at multiple gamma-ray energies and the associated FWHMs were extracted. Figure 4.18 shows the FWHM at 662 keV versus channel number. Note the few outliers with FWHMs greater than 3.5 keV; these correspond to edge detector strips. Furthermore, Table 4.3 displays both the average and best energy resolutions of the individual channels for each detector at multiple energies. At 662 keV, the average falls at about 2.62 keV (0.396%) and 2.34 keV (0.354%) for the front and back detectors, respectively.

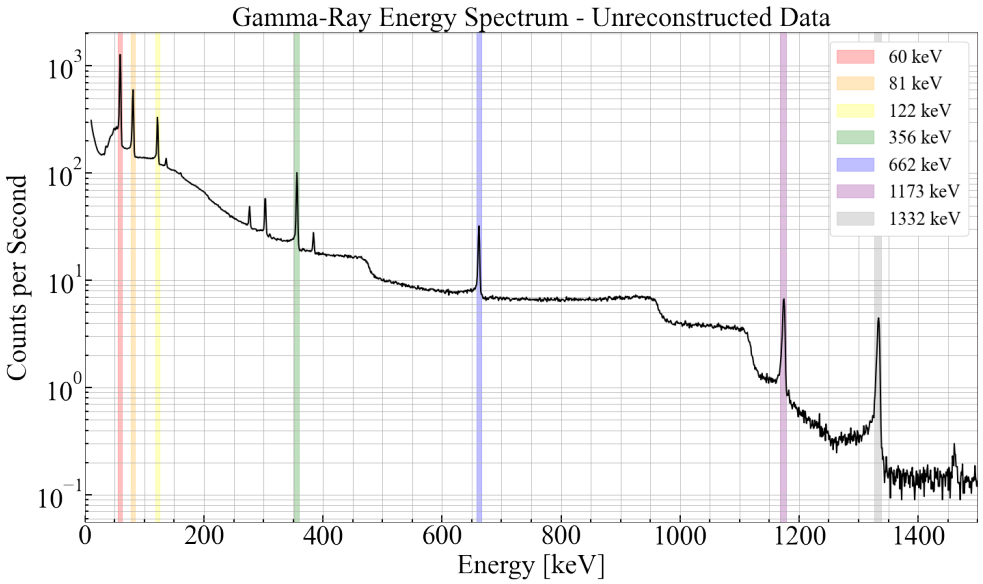

Figure 4.16: Unreconstructed energy spectrum produced after a 5-minute multi-source measurement with the Dual-Modality Imager. This spectrum incorporates data from all 148 detector channels.

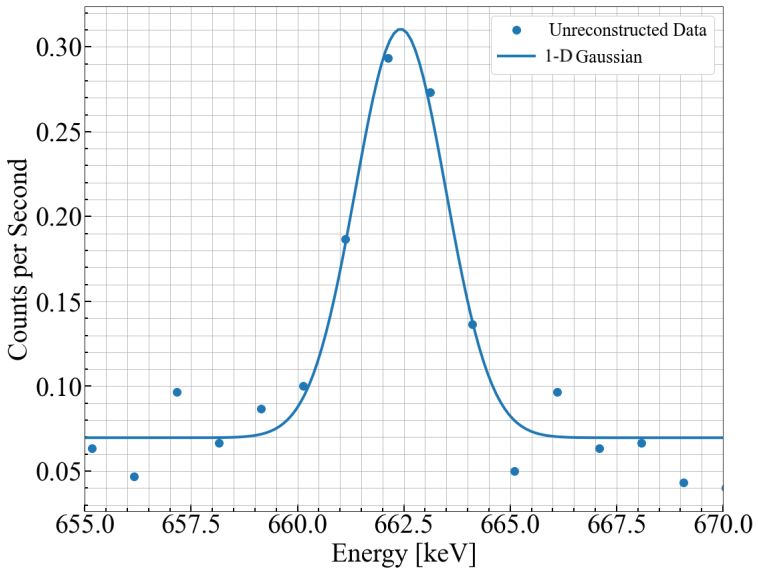

Figure 4.17: A photopeak at 662 keV from the unreconstructed data of an individual channel. A 1-D Gaussian model was fit to the photopeak to provide an estimate of the energy resolution in FWHM. The spectral data was taken from the same measurement displayed in Figure 4.16.

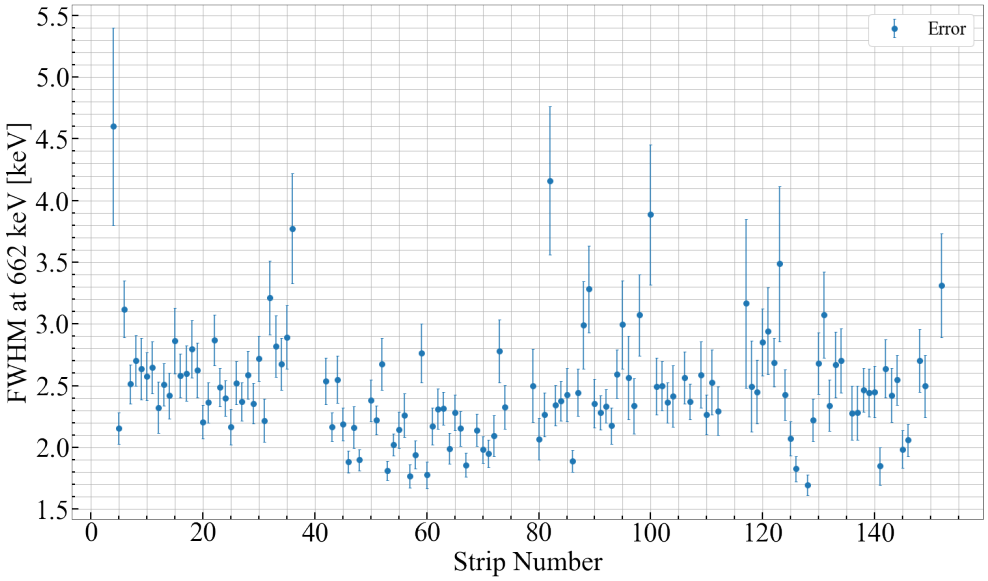

Figure 4.18: Energy resolution of the individual channels of the Dual-Modality Imager. Resolution values are recorded in terms of the FWHM (in keV) at 662 keV. The error bars reflect the uncertainty in the Gaussian model used to fit the peaks. The spectral data was taken from the same measurement displayed in Figure 4.16.

Table 4.3: Best and average energy resolutions of the individual channels for the front and back detectors of Dual-Modality Imager. Resolution values are recorded in terms of the FWHM (in keV). The error reflects the uncertainty in the 1-D Gaussian model used to fit the peaks. The spectral data was taken from the same measurement displayed in Figure 4.16.

Isotope	Energy (keV)	Front Detector		Back Detector	
		Average	Best	Average	Best
^{241}Am	60	1.81 ± 0.0595 (3.01%)	1.62 ± 0.0370 (2.71%)	1.79 ± 0.116 (2.99%)	1.59 ± 0.0837 (2.65%)
^{133}Ba	81	1.98 ± 0.0816 (2.44%)	1.79 ± 0.0582 (2.21%)	1.96 ± 0.111 (2.41%)	1.68 ± 0.0977 (2.07%)
^{57}Co	122	1.89 ± 0.0954 (1.55%)	1.68 ± 0.0487 (1.38%)	1.86 ± 0.118 (1.52%)	1.55 ± 0.176 (1.27%)
^{133}Ba	356	2.08 ± 0.127 (0.584%)	1.74 ± 0.120 (0.490%)	1.95 ± 0.107 (0.549%)	1.60 ± 0.0949 (0.449%)
^{137}Cs	662	2.62 ± 0.231 (0.396%)	1.89 ± 0.0888 (0.285%)	2.34 ± 0.197 (0.354%)	1.69 ± 0.0833 (0.256%)
^{60}Co	1173	3.37 ± 0.545 (0.287%)	1.49 ± 0.0951 (0.127%)	2.91 ± 0.371 (0.248%)	1.78 ± 0.0986 (0.152%)
^{60}Co	1332	3.75 ± 0.608 (0.281%)	1.85 ± 0.160 (0.139%)	2.81 ± 0.286 (0.211%)	1.61 ± 0.0988 (0.121%)

The energy resolutions of the individual channels do not accurately portray the overall energy resolution of the system, because they do not account for effects related to the event reconstruction process. A better indicator is the energy resolution as determined by reconstructed events as these events are the ultimate inputs for image reconstruction. Figure 4.19 shows an energy spectrum from both single- and double-interaction events from the same same multi-source measurement displayed in Figure 4.16. Note the ratio of single- to double-interaction events grows smaller with increasing photon energy. This should be expected as high-energy photons are more likely to induce scattering events.

Table 4.4 displays the energy resolution as determined by single and double-interaction events. Compared to single-interaction events, those of double-interaction have degraded

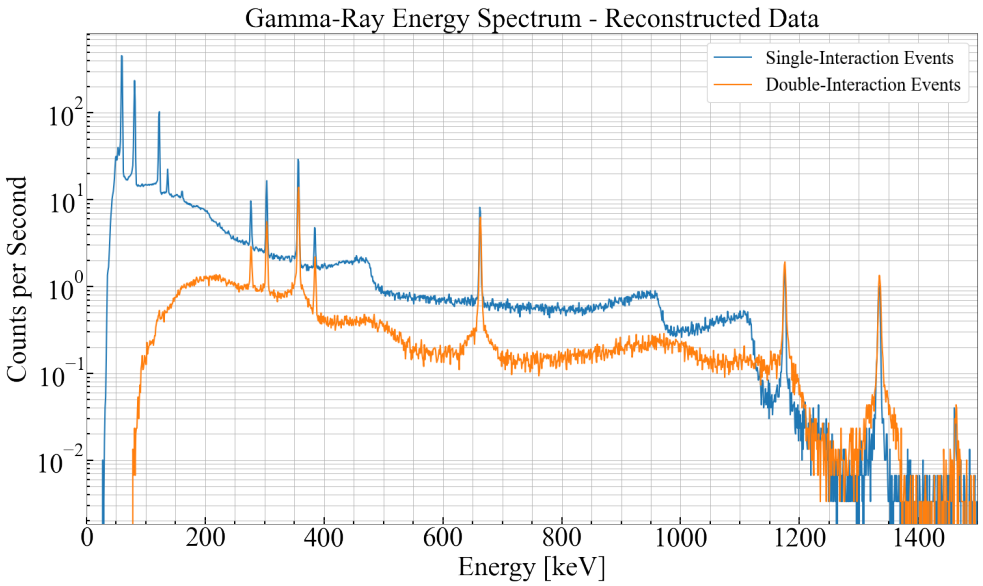

Figure 4.19: Energy spectrum from both single- and double-interaction events produced after a 5-minute multi-source measurement with the Dual-Modality Imager.

energy resolution due to the added uncertainty associated with the second energy deposition. While this additional uncertainty can worsen the ability of the imager to distinguish gamma-ray energies, it does not necessarily impact the angular resolution of the Compton imager. If the incident photon energy is known, then Equation 3.75 states that only the uncertainty in the first energy deposition will propagate to the angular uncertainty in the Compton cone. For this reason, single-interaction events are a better measure of the energy uncertainty that contributes to the Compton angular resolution.

4.5.1.2 Imaging Sensitivity

Imaging sensitivity is an important performance measure that impacts the time required to image sources of a given strength. Having a high sensitivity is particularly critical to applications that involve weak sources and/or strict time requirements. Unlike in Sections 4.1.2, 4.3.4, and 4.4.3 where the sensitivity is defined as the fraction of total photons emitted that are registered by the detector, here the sensitivity is defined as the fraction of total photons emitted *within the solid angle* (subtended by the front surface area of the front detector) that result in events used in the image reconstruction. This is a more convenient definition of sensitivity as this definition is valid regardless of the source-to-detector distance.

To determine the imaging sensitivity of the Dual-Modality Imager, both simulated and experimental data were acquired from gamma-ray sources of various energies. On the simulation side, the two HPGe detectors were modeled in Geant4. The coded aperture mask was not included in this model. One million photons were simulated at a standoff distance of

Table 4.4: Energy resolution of the Dual-Modality Imager for both single- and double-interaction events. Resolution values are recorded in terms of the FWHM (in keV). The error reflects the uncertainty in the Gaussian model used to fit the peaks. The spectral data was taken from the same measurement displayed in Figure 4.16.

Isotope	Energy (keV)	Single Events	Double Events	
^{241}Am	60	1.85 ± 0.0370 (3.08 %)	–	
^{133}Ba	81	1.98 ± 0.0377 (2.44 %)	–	
^{57}Co	122	1.83 ± 0.0385 (1.50 %)	–	
^{133}Ba	356	2.08 ± 0.0283 (0.583 %)	2.75 ± 0.0519 (0.772 %)	
^{137}Cs	662	2.38 ± 0.0309 (0.359 %)	3.24 ± 0.0726 (0.490 %)	
^{60}Co	1173	3.53 ± 0.0998 (0.301 %)	4.13 ± 0.155 (0.352 %)	
^{60}Co		1333 (0.293 %)	3.90 ± 0.0109 (0.342 %)	4.56 ± 0.193

40 mm in the center of the field-of-view of the imager. Photons were simulated at energies ranging from 10 keV to 1.5 MeV. Using the event selection processes outlined in Sections 4.3.1 and 4.4.1, the total number of coded aperture and Compton events were tallied. The former was divided by a factor of two to account for the 50% open fraction of the mask. The total number of events were then divided by the number of simulated photons in the solid angle of the imager. The result is the imaging sensitivity of the system.

Figure 4.20 shows the imaging sensitivities of the coded aperture and Compton imagers with respect to photon energy as determined by Geant4. According to simulations, the maximum coded aperture sensitivity that can be achieved is about 0.430 at 20 keV, and the maximum Compton sensitivity that can be achieved is about 0.0188 at 200 keV. Of course, in reality, these values should be lower due to losses related to the dead time of the data acquisition system and the event reconstruction process. Regarding the latter, charge loss

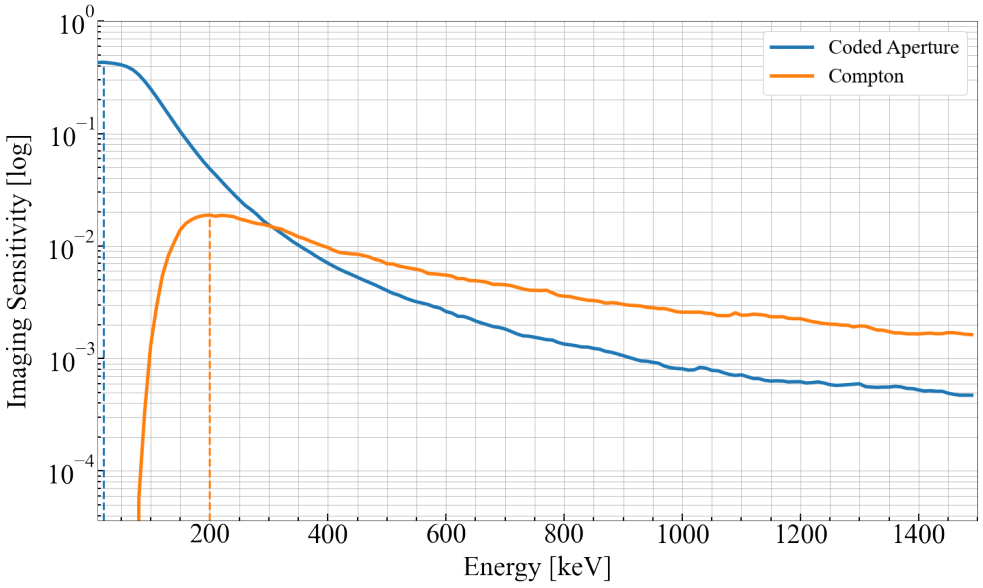

Figure 4.20: Imaging sensitivities of the coded aperture (in blue) and Compton (in orange) imagers with respect to photon energy as determined by simulation. Here imaging sensitivity is defined as the fraction of photons in the solid angle that result in events used in the image reconstruction. Vertical dashed lines indicate the photon energy at which the maximum sensitivity is reached. The maximum coded aperture sensitivity that can be achieved is 0.430 at 20 keV, and the maximum Compton sensitivity that can be achieved is 0.0188 at 200 keV.

can result from interactions that take place in between strips or on dead strips. Furthermore, if multiple interactions occur within a volume smaller than the detector granularity, those interactions cannot be recovered.

For the coded aperture imager, the imaging sensitivity exhibits a downward trend with increasing energy. This should be expected as single-interaction events become less likely[6]. The Compton imager, on the other hand, sees a slight increase in sensitivity up to about 200 keV due to the increased likelihood of scattering. Beyond about 200 keV, the Compton sensitivity gradually decreases as events of higher multiplicity than two become more common[7]. Furthermore, above about 310 keV, the Compton camera exhibits superior performance in sensitivity compared to the coded aperture imager. Of course this threshold will vary depending on the rigor of the event selection process.

[6]In this work, only single-interaction events are considered for coded aperture imaging for reasons discussed in Section 4.3.1.

[7]In this work, only double-interaction events are considered for Compton imaging for reasons discussed in Section 4.4.1.

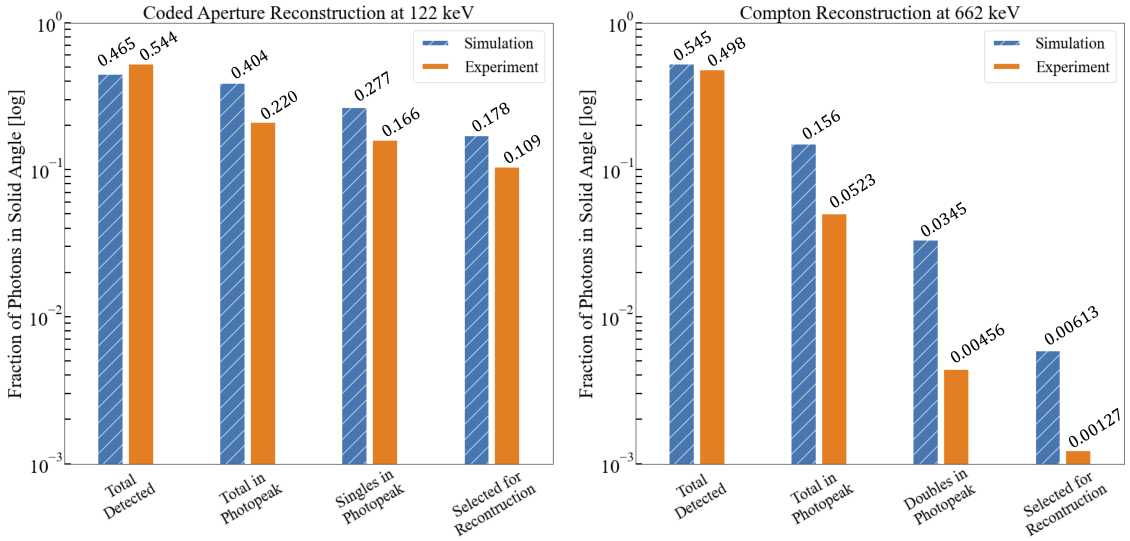

Figure 4.21: Multiple stages of photon selection in the (a) coded aperture and (b) Compton image reconstruction processes as determined by simulation and experimentation. In case (a), a 97 kBq ^{57}Co disk source was positioned at a standoff distance of 180 mm and evaluated at 122 keV. In case (b), a 260 kBq ^{137}Cs disk source was positioned at a standoff distance of 120 mm and evaluated at 662 keV. At the 'Total Detected' stage, environmental background was subtracted. At the 'Total in Photopeak' stage, both environmental and Compton background were subtracted.

The imaging sensitivity of the Dual-Modality Imager was also determined via experimentation using gamma-ray sources with well-defined activities and locations. In the coded aperture mode, a 97 kBq ^{57}Co disk source was positioned in the center of the field-of-view at source-to-detector distance of 180 mm (magnification factor $m = 2$) and was evaluated at 122 keV. Furthermore, in the Compton mode with the mask removed, a 260 kBq ^{137}Cs disk source was positioned in the center of the field-of-view at source-to-detector distance of 120 mm and was evaluated at 662 keV.

Figure 4.21 shows the fraction of photons in the solid angle that were collected at major stages in the (a) coded aperture and (b) Compton image reconstruction processes as determined by simulation and experimentation. The 'Total Detected' stage represents the fraction of photons emitted within the solid angle that are incident on the detector. At this stage, environmental background was subtracted from the experimental data. The 'Total in Photopeak' stage represents the fraction of photons emitted within the solid angle that are in the photopeak of interest. At this stage, both environmental and Compton background were subtracted from the experimental data. The 'Singles in Photopeak' and 'Doubles in Photopeak' stages represent the fraction of photons emitted within the solid angle that result in single- and double-interaction events in the photopeak, respectively. Finally, the 'Selected for Reconstruction' stage represents the fraction of photons emitted within the solid angle

that are selected for image reconstruction based on the coded aperture and Compton event selection criteria in Sections 4.4.1 and 4.4.1, respectively. Note criterion 5 for Compton event selection is excluded from this calculation.

In directly comparing the simulated and experimental sensitivities, the latter are significantly lower. At the 'Total Detected' stage, the experimental sensitivity of the Compton camera is about 9% lower. This should be expected given the dead time of the data acquisition system. Dead time, for the most part, is only significant in the Compton mode for the following reason. The Compton camera generally observes higher count rates due to the absence of an intervening collimator and closer proximity.

It should be noted here that the Dual-Modality Imager has a maximum count rate limit due to a bottleneck in the data acquisition system. This limit varies depending on the radioisotope due to the dependence of signal multiplicity on photon energy. With increased energy, photons induce more scattering events within the detector, and subsequently, fewer counts can be registered. This limit was measured to be around 7000 cps for ^{57}Co and 4000 cps for ^{137}Cs and is often surpassed in the Compton mode. To reduce the count rate, we can increase the source-to-detector distance (at a cost of resolution) and/or add layers of attenuating material between the source and imager.

The gap between the experimental and simulated sensitivities widens at the 'Total in Photopeak' stage. The coded aperture and Compton imagers have experimental sensitivities that are now 46% and 66% lower, respectively. This deviation is related to information loss during the event reconstruction process. Going forward, to mitigate information loss, the granularity of the detectors should be reduced and more advanced signal processing techniques should be applied [95].

The remainder of this section provides an interpretation of the experimental results in Figure 4.21, highlighting the reasons for sensitivity loss at each stage in the image reconstruction process. Table 4.5 summarizes these reasons.

At the 'Total Detected' stage, the coded aperture loses 46% of photons at 122 keV. This loss is unavoidable due to the 50% open fraction of the mask. The Compton camera exhibits a 50% loss at 662 keV, which can be partially explained by photon penetration through the detector. For 30-mm-thick HPGe, there is a 32% transmission probability at 662 keV. The dead time of the acquisition system also plays a role.

At the 'Total in Photopeak' stage, the coded aperture and Compton modalities show 60% and 90% added losses, respectively. In both cases, these losses are best explained by limitations in the event reconstruction process. Another explanation is partial energy deposition followed by escape from the detector.

At the 'Singles in Photopeak' and 'Doubles in Photopeak' stages, the sensitivity is reduced further by imposing a criterion that limits events based on interaction type. In the case of the coded aperture imager, only single-interaction events in the photopeak are considered. The impact is a 25% added loss at 122 keV. The sensitivity of the Compton camera is far more impacted by the interaction-type criterion, which in this case, requires a double-interaction event in the photopeak. At high photon energies, a multitude of interaction scenarios can take place, and by neglecting all possible events, there is a 91% added loss at 662 keV.

Table 4.5: Sensitivities and associated losses at multiple stages in the coded aperture and Compton image reconstruction processes as determined by experimentation and illustrated in Figure 4.21. At the 'Total Detected' stage, environmental background was subtracted. At the 'Total in Photopeak' stage, both environmental and Compton background were subtracted.

Coded Aperture Reconstruction at 122 keV			
Stage	Sensitivity	Added Loss	Reason for Loss
Total Detected	0.544	45.6%	mask open fraction ($\rho = 0.5$)
Total in Photopeak	0.220	59.6%	signal processing, partial energy deposition followed by escape
Singles / Doubles in Photopeak	0.166	24.5%	photon scatter
Selected for Reconstruction	0.109	34.3%	criterion 3 (Section 4.3.1)

Compton Reconstruction at 662 keV			
Stage	Sensitivity	Added Loss	Reason for Loss
Total Detected	0.498	50.2%	photon escape, detector dead time
Total in Photopeak	0.0523	89.5%	signal processing, partial energy deposition followed by escape
Singles / Doubles in Photopeak	0.00456	91.2%	photoelectric absorption, multiple photon scatter
Selected for Reconstruction	0.00127	72.1%	criterion 3 & 4 (Section 4.4.1)

The final restrictions imposed on sensitivity are enforced to improve image quality. To be selected for coded aperture reconstruction at the 'Selected for Reconstruction' stage, single-interaction events in the photopeak must occur within the top 6-mm layer of the detector. With this requirement, there is a 34% added loss in events at 122 keV. To be selected for Compton image reconstruction, double-interaction events in the photopeak must have a lever arm greater than 14 mm and an opening angle in the range $-0.4 < cos\theta < 1$. These criteria result in an additional 72% loss of events at 662 keV. Given all of the above restrictions, the Dual-Modality Imager exhibits sensitivities on the order of 10^{-1} at 122 keV and 10^{-3} at 662 keV in the coded aperture and Compton modes, respectively.

4.5.2 Coded Aperture Imaging Performance

As previously discussed in Section 3.5.3, the resolution of a coded aperture imager is governed by both the detector and aperture designs and depends strongly on magnification. Given a fixed imager design, the resolution improves by increasing the magnification factor m as defined in Equation 3.53. This objective can be realized by decreasing the source-to-mask distance a and/or increasing the mask-to-detector distance b. To demonstrate this, a ^{57}Co disc source with a 2-mm diameter was imaged at two magnifications: $m = 1.5$ and $m = 2$. In both cases, the source was positioned near the center of the field-of-view at a mask-to-detector distance of $b = 90$ mm. Using the event selection criteria in Section 4.3.1, back-projected images were generated from Equation 4.71 with the number of iterations set to $k = 1$.

Figure 4.22 shows the back-projections of the source at $m = 1.5$ and $m = 2$ as well as their respective linear cross-sections (parallel to the x-axis). The cross sections were taken at the highest intensity image voxel and were fitted with a 1-D Gaussian model. The FWHM of the Gaussian gives an estimate of the resolution and was found to be 6.89 mm at $m = 1.5$ and 4.60 mm at $m = 2$. Note these values do not account for the extent of the source. To better estimate the resolution, the diameter L of the source can be deconvolved in the following manner:

$$\delta r_{ca} \approx 2.36\sqrt{\sigma_{gauss}^2 - [(K)(L)]^2} \quad . \tag{4.95}$$

The above correction represents a 1-D deconvolution, where σ_{gauss} is the standard deviation of the 1-D Gaussian fit and K is a constant that depends on the source shape, e.g. $K = \sqrt{3}/6$ for a disc and $K = \sqrt{5}/10$ for a sphere. Applying the 1-D deconvolution in the case of the 2-mm disc source, the resolution is about 6.77 mm at $m = 1.5$ and 4.40 mm at $m = 2$. According to Equation 3.58, the resolution theoretically should be about 7.21 mm at $m = 1.5$ and 4.47 mm at $m = 2$; these values are consistent with those determined via experimentation.

In reality, the event selection process impacts the resolution of a coded aperture imager as well. As previously discussed in Section 4.3.2, spatial errors can be introduced by photons that hit the detector at oblique angles of incidence and interact at distances sufficiently far

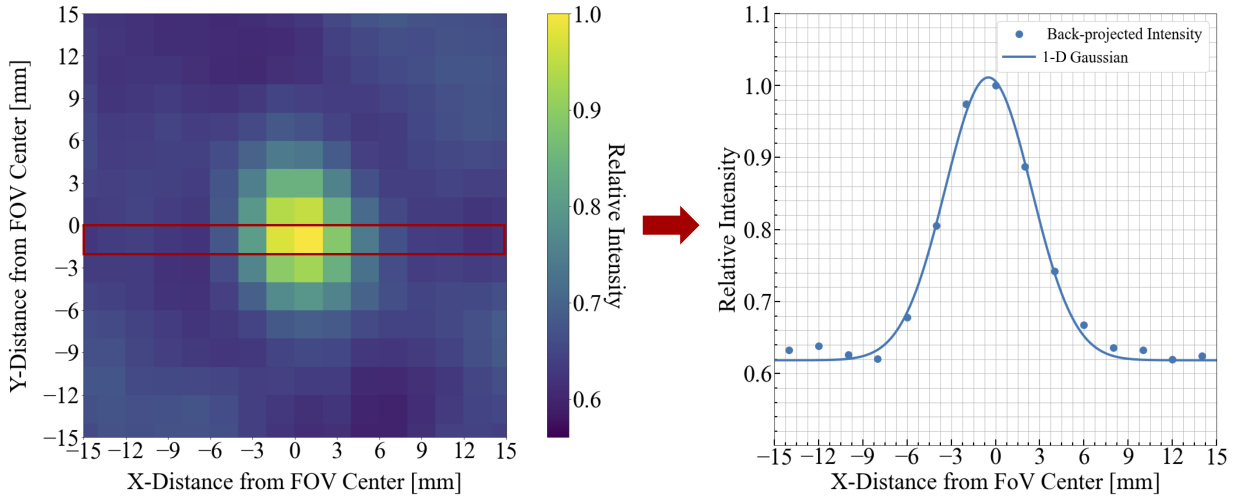

(a) $m = 1.5$

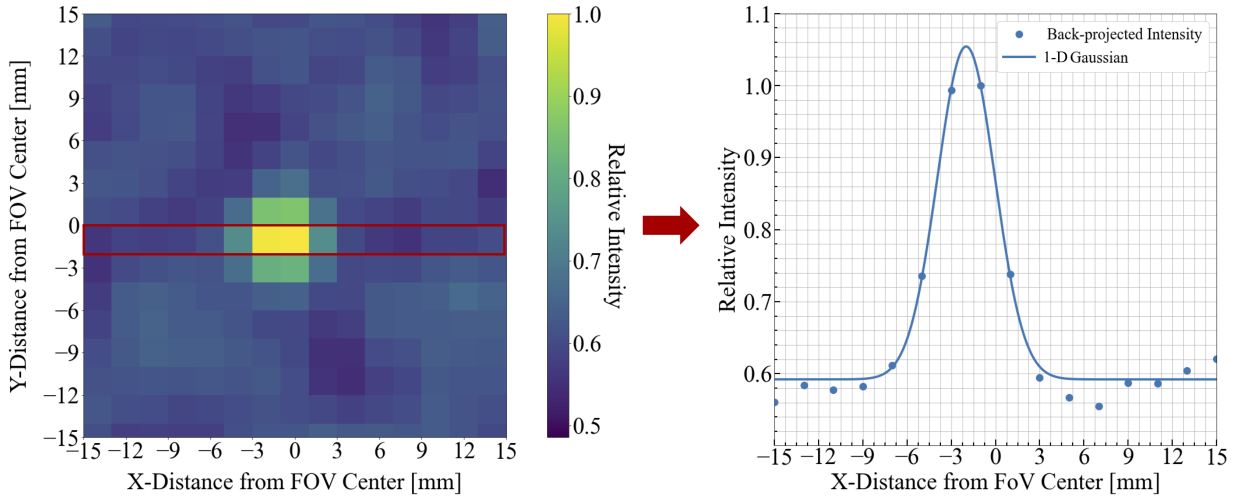

(b) $m = 2$

Figure 4.22: Back-projections a ^{57}Co disk source at a magnification of (a) $m = 1.5$ and (b) $m = 2$ in the coded aperture mode. The left shows a 2-D (x, y) slice of the back-projected image. The red box outlines the linear cross section (parallel to the x-axis) at the highest intensity image voxel. The right shows the same linear cross-section fitted with a 1-D Gaussian model. The FWHM of the Gaussian was found to be 6.9 mm at $m = 1.5$ and 4.6 mm at $m = 2$.

from the detector surface. To combat this, this work only select events that take place within a finite depth from the surface. This depth threshold varies based on the mask-to-detector distance b, and in the case of the Dual-Modality Imager, ranges from 3 mm to 6 mm for $50 \leq b \leq 90$ mm.

To demonstrate the impact of depth-of-interaction on resolution, a ^{57}Co disc source was imaged both on- and off-axis. For both measurements, the source was positioned at a mask-to-detector distance of $b = 90$ mm and a magnification of $m = 2$. Back-projected images were then generated using detector responses that (1) considered the depth-of-interaction and (2) did not. In case (1), only single-interaction events within 6 mm from the detector surface were considered, and in case (2), all single-interaction events within the detector volume were considered. In both cases, only single-interaction events that fell within the specified ROI were selected.

Figure 4.23 shows the linear cross-sections of the back-projections with and without the depth-of-interaction criterion. A 1-D Gaussian model was fit to each distribution to provide an estimate of the resolution in FWHM. In the cases of both the on- and off-axis sources, the width of the distribution narrows by accounting for the depth-of-interaction. This indicates improved resolution. For the on-axis source, the improvement is subtle. The FWHMs are 4.60 mm and 4.61 mm with and without the depth-of-interaction criterion, respectively. For the off-axis source, the improvement is more significant, because photons are hitting the detector at more oblique angles of incidence. The FWHMs are 4.74 mm and 5.40 mm with and without the criterion, respectively.

In theory, by accounting for the depth-of-interaction, the back-projections of the on- and off-axis sources should have equivalent resolutions. However, here the off-axis source shows slightly more blurring with a FWHM of 4.74 mm compared to 4.60 mm for the on-axis source. This should be expected given that the detector has a finite resolution in depth. Because off-axis sources have more oblique angles of incidence, the depth resolution of the detector has a larger impact in such cases.

4.5.3 Compton Imaging Performance

The lateral resolution δr_{ci} of a Compton imager in FWHM can be defined as:

$$\delta r_{ci} \approx (2z) \tan\left(\frac{\delta\theta}{2}\right) \tag{4.96}$$

where z can be approximated as the normal distance between the source and the detector surface that faces the source and $\delta\theta$ is the angular resolution. In Compton imaging, as previously discussed in Section 3.6.2, the angular resolution is determined by uncertainties in the energy depositions and positions of interaction. The former uncertainty is governed by Doppler broadening and the finite energy resolution of the detectors, while the latter uncertainty is governed by the finite position resolution of the detectors.

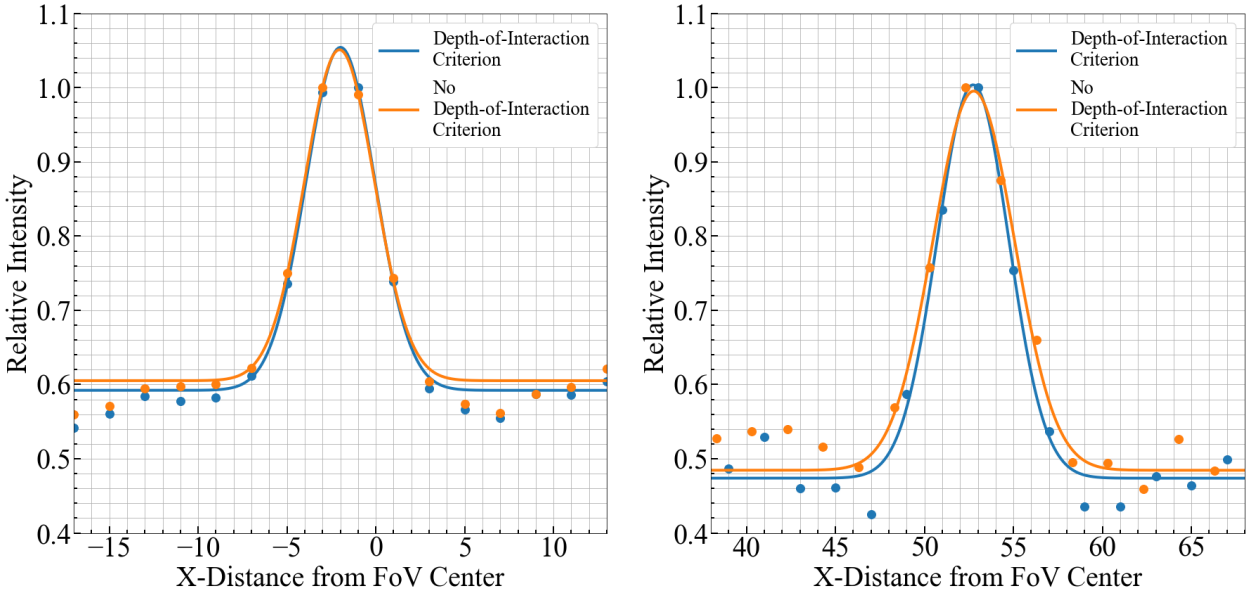

(a) On-Axis (b) Off-Axis

Figure 4.23: Linear cross-sections of back-projections of a ^{57}Co disk source positioned (a) on-axis and (b) off-axis at a lateral x-distance of about 55 mm from the center of the FOV. Both (a) and (b) were positioned at a fixed mask-to-detector distance of $b = 90$ mm and a magnification of $m = 2$. The back-projections were generated from detector responses that (1) considered the depth-of-interaction (in blue) and (2) did not (in orange).

The most straightforward approach in determining the Compton angular resolution is to measure the FWHM of the angular resolution metric (ARM) distribution. The ARM metric can be defined as the angular separation between the Compton cone and known source location. ARM distributions were generated from Geant4 simulations. The two HPGe detectors were modeled to have a geometry and resolution (in position and energy) that matched those of the Dual-Modality Imager. One million photons were simulated from an on-axis point source located at a distance of 40 mm from the surface of the front detector. This simulation was performed at six different photon energies: $E_\gamma = 122,\ 218,\ 440,\ 662,\ 1001,$ and 1408 keV.

Figure 4.24 shows the ARM distributions at the various photon energies. For each energy, multiple ARM distributions were generated based on different event selection criteria: (1) all double-interaction events, (2) only double-interaction events with a scattering angle θ in the range $-0.4 < cos\theta < 1$, (3) only double-interaction events with a lever arm greater than 14 mm, and (4) only double-interaction events that meet both criteria 2 and 3. A 1-D Lorentzian model was fit to each distribution to provide an estimate of the angular resolution in FWHM. Note as the selection criteria becomes more strict, the width of the distribution

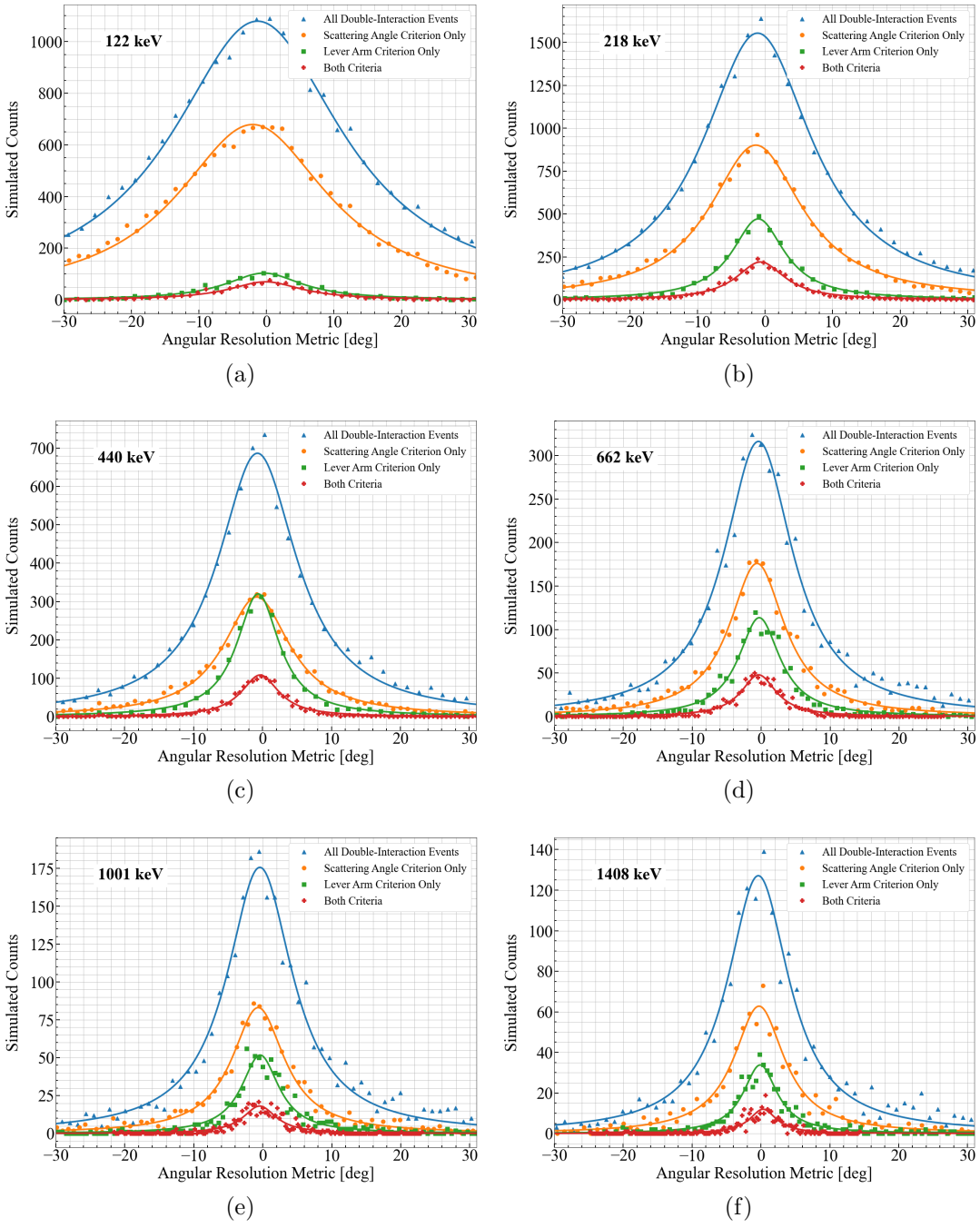

Figure 4.24: ARM distributions as determined by simulation. 1 million photons were simulated at (a) 122 keV, (b) 218 keV, (c) 440 keV, (d) 662 keV, (e) 1001 keV, and (f) 1408 keV for an on-axis point source at a distance of 40 mm from the surface of the front detector. The ARM distributions were generated for different event selection criteria: (1) all double-interaction events (in blue), (2) double-interaction events with a scattering angle θ in the range $-0.4 < cos\theta < 1$ (in orange), (3) double-interaction events with a lever arm greater than 14 mm (in green), and (4) double-interaction events that meet both criteria 2 and 3 (in red).

Table 4.6: Tradeoff between angular resolution (in FWHM) and imaging sensitivity (ϵ) at various photon energies given different event selection criteria. The angular resolution and sensitivities were determined from the the ARM distributions in Figure 4.24.

	All Doubles Events		Scattering Angle Criterion Only		Lever Arm Criterion Only		Both Criteria	
E [keV]	FWHM	ϵ	FWHM	ϵ	FWHM	ϵ	FWHM	ϵ
122	31.0°	0.131	27.5°	0.0996	13.8°	0.00661	13.1°	0.00607
218	19.8°	0.128	16.8°	0.0891	9.48°	0.0228	8.81°	0.0188
440	14.2°	0.0473	11.7°	0.0291	7.52°	0.0124	6.69°	0.00865
662	12.2°	0.0262	9.86°	0.0147	7.32°	0.00771	6.17°	0.00493
1001	11.6°	0.0153	9.42°	0.00801	6.52°	0.00471	5.84°	0.00265
1408	10.9°	0.00991	8.92°	0.00486	6.01°	0.00312	4.78°	0.00168

narrows. This indicates improved angular resolution. However, with more restrictions in place, there is also a loss in sensitivity as shown by the smaller peak amplitude.

Table 4.6 summarizes the tradeoff between angular resolution and imaging sensitivity at the various photon energies. The angular resolution was determined from the FWHM of the ARM distributions in Figure 4.24. The imaging sensitivity was computed as the fraction of simulated photons within the solid angle of the Compton camera that meet the given event selection criterion. If all event selection criteria are imposed, the angular resolutions that can be achieved are FWHM = 13.1°, 8.81°, 6.69°, 6.17°, 5.84°, and 4.78° at $E_\gamma = 122,\ 218,\ 440,\ 662,\ 1001$, and 1408 keV, respectively. The improvement in resolution with increased energy should be expected. At higher energies, both Doppler broadening and energy resolution have a smaller impact, and photons produce longer lever arms due to a greater penetrative power. All of the above contribute to a more accurate Compton cone [108].

To validate the simulations, ARM distributions were generated via experimentation. Compton events were acquired from ^{137}Cs (662 keV) and ^{152}Eu (1408 keV) disc sources. Each source was positioned at a distance of 200 mm from the surface of the front detector of the Dual-Modality Imager. The standoff distance was selected to be large so that the source appeared point-like to the imager. Figure 4.25 shows the ARM distributions for each source. These distributions were generated from double-interaction events that met both the scattering angle and lever arm criteria laid out in Section 4.4.1. The FWHMs of the ^{137}Cs and ^{152}Eu ARM distributions were measured to be 5.72° and 4.95°, respectively; these values are consistent with those determined via simulation.

According to Equation 4.96, angular errors are magnified by the source-to-detector distance z. For this reason, we want to position the source as close as possible to the detector;

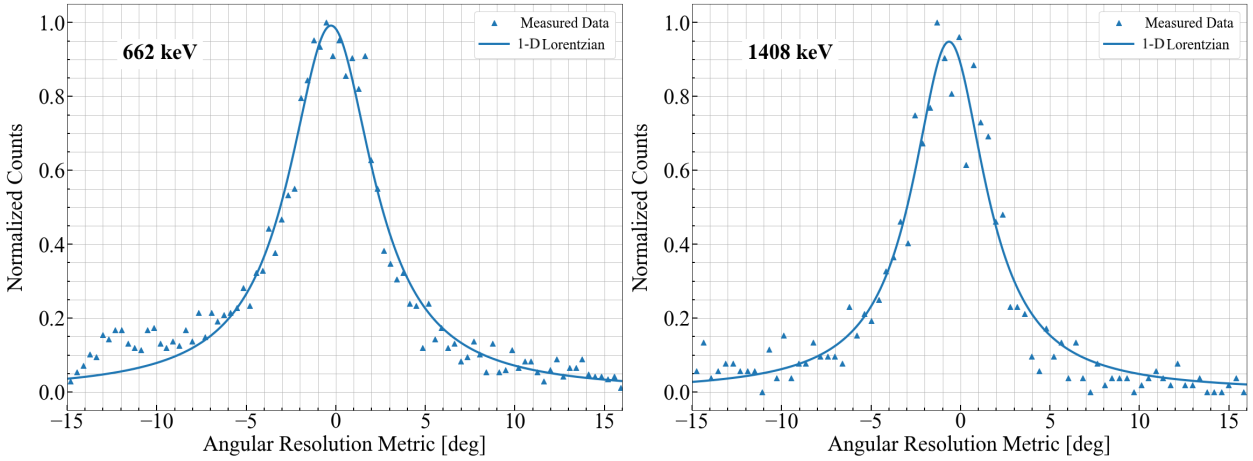

Figure 4.25: ARM distributions for (a) ^{137}Cs (662-keV) and (b) ^{152}Eu (1408-keV) disk sources at a distance of 200 mm from the surface of the front detector of the Dual-Modality Imager. The distributions were generated from Compton events that met criteria 1-4 laid out in Section 4.4.1. A 1-D Lorentzian model was fit to each distribution to provide an estimate of the angular resolution in FWHM. The FWHMs of the ^{137}Cs and ^{152}Eu ARM distributions were measured to be $FWHM = 5.72°$, and $4.95°$, respectively.

this is also advantageous from a sensitivity standpoint. The minimum standoff distance in the Compton mode (with the source positioned directly on top of the detector cryostat) is $z = 20$ mm. At this distance, the Compton camera should achieve a lateral resolution of about 2.0 mm in FWHM at 662 keV.

Chapter 5

Results of Dual-Modality Imaging

Chapter 5 demonstrates the broad imaging capabilities of the Dual-Modality Imager in the near field. Section 5.1 discusses the use of coded aperture and Compton imaging in the context of nuclear safeguards, namely for the visualization of uranium holdup, and provides 3-D images of highly-enriched uranium (HEU), ^{57}Co, and ^{137}Cs sources with varying shapes. Section 5.2 proposes the use of coded aperture and Compton imaging in the preclinical evaluation of ^{225}Ac-based radiopharmaceuticals for TAT and presents image reconstructions and quantification estimates of ^{225}Ac agents in tumor-bearing mice.

5.1 Nuclear Safeguards

Safeguarding special nuclear materials (SNM) in processing facilities through materials accounting and control is essential to the health and safety of the workers and public as well as in the prevention of SNM diversion. One of the more insidious problems of material accounting is holdup or hidden deposits of nuclear materials within process equipment. Holdup of highly enriched uranium (HEU) - a core component of nuclear power generation and nuclear weapons - evokes considerable concern as only a small difficult-to-detect mass of HEU is necessary to create a catastrophic event.

There are three naturally occurring isotopes of uranium: ^{234}U, ^{235}U, and ^{238}U. The composition of natural uranium by mass is 0.0054% ^{234}U, 0.7% ^{235}U, and 99.3% ^{238}U. Enriched uranium refers to uranium whose ^{235}U content has been increased above that found in natural uranium, e.g. via gaseous diffusion or centrifugation. For a nuclear weapon, uranium must be enriched to approximately 93% ^{235}U. This is known as weapons grade uranium (WGU). It may also be referred to as HEU, which is uranium enriched to more than 20% ^{235}U.

The key signature of uranium is gamma rays. Uranium-235 emits a 186-keV gamma ray with a branching ratio of 57.2%. Furthermore, a 1001-keV emission arises from ^{234m}Pa, the granddaughter of ^{238}U, with a branching ratio of 0.834%. Given these emissions, gamma-ray spectroscopy is often employed to estimate holdup activities. One of the most conventional spectroscopic methods is based on the Generalized Geometry Holdup (GGH) model [127].

This model simplifies deposit shapes as being either a point, a line (e.g. in a pipe) or an area source to provide quantitative estimates. However, the shapes and sizes of holdup deposits can vary significantly, and the bias introduced by the GGH model can lead to material loss.

Gamma-ray imaging can be applied to solve this problem by offering the exciting possibility of both visualizing and quantifying uranium holdup. This work proposes coded aperture and Compton imaging as complementary modalities with the former suited to the 186-keV emission line of ^{235}U and the latter suited to the 1001-keV of ^{238}U. In the following sections, the Dual-Modality Imager is employed to image HEU and radioisotopes with similar gamma-ray signatures to ^{235}U and ^{238}U. These sources have varying shapes to mimic the diversity of HEU deposits in processing facilities. Other studies have performed similar measurements using a dual-modality approach [25, 128]. The key distinction is that the Dual-Modality Imager is operated in the near field. Operating in this regime enables both maximum sensitivity and spatial resolution and the possibility of 3-D imaging. All of the above can enable more accurate quantification with fewer assumptions, e.g. about self-attenuation.

It should be noted here that all of the coded aperture images presented in this section were produced from eight different perspectives via rotation of the source. The Compton images, however, were generated from a single viewing angle. In the Compton mode, for the sources to have been rotated and observed at multiple angles, a larger standoff distance would have been required; and subsequently, the overall image resolution would have suffered. Furthermore, all of the images were visualized using a visualization application known as ParaView [129] and are displayed as either cross-sections or volume renderings in which the opacity of each image voxel scales proportionally with its intensity. The coordinate systems of the images are independent of that of the imager.

5.1.1 Highly Enriched Uranium Pellets

An HEU source was imaged in both the coded aperture and Compton modes. The source consisted of twelve uranium dioxide pellets, each with a ^{235}U enrichment of 43% and a net weight of 12.3 g. The pellets were stacked in a hard-walled plastic pigtail molded into a C-shape. Figure 5.1a shows a coronal CT image of the source. Note the asymmetry of the pellet distribution.

The count rate was measured along the length of the source to serve as the ground truth of its activity distribution. This measurement was performed by employing a makeshift lead-brick collimator with a 5-mm-wide slit. The collimator was positioned in front of the detectors with the coded aperture removed. The pigtail was extended into a straight line and positioned on top of the collimator wall furthest away from the detectors. The source was then slid across the collimator opening in 5-mm increments. For each incremental section of the pigtail exposed to the detector, the count rate was acquired at the 186-keV emission line of ^{235}U. Figure 5.1b displays the count rate profile of the source, which, for all practical purposes, exhibits a uniform activity distribution.

Figure 5.2a shows the setup of the HEU source in the coded aperture mode. The source was centrally positioned on top of a rotating mount. The rotation axis was located at a

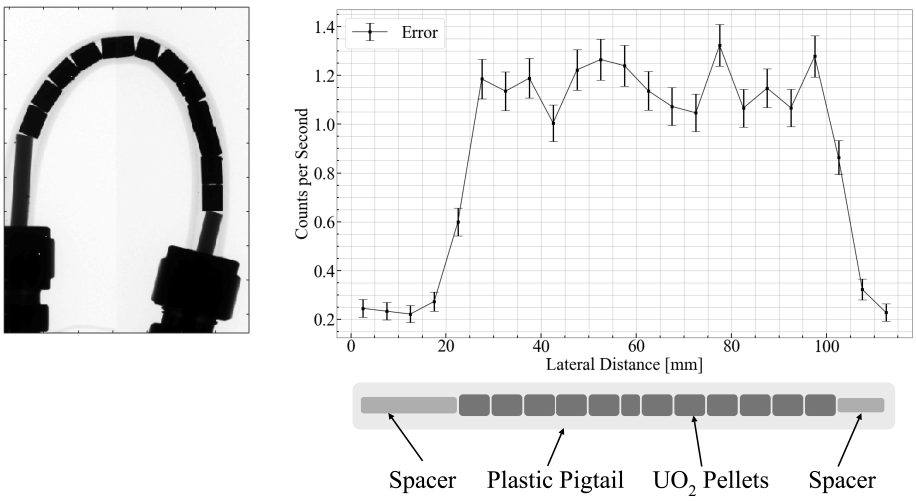

(a) (b)

Figure 5.1: (a) Coronal CT image of the HEU source. Note the asymmetry of the pellet distribution. (b) Count rate profile of the HEU source (in an extended position) at the 186-keV emission line of ^{235}U.

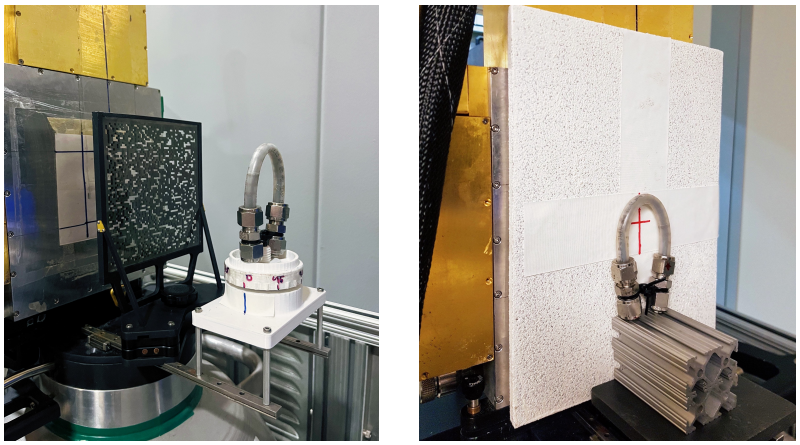

(a) Coded Aperture Setup (b) Compton Setup

Figure 5.2: Experimental setup of the HEU source in the (a) coded aperture mode at a source-to-detector distance of 205 mm with a mask-to-detector distance of 90 mm and (b) Compton mode at a source-to-detector distance of 30 mm. In setup (a), coded aperture data was acquired at 8 viewing angles in 45° increments. In setup (b), Compton data was acquired at a single viewing angle.

distance of 115 mm from the mask with the mask positioned at a distance of 90 mm from the detector (magnification factor $m = 1.8$). In this configuration, the resolution of the coded aperture imager theoretically should be about $\delta r_{ca} \approx 5.2$ mm in FWHM. The mount was rotated in 45° increments, and at each viewing angle, coded aperture data was acquired for 20 minutes at the 186-keV emission line of ^{235}U. It should be noted here that self-attenuation can be significant with HEU sources, particularly at 186 keV, and the attenuation will vary with each rotation. For all of the sources presented in this work, however, we do not correct for self-attenuation or any other attenuation factors outside of the imager.

Figure 5.2b shows the setup of the HEU source in the Compton mode. The center of the source was positioned at a standoff distance of 30 mm from the surface of the front detector. In this configuration, the resolution of the Compton imager theoretically should be about $\delta r_{ci} \approx 3.1$ mm in FWHM at 1001 keV. A 5-mm-thick lead slab was situated in between the detector and source to reduce the gross count rate below the maximum allowable limit. With the source in a fixed position, Compton data was acquired for 3.5 days. A long measurement time was needed to provide sufficient statistics to image the 1001-keV emission line.

Using ML-EM with TV and Tikhonov regularization as described in Sections 4.3.4 and 4.4.3, the HEU source was reconstructed in 3-D from the coded aperture and Compton data at the 186-keV emission line of ^{235}U and 1001-keV emission line of ^{238}U, respectively. The coded aperture and Compton images were generated from eight and one viewing angles, respectively, each after 100 iterations. Figure 5.3 shows the volume renderings. Furthermore, Figure 5.4 shows (x, y) coronal slices of the coded aperture and Compton images, each fused with the coronal CT image of the source. The CT image was acquired separately from the gamma-ray images with the orientation of the source differing between measurements; thus, the image co-registration is not precise.

Both the coded aperture and Compton images in Figure 5.4 closely align with the CT image and show a uniform intensity distribution as would be expected given the ground truth in Figure 5.1. That said, the uniformity is biased based on the total variation parameter η in the ML-EM algorithm. Also note that the coded aperture and Compton images show slightly different distributions despite the same source being imaged. This variation can be best explained by the distinct resolution profiles of the two modalities.

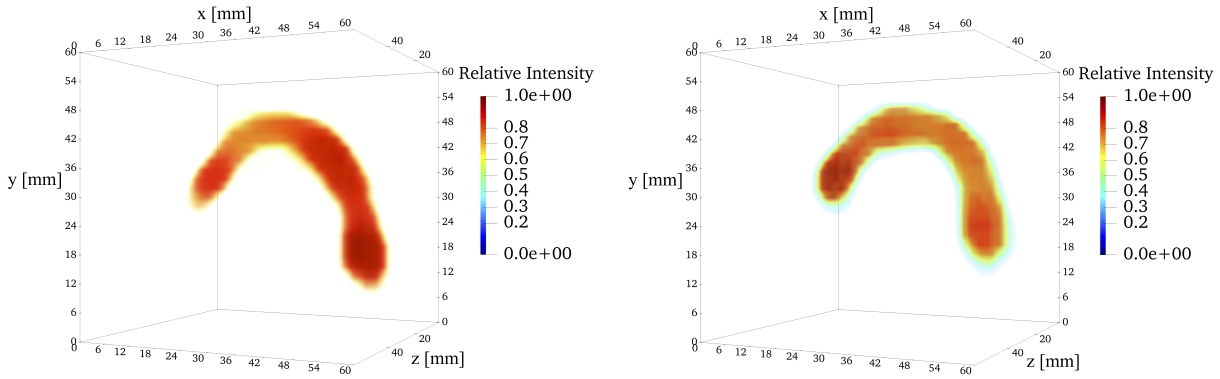

(a) 3-D Coded Aperture (b) 3-D Compton

Figure 5.3: Volume renderings of the (a) coded aperture image of the HEU pigtail at the 186-keV emission line of ^{235}U after 100 iterations with $\epsilon = 0.05$ and $\eta = 0.03$ and (b) Compton image of the HEU pigtail at the 1001-keV emission line of ^{238}U after 100 iterations with $\epsilon = 0.1$ and $\eta = 0.02$. Image (a) was generated from eight viewing angles, and image (b) was generated from a single viewing angle. For better visibility, both images (a) and (b) were 'zoomed-in' and low intensity voxels were suppressed.

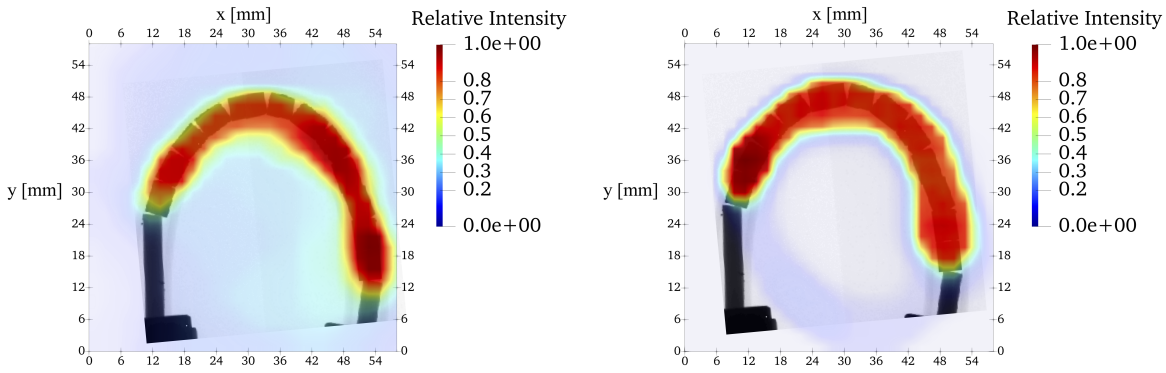

(a) 2-D Coded Aperture + CT (b) 2-D Compton + CT

Figure 5.4: Coronal (x, y) slices of the (a) coded aperture and (b) Compton images of the HEU pigtail, each fused with a CT coronal image. For better visibility, both images (a) and (b) were 'zoomed-in'.

5.1.2 Cobalt-57 Flexible Line Source

Acquiring and working with HEU in practice can be challenging due to proliferation concerns. In testing the coded aperture and Compton modalities, good substitutes for the 186-keV and 1001-keV emission lines are the 122-keV and 662-keV emission lines of ^{57}Co and ^{137}Cs,

respectively. These radioisotopes are readily accessible and available in a variety of shapes, sizes, and activities.

A 850 kBq ^{57}Co flexible line source was imaged in the coded aperture mode. Figure 5.5a shows the experimental setup. The source had a uniform active length and diameter of 500 mm and 0.8 mm, respectively, and was shaped in a spiral fashion around a polyethylene rod with a diameter of 25 mm. The rod was centrally positioned on top of a rotating mount. The rotation axis was located at a distance of 115 mm from the mask with the mask positioned at a distance of 90 mm from the detector (magnification factor $m = 1.8$). In this configuration, the resolution of the coded aperture imager theoretically should be about $\delta r_{ca} \approx 5.2$ mm in FWHM. The mount was rotated in 45° increments, and at each viewing angle, coded aperture data was acquired for 15 minutes.

Using ML-EM with TV and Tikhonov regularization, the ^{57}Co source was reconstructed in 3-D from the eight projection angles at the 122-keV emission line after 100 iterations. Figures 5.5b and c show the front and top views of the volume rendering, respectively. This image demonstrates the ability of the coded aperture to image sources distributed extensively in a volume as opposed to those that are distributed more or less within a single plane.

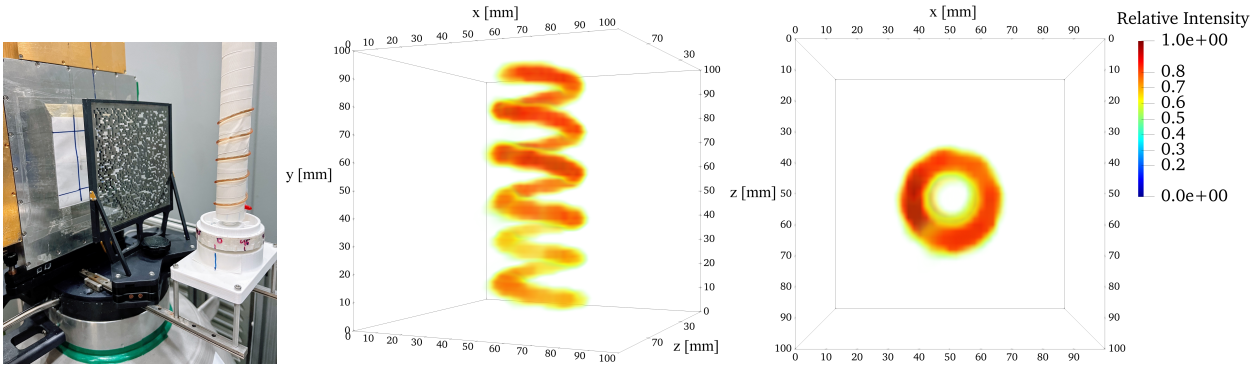

(a) Coded Aperture Setup (b) 3-D Front View (c) 3-D Top View

Figure 5.5: (a) Experimental setup of the ^{57}Co flexible line source in the coded aperture mode. (b) Front and (c) top views of the volume rendering of the coded aperture image. The image was generated from eight viewing angles at the 122-keV emission line after 100 iterations with $\epsilon = 0.05$ and $\eta = 0.02$. For better visibility, images (b) and (c) were 'zoomed-in' and low intensity voxels were suppressed.

5.1.3 Cesium-137 Rigid Line Source

A 270 kBq ^{137}Cs rigid line source was imaged in the Compton mode. Figure 5.6a shows the experimental setup. The line source had a uniform active length and diameter of 40 mm and

1 mm, respectively, and was positioned in a diagonal fashion at a distance of 40 mm from the surface of the front detector. In this configuration, the resolution of the Compton imager theoretically should be about $\delta r_{ci} \approx 4.3$ mm in FWHM at 662 keV. A 20-mm-thick Ecomass brick was situated in between the source and imager to reduce the count rate. With the source in a fixed position, Compton data was acquired for 55 minutes.

The ^{137}Cs source was reconstructed in 3-D from the single projection at the 662-keV emission line after 100 iterations using two different formulations of the ML-EM algorithm: (1) ML-EM with Tikhonov regularization only and (2) ML-EM with both TV and Tikhonov regularization. Figure 5.6b shows a coronal (x, y) slice of the image using method (1), and Figure 5.6c shows the same slice using method (2). Images (b) and (c) are on the same relative intensity scale with respect to the highest intensity voxel in image (b).

Both the (b) ML-EM + Tikhonov and (c) ML-EM + TV + Tikhonov images show a similarly-sized line source with an extent of about 41 mm; this is consistent with the 40-mm active length. Furthermore, the difference in the sum total of intensity between the two images is small, on the order of 1%. The key distinction is that the (b) ML-EM + TV + Tikhonov image better reflects the uniformity of the line source as the TV penalty function by design suppresses variation; but this comes at the expense of resolution.

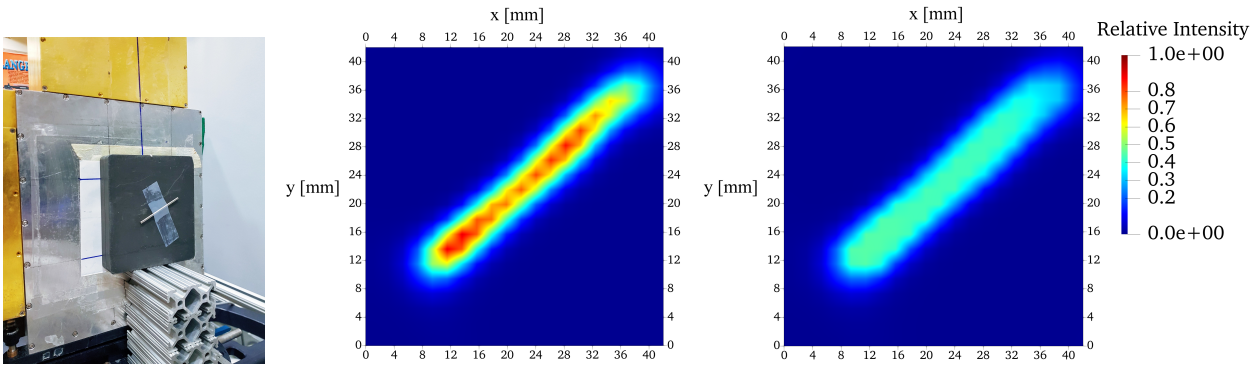

(a) Compton Setup (b) ML-EM + Tikhonov (c) ML-EM + TV + Tikhonov

Figure 5.6: (a) Experimental setup of the ^{137}Cs rigid line source in the Compton mode. Coronal (x, y) slices of the Compton image using (b) ML-EM with Tikhonov regularization only with $\epsilon = 0.1$ and $\eta = 0$ and (c) ML-EM with TV and Tikhonov regularization with $\epsilon = 0.1$ and $\eta = 0.02$. Each image was generated in 3-D from one viewing angle at the 662-keV emission line after 100 iterations. Images (b) and (c) are on the same relative intensity scale with respect to the highest intensity voxel in image (b), and both were 'zoomed-in' for better visibility. The difference in the sum total of intensity between the two images is on the order of 1%.

5.1.4 Discussion

The results presented in this section demonstrate the feasibility of using coded aperture and Compton imaging for visualizing holdup accumulations, but more importantly, show the broad imaging capabilities of the Dual-Modality Imager. The imaging system resolved morphological features of gamma-ray sources of various shapes, including C-shaped, spiral, and line, and energies in the range of 122 keV to 1 MeV in the near field.

Three-dimensional coded aperture and Compton images of an HEU source were produced via the 186-keV emission line of ^{235}U and 1001-keV emission line of ^{238}U, respectively. These images are of growing interest to nuclear safeguards. The ability to observe both the 186-keV and 1001-keV emission lines can be of great use in visualizing and quantifying holdup at processing facilities. That said, the images in this section give no indication of the source activity as they were shown on a relative intensity scale. More work needs to be done on developing a comprehensive approach for quantifying activities and estimating the associated uncertainties.

Currently, one of the more challenging aspects of holdup quantification is correcting for self-attenuation and attenuation through process equipment. Previous studies have provided preliminary quantification estimates of holdup via coded aperture and Compton imaging in the far field [25, 128]. However, in correcting for self-attenuation, these works rely on assumptions about the source thickness. Here, if quantification were pursued, such assumptions would not be necessary as near-field operation enables visualization of the source thickness.

Going forward, a specialized imager should be built with greater mobility to be practical for safeguards applications. While the current system is mobile via a cart-based platform, handheld operation is ideal as it enables up-close imaging of less accessible sites within a nuclear facility. The bulkiness of the system can be dramatically reduced by replacing the HPGe detectors with ones that do not require cooling. Detectors based on CZT are a good option, because they operate at room temperature and provide both high sensitivity and suitable energy resolution.

5.2 Targeted Alpha-Particle Therapy

Targeted delivery of alpha-particle-emitting radioisotopes has great potential as a cancer therapy. The short range and high linear energy transfer (LET) of alpha particles enables highly-selective and effective killing of tumors while sparing normal tissues [37, 130, 131]. In theory, the efficacy of the delivered dose can be enhanced further by employing radioisotopes with decay progeny that also emit alpha particles. One of the more attractive so-called nanogenerators that has been proposed is ^{225}Ac [52, 51, 69, 70, 132, 133]. As mentioned previously in Section 2.2, ^{225}Ac is a relatively long-lived radiometal with a half-life $t_{1/2}$ of 10 days and decays via a sequence of six short-lived daughters to stable ^{209}Bi. The predominant decay pathway of ^{225}Ac yields four alpha particles with contributions from the daughters ^{221}Fr ($t_{1/2} = 4.90$ min), ^{213}Bi ($t_{1/2} = 45.6$ min), and ^{213}Po ($t_{1/2} = 4.2$ μs).

Despite great promise, the development of ^{225}Ac-based therapies has been hampered, because there has been no effective means to study the daughter redistribution [134, 135]. Alpha-particle-emitting daughters, once formed, can possibly break free from the chelator of the radiopharmaceutical due to a high recoil energy and different chemical properties. If the daughters are generated and retained inside the cancerous cells after internationalization, they can greatly contribute to the cytotoxic effect. Otherwise, free daughters, produced either on the surface of the target cell or during circulation of the radiopharmaceutical, can diffuse or be transported to various healthy organs; thereby resulting in unwanted toxicity. In the case of ^{225}Ac, the redistribution of its longer-lived daughters, namely ^{221}Fr and ^{213}Bi, evokes the most concern.

Conveniently, ^{221}Fr emits a 218-keV gamma ray with a branching ratio of 11.6%, and ^{213}Bi emits a 440-keV gamma ray with a branching ratio of 26.1%. The ability to image the daughters via these emissions would be a boon for the development of TAT. In nuclear medicine, the imaging modalities that have received the greatest attention are PET and SPECT [76, 136]. While PET and SPECT have been employed to great effect in the past, there are several considerations that confound their employment in the preclinical evaluation of the daughter redistribution, which has been the Achilles heel in developing ^{225}Ac-based radiopharmaceuticals.

PET scanners require positron emission, which does not appear in the ^{225}Ac decay scheme. To directly image ^{225}Ac agents using PET, the radiopharmaceutical must be modified to accommodate a positron-emitting isotope. Consequently, a variety of positron emitters have been investigated as chemical surrogates for ^{225}Ac, including ^{68}Ga, ^{89}Zr, and ^{134}Ce. Cerium-134 is one of the more promising surrogates due to its similar chemical properties and half-life of 75.9 hours, which enables the radiopharmaceutical to be tracked over several days [85]. While PET surrogates can provide valuable insight on the biodistribution of ^{225}Ac agents, they do not provide information about the daughter redistribution.

In principle, SPECT scanners can directly image radionuclides if photon emissions accompany their decay. Indeed, the ^{225}Ac decay scheme includes gamma-ray emissions from ^{221}Fr at 218-keV and ^{213}Bi at 440-keV. SPECT traditionally employs either a pinhole or parallel-hole collimator, both of which are known to achieve high spatial resolution on a sub-millimeter scale [137, 138]. However, collimator-based imagers have a limited photon energy range at which they are effectively operational. At energies above about 300 keV, SPECT systems experience a degradation of response due to the increased likelihood of unwanted photon transmission through the collimator. This eliminates the potential of effectively utilizing the 440-keV emission line of ^{213}Bi.

Furthermore, even at energies below 300 keV, conventional SPECT systems have poor imaging sensitivity, on the order of 10^{-4} for small-animal applications, due to a collimator-driven trade-off between sensitivity and resolution. This tradeoff is not ideal for preclinical studies, which involve imaging low doses of radiation on a small scale. In the case of alpha-particle-based radiopharmaceuticals, studies would require particularly low amounts of activity to be injected due to the high efficacy of alpha particles; on the order of 20 kBq in small mice with only a fraction of that reaching the tumor site.

To overcome the limitations of existing small-animal molecular imagers, this work proposes coded aperture and Compton imaging as complementary modalities with the former suited to the 218-keV emission line of ^{221}Fr and the latter suited to the 440-keV emission line of ^{213}Bi. For energies below a few hundred keV, coded aperture imagers are advantageous as they provide the maximum possible sensitivity among collimator-based systems without a cost to resolution. For energies above a few hundred keV, Compton cameras are appealing as they rely on the dominant interaction process at these energies, namely Compton scattering, and they do not require a collimator that would otherwise decrease the instrument sensitivity [139]. By incorporating the coded aperture and Compton modalities with a PET scanner, which can provide an estimate of the ^{225}Ac biodistribution via positron-emitting surrogates, a full picture of the daughter redistribution can be painted.

There are several critical design considerations in applying both the coded aperture and Compton imaging concepts to small-animal applications. Because these applications involve weak and small-scale radiation distributions, they require an imager that exhibits both high resolution and sensitivity. To maximize both of these parameters, the distance between the small animal and imager should be minimized. Under such near-field conditions, coded apertures are subject to more severe collimation and magnification effects due to the diverging nature of the incident gamma rays [27, 28, 29]. Section 4.1.2 discusses how these effects are addressed via the coded aperture design employed in this work.

For Compton cameras, one of the more critical design considerations is the detector granularity [108]. This characteristic can be defined as the ability of the imager to discriminate multiple interactions induced by the same incident gamma ray. In other words, a finer granularity corresponds to a smaller volume in which two interactions can be discriminated; thereby increasing the fraction of detected events that are correctly identified. Furthermore, the energy and position resolution of the detectors must be considered as these two parameters strongly impact the attainable image resolution [140].

The remainder of this section demonstrates the feasibility of imaging the ^{225}Ac daughters in small animals using coded aperture and Compton techniques. To start, coded aperture and Compton images of ^{221}Fr and ^{213}Bi, respectively, in an ^{225}Ac-filled phantom are presented. These images provide quantification factors, which are applied to the subsequent images of the daughters in tumor-bearing mice injected with ^{225}Ac-Macropa-PEG8(7)-YS5 and ^{225}Ac-DOTA-YS5 agents. *Ex-vivo* biodistribution analyses of the mice are also provided to validate the coded aperture and Compton images. A discussion of the results follows.

It should be noted here that all of the coded aperture images presented in this section were produced from events that took place within the full volume of the detector. Due to the low activities of the ^{225}Ac agents, criteria 3 in Section 4.3.1 was disregarded to increase sensitivity. To mitigate image blurring, the system response should have been expanded to account for the multiple depths-of-interaction in the detector. However, here the system response was calculated at a single depth-of-interaction of 2 mm from the surface of the detector, around which the majority of events took place. A more expansive system response would have required more computational power than was available.

5.2.1 Phantom Filled with Actinium-225

This section presents coded aperture and Compton images of ^{221}Fr and ^{213}Bi, respectively, in an ^{225}Ac-filled phantom. These images serve as the ground truth for the performance of the Dual-Modality Imager and provide quantification factors for the subsequent small-animal images. Figure 5.7a shows the phantom, which has a cylindrical body with an inner diameter and height of 40 and 82 mm, respectively. The body houses three micro-hollow spheres of various sizes. The inner diameters of the spheres are 4.6 mm, 6.6 mm, and 8.3 mm, and the corresponding volumes are 50 μL, 150 μL, and 300 μL, respectively.

Figure 5.7b shows the configuration of the spheres inside the phantom. The sphere centers are positioned in a triangular fashion on the same (x, z) transverse plane. The centers of the large and medium spheres are separated by a distance of 25.4 mm. The center of the small sphere is located at a distance of 18.0 mm from the centers of both the large and medium spheres.

The phantom body was filled completely with water. The spheres were each filled fully with the same mixture of water and ^{225}Ac. The activity concentration was 0.44 kBq/μL at the time of preparation. Given this concentration, the smallest sphere contained 22 kBq, the medium sphere contained 67 kBq, and the largest sphere contained 133 kBq.

Figure 5.7c shows the experimental setup of the phantom in the coded aperture mode at 2 days post-preparation. By the time of this measurement, the activities inside the spheres had decayed to 19 kBq, 58 kBq, and 117 kBq in order of the smallest to largest sphere. The phantom was centrally positioned on top of a rotating mount. The rotation axis was located at a distance of 95 mm from the mask with the mask positioned at a distance of 50 mm from the detector. In this configuration, the resolution of the coded aperture imager theoretically should be about $\delta r_{ca} \approx 6.9$ mm in FWHM. The mount was rotated in 45° increments. At each viewing angle, 3.1×10^4 events were acquired on average at the 218-keV emission line of the daughter ^{221}Fr after 30 minutes. The total imaging time amounted to 4 hours.

Figure 5.7d shows the experimental setup of the phantom in the Compton mode at 14 days post-preparation. By the time of this measurement, the activities inside the spheres had decayed to 8 kBq, 25 kBq, and 51 kBq in order of the smallest to largest sphere. The phantom was centrally positioned on top of a rotating mount. For maximum resolution and sensitivity, the mount was positioned as close as possible to the detector with the rotation axis located at a distance of 55 mm from the surface of the first detector. In this configuration, the resolution of the Compton imager theoretically should be about $\delta r_{ci} \approx 6.4$ mm in FWHM at 440 keV. The mount was rotated in 45° increments. At each viewing angle, 8.4×10^3 events were acquired on average at the 440-keV emission line of the daughter ^{213}Bi after 30 minutes. The total imaging time amounted to 4 hours.

Using ML-EM with TV and Tikhonov regularization as described in Sections 4.3.4 and 4.4.3, the phantom was reconstructed in 3-D from the coded aperture and Compton data at the 218-keV emission line of ^{221}Fr and 440-keV emission line of ^{213}Bi, respectively. Both the coded aperture and Compton images were generated from eight viewing angles after 250 iterations. Figure 5.8 shows the central (x, z) transverse slices of the phantom images.

(a) Phantom

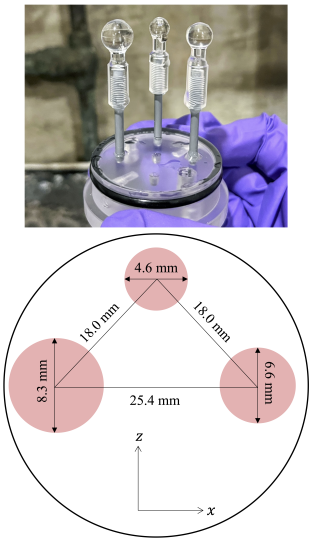

(b) Microspheres

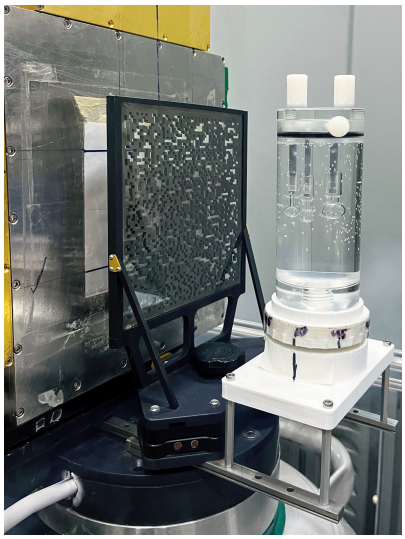

(c) Coded Aperture Setup

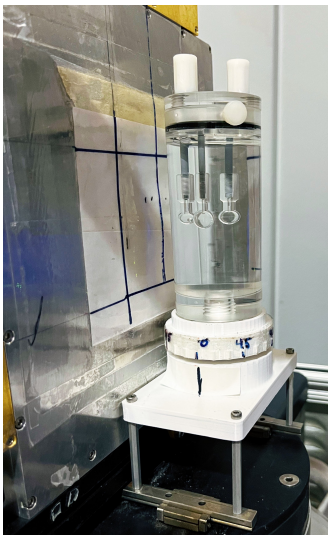

(d) Compton Setup

Figure 5.7: (a) The phantom body filled with water. The phantom houses (b) three micro-hollow spheres with inner diameters of 4.6 mm, 6.6 mm, and 8.3 mm and each filled with an equal concentration of ^{225}Ac. The sphere centers are positioned and their centers are positioned in a triangular fashion on the same (x, z) transverse plane. (c) Experimental setup of the phantom in the coded aperture mode at a source-to-detector distance of 145 mm with a mask-to-detector distance of 50 mm and (d) Compton mode at a source-to-detector distance of 55 mm.

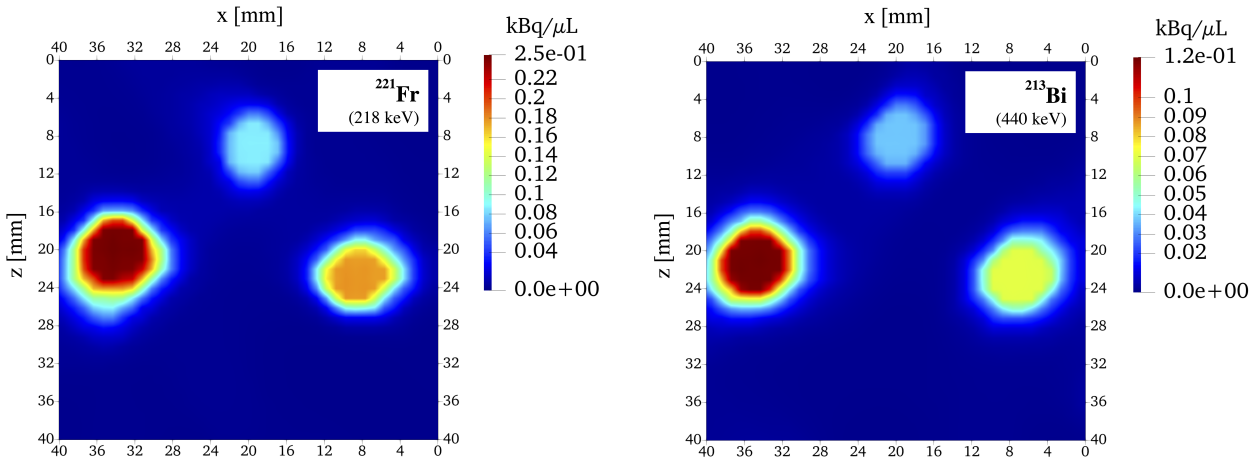

(a) Coded Aperture (b) Compton

Figure 5.8: (a) Coded aperture and (b) Compton images of the ^{225}Ac-filled phantom (Figure 5.7) displayed as 2-D transverse (x, z) slices; images (a) and (b) were 'zoomed-in' for better visibility. The coded aperture image was generated from a total of 2.5×10^5 events at the 218-keV emission line of ^{221}Fr after 250 iterations with $\epsilon = 0.05$ and $\eta = 0.03$, and the Compton image was generated from a total of 6.7×10^4 events at the 440-keV emission line of ^{213}Bi after 250 iterations with $\epsilon = 0.01$ and $\eta = 0.02$. Both images were produced from eight viewing angles. Note the intensity scales of the two images differ, because the Compton measurement took place 12 days after the coded aperture measurement.

Up until now, all of the images presented in this work were on relative intensity scales. Here the images are in units of activity per volume (kBq/μL). To convert the image intensity to a quantifiable value, respective quantification factors Q were derived from the coded aperture and Compton images of the phantom:

$$Q = \frac{I}{A \cdot T \cdot \left(\frac{1}{R^2}\right) \cdot e^{-(\mu_{H2O})(t)}} \tag{5.1}$$

where I is the sum total of intensity in the three reconstructed microspheres as determined by the ML-EM algorithm, A is the known activity of the phantom at the time of measurement, T is the imaging time, R is the normal distance between the center of the phantom and surface of the first detector, and the exponential $e^{-(\mu_{H2O})(t)}$ corrects for photon attenuation in water. The attenuation distance t is assumed to be the radius of the phantom body, and the water linear attenuation coefficient μ_{H2O} is evaluated at 218 keV for the coded aperture modality and 440 keV for the Compton modality. The coded aperture and Compton quantification factors Q are assumed constant and applied to subsequent images of ^{221}Fr and ^{213}Bi, respectively. By simply plugging the constant Q into a rearranged Equation 5.1, the

activity A, now considered an unknown, can be determined.

Table 5.1 summarizes the activities and diameters of the three reconstructed microspheres in Figure 5.8. In the coded aperture images, the sum totals of activity in each reconstructed sphere are 19 kBq, 56 kBq, and 119 kBq in order of the smallest to largest sphere, respectively. These values are consistent with the actual activities at the time of measurement. Furthermore, the extents of the reconstructed spheres at the central linear cross-section are 7.2 mm, 7.9 mm, and 8.1 mm in FWHM in order of the smallest to largest sphere, respectively.

In the Compton images, the sum totals of activity in each reconstructed sphere are 9 kBq, 25 kBq, and 50 kBq in order of the smallest to largest sphere, respectively. These values are consistent with the actual activities at the time of measurement. Furthermore, the extents of the reconstructed spheres at the central linear cross-section are 6.8 mm, 7.6 mm, and 7.9 mm in FWHM in order of the smallest to largest sphere, respectively.

The images in Figure 5.8 are representative of results that are attainable with the current imaging system. In reality, the three microspheres have an equal activity concentration, but different sizes. Given an ideal system, the reconstructed spheres would display equal intensity with the appropriate sizes for each sphere. Because of the limited spatial resolution of the Dual-Modality Imager, the three reconstructed spheres appear to be roughly the same size. Nonetheless, the images produces three spheres with the correct total activity, but distributed over the larger volumes. Consequently, the smaller two spheres appear less intense, rather than smaller, in the images. Better spatial resolution would solve this problem.

Table 5.1: Activities and diameters (in FWHM) of the reconstructed microspheres in Figure 5.8 versus the ground truth values. Note the activities derived from the coded aperture and Compton images differ, because the Compton measurement took place 12 days after the coded aperture measurement.

	Coded Aperture			Compton		
True Dia. [mm]	Recon. Dia. [mm]	True Act. [kBq]	Recon. Act. [kBq]	Recon. Dia. [mm]	True Act. [kBq]	Recon. Act. [kBq]
4.6	7.2	19	19	6.8	8	9
6.6	7.9	58	56	7.6	25	25
8.3	8.1	117	119	7.9	51	50

5.2.2 Tumor-Bearing Mice Injected with Actinium-225 Agents

Five- to six-week-old male athymic mice were implanted subcutaneously with 5×10^6 22Rv1 prostate cancer cells into the right flank at the Molecular Imaging Laboratory at the Univer-

sity of California San Francisco (UCSF). Approximately $3-5$ weeks after tumor implantation, the mice were injected with either ^{225}Ac-Macropa-PEG8(7)-YS5 or ^{225}Ac-DOTA-YS5 via the tail vein and sacrificed at different time intervals to evaluate the tumor-targeting specificity. The synthesis and biodistribution results for each of these ^{225}Ac agents have been reported in conference proceedings [141, 142] and will be published separately. Furthermore, these radioimmunotherapy agents are similar to previously reported ^{89}Zr-labeled PET radiopharmaceuticals that target the antigen CD46, which is highly expressed on the surface of prostate and other cancers [143].

This work received two of the mice, hereinafter labeled as A and B, from the UCSF study. Mice A and B were injected with 20 kBq of ^{225}Ac-Macropa-PEG8(7)-YS5 and ^{225}Ac-DOTA-YS5, respectively. Following injection, mice A and B were euthanized at 2 and 4 days, respectively. The mice were each housed in a 50 mL falcon tube and stored in a freezer at 20°F when not in use. Each mouse was imaged in both the coded aperture and Compton modes to determine the feasibility of using these modalities to assess the daughter redistribution of ^{225}Ac-based radiopharmaceuticals in small animals. Furthermore, the coded aperture and Compton images are correlated to an *ex-vivo* biodistribution analysis. The following sections discuss the experiments and results in more detail.

5.2.2.1 Tumor-Bearing Mouse A Injected with ^{225}Ac-Macropa-PEG8(7)-YS5

Figure 5.9a shows the experimental setup of mouse A in the coded aperture mode at 2 days post-injection. The falcon tube containing the mouse was centrally positioned on top of a rotating mount in an upright orientation. The rotation axis was located at a distance of 95 mm from the mask with the mask positioned at a distance of 50 mm from the detector. In this configuration, the resolution of the coded aperture imager theoretically should be about $\delta r_{ca} \approx 6.9$ mm in FWHM. The mount was rotated in 45° increments. At each rotation, 4.2×10^3 events were acquired on average at the 218-keV emission line of ^{221}Fr after 60 minutes. The total imaging time amounted to 8 hours.

Figure 5.9b shows mouse A in the Compton mode at 4 days post-injection. To maximize resolution and sensitivity, the falcon tube was positioned as close as possible to the detector in an upright orientation. The central axis of the tube was located at a distance of 35 mm from the surface of the first detector. In this configuration, the resolution of the Compton imager theoretically should be about $\delta r_{ci} \approx 4.1$ mm in FWHM at 662 keV. The falcon tube was rotated by hand in 45° increments. At each rotation, 4.1×10^3 events were acquired on average at the 440-keV emission line of ^{213}Bi after 75 minutes. The total imaging time amounted to 10 hours.

Using ML-EM with TV and Tikhonov regularization, mouse A was reconstructed in 3-D from the coded aperture and Compton data at the 218-keV emission line of ^{221}Fr and 440-keV emission line of ^{213}Bi, respectively. Both the coded aperture and Compton images were generated from eight viewing angles after 250 iterations. Figures 5.10b-c show the maximum intensity projections of the coded aperture and Compton images, each fused with a CT maximum intensity projection (MIP) [144]. Furthermore, Figures 5.10e-f show (x, y) coronal

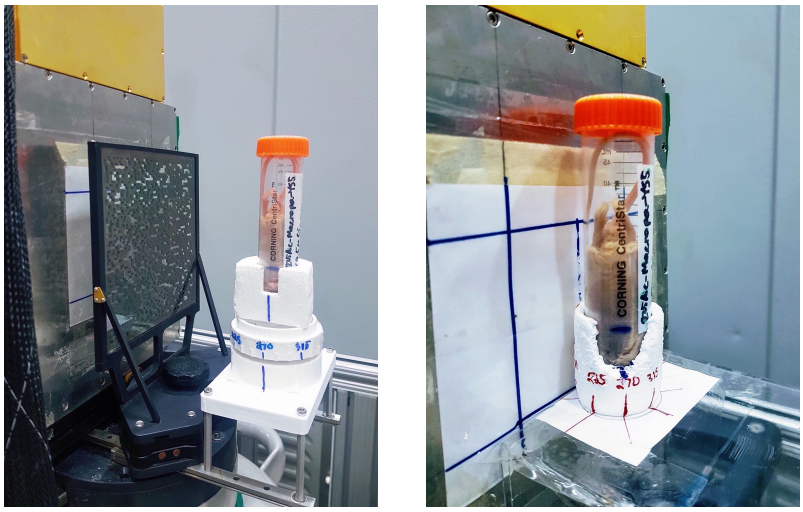

(a) Coded Aperture Setup (b) Compton Setup

Figure 5.9: Experimental setup of mouse A in the (a) coded aperture mode at a source-to-detector distance of 145 mm with a mask-to-detector distance of 50 mm and (b) Compton mode at a source-to-detector distance of 35 mm.

slices of the coded aperture and Compton images, each fused with a coronal CT image. The CT scan was performed separately from the dual-modality measurements; and thus the co-registration is not precise. The quantification factor Q, determined by the phantom measurements in Section 5.2.1, was applied to each image so that the intensity scale is in units of percent injected dose per cubic centimeter (%ID/cc). Additionally, the intensity scales are decay corrected to the day of injection.

Following the dual-modality measurements, an *ex-vivo* biodistribution analysis was performed to validate the images. Major organs (including the liver, heart, kidney, lungs, spleen, pancreas, muscle, bone, and subcutaneous tumor) were harvested, weighed, and counted by a Hidex Automated Gamma Counter [145]. Table 5.2 displays the activity estimates of ^{221}Fr and ^{213}Bi in the various organs as determined by the biodistribution and coded aperture and Compton images. These activities are decay corrected to the day of injection.

According to the biodistribution of mouse A, the tumor exhibits the highest uptake of the daughters with a total accumulation of about 1152 Bq of ^{221}Fr and 1064 Bq of ^{213}Bi. This is consistent with the coded aperture and Compton images (in Figure 5.10), which show total accumulations of about 1219 Bq of ^{221}Fr and 1035 Bq of ^{213}Bi, respectively. While the quantification estimates extracted from the biodistribution and images are in close agreement, more work needs to be done to determine the associated uncertainties.

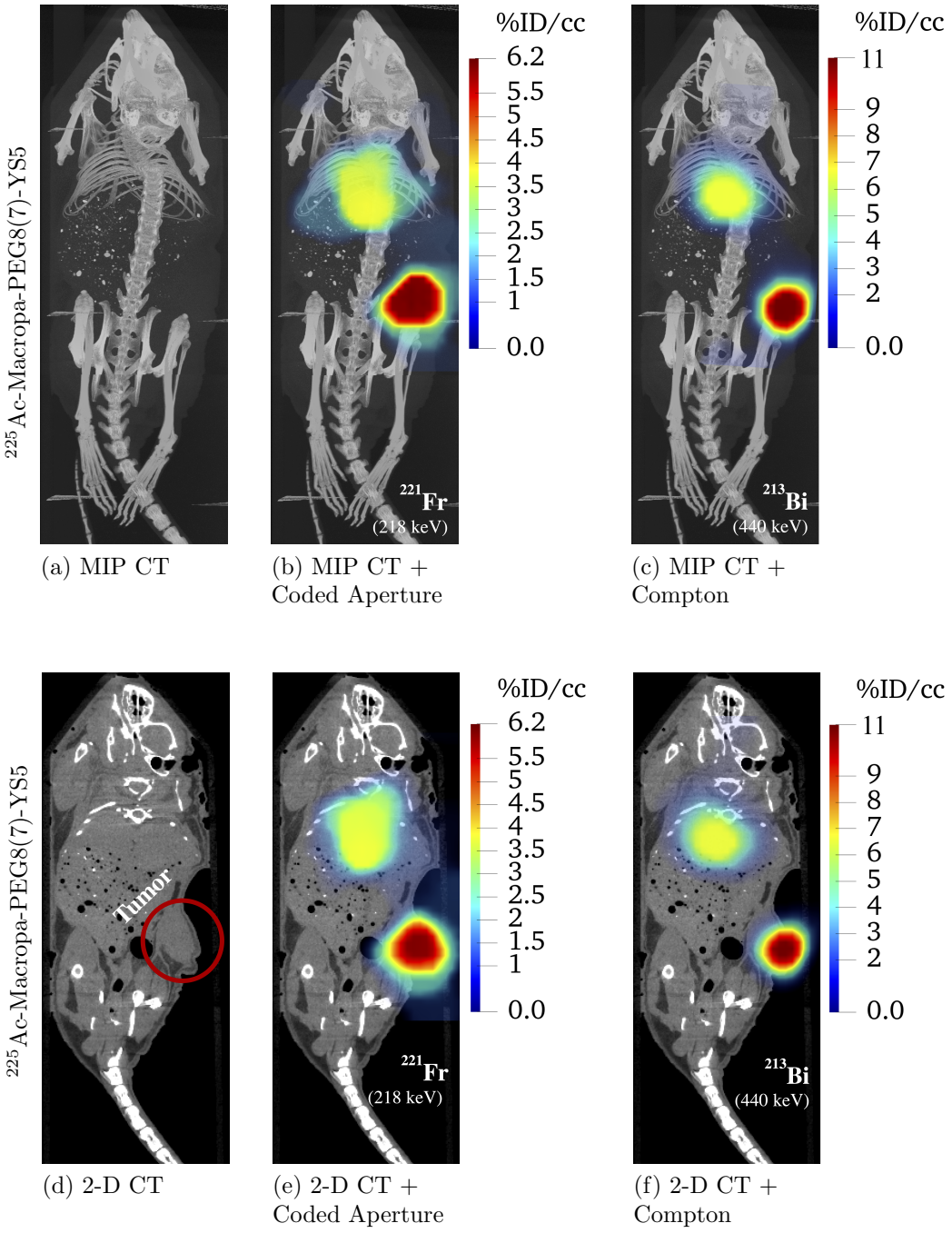

(a) MIP CT (b) MIP CT + Coded Aperture (c) MIP CT + Compton

(d) 2-D CT (e) 2-D CT + Coded Aperture (f) 2-D CT + Compton

Figure 5.10: Coded aperture and Compton images of tumor-bearing mouse A injected with 20 kBq of ^{225}Ac-Macropa-PEG8(7)-YS5 and sacrificed at 2 days post-injection. (a) CT MIP of mouse A fused with the (b) coded aperture and (c) Compton MIPs. (d) CT coronal slice of mouse A fused with coronal slices of the (e) coded aperture and (f) Compton images. The coded aperture images was generated from a total of 3.4×10^4 events at the 218-keV emission line of ^{221}Fr after 250 iterations with $\epsilon = 0.05$ and $\eta = 0.03$, and the Compton images was generated from a total of 3.3×10^4 events at the 440-keV emission line of ^{213}Bi after 250 iterations with $\epsilon = 0.01$ and $\eta = 0.01$. All images were produced from eight viewing angles. The intensity scales are decay corrected to the day of injection.

The biodistribution also shows significant uptake in the liver, heart, and lungs. In combination, these three organs show total activity accumulations of about 1209 Bq of ^{221}Fr and 1140 Bq of ^{213}Bi. This is consistent with the coded aperture and Compton images, which show accumulations of about 1298 Bq of ^{221}Fr and 1220 Bq of ^{213}Bi, respectively, in the central region of the mouse.

Note the coded aperture and Compton images show no clear distinction between the central organs. This can be partially explained by the limited resolution of the imaging modalities; and thus going forward improvements in resolution should be a priority. Another possible explanation could be related to the upright position of the mouse during the imaging process. In this orientation, the mouse carcass compressed vertically due to gravity, possibly resulting in an amalgamation of organs.

Table 5.2: Mouse A injected with 20 kBq of ^{225}Ac-Macropa-PEG8(7)-YS5 and sacrificed at 2 days post-injection. Activity estimates in major organs as determined by the ex-vivo biodistribution and coded aperture and Compton images. The biodistribution data are displayed as both percent injected dose per gram (%IG/g) and activity in units of Becquerel (Bq). The image data are displayed as activity (Bq). The central organs encompass the liver, heart, and lungs. All reported values are decay corrected to the day of injection.

		Ex-vivo Biodistribution				Coded Aperture	Compton
Organ	Weight [g]	^{221}Fr [%ID/g]	^{213}Bi [%ID/g]	^{221}Fr [Bq]	^{213}Bi [Bq]	^{221}Fr [Bq]	^{213}Bi [Bq]
Tumor	0.300	19.2	17.8	1152	1064	1219	1035
Liver	0.597	6.58	5.91	786	706	–	–
Heart	0.252	4.89	4.74	246	239	–	–
Lungs	0.174	5.06	5.59	176	195	–	–
Kidneys	0.327	2.93	3.21	192	210	–	–
Central Organs	–	–	–	1208	1140	1298	1220

5.2.2.2 Tumor-Bearing Mouse B Injected with ^{225}Ac-DOTA-YS5

Figure 5.11 shows the experimental setup of mouse B in the coded aperture and Compton modes. The geometric arrangements were identical to those described for mouse A. Here the coded aperture measurement took place at 4 days post-injection, and data were acquired for 120 minutes at each 45° viewing angle. The total imaging time amounted to 16 hours, and 3.9×10^3 events were acquired

on average at the 218-keV emission line of ^{221}Fr at each rotation. The Compton measurement took place at 6 days post-injection, and data were acquired for 70 minutes at each 45° viewing angle. The total imaging time amounted to 9.3 hours, and 1.6×10^3 events were acquired on average at the 440-keV emission line of ^{213}Bi at each rotation.

Despite mice A and B being administered the same amount of activity, the count rate observed in the latter was about a factor of two lower. This should be expected. Mouse B was sacrificed two days later than mouse A; thereby excreting more of the radiopharmaceutical. To have sufficient statistics for coded aperture imaging, mouse B required double the imaging time of mouse A.

Figures 5.12b-c show the maximum intensity projections of the coded aperture and Compton images, each fused with a CT maximum intensity projection. Furthermore, Figures 5.12e-f show (x, y) coronal slices of the coded aperture and Compton images, each fused with a coronal CT image. The intensity scales are decay corrected to the day of injection.

Following the dual-modality measurements, an *ex-vivo* biodistribution analysis was performed. Table 5.3 displays the activity estimates of ^{221}Fr and ^{213}Bi in the various organs as determined by the biodistribution and coded aperture and Compton images. These activities are decay corrected to the day of injection.

According to the biodistribution of mouse B, the tumor exhibits the highest uptake of the daughters with a total accumulation of about 217 Bq of ^{221}Fr and 198 Bq of ^{213}Bi. This is consistent with the coded aperture and Compton images (in Figure 5.12), which show total accumulations of about 299 Bq of ^{221}Fr and 242 Bq of ^{213}Bi, respectively.

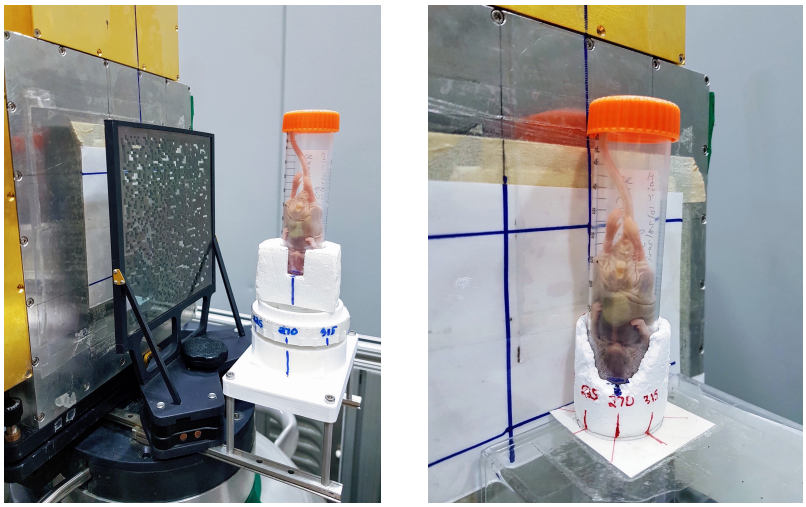

(a) Coded Aperture Setup (b) Compton Setup

Figure 5.11: Experimental setup of mouse B in the (a) coded aperture mode at a source-to-detector distance of 145 mm with a mask-to-detector distance of 50 mm and (b) Compton mode at a source-to-detector distance of 35 mm.

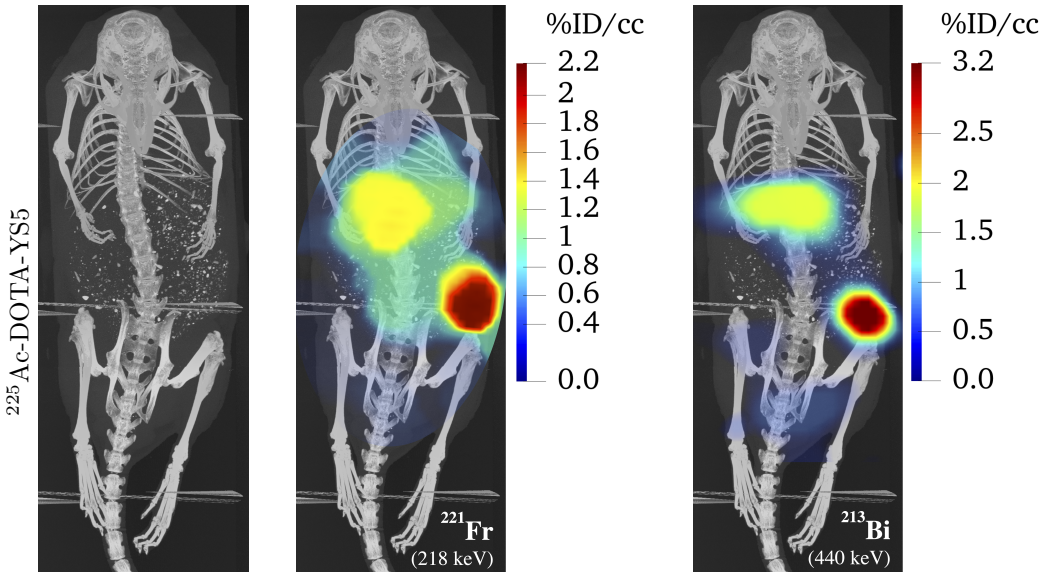

(a) MIP CT (b) MIP CT + Coded Aperture (c) MIP CT + Compton

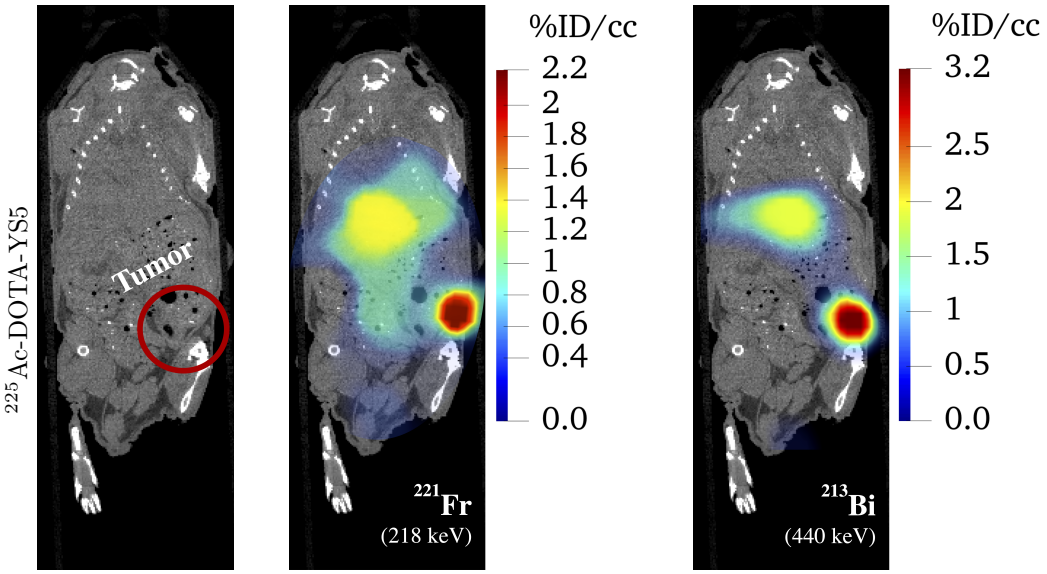

(d) 2-D CT (e) 2-D CT + Coded Aperture (f) 2-D CT + Compton

Figure 5.12: Coded aperture and Compton images of tumor-bearing mouse B injected with 20 kBq of ^{225}Ac-DOTA-YS5 and sacrificed at 4 days post-injection. (a) CT MIP of mouse B fused with the (b) coded aperture and (c) Compton MIPs. (d) CT coronal slice of mouse B fused with coronal slices of the (e) coded aperture and (f) Compton images. The coded aperture images was generated from a total of 3.1×10^4 events at the 218-keV emission line of ^{221}Fr after 250 iterations with $\epsilon = 0.05$ and $\eta = 0.03$, and the Compton images was generated from a total of 1.2×10^4 events at the 440-keV emission line of ^{213}Bi after 250 iterations with $\epsilon = 0.01$ and $\eta = 0.01$. All images were produced from eight viewing angles. The intensity scales are decay corrected to the day of injection.

The biodistribution also shows significant uptake in the liver, heart, and lungs. In combination, these three organs show total activity accumulations of about 437 Bq of ^{221}Fr and 434 Bq of ^{213}Bi. The images show significant uptake in the central organs as well. The coded aperture and Compton images show accumulations of about 610 Bq of ^{221}Fr and 575 Bq of ^{213}Bi, respectively. Here the biodistribution shows significantly lower activities than the images. This discrepancy can be partially explained by a suboptimal biodistribution analysis. Upon dissection, several organs were found to be damaged and may not have been fully harvested.

Table 5.3: Mouse B injected with 20 kBq of ^{225}Ac-DOTA-YS5 and sacrificed at 4 days post-injection. Activity estimates in major organs as determined by the ex-vivo biodistribution and coded aperture and Compton images. The biodistribution data are displayed as both percent injected dose per gram (%IG/g) and activity in units of Becquerel (Bq). The image data are displayed as activity (Bq). The central organs encompass the liver, heart, and lungs. All reported values are decay corrected to the day of injection.

		Ex-vivo Biodistribution				Coded Aperture	Compton
Organ	Weight [g]	^{221}Fr [%ID/g]	^{213}Bi [%ID/g]	^{221}Fr [Bq]	^{213}Bi [Bq]	^{221}Fr [Bq]	^{213}Bi [Bq]
Tumor	0.186	5.84	5.33	217	198	299	242
Liver	0.731	1.64	1.63	240	238	–	–
Heart	0.153	2.46	2.33	75	71	–	–
Lungs	0.199	3.06	3.14	122	125	–	–
Kidneys	0.423	1.32	1.11	111	94	–	–
Central Organs	–	–	–	437	434	610	575

5.2.3 Discussion

The ability to image the daughters of ^{225}Ac, namely ^{221}Fr and ^{213}Bi, in small animals would expedite the development of ^{225}Ac-based radiopharmaceuticals, which have been demonstrated as a promising cancer treatment [51, 69, 70]. This is the first time these daughters have been imaged in mice via gamma-ray emissions using coded aperture and Compton techniques. That said, a previous study by Darpan et al. imaged ^{225}Ac agents in live mice via Cherenkov emissions using Cerenkov luminescence imaging (CLI) [146]. This technique, however, has several limitations. Firstly, the origins of Cherenkov emissions from ^{225}Ac remain uncertain, and thus the daughter redistribution of ^{221}Fr and ^{213}Bi cannot be evaluated. Gamma-ray emissions, on the other hand, are unique to the radioisotopes that emit them. This enables discrimination between the various

daughters. Secondly, Cherenkov radiation, unlike gamma rays, has low penetration depth in tissue. This challenges the ability of CLI to produce both three-dimensional and quantitative images. Quantification is particularly critical in small-animal studies in which the dose delivered to various organs must be determined. This work provides the first quantification estimates of ^{221}Fr and ^{213}Bi in mice via coded aperture and Compton imaging. And lastly, the CLI study tested mice with an injected activity of 1900 kBq, which is nearly 100 times greater than the tested activity in this work, i.e. 20 kBq. The latter activity is on the order of what would be required at the preclinical stage.

Other works have already proposed a Compton camera for the preclinical evaluation of the ^{225}Ac daughters [147, 148]; however, none have demonstrated the feasibility of this modality via experimentation. The most recent study by Caravaca et al. [148] simulates the responses of both Compton and proximity imagers based on CZT. As would be expected, the simulated results show the ability of the Compton camera to image ^{213}Bi via its 440-keV gamma-ray emission in a mouse phantom injected with 20 kBq of ^{225}Ac. Furthermore, Caravaca et al. demonstrates the ability of the proximity modality to image ^{221}Fr via its 218-keV gamma-ray emission in a point-like phantom. This simulation, however, is overly optimistic as the point-like phantom was positioned at a 1-mm standoff distance. In small-animal imaging, a more realistic distance is on the order of the extent of the animal body, and at such distances, proximity imaging cannot provide reasonable resolution.

Previous works have proposed and employed coded apertures for small-animal imaging [149, 150], but as far as we know, this work is the first to recommend a coded aperture for imaging ^{221}Fr in small animals via the 218-keV emission line. Other analogous collimator-based systems have been employed to image ^{221}Fr [151, 152]. These studies show preliminary images of ^{225}Ac-filled phantoms, but none have demonstrated sufficient sensitivity to image activities as low as 20 kBq.

A study by Wang et al. [143] presents both a biodistribution analysis and PET image of a [^{89}Zr]DFO-YS5 agent in a mouse implanted with the same 22Rv1 prostate cancer cells as the mice presented here. The ^{89}Zr agent is similar to the ^{225}Ac-Macropa-PEG8(7)-YS5 and ^{225}Ac-DOTA-YS5 agents injected in mice A and B, respectively. ^{89}Zr is oftentimes employed as a PET surrogate due to its long half-life (78.4 hours) and availability, but other positron emitters, namely ^{134}Ce, better match the unique chemistry of ^{225}Ac [85]. Nevertheless, the results in Wang et al. provide an estimate of the ^{225}Ac biodistribution, which can serve as a foundation for assessing the daughter redistribution.

The biodistribution analysis of the [^{89}Zr]DFO-YS5 agent shows a tumor uptake of 14.5 $\pm$ 3.2 %ID/g at 4 days post-injection and less than 5 %ID/g in all other organs. In this work, the biodistribution of mouse A shows 19.2 %ID/g of ^{221}Fr and 17.8 %ID/g of ^{213}Bi in the tumor at 2 days post-injection and less than 7 %ID/g of both isotopes in all other organs. The biodistribution of mouse B shows significantly lower uptake. The tumor has 5.84 %ID/g of ^{221}Fr and 5.33 %ID/g of ^{213}Bi at 4 days post-injection, and all other organs have less than 3 %ID/g of both isotopes. The lower uptake could be related to a number of factors, including biological variations and a suboptimal tumor dissection. In regards to the latter, if the harvested tumor also included adjacent skin or muscle, then the uptake would appear less. This is a likely cause given that organs were found damaged upon dissection.

Similarly to the biodistribution analyses, the PET image of ^{89}Zr (Figure 3a in Wang et al.) and the coded aperture and Compton images of ^{221}Fr and ^{213}Bi, respectively, show the highest uptake in the tumor and noticeable uptake in the central organs. The PET image of ^{89}Zr has an

intensity scale that ranges up to 20 %ID/cc, whereas the coded aperture and Compton images have intensity scales with maximums between 2 %ID/cc and 11 %ID/cc. The intensity variations between the PET image of ^{89}Zr and the gamma-ray images of ^{221}Fr and ^{213}Bi might be indicative of the daughters redistributing, but for now, such claims cannot be made. The discrepencies might also be a result of biological variations associated with using different mice and radioimmunotherapy agents. A more concrete explanation is the distinct resolution profiles of the imaging modalities. The coded aperture and Compton imagers have resolutions that are a factor of 5 and 3 times worse than PET, respectively, and thus the intensities of the coded aperture and Compton images spread over more voxels. Going forward, the resolutions of the two modalities will need to match that of PET so that the daughter redistribution can be properly assessed.

The consistency between the gamma-ray images and biodistribution analyses of the ^{225}Ac daughters contributes to the credibility of this work. For mouse A, the coded aperture and Compton images show the highest uptake in the tumor with total activity accumulations of about 1219 Bq of ^{221}Fr and 1035 Bq of ^{213}Bi, respectively. The biodistribution also shows the highest uptake in the tumor with total accumulations of 1152 Bq of ^{221}Fr and 1064 Bq of ^{213}Bi. For mouse B, the gamma-ray images and biodistribution, once again, show the highest uptake in the tumor. The coded aperture and Compton images show total activity accumulations of about 299 Bq of ^{221}Fr and 242 Bq of ^{213}Bi, respectively, and the biodistribution shows 217 Bq of ^{221}Fr and 198 Bq of ^{213}Bi. In the cases of both mice, the quantification estimates from the images and biodistribution analyses are in close agreement. However, more work needs to be done to determine the associated uncertainties.

Going forward, a more specialized imager should be built to enhance image resolution. While the small-animal images presented in this paper are promising, the current system could not discriminate the central organs, e.g. liver, heart, and lungs, given the 6.9 mm and 4.1 mm resolutions in FWHM of the coded aperture and Compton modalities, respectively. The image resolution can be improved by reducing the strip pitch of the detectors and size of the mask elements. For example, by using a 0.5-mm strip pitch with mask elements to match, the coded aperture resolution would improve by about 75% at the current magnification of 1.5, and the Compton resolution would improve by about 40% at a photon energy of 440 keV and source-to-detector distance of 35 mm. Additional improvements to the coded aperture resolution can be realized by increasing the magnification factor. If a magnification of 3 were realized, then the coded aperture resolution would improve by an additional 50%. The Compton resolution can be further improved by decreasing the source-to-detector distance. If a distance of 20 mm were realized, then the Compton resolution would improve by an additional 40%. These calculations are provided in Appendix A.

While the current system has a sensitivity advantage over existing medical imagers, improvements to imaging sensitivity should also be a priority, so that organs with relatively low uptake (e.g. kidneys) can be resolved. The sensitivity can be enhanced by increasing both the efficiency and solid angle coverage of the detectors. The latter can be achieved by introducing multiple panels of coded aperture and Compton imagers around the small animal. If two panels of each modality were employed, then the sensitivity of both modalities would increase by a factor of 2. Further sensitivity improvements can be realized by mitigating information loss in the event reconstruction process[1]. This can be achieved by reducing the granularity of the detectors via a smaller strip pitch

[1]The coded aperture and Compton modalities have imaging sensitivities that are about 46% and 66% lower, respectively, than a simulated system with perfect event reconstruction and no dead time (Section 4.5.1.2).

and employing more advanced signal processing techniques.

Chapter 6

Conclusion

6.1 Summary

A broad range of fields, including astrophysics, emergency response and contamination remediation, nuclear security and safeguards, and nuclear medicine, require a means to detect, localize, and characterize radiological materials. These ends can be achieved via gamma-ray imaging. Of particular interest here is the application of gamma-ray imaging in situations that necessitate close proximity to sources that emit a broad spectrum of energies ranging from about 100 keV to 1 MeV. To enable effective operation in this energy range, this work transformed an existing Compton camera into the Dual-Modality Imager by integrating a novel coded aperture design.

The coded aperture design was heavily influenced by the pre-existing Compton camera, as well as the near field conditions under which the new system was to be operated. In general, designing a coded aperture for the near field comes with several challenges due to the presence of collimation and magnification effects, both of which can result in image artifacts. To mitigate collimation effects, this work employed a mask with slanted septa that either diverge or converge in the image space with the optimal mode of operation depending on the application. Furthermore, the mask elements are arranged in a random pattern that was optimized across a range of magnifications. An analytical performance comparison between the random array employed in this work and a conventional MURA was provided. The results show superior performance by the random array in the near field, where magnification effects exist.

A large portion of this work focused on developing methodologies for coded aperture and Compton image reconstruction. These methodologies encompass strategies for reconstructing and selecting detector events, modeling system responses, and developing image reconstruction algorithms. Great attention was given in the development of a ray-tracing algorithm to calculate the coded aperture system response. This algorithm was designed to be computationally-efficient and versatile so that the system response could be computed quickly for a multitude of imaging scenarios. Furthermore, for both coded aperture and Compton image reconstruction, efforts were made to enhance the standard ML-EM algorithm. Penalty functions based on Tikhonov regularization and total variation were incorporated into the iterative reconstruction algorithm, with the former suppressing undue noise amplification and the latter suppressing variation.

To demonstrate the broad imaging capabilities of the Dual-Modality Imager, gamma-ray sources

of relevance to both nuclear safeguards and nuclear medicine were imaged. These included HEU, ^{57}Co, and ^{137}Cs sources of various shapes to mimic uranium holdup scenarios, as well as ^{225}Ac-based radiopharmaceuticals in mice. All of above were imaged in the near field. This regime offers several distinct advantages over the far field, including both higher sensitivity and spatial resolution and the possibility of 3-D imaging. However, as mentioned earlier, near-field operation challenges the performance of the system, particularly in the case of the coded aperture. Several works have highlighted the difficulties in adapting the coded aperture concept to the near field [27, 28, 29], and little success has been achieved in imaging volumetric sources via this technique. A study by Mu et al. [29] from 2009 presents a promising 3-D coded aperture image of a pyramid-shaped phantom filled with ^{99m}Tc. Since then, there have been few, if any, demonstrations of 3-D coded aperture imaging in the near field. The images presented in this work, especially that of the ^{57}Co spiral, reinforce the idea that coded apertures have 3-D imaging capabilities. Furthermore, to our knowledge, this work is the first demonstration of both 3-D coded aperture and Compton imaging in the near field via a single detection system.

Arguably the most significant contribution of this dissertation is the application of the coded aperture and Compton imaging concepts to the preclinical evaluation of the daughter redistribution of ^{225}Ac-based radiopharmaceuticals. Up until now, there has been no effective means to study the daughter redistribution in small animals, which is an integral step towards clinical approval. This work presented both coded aperture and Compton images of ^{221}Fr and ^{213}Bi, respectively. Activity estimates were extracted from each image using a quantification factor derived from phantom measurements and were validated by an *ex-vivo* biodistribution analysis. These results are the first demonstration of visualizing and quantifying the ^{225}Ac daughters in small animals via gamma-ray imaging.

6.2 Future Outlook

The Dual-Modality Imager was not designed for a specific application, but rather envisioned for more general-purpose imaging scenarios. This dissertation serves as a proof-of-concept for 3-D coded aperture and Compton imaging in the near field. A more specialized imager needs to be designed according to the application. For example, preclinical studies would benefit from a gamma-ray imager that exhibits both high resolution (on a sub-millimeter scale) and sensitivity. While this work produced promising small-animal images, the image resolution and sensitivity can be improved upon greatly by the following design and procedural upgrades:

1. The DSSDs should be fabricated with a finer strip pitch.
2. Advanced signal processing methods which facilitate position interpolation between strips should be pursued.
3. The coded aperture should be designed with smaller elements to match the strip pitch of the updated DSSDs.
4. The coded aperture pattern should be optimized for higher magnification: $m > 2$
5. The coded aperture should have a smaller open fraction: $\rho < 0.5$.

6. Multiple imager panels should be included for greater solid angle coverage.

7. Advanced signal processing methods which mitigate information loss in the event reconstruction process should be pursued.

8. The coded aperture and Compton modalities should be operated via separate detection systems.

The implementation of $1-4$ improves image resolution with $3-4$ focused on the coded aperture resolution only, while 5 seeks to enhance the SNR of the coded aperture. Appendix A provides a quantitative analysis of the image resolutions that can be achieved with these design changes. Upgrades $6-7$ serve to increase the imaging sensitivity of both modalities, which would enable a reduction in measurement time. Fast timing would be essential if *in-vivo* imaging were pursued but was less critical to this work given that *ex-vivo* mice were imaged. Finally, upgrade 8 allows the coded aperture and Compton imagers to be operated simultaneously in a configuration that optimizes the resolution and sensitivity of each modality.

Another area of improvement is on quantification. The majority of images were shown on a relative intensity scale; they gave no indication of the source activity. Furthermore, even the activities derived from the small-animal images had no associated uncertainties. Developing a comprehensive approach for quantifying activities and estimating the associated uncertainties should be a priority moving forward.

The radiopharmaceutical studies in this work focused solely on ^{225}Ac agents in small animals. The proposed imaging concept, however, can be applied to any radionuclide that emits gamma rays with energies below a few MeV. Furthermore, the scope of coded aperture and Compton imaging in nuclear medicine is not limited to preclinical applications. These two modalities can be adapted and scaled up to meet clinical demands.

Bibliography

[1] V. Schonfelder, H. Aarts, K. Bennett, H. Deboer, J. Clear, W. Collmar, A. Connors, A. Deerenberg, R. Diehl, A. Von Dordrecht, *et al.*, "Instrument description and performance of the imaging gamma-ray telescope comptel aboard the compton gamma-ray observatory," *Astrophysical Journal Supplement Series*, 1993.

[2] K. Vetter, R. Barnowski, J. W. Cates, A. Haefner, T. Joshi, R. Pavlovsky, and B. J. Quiter, "Advances in nuclear radiation sensing: Enabling 3-d gamma-ray vision," *Sensors*, vol. 19, no. 11, p. 2541, 2019.

[3] K. Vetter, R. Barnowksi, A. Haefner, T. Joshi, R. Pavlovsky, and B. J. Quiter, "Gamma-ray imaging for nuclear security and safety: Towards 3-d gamma-ray vision," *Nuclear Instruments and Methods in Physics Research Section A: Accelerators, Spectrometers, Detectors and Associated Equipment*, vol. 878, pp. 159–168, 2018.

[4] H. B. Barber, "Applications of semiconductor detectors to nuclear medicine," *Nuclear Instruments and Methods in Physics Research Section A: Accelerators, Spectrometers, Detectors and Associated Equipment*, vol. 436, no. 1-2, pp. 102–110, 1999.

[5] F. A. Harrison, F. E. Christensen, W. Craig, C. Hailey, W. Baumgartner, C. Chen, J. Chonko, W. R. Cook, J. Koglin, K. K. Madsen, M. Pivavoroff, S. Boggs, and D. Smith, "Development of the heft and nustar focusing telescopes," *Experimental Astronomy*, vol. 20, no. 1-3, pp. 131–137, 2005.

[6] J. E. Koglin, H. An, K. L. Blaedel, N. F. Brejnholt, F. E. Christensen, W. W. Craig, T. A. Decker, C. J. Hailey, L. C. Hale, F. A. Harrison, C. P. Jensen, K. K. Madsen, K. Mori, M. J. Pivovaroff, G. Tajiri, and W. W. Zhang, "NuSTAR hard x-ray optics design and performance," *Optics for EUV, X-Ray, and Gamma-Ray Astronomy IV*, vol. 7437, pp. 107–114, 2009.

[7] N. Barriere, P. von Ballmoos, L. Natalucci, G. Roudil, P. Bastie, P. Courtois, M. Jentschel, N. V. Abrosimov, and J. Rousselle, "Laue lens: the challenge of focusing gamma rays," *International Conference on Space Optics ICSO 2008*, vol. 10566, pp. 16–22, 2017.

[8] J. G. Ables, "Fourier transform photography: a new method for x-ray astronomy," *Proceedings of the Astronomical Society of Australia*, vol. 1, p. 172, 1968.

[9] R. H. Dicke, "Scatter-hole cameras for x-rays and gamma rays," *The astrophysical journal*, vol. 153, p. L101, 1968.

[10] H. Barrett and F. Horrigan, "Fresnel zone plate imaging of gamma rays," *Applied Optics*, vol. 12, no. 11, pp. 2686–2702, 1973.

[11] T. A. Prince, G. J. Hurford, H. S. Hudson, and C. J. Crannell, "The rhessi imaging concept," *Solar Physics*, vol. 118, pp. 269–290, 1988.

[12] G. J. Hurford, E. J. Schmahl, R. A. Schwartz, A. J. Conway, M. J. Aschwanden, A. Csillaghy, B. R. Dennis, C. Johns-Krull, S. Krucker, R. P. Lin, J. McTiernan, T. R. Metcalf, J. Sato, and D. M. Smith, "Gamma-ray and hard x-ray imaging of solar flares," *Solar Physics*, vol. 210, pp. 61–86, 2002.

[13] K. Ziock, N. Madden, E. Hull, W. Craig, T. Lavietes, and C. Cork, "A germanium-based coded aperture imager," *IEEE Transactions on Nuclear Science*, vol. 49, no. 4, pp. 1737–1742, 2002.

[14] R. W. Todd, J. M. Nightingale, and D. B. Everett, "A proposed γ camera," *Nature*, vol. 251, no. 5471, pp. 132–134, 1974.

[15] V. Schonfelder, R. Diehl, G. G. Lichti, H. Steinle, B. N. Swanenburg, A. J. M. Deerenberg, H. Aarts, J. Lockwood, W. Webber, J. Macri, J. Ryan, G. Simpson, B. G. Taylor, K. Bennett, and M. Snelling, "The imaging compton telescope comptel on the gamma ray observatory," *IEEE Transactions on Nuclear Science*, vol. 31, no. 1, pp. 766–770, 1984.

[16] B. Phlips, W. Johnson, R. Kroeger, J. Kurfess, G. Phillips, E. Wulf, and P. Luke, "Development of germanium strip detectors for environmental remediation," *IEEE Transactions on Nuclear Science*, vol. 49, no. 2, pp. 597–600, 2002.

[17] K. Vetter, M. Burks, and L. Mihailescu, "Gamma-ray imaging with position-sensitive hpge detectors," *Nuclear Instruments and Methods in Physics Research Section A*, vol. 525, no. 1-2, pp. 322–327, 2004.

[18] L. E. Smith, *Design, modeling and performance of a hybrid portable gamma camera.* University of Michigan, 1998.

[19] L. J. Schultz, M. S. Wallace, M. C. Galassi, A. S. Hoover, M. Mocko, D. M. Palmer, S. R. Tornga, R. M. Kippen, M. V. Hynes, M. J. Toolin, *et al.*, "Hybrid coded aperture and compton imaging using an active mask," *Nuclear Instruments and Methods in Physics Research Section A: Accelerators, Spectrometers, Detectors and Associated Equipment*, vol. 608, no. 2, pp. 267–274, 2009.

[20] W. Lee, D. K. Wehe, M. Jeong, P. Barton, and J. Berry, "A dual modality gamma camera using $lacl_3$(ce) scintillator," *IEEE Transactions on Nuclear Science*, vol. 56, no. 1, pp. 308–315, 2009.

[21] D. Hellfeld, P. Barton, D. Gunter, L. Mihailescu, and K. Vetter, "A spherical active coded aperture for 4π gamma-ray imaging," *IEEE Transactions on Nuclear Science*, vol. 64, no. 11, pp. 2837–2842, 2017.

[22] C. G. Wahl, S. Brown, W. Kaye, K. Moran, F. Zhang, J. Sowers, J. M. Jaworski, Y. A. Boucher, H. Yang, T. Slatina, *et al.*, "Coded-aperture imaging with high-resolution large-volume czt," *2018 IEEE Nuclear Science Symposium and Medical Imaging Conference Proceedings (NSS/MIC)*, pp. 1–5, 2018.

[23] M. Sakai, Y. Kubota, R. K. Parajuli, M. Kikuchi, K. Arakawa, and T. Nakano, "Compton imaging with 99m tc for human imaging," *Scientific reports*, vol. 9, no. 1, pp. 1–8, 2019.

[24] E. Caroli, J. B. Stephen, G. Di Cocco, L. Natalucci, and A. Spizzichino, "Coded aperture imaging in x-and gamma-ray astronomy," *Space Science Reviews*, vol. 45, no. 3-4, pp. 349–403, 1987.

[25] K. P. Ziock, S. O'Brien, K. Schmitt, R. Venkataraman, and J. Mitchell, "Gamma-ray imaging to monitor accumulating holdup," tech. rep., Oak Ridge National Lab.(ORNL), Oak Ridge, TN (United States), 2022.

[26] M. J. DeWeert and B. P. Farm, "Lensless coded-aperture imaging with separable doubly-toeplitz masks," *Optical Engineering*, vol. 54, no. 2, p. 023102, 2015.

[27] L. Zhang, *Near field three-dimensional coded aperture techniques: theoretical and experimental exploration for applications in imaging and detection systems*. PhD thesis, Massachusetts Institute of Technology, 1998.

[28] R. Accorsi, *Design of a near-field coded aperture cameras for high-resolution medical and industrial gamma-ray imaging*. PhD thesis, Massachusetts Institute of Technology, 2001.

[29] Z. Mu, B. Hong, S. Li, and Y. Liu, "A novel three-dimensional image reconstruction method for near-field coded aperture single photon emission computerized tomography," *Medical physics*, vol. 36, no. 5, pp. 1533–1542, 2009.

[30] IAEA, *The radiological accident in Goiania*. IAEA, 1988.

[31] E. A. Frame, "Passive detection and active interrogation methods for the detection and identification of depleted uranium," 2015. not published.

[32] *Use of Nuclear Material Accounting and Control for Nuclear Security Purposes at Facilities*. No. 25-G in Implementing Guides, Vienna: INTERNATIONAL ATOMIC ENERGY AGENCY, 2015.

[33] S. Hertz and A. Roberts, "Radioactive iodine in the study of thyroid physiology: Vii. the use of radioactive iodine therapy in hyperthyroidism," *Journal of the American Medical Association*, vol. 131, no. 2, pp. 81–86, 1946.

[34] M. R. Harrison, T. Z. Wong, A. J. Armstrong, and D. J. George, "Radium-223 chloride: a potential new treatment for castration-resistant prostate cancer patients with metastatic bone disease," *Cancer management and research*, vol. 5, p. 1, 2013.

[35] E. Frame, R. Barnowski, D. Gunter, L. Mihailescu, and K. Vetter, "A dual-modality volumetric gamma-ray imager for near-field applications," *IEEE Transactions on Nuclear Science*, 2022.

[36] E. A. Frame, K. N. Bobba, D. L. Gunter, L. Mihailescu, A. P. Bidkar, R. R. Flavell, and K. Vetter, "Coded aperture and compton imaging for the development of targeted alpha-particle therapy," *under submission*, 2022.

[37] S. Poty, L. C. Francesconi, M. R. McDevitt, M. J. Morris, and J. S. Lewis, "Alpha-emitters for radiotherapy: from basic radiochemistry to clinical studies-part 1," *Journal of Nuclear Medicine*, vol. 59, no. 6, pp. 878–884, 2018.

[38] G. Makrigiorgos, S. J. Adelstein, and A. I. Kassis, "Auger electron emitters: insights gained from in vitro experiments," *Radiation and environmental biophysics*, vol. 29, no. 2, pp. 75–91, 1990.

[39] R. B. Michel, M. W. Brechbiel, and M. J. Mattes, "A comparison of 4 radionuclides conjugated to antibodies for single-cell kill," *Journal of Nuclear Medicine*, vol. 44, no. 4, pp. 632–640, 2003.

[40] T. G. Turkington, M. R. Zalutsky, R. J. Jaszczak, P. K. Garg, G. Vaidyanathan, and R. E. Coleman, "Measuring astatine-211 distributions with spect," *Physics in Medicine & Biology*, vol. 38, no. 8, p. 1121, 1993.

[41] E. L. Johnson, T. G. Turkington, R. J. Jaszczak, D. R. Gilland, G. Vaidyanathan, K. L. Greer, R. E. Coleman, and M. R. Zalutsky, "Quantitation of 211at in small volumes for evaluation of targeted radiotherapy in animal models," *Nuclear medicine and biology*, vol. 22, no. 1, pp. 45–54, 1995.

[42] A. Omata, M. Masubuchi, N. Koshikawa, J. Kataoka, H. Kato, A. Toyoshima, T. Teramoto, K. Ooe, Y. Liu, K. Matsunaga, *et al.*, "Multi-modal 3d imaging of radionuclides using multiple hybrid compton cameras," *Scientific Reports*, vol. 12, no. 1, pp. 1–9, 2022.

[43] M. Masubuchi, A. Omata, N. Koshikawa, J. Kataoka, H. Kato, A. Toyoshima, K. Ooe, D. Katayama, T. Teramoto, K. Matsunaga, *et al.*, "Wide-band x-ray and gamma-ray imaging of living mouse to reveal pharmacokinetics of at-211," *Nuclear Instruments and Methods in Physics Research Section A: Accelerators, Spectrometers, Detectors and Associated Equipment*, p. 167581, 2022.

[44] S. Mirzadeh, "Generator-produced alpha-emitters," *Applied radiation and isotopes*, vol. 49, no. 4, pp. 345–349, 1998.

[45] M. Zalutsky and M. Pruszynski, "Astatine-211: production and availability," *Current radiopharmaceuticals*, vol. 4, no. 3, pp. 177–185, 2011.

[46] A. Robertson, C. F. Ramogida, P. Schaffer, and V. Radchenko, "Development of 225ac radiopharmaceuticals: Triumf perspectives and experiences," *Current Radiopharmaceuticals*, vol. 11, no. 3, pp. 156–172, 2018.

[47] J. Morrell, *Next-Generation Isotope Production via Deuteron Breakup*. University of California, Berkeley, 2021.

[48] M. R. Zalutsky, D. A. Reardon, G. A, R. E. C, A. H. Friedman, H. S. Friedman, R. E. McLendon, T. Z. Wong, and D. D. Bigner, "Clinical experience with alpha-particle-emitting 211at: treatment of recurrent brain tumor patients with 211at-labeled chimeric antitenascin monoclonal antibody 81c6," *Journal of Nuclear Medicine*, vol. 49, no. 1, pp. 30–38, 2008.

[49] H. Andersson, E. Cederkrantz, T. Back, C. Divgi, J. Elgqvist, J. Himmelman, G. Horvath, L. Jacobsson, H. Jensen, S. Lindegren, *et al.*, "Intraperitoneal alpha-particle radioimmunotherapy of ovarian cancer patients," *Journal of Nuclear Medicine*, vol. 50, no. 7, pp. 1153–1160, 2009.

[50] J. G. Jurcic, S. M. Larson, G. Sgouros, M. R. McDevitt, R. D. Finn, C. R. Divgi, M. Ballangrud, K. A. Hamacher, D. Ma, J. L. Humm, *et al.*, "Targeted α particle immunotherapy for myeloid leukemia," *Blood, The Journal of the American Society of Hematology*, vol. 100, no. 4, pp. 1233–1239, 2002.

[51] C. Kratochwil, F. Bruchertseifer, F. L. Giesel, M. Weis, F. A. Verburg, F. Mottaghy, K. Kopka, C. Apostolidis, U. Haberkorn, and A. Morgenstern, "225ac-psma-617 for psma-targeted α-radiation therapy of metastatic castration-resistant prostate cancer," *Journal of Nuclear Medicine*, vol. 57, no. 12, pp. 1941–1944, 2016.

[52] A. Morgenstern, C. Apostolidis, C. Kratochwil, M. Sathekge, L. Krolicki, and F. Bruchertseifer, "An overview of targeted alpha therapy with 225actinium and 213bismuth," *Current Radiopharmaceuticals*, vol. 11, no. 3, pp. 200–208, 2018.

[53] T. L. Rosenblat, M. R. McDevitt, D. A. Mulford, N. Pandit-Taskar, C. R. Divgi, K. S. Panageas, M. L. Heaney, S. Chanel, A. Morgenstern, G. Sgouros, *et al.*, "Sequential cytarabine and α-particle immunotherapy with bismuth-213–lintuzumab (hum195) for acute myeloid leukemia," *Clinical Cancer Research*, vol. 16, no. 21, pp. 5303–5311, 2010.

[54] M. Berger, J. Jurcic, and D. Scheinberg, "Efficacy of ac-225-labeled anti-cd33 antibody in acute myeloid leukemia (aml) correlates with peripheral blast count," *Proceedings of the 10th International Symposium on Targeted Alpha Therapy, Kanazawa, Japan*, p. 22, 2017.

[55] D. Schmidt, F. Neumann, C. Antke, C. Apostolidis, S. Martin, A. Morgenstern, R. Molinet, S. Heeger, R. Kronenwett, H. W. Müller, *et al.*, "Phase 1 clinical study on alpha-therapy for non-hodgkin lymphoma," *4th Alpha-Immunotherapy Symposium*, p. 12, 2004.

[56] B. J. Allen, C. Raja, S. Rizvi, Y. Li, W. Tsui, P. Graham, J. Thompson, R. Reisfeld, J. Kearsley, A. Morgenstern, *et al.*, "Intralesional targeted alpha therapy for metastatic melanoma," *Cancer biology & therapy*, vol. 4, no. 12, pp. 1318–1324, 2005.

[57] C. Raja, P. Graham, S. Rizvi, E. Song, H. Goldsmith, J. Thompson, A. Bosserhoff, A. Morgenstern, C. Apostolidis, J. Kearsley, *et al.*, "Interim analysis of toxicity and response in phase 1 trial of systemic targeted alpha therapy for metastatic melanoma," *Cancer biology & therapy*, vol. 6, no. 6, pp. 846–852, 2007.

[58] B. J. Allen, A. A. Singla, S. Rizvi, P. Graham, F. Bruchertseifer, C. Apostolidis, and A. Morgenstern, "Analysis of patient survival in a phase i trial of systemic targeted α-therapy for metastatic melanoma," *Immunotherapy*, vol. 3, no. 9, pp. 1041–1050, 2011.

[59] M. E. Autenrieth, T. Horn, F. Kurtz, K. Nguyen, A. Morgenstern, F. Bruchertseifer, M. Schwaiger, M. Blechert, C. Seidl, R. Senekowitsch-Schmidtke, *et al.*, "Intravesical radioimmunotherapy of carcinoma in situ of the urinary bladder after bcg failure," *Der Urologe. Ausg. A*, vol. 56, no. 1, pp. 40–43, 2017.

[60] M. E. Autenrieth, C. Seidl, F. Bruchertseifer, T. Horn, F. Kurtz, B. Feuerecker, C. D'Alessandria, C. Pfob, C. Nekolla, Sand Apostolidis, *et al.*, "Treatment of carcinoma in situ of the urinary bladder with an alpha-emitter immunoconjugate targeting the epidermal growth factor receptor: a pilot study," *European journal of nuclear medicine and molecular imaging*, vol. 45, no. 8, pp. 1364–1371, 2018.

[61] S. Kneifel, D. Cordier, S. Good, M. Ionescu, A. Ghaffari, S. Hofer, M. Kretzschmar, M. Tolnay, C. Apostolidis, B. Waser, *et al.*, "Local targeting of malignant gliomas by the diffusible peptidic vector 1, 4, 7, 10-tetraazacyclododecane-1-glutaric acid-4, 7, 10-triacetic acid-substance p," *Clinical cancer research*, vol. 12, no. 12, pp. 3843–3850, 2006.

[62] D. Cordier, F. Forrer, F. Bruchertseifer, A. Morgenstern, C. Apostolidis, S. Good, J. Müller-Brand, H. Mäcke, J. C. Reubi, and A. Merlo, "Targeted alpha-radionuclide therapy of functionally critically located gliomas with 213 bi-dota-[thi 8, met (o 2) 11]-substance p: a pilot trial," *European journal of nuclear medicine and molecular imaging*, vol. 37, no. 7, pp. 1335–1344, 2010.

[63] D. Cordier, F. Forrer, S. Kneifel, M. Sailer, H. Mariani, Land Macke, J. Muller-Brand, and A. Merlo, "Neoadjuvant targeting of glioblastoma multiforme with radiolabeled dotaga-substance p-results from a phase i study," *Journal of neuro-oncology*, vol. 100, no. 1, pp. 129–136, 2010.

[64] L. Krolicki, F. Bruchertseifer, J. Kunikowska, H. Koziara, B. Królicki, M. Jakuciński, D. Pawlak, C. Apostolidis, S. Mirzadeh, R. Rola, *et al.*, "Prolonged survival in secondary glioblastoma following local injection of targeted alpha therapy with 213 bi-substance p analogue," *European journal of nuclear medicine and molecular imaging*, vol. 45, no. 9, pp. 1636–1644, 2018.

[65] L. Królicki, F. Bruchertseifer, J. Kunikowska, H. Koziara, B. Królicki, M. Jakuciński, D. Pawlak, C. Apostolidis, S. Mirzadeh, R. Rola, *et al.*, "Safety and efficacy of targeted alpha therapy with 213 bi-dota-substance p in recurrent glioblastoma," *European journal of nuclear medicine and molecular imaging*, vol. 46, no. 3, pp. 614–622, 2019.

[66] L. Królicki, J. Kunikowska, F. Bruchertseifer, H. Koziara, B. Królicki, M. Jakuciński, D. Pawlak, R. Rola, A. Morgenstern, E. Rosiak, *et al.*, "225ac-and 213bi-substance p analogues for glioma therapy," *Seminars in Nuclear Medicine*, vol. 50, no. 2, pp. 141–151, 2020.

[67] C. Kratochwil, F. L. Giesel, F. Bruchertseifer, W. Mier, C. Apostolidis, R. Boll, K. Murphy, U. Haberkorn, and A. Morgenstern, "213 bi-dotatoc receptor-targeted alpha-radionuclide therapy induces remission in neuroendocrine tumours refractory to beta radiation: a first-in-human experience," *European journal of nuclear medicine and molecular imaging*, vol. 41, no. 11, pp. 2106–2119, 2014.

[68] C. Kratochwil, F. Bruchertseifer, F. Giesel, C. Apostolidis, U. Haberkorn, and A. Morgenstern, "Ac-225-dotatoc-an empiric dose finding for alpha particle emitter based radionuclide therapy of neuroendocrine tumors," *Journal of Nuclear Medicine*, vol. 56, no. supplement 3, pp. 1232–1232, 2015.

[69] C. Kratochwil, F. Bruchertseifer, H. Rathke, M. Bronzel, C. Apostolidis, W. Weichert, U. Haberkorn, F. L. Giesel, and A. Morgenstern, "Targeted alpha therapy of mcrpc with 225actinium-psma-617: dosimetry estimate and empirical dose finding," *Journal of Nuclear Medicine*, pp. jnumed–117, 2017.

[70] C. Kratochwil, F. Bruchertseifer, H. Rathke, M. Hohenfellner, F. L. Giesel, U. Haberkorn, and A. Morgenstern, "Targeted alpha therapy of mcrpc with 225actinium-psma-617: swimmer-plot analysis suggests efficacy regarding duration of tumor-control," *Journal of Nuclear Medicine*, pp. jnumed–117, 2018.

[71] L. Z. Benet and P. Zia-Amirhosseini, "Basic principles of pharmacokinetics," *Toxicologic pathology*, vol. 23, no. 2, pp. 115–123, 1995.

[72] P. E. Borchardt, R. R. Yuan, M. Miederer, M. R. McDevitt, and D. A. Scheinberg, "Targeted actinium-225 in vivo generators for therapy of ovarian cancer," *Cancer Research*, vol. 63, no. 16, pp. 5084–5090, 2003.

[73] J. S. Jaggi, S. V. Seshan, M. R. McDevitt, K. LaPerle, G. Sgouros, and D. A. Scheinberg, "Renal tubulointerstitial changes after internal irradiation with alpha-particle–emitting actinium daughters," *Journal of the American Society of Nephrology*, vol. 16, no. 9, pp. 2677–2689, 2005.

[74] E. Salvanou, D. Stellas, C. Tsoukalas, B. Mavroidi, M. Paravatou-Petsotas, N. Kalogeropoulos, S. Xanthopoulos, G. Denat, Fand Laurent, R. Bazzi, *et al.*, "A proof-of-concept study on the therapeutic potential of au nanoparticles radiolabeled with the alpha-emitter actinium-225," *Pharmaceutics*, vol. 12, no. 2, p. 188, 2020.

[75] Y. Seo, "Quantitative imaging of alpha-emitting therapeutic radiopharmaceuticals," *Nuclear medicine and molecular imaging*, vol. 53, no. 3, pp. 182–188, 2019.

[76] S. R. Cherry and S. S. Gambhir, "Use of positron emission tomography in animal research," *ILAR journal*, vol. 42, no. 3, pp. 219–232, 2001.

[77] S. Tong, A. M. Alessio, and P. E. Kinahan, "Image reconstruction for pet/ct scanners: past achievements and future challenges," *Imaging in medicine*, vol. 2, no. 5, p. 529, 2010.

[78] E. P. Visser, J. A. Disselhorst, M. Brom, P. Laverman, M. Gotthardt, W. Oyen, and O. C. Boerman, "Spatial resolution and sensitivity of the inveon small-animal pet scanner," *Journal of Nuclear Medicine*, vol. 50, no. 1, pp. 139–147, 2009.

[79] S. España, R. Marcinkowski, V. Keereman, S. Vandenberghe, and R. Van Holen, "Digipet: sub-millimeter spatial resolution small-animal pet imaging using thin monolithic scintillators," *Physics in Medicine & Biology*, vol. 59, no. 13, p. 3405, 2014.

[80] S. Abbaszadeh, Y. Gu, P. D. Reynolds, and C. S. Levin, "Characterization of a sub-assembly of 3d position sensitive cadmium zinc telluride detectors and electronics from a sub-millimeter resolution pet system," *Physics in Medicine & Biology*, vol. 61, no. 18, p. 6733, 2016.

[81] P. P. Bruyant, "Analytic and iterative reconstruction algorithms in spect," *Journal of Nuclear Medicine*, vol. 43, no. 10, pp. 1343–1358, 2002.

[82] M. Lyra and A. Ploussi, "Filtering in spect image reconstruction," *International Journal of Biomedical Imaging*, vol. 2011, 2011.

[83] F. J. Beekman, F. van der Have, B. Vastenhouw, A. van der Linden, P. P. van Rijk, J. P. H. Burbach, and M. P. Smidt, "U-spect-i: a novel system for submillimeter-resolution tomography with radiolabeled molecules in mice," *Journal of Nuclear Medicine*, vol. 46, no. 7, pp. 1194–1200, 2005.

[84] B. L. Franc, P. D. Acton, C. Mari, and B. H. Hasegawa, "Small-animal spect and spect/ct: important tools for preclinical investigation," *Journal of nuclear medicine*, vol. 49, no. 10, pp. 1651–1663, 2008.

[85] T. A. Bailey, V. Mocko, K. M. Shield, D. D. An, A. C. Akin, E. R. Birnbaum, M. Brugh, J. C. Cooley, J. W. Engle, M. E. Fassbender, *et al.*, "Developing the 134ce and 134la pair as companion positron emission tomography diagnostic isotopes for 225ac and 227th radiotherapeutics," *Nature Chemistry*, vol. 13, no. 3, pp. 284–289, 2021.

[86] M. F. Smith, R. J. Jaszczak, and H. Wang, "Pinhole aperture design for i-131 tumor imaging," *IEEE Transactions on Nuclear Science*, vol. 44, no. 3, pp. 1154–1160, 1997.

[87] S. Glasstone and A. Sesonske, *Nuclear Reactor Engineering*. Van Nostrand Reinhold Company, 1967.

[88] G. F. Knoll, *Radiation Detection and Measurement*. John Wiley & Sons, 2010.

[89] W. Heitler, *The quantum theory of radiation*. Courier Corporation, 1984.

[90] W. Shockley, "Currents to conductors induced by a moving point charge," *Journal of applied physics*, vol. 9, no. 10, pp. 635–636, 1938.

[91] S. Ramo, "Currents induced by electron motion," *Proceedings of the IRE*, vol. 27, no. 9, pp. 584–585, 1939.

[92] Z. He, "Review of the shockley–ramo theorem and its application in semiconductor gamma-ray detectors," *Nuclear Instruments and Methods in Physics Research Section A: Accelerators, Spectrometers, Detectors and Associated Equipment*, vol. 463, no. 1-2, pp. 250–267, 2001.

[93] C. W. Fabjan and H. Schopper, *Particle Physics Reference Library: Volume 2: Detectors for Particles and Radiation*, vol. 2. Springer Nature, 2020.

[94] L. L. N. Laboratory, *Technical Report Compact Compton Imager*. 2005.

[95] L. O. Supic, *Enhancing gamma ray detection and imaging characteristics of segmented Ge detectors employing signal decomposition algorithms.* PhD thesis, 2014.

[96] D. H. Chivers, *Pulse shape parameterization and signal decomposition for high sensitivity Compton imaging using high-purity germanium double-sided strip detectors.* PhD thesis, 2008.

[97] S. R. Cherry, J. A. Sorenson, and M. E. Phelps, *Physics in nuclear medicine.* Elsevier Health Sciences, 2012.

[98] J. L. Prince and J. M. Links, *Medical imaging signals and systems.* Pearson Prentice Hall Upper Saddle River, 2006.

[99] G. T. Herman and A. Lent, "Iterative reconstruction algorithms," *Computers in biology and medicine*, vol. 6, no. 4, pp. 273–294, 1976.

[100] M. Beister, D. Kolditz, and W. A. Kalender, "Iterative reconstruction methods in x-ray ct," *Physica medica*, vol. 28, no. 2, pp. 94–108, 2012.

[101] D. L. Gunter, "Applied nuclear physics derivations," 2022. lecture notes.

[102] L. A. Shepp and Y. Vardi, "Maximum likelihood reconstruction for emission tomography," *IEEE Trans Med Imaging*, pp. 112–113, 1982.

[103] C. Brown, *Multiplex imaging with random arrays.* PhD thesis, The University of Chicago, 1972.

[104] R. L. Blake, A. J. Burek, E. Fenimore, and R. Puetter, "Solar x-ray photography with multiplex pin-hole camera," *Review of Scientific Instruments*, vol. 45, no. 4, pp. 513–516, 1974.

[105] E. E. Fenimore and T. M. Cannon, "Coded aperture imaging with uniformly redundant arrays," *Applied optics*, vol. 17, no. 3, pp. 337–347, 1978.

[106] R. Accorsi, F. Gasparini, and R. C. Lanza, "Optimal coded aperture patterns for improved snr in nuclear medicine imaging," *Nuclear Instruments and Methods in Physics Research Section A: Accelerators, Spectrometers, Detectors and Associated Equipment*, vol. 474, no. 3, pp. 273–284, 2001.

[107] E. E. Fenimore, "Coded aperture imaging: predicted performance of uniformly redundant arrays," *Applied Optics*, vol. 17, no. 22, pp. 3562–3570, 1978.

[108] L. Mihailescu, K. M. Vetter, M. T. Burks, E. L. Hull, and W. W. Craig, "Speir: a ge compton camera," *Nuclear Instruments and Methods in Physics Research Section A: Accelerators, Spectrometers, Detectors and Associated Equipment*, vol. 570, no. 1, pp. 89–100, 2007.

[109] D. Brusa, G. Stutz, J. A. Riveros, J. M. Fernández-Varea, and F. Salvat, "Fast sampling algorithm for the simulation of photon compton scattering," *Nuclear Instruments and Methods in Physics Research Section A: Accelerators, Spectrometers, Detectors and Associated Equipment*, vol. 379, no. 1, pp. 167–175, 1996.

[110] C. E. Ordonez, A. Bolozdynya, and W. Chang, "Doppler broadening of energy spectra in compton cameras," *1997 IEEE Nuclear Science Symposium Conference Record*, vol. 2, pp. 1361–1365, 1997.

[111] F. Biggs, L. B. Mendelsohn, and J. B. Mann, "Hartree-fock compton profiles for the elements," *Atomic data and nuclear data tables*, vol. 16, no. 3, pp. 201–309, 1975.

[112] R. W. Barnowski, *Development and Evaluation of Real-Time Volumetric Compton Gamma-Ray Imaging*. PhD thesis, University of California, Berkeley, 2016.

[113] S. R. Gottesman and E. E. Fenimore, "New family of binary arrays for coded aperture imaging," *Applied optics*, vol. 28, no. 20, pp. 4344–4352, 1989.

[114] A. Busboom, H. Elders-Boll, and H. D. Schotten, "Uniformly redundant arrays," *Experimental Astronomy*, vol. 8, no. 2, pp. 97–123, 1998.

[115] A. R. Gourlay and J. B. Stephen, "Geometric coded aperture masks," *Applied optics*, vol. 22, no. 24, pp. 4042–4047, 1983.

[116] K. Byard, "Index class apertures - a class of flexible coded aperture," *Applied Optics*, vol. 51, no. 16, pp. 3453–3460, 2012.

[117] A. Busboom, H. Elders-Boll, and H. D. Schotten, "Combinatorial design of near-optimum masks for coded aperture imaging," *1997 IEEE International Conference on Acoustics, Speech, and Signal Processing*, vol. 4, pp. 2817–2820, 1997.

[118] G. Dueck, "New optimization heuristics: The great deluge algorithm and the record-to-record travel," *Journal of Computational physics*, vol. 104, no. 1, pp. 86–92, 1993.

[119] M. A. Alnafea, "Non monte carlo method for intrinsic investigation of the potential use of modified uniformly redundant arrays (muras) coded apertures for early breast tumor imaging," *J Nucl Med Radiol Radiat Ther*, 2021.

[120] V. T. Jordanov and G. F. Knoll, "Digital synthesis of pulse shapes in real time for high resolution radiation spectroscopy," *Nuclear Instruments and Methods in Physics Research Section A: Accelerators, Spectrometers, Detectors and Associated Equipment*, vol. 345, no. 2, pp. 337–345, 1994.

[121] V. B. Berestetskii, E. M. Lifshitz, and L. P. Pitaevskii, *Quantum Electrodynamics: Volume 4*, vol. 4. Butterworth-Heinemann, 1982.

[122] M. Berger, J. Hubbell, S. Seltzer, J. Coursey, and D. Zucker, "Xcom: Photon cross section database (version 1.2)," 1999-01-01 1999.

[123] Z. Mu and Y. H. Liu, "Aperture collimation correction and maximum-likelihood image reconstruction for near-field coded aperture imaging of single photon emission computerized tomography," *IEEE transactions on medical imaging*, vol. 25, no. 6, pp. 701–711, 2006.

[124] S. Berrim, A. Lansiart, and J. L. Moretti, "Implementing of maximum likelihood in tomographical coded aperture," *Proceedings of 3rd IEEE International Conference on Image Processing*, vol. 2, pp. 745–748, 1996.

[125] D. Gunter, R. Barnowski, A. Haefner, D. Hellfeld, K. Knecht, L. Michailescu, E. Frame, R. Pavlovski, T. Joshi, M. Bandstra, J. Vavrek, B. Quiter, and K. Vetter, *Modeling the Compton Camera Response for Extended Voxel Sources*. Lawerence Berekely National Laboratory, 2021. internal report.

[126] L. Parra and H. H. Barrett, "List-mode likelihood: Em algorithm and image quality estimation demonstrated on 2-d pet," *IEEE transactions on medical imaging*, vol. 17, no. 2, pp. 228–235, 1998.

[127] P. A. Russo, "Gamma-ray measurements of holdup plant-wide: application guide for portable, generalized approach," *LA-14206*, 2005.

[128] R. Venkataraman, K. P. Ziock, M. Blackston, A. Lousteau, S. Croft, K. Bledsoe, J. Lefebvre, J. Preston, and J. Knowles, "Gamma ray imaging based methods to improve the accuracy of uranium holdup quantification," tech. rep., Oak Ridge Y-12 Plant (Y-12), Oak Ridge, TN (United States), 2020.

[129] J. Ahrens, B. Geveci, and C. Law, "Paraview: An end-user tool for large data visualization," *The visualization handbook*, vol. 717, no. 8, 2005.

[130] J. P. Pouget, I. Navarro-Teulon, M. Bardies, N. Chouin, G. Cartron, A. Pelegrin, and D. Azria, "Clinical radioimmunotherapy-the role of radiobiology," *Nature reviews Clinical oncology*, vol. 8, no. 12, pp. 720–734, 2011.

[131] C. Parker, V. Lewington, N. Shore, C. Kratochwil, M. Levy, O. Linden, W. Noordzij, J. Park, F. Saad, T. A. T. W. Group, *et al.*, "Targeted alpha therapy, an emerging class of cancer agents: a review," *JAMA oncology*, vol. 4, no. 12, pp. 1765–1772, 2018.

[132] M. R. McDevitt and D. A. Scheinberg, "Ac-225 and her daughters: the many faces of shiva," *Cell death and differentiation*, vol. 9, no. 6, pp. 593–594, 2002.

[133] H. Song, R. F. Hobbs, R. Vajravelu, D. L. Huso, C. Esaias, C. Apostolidis, A. Morgenstern, and G. Sgouros, "Radioimmunotherapy of breast cancer metastases with alpha-particle emitter 225ac: comparing efficacy with 213bi and 90y," *Cancer research*, vol. 69, no. 23, pp. 8941–8948, 2009.

[134] J. Singh Jaggi, B. J. Kappel, M. R. McDevitt, G. Sgouros, C. D. Flombaum, C. Cabassa, and D. A. Scheinberg, "Efforts to control the errant products of a targeted in vivo generator," *Cancer research*, vol. 65, no. 11, pp. 4888–4895, 2005.

[135] R. M. De Kruijff, H. T. Wolterbeek, and A. G. Denkova, "A critical review of alpha radionuclide therapy-how to deal with recoiling daughters?," *Pharmaceuticals*, vol. 8, no. 2, pp. 321–336, 2015.

[136] S. R. Meikle, P. Kench, and R. B. Kassiou, Mand Banati, "Small animal spect and its place in the matrix of molecular imaging technologies," *Physics in Medicine & Biology*, vol. 50, no. 22, p. R45, 2005.

[137] D. P. McElroy, L. R. MacDonald, F. J. Beekman, Y. Wang, B. E. Patt, J. S. Iwanczyk, B. Tsui, and E. J. Hoffman, "Performance evaluation of a-spect: a high resolution desktop pinhole spect system for imaging small animals," *IEEE Transactions on Nuclear Science*, vol. 49, no. 5, pp. 2139–2147, 2002.

[138] F. Van Der Have, B. Vastenhouw, R. M. Ramakers, W. Branderhorst, J. O. Krah, C. Ji, S. G. Staelens, and F. J. Beekman, "U-spect-ii: an ultra-high-resolution device for molecular small-animal imaging," *Journal of Nuclear Medicine*, vol. 50, no. 4, pp. 599–605, 2009.

[139] K. Vetter, M. Burks, C. Cork, M. Cunningham, D. Chivers, E. Hull, T. Krings, H. Manini, L. Mihailescu, K. Nelson, *et al.*, "High-sensitivity compton imaging with position-sensitive si and ge detectors," *Nuclear Instruments and Methods in Physics Research Section A: Accelerators, Spectrometers, Detectors and Associated Equipment*, vol. 579, no. 1, pp. 363–366, 2007.

[140] T. C. Nurdan, K. Nurdan, A. B. Brill, and A. H. Walenta, "Design criteria for a high energy compton camera and possible application to targeted cancer therapy," *Journal of Instrumentation*, vol. 10, no. 07, p. C07018, 2015.

[141] K. Bobba, A. Bidkar, S. Wang, S. Bidlingmaier, R. Tang, Y. Su, H. VanBrocklin, B. Liu, Y. Seo, and R. Flavell, "Influence of short peg linkers on biodistribution of 225ac-macropays5, an immunoconjugate for treating cd46 expressing cancer," *Nuclear Medicine and Biology*, vol. 108, p. S53, 2022.

[142] A. Bidkar, S. Wang, K. Bobba, S. Bidlingmaier, Y. Su, E. Egusa, R. Tang, J. Chou, R. Aggarwal, J. He, *et al.*, "Cd46 targeted, actinium-225 labelled antibody for treatment of prostate cancer xenografts," *Nuclear Medicine and Biology*, vol. 108, p. S31, 2022.

[143] S. Wang, J. Li, J. Hua, Y. Su, D. R. Beckford-Vera, W. Zhao, M. Jayaraman, T. L. Huynh, N. Zhao, Y. Wang, *et al.*, "Molecular imaging of prostate cancer targeting cd46 using immunopetmolecular imaging of prostate cancer targeting cd46," *Clinical Cancer Research*, vol. 27, no. 5, pp. 1305–1315, 2021.

[144] J. W. Wallis, T. R. Miller, C. A. Lerner, and E. C. Kleerup, "Three-dimensional display in nuclear medicine," *IEEE transactions on medical imaging*, vol. 8, no. 4, pp. 297–230, 1989.

[145] Hidex, "Hidex automatic gamma counter."

[146] D. N. Pandya, R. Hantgan, M. M. Budzevich, N. D. Kock, D. L. Morse, I. Batista, A. Mintz, K. C. Li, and T. J. Wadas, "Preliminary therapy evaluation of 225ac-dota-c (rgdyk) demonstrates that cerenkov radiation derived from 225ac daughter decay can be detected by optical imaging for in vivo tumor visualization," *Theranostics*, vol. 6, no. 5, p. 698, 2016.

[147] C. Yoon, S. Jo, Y. Cho, N. Kim, and T. Lee, "Estimate of the 225ac radioactive isotope distribution by means of doi compton imaging in targeted alpha radiotherapy: A monte carlo simulation," *Journal of the Korean Physical Society*, vol. 76, no. 10, pp. 954–960, 2020.

[148] J. Caravaca, Y. Huh, G. T. Gullberg, and Y. Seo, "Compton and proximity imaging of 225ac in vivo with a czt gamma camera: a proof of principle with simulations," *IEEE Transactions on Radiation and Plasma Medical Sciences*, 2022.

[149] R. Accorsi, F. Gasparini, and R. C. Lanza, "A coded aperture for high-resolution nuclear medicine planar imaging with a conventional anger camera: experimental results," *IEEE transactions on nuclear science*, vol. 48, no. 6, pp. 2411–2417, 2001.

[150] R. Accorsi, L. Celentano, P. Laccetti, R. C. Lanza, M. Marotta, G. Mettivier, M. C. Montesi, G. Roberti, and P. Russo, "High-resolution ^{125}i small animal imaging with a coded aperture and a hybrid pixel detector," *IEEE Transactions on Nuclear Science*, vol. 55, no. 1, pp. 481–490, 2008.

[151] A. Robertson, C. F. Ramogida, C. Rodriguez-Rodriguez, S. Blinder, P. Kunz, V. Sossi, and P. Schaffer, "Multi-isotope spect imaging of the 225ac decay chain: feasibility studies," *Physics in Medicine & Biology*, vol. 62, no. 11, p. 4406, 2017.

[152] L. Cai, E. M. Zannoni, X. Nie, and L. J. Meng, "Hyperspectral single photon imaging of targeted alpha therapy," 2021.

[153] T. Ito and S. Fujimura, "Improvement on depth resolution and reduction of poisson noise in coded aperture emission ct," *Proceedings of 3rd IEEE International Conference on Image Processing*, vol. 2, pp. 757–760, 1996.

[154] M. Amman and P. N. Luke, "Three-dimensional position sensing and field shaping in orthogonal-strip germanium gamma-ray detectors," *Nuclear Instruments and Methods in Physics Research Section A: Accelerators, Spectrometers, Detectors and Associated Equipment*, vol. 452, no. 1-2, pp. 155–166, 2000.

[155] J. Zhang, E. M. Zannoni, Y. Du, E. Frey, and L. J. Meng, "Alpha-spect: Hyperspectral single photon imaging of targeted α-emission therapy," 2019.

Appendix A

Image Resolution Analysis

The following analyzes the impact of various design parameters on the coded aperture and Compton image resolutions.

The coded aperture image resolution δr_{ca} can be approximated as:

$$\delta r_{ca} \approx \left(\frac{1}{m-1}\right)\sqrt{\left[(m)\,(w_m)\right]^2 + w_d^2} \tag{A.1}$$

in FWHM. Here m is the magnification factor, w_m is the width of the mask pixels, and w_d is the lateral position resolution of the detector in FWHM. For all practical purposes, w_d can be approximated as the strip pitch of the DSSD. According to the above, the coded aperture resolution can be improved by decreasing both w_d and w_m. The current system has $w_d = w_m = 2$ mm. By employing a strip pitch of 0.5 mm with mask elements to match, the coded aperture resolution would improve by about 75%:

$$\delta r_{ca}\,(w_d = 2 \text{ mm},\ w_m = 2 \text{ mm},\ m = 1.5) \approx 6.9 \text{ mm} \tag{A.2}$$

$$\delta r_{ca}\,(w_d = 0.5 \text{ mm},\ w_m = 0.5 \text{ mm},\ m = 1.5) \approx 1.7 \text{ mm} \tag{A.3}$$

at a fixed magnification of $m = 1.5$. This magnification was employed for the small animal measurements in Section 5.2 and was determined as follows:

$$m = 1 + \frac{b}{a} = 1 + \frac{50}{95} = 1.5 \tag{A.4}$$

where a is the mask-to-detector distance and b is the source-to-mask distance. Further improvements to the coded aperture resolution can be realized by increasing the magnification factor m. If $m = 3$ were realized, then the coded aperture resolution would improve by an additional 50%:

$$\delta r_{ca}\,(w_d = 0.5 \text{ mm},\ w_m = 0.5 \text{ mm},\ m = 1.5) \approx 1.7 \text{ mm} \tag{A.5}$$

$$\delta r_{ca}\,(w_d = 0.5 \text{ mm},\ w_m = 0.5 \text{ mm},\ m = 3) \approx 0.79 \text{ mm} \tag{A.6}$$

at a fixed $w_d = w_m = 0.5$ mm.

The Compton image resolution δr_{ca} can be approximated as:

$$\delta r_{ci} \approx (2z)\tan\left(\frac{\delta\theta}{2}\right) \tag{A.7}$$

in FWHM. Here $\delta\theta$ is the angular resolution of the Compton imager and z is the source-to-detector distance. The angular resolution $\delta\theta$ can be improved by reducing the strip pitch of the detectors. Figure A.1 shows simulated ARM distributions for DSSDs with strip pitches of 2 mm and 0.5 mm at a photon energy of 440 keV. Note the FWHM of the distribution narrows as the pitch decreases. The FWHMs provide an estimate of $\delta\theta$ and were found to be 6.7° and 3.7° for 2 mm and 0.5 mm, respectively. This yields a 40% improvement in the Compton image resolution:

$$\delta r_{ci}\left(\delta\theta|_{E_\gamma=440\text{ keV},\ w_d=2\text{ mm}} = 6.7^\circ,\ z = 35\text{ mm}\right) \approx 4.1\text{ mm} \tag{A.8}$$

$$\delta r_{ci}\left(\delta\theta|_{E_\gamma=440\text{ keV},\ w_d=0.5\text{ mm}} = 3.7^\circ,\ z = 35\text{ mm}\right) \approx 2.3\text{ mm} \tag{A.9}$$

at a fixed source-to-detector distance of $z = 35$ mm. This distance was employed for the small animal measurements in Section 5.2. If $z = 20$ mm were realized, then the Compton resolution would improve by an additional 40%:

$$\delta r_{ci}\left(\delta\theta|_{E_\gamma=440\text{ keV},\ w_d=0.5\text{ mm}} = 3.7^\circ,\ z = 35\text{ mm}\right) \approx 2.3\text{ mm} \tag{A.10}$$

$$\delta r_{ci}\left(\delta\theta|_{E_\gamma=440\text{ keV},\ w_d=0.5\text{ mm}} = 3.7^\circ,\ z = 20\text{ mm}\right) \approx 1.3\text{ mm} \tag{A.11}$$

at a fixed angular resolution of $\delta\theta = 3.7^\circ$.

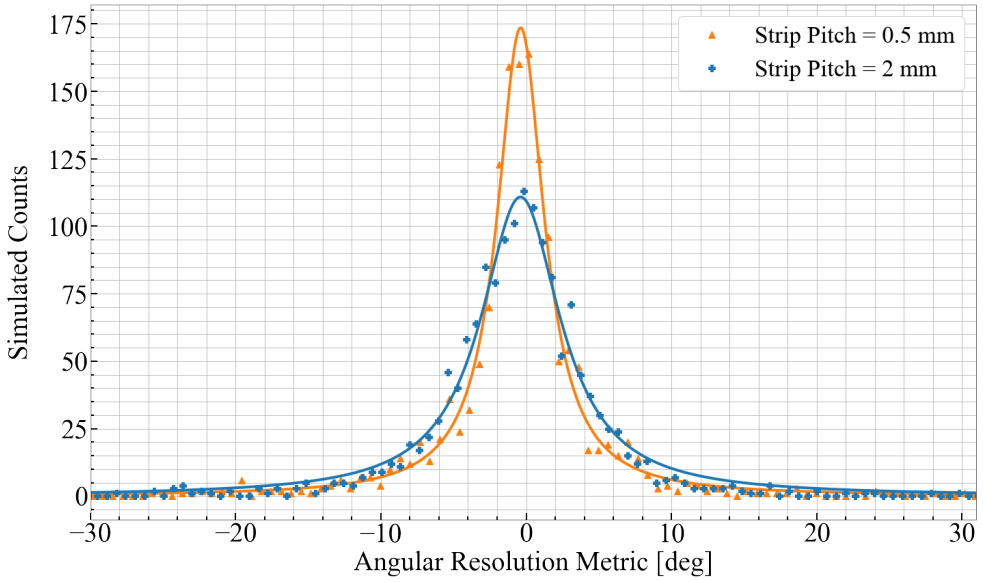

Figure A.1: ARM distributions at 440 keV for different strip pitches: (a) 0.5 mm (in blue) and (b) 2 mm (in orange) from simulated (Geant4) Compton data.